DEVELOPMENT OF INORGANIC-ORGANIC HYBRID MATERIALS FOR WASTE WATER TREATMENT

SUN JIULONG

(*B.Sc. QUST*)

A THESIS SUBMITTED

FOR THE DEGREE OF DOCTOR OF PHILOSOPHY

DEPARTMENT OF CHEMISTRY

NATIONAL UNIVERSITY OF SINGAPORE

2014

Declaration

I hereby declare that this thesis is my original work and it has been written by me in its entirety, under the supervision of A/P Stephan Jaenicke, (in the laboratory catalysis lab), Chemistry Department, National University of Singapore, between 10/01/2011 and 10/12/2014.

I have duly acknowledged all the sources of information which have been used in the thesis.

This thesis has also not been submitted for any degree in any university previously.

Sun Jiulong		10 DEC 2014
Name	Signature	Date

ACKNOWLEDGEMENT

A doctoral thesis like this which involves knowledge from various fields would not be possible without the help and support from many people. It has been a truly memorable learning journey in completing the 4 years research work. Therefore, I would like to take this great opportunity to acknowledge those who have been helping me along the way.

First and foremost, I would like to express my deepest gratitude to my dear supervisor, Associate Professor, Dr. Stephan Jaenicke, for giving me the opportunity to join his team and work together with him. Dr. Stephan Jaenicke is someone you will instantly love and never forget once you met with him. He is the most knowledgeable and smartest people I have even met. He always gives us freedom to pursue various researching project; he always welcomes us to discuss research results with him, and he always make insightful comments and suggestions on the projects. So without his immense knowledge, stimulating suggestions, guidance, encouragement, patience and understanding, my research results and this thesis wouldn't have been possible.

I would also like to thank Associate Professor Dr. Chuah Gaik Khuan for her constant help and invaluable advice throughout my research and the writing of this thesis. I truly appreciate all the time she has taken to read and correct my writings and manuscripts.

My sincere thanks also go to Professor Li Fong Yau, Sam, Associate Professor Wu Jishan, Professor Lee Hian Kee, Madam Toh Soh Lian, Miss Tan Lay San, Miss Suriawati Bte Sa'Ad, Mr Lee Ka Yau, Dr Chui Sin Yin, Dr Yuan Cheng Hui, Mr Sha Zhou and Mr Lin Xuanhao for all the help and supporting they have rendered during my work.

This thesis would not have been possible without the help and support from my dear fellow lab mates: Dr. Fan Ao, Mr. Do Dong Minh, Dr Liu Huihui, Dr Toy Xiuyi, Dr. Wang Jie, Miss Han Aijuan, Miss Gao Yanxiu, Mr Goh Sook Jin, Mr Irwan Iskandar Bin Roslan, Miss Angela Chian, Mr. Zhang Hongwei and Mr Parvinder Singh.

I am also grateful to QinDie, my grandparents, my parents and parents-in-law, and my wife for their unconditional love, encouragement, motivation and understanding. I would like to give my special thanks to my wife, Wang Xiaoxue, for believing in me and giving me the unconditional trust and supporting.

Last but not least, I am indebted to the Singapore Peking Oxford Research and Enterprise (SPORE) and to the National University of Singapore for offering me this great opportunity to work with my supervisor and my lab mates and as well as a valuable research scholarship.

TABLE OF CONTENTS

Summary

Water pollution has become one of the most urgent problems facing the world. The discharge of untreated waste water does not only directly threaten human wellbeing, but also affects ecological systems causing the collapse of the aqueous ecosystem. Among the pollutants, heavy metal ions and organic pollutants are the most toxic species. Cr(VI) and Rhodamine B (RhB) as models for these two classes of real pollutants were examined in this thesis.

Inorganic-organic hybrid adsorbents based on the metal organic frameworks UIO-66 and MIL-125(Ti) were prepared. NH_2-UIO-66, NH_2-MIL-125(Ti), N-KIT-6 and NNN-KIT-6, were employed to remove Cr(VI) from waste water. The adsorption capacity of unmodified UIO-66 was 93.0 mg/g, whereas the modified materials NH_2-UIO-66, NH_2-MIL-125(Ti), N-KIT-6 and NNN-KIT-6 had capacities of 195.4, 140.5, 142.9 and 241.3 mg/g, respectively. An ultimate Cr(VI) concentration conforming to drinking water standards (<0.05 mg/L) could only be achieved with the amino-functionalized KIT-6. These amino-functionalized mesoporous materials are promising for applications to control Cr(VI) pollution.

Molecular doping and heterojunction technologies were introduced to develop a novel inorganic-organic hybrid photocatalyst for photodegradation of Rhodamine B. The molecular doping opens an opportunity to purposefully design a photocatalyst with desired band gap, to improve porosity and to

greatly increase the surface area of the photocatalyst. Charge-injection from the ligand to the inorganic component leads to efficient charge separation after photo-excitation. The heterojunction materials containing MOF/metal oxide and MOF/metal oxyhalides possess significantly enhanced photocatalytic activity compared with P25 for the degradation of RhB under sunlight irradiation. This thesis offers a promising practical application prospect in future for inorganic-organic hybrid materials on water treatment.

LIST OF TABLES PAGE

LIST OF FIGURES PAGE

LIST OF SCHEMES

Chapter 1. Introduction

1.1 Water pollution

Clean drinking water plays an important role to humans as well as animals. Although around 3/4 of the earth is covered by water, less than 1% of the world's fresh water (about 0.007% of the water on the earth) is suitable for direct use by humans. Indeed, a recent report showed that one fifth of the world’s population lacks access to clean water. The situation will be even worse in 2025 [1], as at that time, more than half of the world population will be facing the problem of water scarcity.

1.1.1 Water pollution

Water pollution is one of the most significant crises confronting the world and it makes water scarcity more serious. With development and growth of industrial activities, over five million chemical compounds were synthesized and around one hundred and fifty million tons of synthetic chemicals are produced annually by industry [2], in addition to billions of tons of oil that are shipped each year. Industries such as metallurgy, petroleum, and chemical produce large amounts of inorganic and organic waste during production,

transportation, storage and consumption. In some places, these waste products are still disposed off directly without treatment. These released chemicals or wastes participate in natural cycles, and the resulting reactions lead to interference and disturbance of natural systems, which are the primary cause of pollution. Water pollution forms when large amounts of waste diffuse into the water system beyond its self-cleansing capacity. Water pollution is usually the main contributor for the deterioration of the living environment. The major pollutants in the water include pathogenic microorganisms, excess nutrients, heavy metals, organic chemicals and sediment [3]. The wastes come from three main sources: industry, agricultural activities and human daily life.

1.1.2 Heavy metals in waste water

Most heavy metal pollution comes from industrial activities. The increased flux of metallic substance into the environment results from the enormous increase in the use of heavy metals over the last few decades. Large tonnages of metals such as Cr, Pb, Hg, As, Cd, Sb, Ni, Zn, Cu, and Co are ending up in the environment, and particularly in the water, from industrial activities [4, 5]. Waste water containing heavy metals, either individual or combination, may be destructive to aquatic organisms and has a severe impact on the aquatic community. Table 1.1 shows the aqueous effluents enriched with heavy metals from industrial process and it also describes various metallic species and their

application in industries.

Table 1.1 Heavy metals in some major industries [6].

Industrial source	Al	Zn	Sn	Sb	Cd	Cr	Cu	Fe	Hg	Mn	Pb	Ni
Automobile		X	X		X	X		X			X	X
Petroleum refining		X				X	X	X			X	X
Pulp and paper		X				X	X		X		X	X
Textile						X						
Steel		X		X	X	X		X			X	X
Organic chemicals	X	X	X		X	X		X	X		X	
Inorganic chemicals	X	X			X	X		X	X		X	
Fertilizer	X	X			X	X	X	X	X	X	X	X
Plastic and synthetics								X				
Leather tanning and finishing						X						
Steel plants		X				X						
Mining					X		X		X	X	X	
Acid mine drainage	X	X					X	X		X		
Metal plating		X			X	X	X					
Coal and gasoline									X		X	

Heavy metal ions can be significantly enriched in the body after intake, which can cause acute or chronic poisoning. These ions can also enter into ecosystem and spread with the food chain. The problem is that heavy metal ions in water show high stability and are difficult to be degraded naturally. If waste water with heavy metal ions is used directly to irrigate fields, as is practiced in some countries, the land will be poisoned by heavy metal ions; it loses its self-purification capability, and the soil becomes a repository for pollutants [7].

Industrial effluents may contain many different heavy metal ions. Cr is a widely employed heavy metal and finds many applications in different industries [8, 9]. Chromium (Cr) is a typical heavy metal present in waste water. Cr in aqueous solution exists mainly in the form of Cr(VI) and Cr(III). Cr(VI) is 10 to 100 times more toxic than Cr(III) [10], because it is highly mobile, and its high oxidation state makes it carcinogenic and mutagenic to the living organisms [11-13]. It also has an effect on human skin, liver, kidney, and respiratory organs because the Cr(VI) ions easily penetrate the cellular membrane. Once it enters the cell, Cr(VI) will oxidize its constituents. The cells undergo a metabolic oxidation that leads to the migration of chromium metabolic complexes to the nucleus of the cell where they interact with DNA. In contrast，Cr (III) is an essential nutrient and is required in amounts of 5-200 μg/day [14]. Because an excess of trivalent and hexavalent chromium can be fatal, limits have been set for the allowed concentration of Cr in drinking water. However, chromium is widely used in a variety of industrial applications such as electroplating, metal finishing, pigments, leather tanning, wood protection, chemical manufacturing, brass, electrical and electronic equipment, catalysis and many others. Table 1.2 lists plant types, productions and chromium compounds. The principal chromium ore is ferro chromite and chrome ore [15]. In 2010, the consumption of ferro chromite and chrome ore were 9.04 and 22.23 million tons, respectively.

Table 1.2 Uses of chromium compounds [16].

Branch of industry	Product	Use
Building industry	Chromium (III) oxide	pigment for coloring building materials
Chemical industry	dichromates, chromium(VI) oxide chromium(III) oxide	oxidation of organic compounds, bleaching of montan waxes, manufacture of chromium complex dyes catalysts
Printing industry	dichromates chromium(VI) oxide	photomechanical reproduction processes chromium plating of printing cylinders
Petroleum industry	chromates(VI)	corrosion protection
Paints and lacquers	chromates, chromium(III) oxide	pigments
Refractory industry	chromium(III) oxide	additive for increasing slag resistance
Electroplating	chromium(VI) oxide	bright and hard chromium plating
Wood industry	chromates, chromium(VI) oxide	in mixtures of salts for protecting wood against fungi and insects
Leather industry	basic chromium(III) sulfates	tanning of smoothed skins
Metal industry	chromium boride, chromium carbide, chromium(III) oxide	flame sprays polishing agents
Metallurgy	chromium(III) oxide	aluminothermic extraction of pure chromium metal
Textile industry	Dichromates basic chromium(III) acetates and chromium(III) fluorides	dyeing with chrome dyes mordanting of textiles
Recording industry	chromium(VI) oxide	magnetic information storage
Pyrotechnics industry	dichromates	additive to igniting mixtures

Due to the ongoing use of outdated technology, the use of chromium in developing countries is far more widespread than in developed countries. Lax local regulatory enforcement and other factors cause a lot of chromium slag and high concentrations of chromium-containing wastewater to be produced. Rain will erode the chromium slag if it is disposed in a casual way in open landfills, and Cr(VI) can leach and infiltrate the groundwater or flow into surface waters such as rivers and lakes to cause serious water pollution. Wastewater containing chromium is still discharged directly into the environment without any treatment in some places. In Japan and the United States, serious incidents of Cr pollution occurred in the 1970s. A more recent case has been reported from China: in 2011, Yunnan Qujing Luliang Chemical Industries Limited Company illegally discharged more than 5000 tons of chromium slag into the Nanpan River, the source of the Pearl River, [17]. A reservoir with 300,000 cubic meters of water had been polluted, and the Cr(VI) concentration of the water in the reservoir exceeded allowed levels by 2,000 times.

The World Health Organization (WHO), European Union, China and Singapore set a permissible limit of total chromium in drinking water at 0.05 mg/L (see table 1.3). But the Cr(VI) concentration of many industrial effluents is significantly higher than this. Contaminants from industrial wastewater rich in Cr(VI) ions remain an important environmental issue and it is extremely

important to reduce or remove Cr(VI) from industrial effluents before discharging in to the environment.

Table 1.3 Drinking-water quality standard

Organization	Cr(VI) (mg/L)	Total amount of Cr (mg/L)	Ref.
WHO		0.05	[18]
USA		0.1	[19]
European Union		0.05	[20]
China	0.05	0.05	[21]
Singapore		0.05	[22]

1.1.3 Organic pollutants in waste water

Domestic, industrial and agricultural activities all produce waste water containing organic matter. The organic pollutants include [23-25]:

- Industrial waste water: plasticizers, greases, oils, solvents, phenols, biphenyls, endocrine disruptors, pharmaceuticals, drug residues and dyes;
- Agricultural waste water: fertilizers (phosphates, nitrate and others), pesticides, herbicides;
- Domestic sewage: detergents, hydrocarbons, proteins.

Generally, high concentrations of organic waste water typically come from industrial and agricultural operations. Normally, water has a significant self-purification capacity, and the organic pollutants are broken down or

decomposed by microbial and other biological activity (biodegradation). For this process, a stoichiometric amount of oxygen is required. The amount of organic pollutants in the water is therefore expressed as biochemical oxygen demand (BOD) [26]. Table 1.4 shows the requirements for discharge of trade effluent into the public sewer system in Singapore. Oxygen is a basic requirement of almost all aquatic life, and if the dissolved oxygen in the receiving water is consumed at a greater rate than it can be replenished, oxygen depletion will result which has severe consequences on the biota [27]. The hydrosphere will be adversely affected if insufficient oxygen is supplied to support the aquatic life. Furthermore, the surrounding biosphere will also suffer from extremely serious impact due to it closely contact with water biosphere.

Table 1.4 Requirements for discharge of trade effluent into public sewer in Singapore [28].

S/No	List of Substances	Limit in mg/L of trade effluent
1	5 Day Biochemical Oxygen Demand (BOD) at 20^{o}C	400
2	Chemical Oxygen Demand	600
3	Detergents (linear alkylate sulphonate as methylene blue active substances)	30
4	Grease and Oil (Hydrocarbon)	60
5	Grease and Oil (Non-hydrocarbon)	100

It should be noted that there are many types organic pollutants in waste water. In this thesis we will concentrate on organic dyes as a model compounds.

Organic dyes are typical organic pollutants with good water solubility. Their color and inherent stability make them the principal indicators for some conventional waste water quality determination [29, 30]. Tens of thousands of different dyes are produced according to the Colour Index International [31. The effluent from 1 ton of processed fabric is able to pollute about 200 tons of water [32]. Because dyes absorb sunlight, the transparency of the water is reduced. This will affect photosynthetic organisms. On settling out, the dyes alter the characteristics of the river bed and render it unsuitable as habitat for many invertebrates [33]. Moreover, most organic dyes are modified aromatic compounds, like haloaromatics, aromatic nitro-compounds and aromatic amines, and most of them are toxic, even carcinogenic. However, dyes are widely used due to the rapid development of industries such as textile, food, leather products, pharmaceuticals, and cosmetics. Currently, the annually global output of dyes is about 9×10^5 tons [34], and a lot of dye waste water is produced particularly from the textile industry. In China, the annual discharge of waste water is more than 390 billion tons, of which 70 billion tons are dye waste water [35]. Traditional biological treatment systems are not suitable for the removal of organic dyes, and their removal therefore became an important issue which has attracted much attention over the last decades.

1.2 Water treatment

Health and safety are the primary considerations for water treatment. As mentioned before, it is quite important to remove Cr(VI) and dyes from water.

1.2.1 Removal of Cr(VI) from waste water

The conventional treatment of Cr(VI)-containing waste water is chemical reduction precipitation, because this technique requires little equipment and is easy to operate. Ferrous sulfate, sulfite or sulfur dioxide are suitable reducing agents to convert Cr(VI) into Cr(III). Alkali is then added to adjust the pH value, so that the chromium hydroxide precipitates out and can be removed from the water. Figure 1.1 illustrates a system with sulfur dioxide as a reducing agent [36].

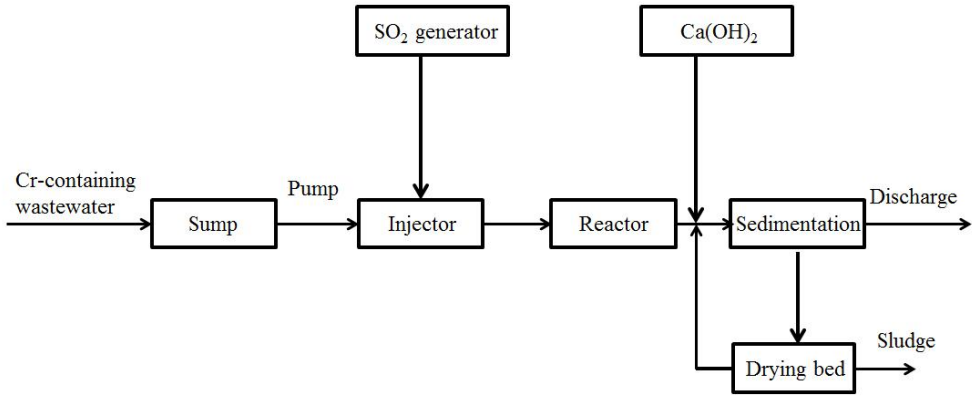

Figure 1.1 Flow diagram of a Cr-removal process with SO_2 as a reducing agent.

The sulfur dioxide is produced by combustion of sulfur and bubbled into the

wastewater, where it will react to form sulfurous acid which is able to reduce Cr(VI) to Cr(III).

$$3SO_2 + Cr_2O_7^{2-} + 2H^+ = 2Cr^{3+} + 3SO_4^{2-} + H_20$$

$Ca(OH)_2$ is used to adjust the pH of the wastewater to about 8, so that the trivalent chromium is precipitated in the form of the chromium hydroxide.

$$Cr^{3+} + 3\,0H^- = Cr(OH)_3 \downarrow$$

After that, waste water is fed into a sedimentation tank where the solids settle out. The upper clarified water is discharged, and the precipitate is dried in drying beds. The disadvantage of precipitation is the production of sludge. This constitutes a solid waste disposal problem. Therefore, various methods to recover Cr(VI) from industrial effluents before discharging into the environment have been attempted, the **Table 1.5** shows the comparison of various treatment techniques.

Among all those techniques, adsorption has evolved as the most suitable process for chromium removal because it has relatively reusable, low costs, large adsorption capacity and high efficiency. Metal oxides [67-69], hydrous metal oxides [70-73], hybrid materials [74], polymers [75], biomaterials [76], activated carbon [77] and carbon nanotubes [78] have been evaluated for Cr(VI) removal.

Table 1.5 The comparison of various treatment techniques for Cr(VI) industrial effluent.

Techniques	Advantages	Disadvantages	Ref.
Electrochemical precipitation	High efficiency	High cost	[37-40]
Ion exchange	High efficiency	High cost	[41-44]
Reduction	High throughput	High cost,	[45-48]
Solvent extraction	High efficiency, recycle Cr	High cost, organic residual	[49-51]
Membrane separation	High throughput	High cost, low efficiency	[52-55]
Flotation	High throughput	High cost	[56]
Sedimentation	High throughput	High cost	[57]
Phytoremediation	Low cost	Low throughput	[58]
Foam separation	High efficiency, High throughput	High cost	[59]
Adsorption	Reusability, low cost, high adsorption capacity, high efficiency	-	[60-63]
Bio-sorption	Reusability, low cost	Low adsorption capacity	[64-66]

1.2.2 Removal of dyes from waste water

The most common technologies used to remove organic dyes from waste water are sedimentation, aerobic biological treatment [79], anaerobic biological treatment [80] and oxidation processes with sodium hypochlorite [81], hydrogen peroxide [82, 83], ozonation process [84], and ultraviolet light (UV) irradiation [85]. Figure 1.2 illustrates a case of textile waste water treatment in the Philippines. Typically, textile waste water needs to be neutralized because most dyeing baths are alkaline. After adding sulfuric acid, the waste water flows into an equalizing basin for pH correction. Subsequently,

the waste water is dosed with coagulation aid and aluminium sulphate (Alum) to bring about the coagulation, flocculation and sedimentation of the suspended solids in the waste water. After separation, the clarified water is oxidized by NaOCl in the next step, and the suspended solids are treated in the sludge bed. The treated water is discharged after oxidation. The filtrate obtained from the sludge bed is returned back to the equalizing basin, and the sludge is sent for drying and final disposal.

In addition, other technologies also have been received much attention and have been extensively studied particularly by academic researchers, such as membrane processes [86], photocatalytic degradation [87-89], electrocatalytic oxidation [90, 91], and ion exchange [92].

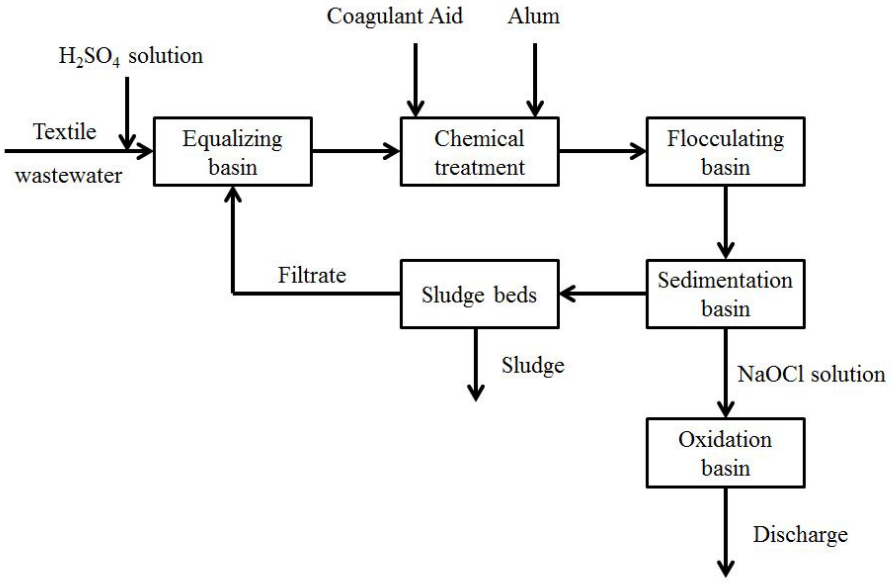

Figure 1.2 Process flow diagram of textile waste water treatment [93].

However, most of these processes have limitations. Physical treatment only transfers the organic dyes from one phase to another and cannot decompose it, while chemical treatment suffers from low degradation efficiency and high operating cost. Biological treatments also have relatively low degradation efficiency and are only efficient for certain organic dyes. Among the technologies mentioned, photocatalytic processes show many advantages like low cost, long life cycle, reusability, low energy consumption. For this reason, they have received wide attention.

In this thesis, adsorption was employed to remove Cr(VI) and photodegradation was examined to remove organic dyes due to the advantages of adsorption and photodegradation. The fundamental theories of adsorption and photodegradation will be introduced in the next two sections.

1.3 Adsorption

Due to its high efficiency, low cost, speed, and easy operation, adsorption has found a wide range of applications in many different industries. The first scientific experiment of gas adsorption was carried out by the German-Swedish apothecary C.W. Scheele in 1773, followed by J.T. Lowitz's experiment in 1785 for solutions [94]. Adsorption is a process where some molecules (adsorbate) from one phase accumulate on and bind to the surface of another phase (adsorbent) by a specific interaction between the adsorbate

and adsorbent.

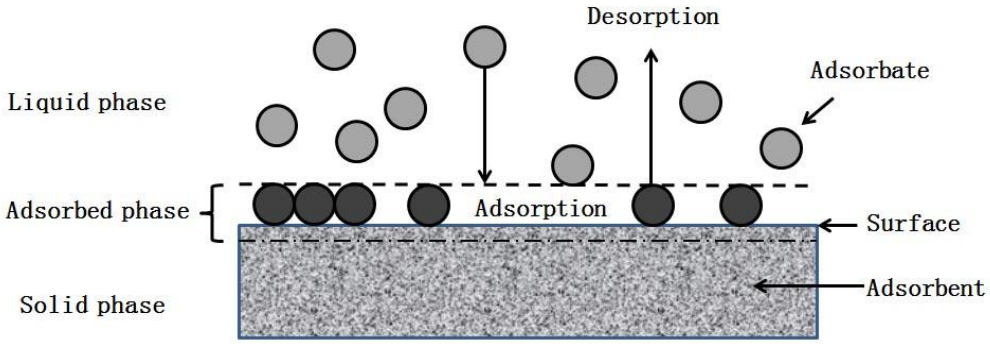

Figure 1.3 Definition of the basic terms of adsorption

Figure 1.3 shows an example of adsorption between an adsorbate contained in the liquid phase and a solid adsorbent. When adsorption occurs between a dissolved adsorbate and a solid adsorbent with a highly porous surface or functional group modified surface, adsorbates from the solution will be deposited at the surface of the adsorbent due to liquid–solid intermolecular forces of attraction. The process is reversible, so that the deposited molecules will leave (desorb from) the surface of the adsorbent if some parameters (pH, temperature or solvent) are changed in a suitable way. In this way, the adsorbate can be separated and obtained from solution by adsorption and desorption.

1.3.1 Categories of Adsorption

Depending on the nature of the attractive forces existing between the

adsorbate and adsorbent, adsorption processes are classified as physical sorption (characterized by weak van der Waals forces) or chemical sorption (characterized by chemical bond forces).

Physical adsorption is a reversible and rapid adsorption process in which the fundamental interacting force between adsorbate and adsorbent is caused by weak van der Waals forces of attraction [95].

Adsorption can also take place from the gas phase. Gas adsorption is a typical physical adsorption process. Figure 1.4 illustrates the BET gas adsorption process. In the 1930's, Langmuir's theory of monolayer adsorption was extended to multilayer adsorption by Brunauer, Emmett and Teller (BET). Their model makes the following assumptions:

(1) Gas molecules can physically adsorb on a solid in many layers; the interaction energy in all but the first layer (where the interaction is directly with the surface) is equal to the heat of condensation of the adsorbate.

(2) There are no lateral interactions between molecules at different sites within one layer.

(3) The Langmuir theory can be applied to each layer.

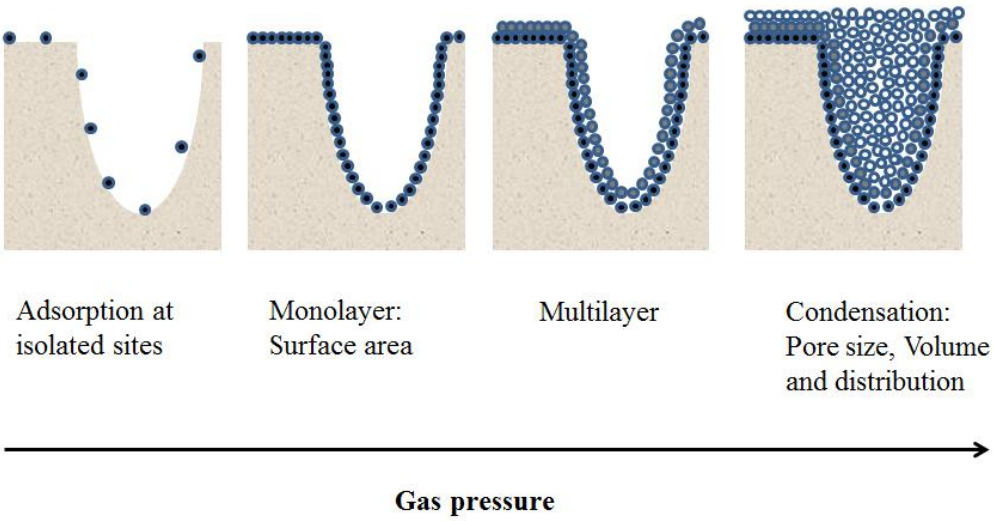

Figure 1.4 Adsorption and pore filling [96].

At the beginning, the surface is clean, and gas molecules can be deposited at any place on the surface of the solid adsorbent. Subsequently, with increase of gas pressure, the gas molecules will be deposited closely on the surface of the adsorbent to from a monolayer. Unlike the Langmuir model, where adsorption is limited to a monolayer, the amount of adsorption can increase infinitely as pressure increases, and adsorption in the second layer can start already before the first monolayer is completed. The surface area, pore size and pore size distribution can be obtained from the gas adsorption isotherm. The BET equation is expressed as [97]:

$$\theta = \frac{v}{v_m} = \frac{c\frac{P}{P_0}}{\left(1-\frac{P}{P_0}\right)\left[1-\frac{P}{P_0}(1-c)\right]} \quad (1.1)$$

where θ = no. of occupied sites/ total no. of possible sites, v = total volume

adsorbed, v_m = volume for monolayer coverage, P = equilibrium pressure, P_0 = saturation pressure of the adsorbate at the temperature of adsorption and c = BET constant which can be expressed as:

$$c = \exp(\frac{E_{ADS} - E_{COND}}{RT}) \quad (1.2)$$

where E_{ADS} = heat of adsorption for first layer, E_{COND} = heat of adsorption for second and higher layer = heat of condensation. Equation (1.1) describes the adsorption isotherm and can be rearranged in a linearized form (BET equation):

$$\frac{1}{V[P/P_0 - 1]} = \frac{1}{V_m C} + \frac{C-1}{CV_m}[\frac{P}{P_0}] \quad (1.3)$$

Physical adsorption requires a low temperature because it is characterized by a relative low energy of adsorption. The activation energy for physical adsorption is only about 20-40 kJ/mol.

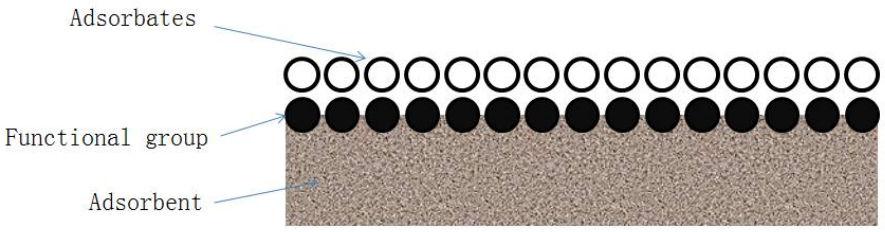

Figure 1.5 Chemical adsorption between adsorbates and an adsorbent with a functional group.

Chemical adsorption occurs as a result of chemical bond formation between the adsorbate molecules and the adsorbent.

Figure 1.5 shows a schematic diagram of chemical adsorption (chemisorption). In the chemical adsorption process, the adsorbate molecules are adsorbed by the active sites of the adsorbent though a chemical interaction, and the adsorbates cannot move freely because the active sites of the adsorbent consist of various types of functional groups. Chemical adsorption is favored by a higher temperature. Chemisorption frequently has an activation barrier and proceeds more rapidly at elevated temperatures. In chemical adsorption, the forces of attraction between the adsorbate and the adsorbent are very strong and the binding energy is in the range of 40-400 kJ/mol, typical for chemical bonds. Table 1.6 lists difference between physical adsorption and chemical adsorption.

Table 1.6 Comparison between Physical adsorption and Chemical adsorption

	Physical adsorption	Chemical adsorption
1	Low heat of adsorption (20-40 kJ/mol)	High heat of adsorption (40-400 kJ/mol)
2	Van der Waal's forces	Chemical bond
3	Low temperature favored	High temperature favored
4	Does not require any activation energy	Requires activation energy
5	Reversible	Irreversible

1.3.2 Adsorption from aqueous solution

The surface of a solid adsorbent in contact with an aqueous solution has the tendency to accumulate a surface layer of solute molecules (adsorbates) at the interface, because of the imbalance of surface forces. When the affinity between adsorbent and adsorbate is larger than the affinity between solvent and adsorbate, adsorption is favored. Therefore, Equation 1.4 can describe the adsorption from aqueous solution.

$$Adsorbant + solution_{with\ adsorbate} \xrightarrow{adsorption} Adsorbent_{with\ adsorbat} + solution \quad (1.4)$$

The affinity between solvent and adsorbate can be obtained directly from the solubility of the adsorbate in this solvent, and an inverse relationship has been found between the adsorbate solubility and adsorption capacity. Because both the adsorbate and water molecules compete for adsorption sites, adsorption is favorable for hydrophobic adsorbents. Normally, adsorption will be limited to a monolayer on the surface of the adsorbent because the adsorptive forces beyond the first layer are too weak. The capacity of adsorption from aqueous solution is normally evaluated and described using either the Langmuir or the Freundlich adsorption isotherm.

1.3.3 Models of Adsorption

The Langmuir isotherm has been extensively used to describe the adsorption of heavy metals, dyes, organic pollutants, etc. It applies to monomolecular layer adsorption. This isotherm is described as a homogeneous one assuming that all the adsorption sites have equal adsorbent affinity and that the adsorption at one site does not impact on the adsorption at an adjacent site. The Langmuir isotherm is utilized to obtain a maximum adsorption capacity produced from the complete monolayer coverage of adsorbent surface. The isotherm equation is represented as follow:

$$\frac{C_e}{q_e} = \frac{1}{Q_0 b} + \frac{C_e}{Q_0} \tag{1.5}$$

where b is an adsorption equilibrium constant (L/mg) that is related to the apparent energy of adsorption and Q_0 is the quantity of adsorbent required to form a single monolayer on a unit mass of adsorbent (mg/g) and q_e is the amount adsorbed per unit mass of adsorbent (mg/g) when the equilibrium concentration is C_e (mg/L).

The Freundlich isotherm describes that the ratio of the amount of solute adsorbed on a given mass of adsorbent to the concentration of solute in the solution is not constant at different concentrations. For many systems, the molar heat of adsorption decreases with increasing extent of adsorption. This

has been well dealt with by the Freundlich isotherm, which had previously been viewed as an empirical isotherm. For adsorption from solution, the Freundlich isotherm is expressed as follow:

$$logq_e = logK_F + \frac{1}{n} logC_e \quad (1.6)$$

where K_F is the Freundlich constant, which indicates the relative adsorption capacity of the adsorbent related to the bonding energy, and n is the heterogeneity factor representing the deviation from linearity of adsorption and is also known as the Freundlich coefficient. q_e is the amount adsorbed per unit mass of the adsorbent (mg/g) at the equilibrium concentration C_e (mg/L).

1.3.4 Adsorbents

Various natural and synthetic materials have been used as adsorbent for the removal of Cr(VI), such as activated carbon, minerals like hydrotalcite, organic adsorbents and natural adsorbents such as saw dust.

Activated carbon has been widely used in various industrial areas and is also the most studied adsorbent. It can be produced form different raw materials such as wood, wood charcoal, peat, or agricultural residues such as coco nut shells and peach pits. The activated carbon can be classified in to several types: activated carbon fiber (ACF), granular activated carbon (GAC), activated carbon cloth (ACC) and powder activated carbon (PAC) [98].

Selomulya et al. investigated several types of activated carbon synthesized from coconut shell, wood and coal dust for the removal of Cr(VI) [99]. The coconut shell and coal dust activated carbons present protonated sites on the surface, but the wood activated carbon exhibits ionized hydroxyl groups. The adsorption capacities are 6.0, 5.1 and 4.4 mg/g for coconut shell, wood and coal dust activated carbon, respectively.

Hamadi et al. used Filtrasorb 400 (Calgon Carbon), a coal based reagglomerated GAC type activated carbon, to remove Cr(VI) from aqueous solutions [100]. They observed that the surface area and adsorption capacity increased with reduction in particle size of the adsorbent. The surface area was measured to be 832 m^2/g, and adsorption capacity was about 53.19 mg/g in this study.

Park and Jung prepared ACFs plated with Cu^{2+} metal to remove Cr(VI) [101]. The introduction of Cu^{2+} on the ACFs had a positive effect on the adsorption of Cr(VI). The adsorption capacity of their material was 40.00 mg/g.

Kobya used an activated carbon from hazelnut shells to remove Cr(VI) [102]. In this study, the Langmuir model described the adsorption very well and the thermodynamic parameters showed that the adsorption was an endothermic process. The adsorption capacity as calculated from the Langmuir isotherm was 170 mg/g.

Natale et al. observed that the adsorption of Cr(VI) was pH dependent. The activated carbon used in this study was prepared from bituminous coal [103]. The maximum value was about 7mg/g at neutral pH.

A similar low value was reported by Xu et al. for functionalized ACFs [104]. The adsorption capacity depended strongly on solution pH, with maximum value around 5.59 mg/g at pH=1. The pH dependence can be explained by the surface characteristics and the capacity of the functionalized ACFs to reduce Cr(VI) to Cr(III). C-O and C=O functional groups were found on the surface of the ACFs. In this case too, the Cr(VI) adsorption data agreed well with the Langmuir isotherm model.

Hydrotalcites are layered hydroxides with the general structural formula $[M_{1-x}^{2+}M_x^{3+}(OH)_2]^{x+}A_{x/n}^{n-}yH_2O$, where M^{2+} and M^{3+} represent divalent (e.g. Mg, Ni, and Zn) and trivalent metals (e.g. Al, Fe, and Cr), respectively. The A^{n-} are interlayer anions, such as NO_3^-, SO_4^{2-}, and CO_3^{2-}, and x typically ranges from 0.17 to 0.33. There are positively charged brucite-like octahedral layers and a negatively charged interlayer region containing anions and water molecules in hydrotalcite. Hydrotalcites have shown a good potential as adsorbents due to the presence of large interlayer spaces and a significant number of exchangeable anions.

Goswamee et al. used uncalcined and calcined Mg–Al, Ni–Al and Zn–Cr

layered double hydroxides as adsorbents [105]. Calcined LDHs showed better adsorption capacity than uncalcined LDH, because uncalcined LDHs adsorbed via ion exchange and calcined LDHs removed Cr(VI) by rehydration. The pH of Cr(VI) solution had no effect on the adsorption by calcined LDH. The adsorption of Cr(VI) on calcined Mg-Al LDH is about 235.45 mg/g.

In a similar study, Lazaridis et al. used calcined Mg–Al–CO_3 hydrotalcite to remove Cr(VI) from aqueous solutions [106]. Release of Cr(VI) from the adsorbent was dependent on the types of anions present in the aqueous phase. CO_3^{2-} was most effective to promote release. Adsorption removal of aqueous Cr(VI) by calcined hydrotalcite ($Mg_6Al_2(OH)_{16}CO_3$ 4H_2O) was also achieved. The adsorption capacity of the hydrotalcite was approximately 120 mg/g.

Das et al. prepared hydrotalcite-like compounds containing varying amounts of Al^{3+}, Zr^{4+}, and Zn^{2+} or Mg^{2+} in the metal hydroxide layer, and uncalcined (as-synthesized) and calcined LDHs were used to remove Cr(VI) [107]. The mixed oxides obtained by calcination at 450 ◦C exhibited a very high adsorption capacity of 166 - 280 mg/g

Tel et al. employed a hydrous titanium(IV) oxide for Cr(III) and Cr(VI) removal in the batch mode [108]. More than 99% of Cr(VI) was removed, whereas less than 1% Cr(III) was adsorbed at pH 2.0. The Langmuir adsorption model fitted the Cr(VI) adsorption data better than the Freundlich

model at pH 2.0 for hydrous TiO_2. The maximum adsorption capacity of Cr(VI) was 5 mg/g.

Rodrigues et al. explored a hydrous zirconium(IV) oxide for Cr(VI) removal in the batch mode [71]. The Cr(VI) sorption data on hydrous ZrO_2 at pH 2.0 was fitted with the Langmuir isotherm and the adsorption capacity increased from 61 to 66mg/g when the temperature was increased from 298 to 338 K. This thermodynamic study suggests an endothermic reaction with increase in randomness at the solid–liquid interface during the adsorption.

Removal of Cr(VI) was also examined with various other low cost materials, including plants [109-112], chitosan [113, 114], peat moss [115, 116], and fly ash [117-120].

1.4 Photodegradation

1.4.1 Model of the photodegradation process

An ideal waste treatment process should be highly efficiency, have low costs and no side-effects, and completely reduce all the pollutants present in the waste water. Complete photodegradation fulfills all the requirments of the ideal waste treatment process because it only generates CO_2, H_2O and inorganic salts. So far, more than 100 different pollutants were examined by using photodegradation [121-123]. The photodegradation mechanism is very

complex. Currently, the mechanism of photo-generated electron-hole pairs and radicals has been widely accepted.

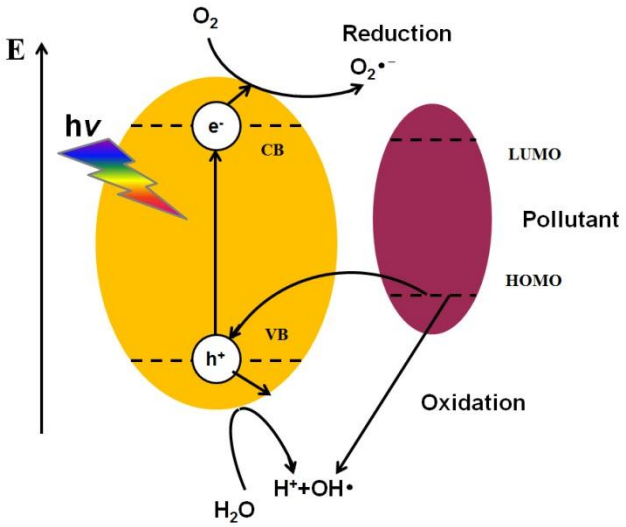

Figure 1.6 Mechanism of photodegradation of pollutant by using photocatalyst.

Figure 1.6 illustrates a model of photodegradation of a pollutant on a photocatalyst. An electron in the photocatalyst is promoted from the valence band (VB) to the conduction band (CB) under solar irradiation. Once the photo-generated electron reaches the surface of the catalyst particle, it will react with O_2 to form an $O_2^{\cdot -}$ radical. On the other hand, a hole is formed in the valence band due to the electron excitation. If the potential of the highest occupied orbital (HOMO) of the pollutant is more negative than that of VB of photocatalyst, the photo-generated hole can react with the pollutant directly. The hole also reacts with water to form an $OH^{\cdot}$ radical which is considered as an active species in the photodegradation reaction, when the potential of VB larger than 2.27 eV (VS NHE). The possible formation of radicals and their

reactions that give rise to the photo-oxidation of pollutants are listed as below:

$$e^- + O_2 \rightarrow O_2^{\cdot -}$$

$$O_2^{\cdot -} + H^+ \rightarrow HOO^{\cdot}$$

$$HOO^{\cdot} + e^- \rightarrow HOO^-$$

$$HOO^- + H^+ \rightarrow H_2O_2$$

$$H_2O_2 + O_2^{\cdot -} \rightarrow OH^{\cdot} + OH^- + O_2$$

$$OH^{\cdot} + pollutant \rightarrow OH^- + pollutant^+ \quad (1.7)$$

$$hole^+ + pollutant \rightarrow pollutant^+ \quad (1.8)$$

$$hole^+ + H_2O \rightarrow OH^{\cdot} + H^+$$

$$hole^+ + OH^- \rightarrow OH^{\cdot}$$

$$OH^{\cdot} + pollutant \rightarrow OH^- + pollutant^+ \quad (1.9)$$

As the above radicals play a very important role in the photodegradation reactions, they will be investigated in this thesis.

1.4.2 Theory of photocatalyst (semiconductor, band structure)

Fujishima and Honda reported in 1972 that an UV irradiated TiO_2 electrode could be employed to split water into hydrogen and oxygen [124]. Later, Ollis and his collaborators [125]; [126] explored the use of semiconductor photocatalysis for water purification. Following these pioneering studies, semiconductor photocatalysis received much attention.

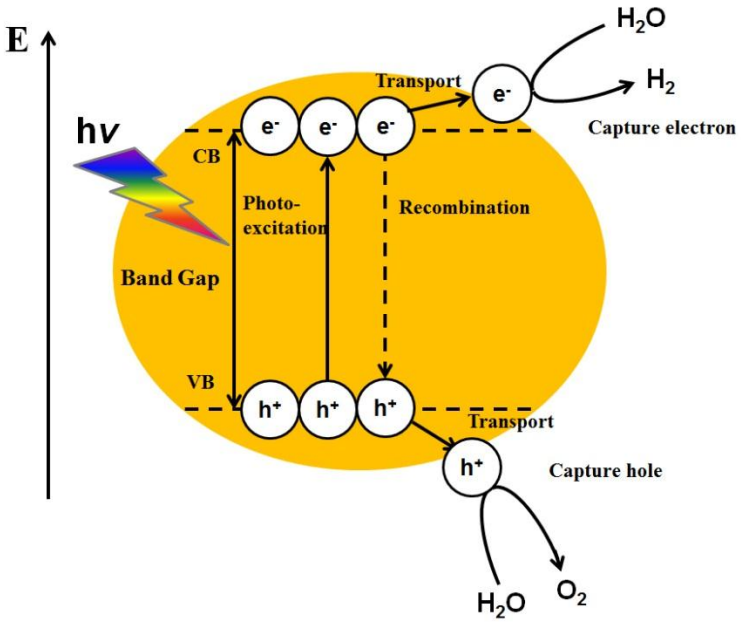

Figure 1.7 Mechanism of electron-hole pair formation, recombination and transport in a semiconductor photocatalyst.

Figure 1.7 displays the mechanism of electron-hole pair formation, recombination and transport in a semiconductor photocatalyst in the case of water splitting. The electron of the semiconductor can only be exited by incident light whose energy must be equivalent or higher than the band gap between VB and CB. The VB consists of the occupied molecular orbitals and it is always full in semiconductors. Similarly, the CB is made up of the unoccupied orbitals that are high in energy and are generally empty in semiconductors. The electron-hole pairs are generated after photo-excitation. Some of the excited electrons will be able to transfer to the surface and are captured by water to form H_2, and the remaining excited electrons will drop back to the VB to recombine with the holes. The uncombined holes will

transfer to the surface of the catalyst to oxidize water to O_2. Therefore, the rate of photo-excitation is the sum of capture rate (k_{CT}) and recombination rate (K_{RT}). Generally, the quantum efficiency is used to describe the actual utilization of solar energy by the photocatalyst, and it can be obtained as:

$$\emptyset = \frac{k_{CT}}{k_{CT} + k_{RT}} \tag{1.10}$$

In the band structure of semiconductors, two types are encountered, one is the indirect band gap and the other is the direct band gap [127, 128].

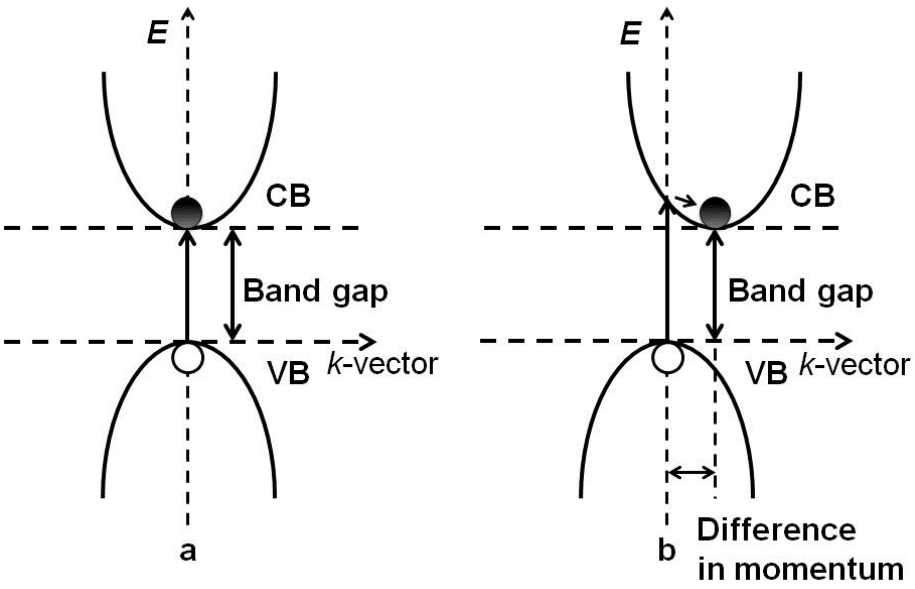

Figure 1.8 (a) Direct and (b) indirect band gap in a semiconductor.

Figure 1.8 illustrates the two situations. In a direct band gap, the maximum of the VB and the minimum of the CB are at the same k-vector. However, they are at different k-vectors in a structure with indirect band gap. The k-vector characterizes the energy state in the VB and CB in the Brillouin zone. Figure

1.9 shows anatase TiO_2 momentums in the Brillouin zone. Compared to a direct electron transition in the case of a direct band gap, the electron-hole pair recombination rate in a photocatalyst with indirect electron transition state is much slower. Therefore, a structure with indirect band gap is favourable for photocatalytic activity in photocatalytic reaction.

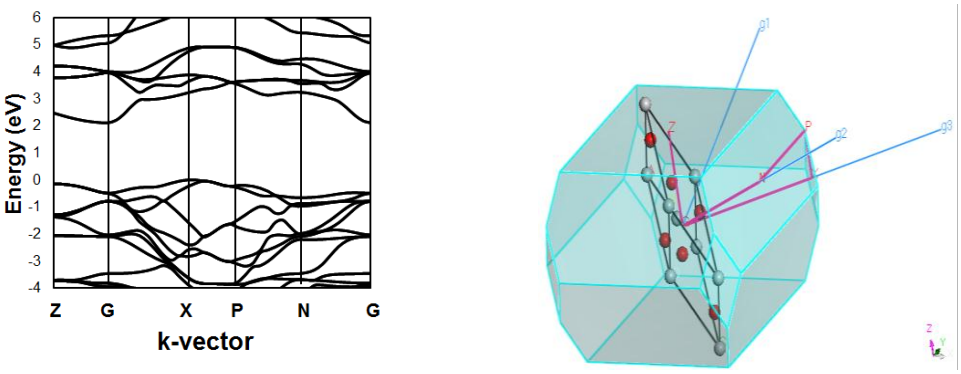

Figure 1.9 Band structure vs. momentum (k-vector) in the 1st Brillouin zone of anatase TiO_2

1.4.3 Strategies to enhance photocatalytic activity (heterojunctions and doping)

TiO_2 is one of the most efficient photocatalysts based on its band structure and band edge positions [129, 130]. However, it can only be excited by UV-light irradiation which constitutes no more than 4 % of the solar energy [131]. Therefore, it is very important to develop visible light-responsive photocatalysts for large scale application of solar energy [132, 133].

Much effort has been expended to enhance photocatalytic activities. As shown

in the previous introduction, two factors determine the overall catalytic activity: (1) the rate of creating electron-hole pairs by promoting electrons into the CB of the semiconductor, and (2) the recombination rate between electrons and holes [134]. In order to increase the photocatalytic activity, it is therefore necessary to either increase the number of electrons that are promoted into the conduction band, or reduce the unproductive electron-hole recombination. At normal light intensity, one absorbed photon will create one electron-hole pair. The minimum energy required is the band gap energy. Higher photon energy will appear as excess energy of the "hot" electron or hole; however, the electron and hole will thermalize within a very short time (pico-seconds), and the hole will move to the top of the valence band; similarly, an electron will give off energy to the lattice and thermalize at the bottom of the conduction band. As shown above, electron-hole recombination will be fast in a direct band gap material, but much slower it there is an indirect band gap. The electron and hole have to move to the surface of the catalyst particle in order to initiate a chemical reaction. Thus, the probability to reach the surface will be inversely proportional to the size (diameter) of the particle. Electron-hole recombination can be counteracted by separating electrons and holes spatially. That is done in a heterojunction structure where two different semiconducting materials (or a semiconductor and a metal) are in tight contact. On the other hand, the number of photogenerated electrons can be increased by increasing

the number of absorbed photons. Photons can only be absorbed when their energy matches electronic transitions in the material. That means, the energy has to be higher than the band gap of the material. “Band gap engineering” by introducing dopants to create additional electron donors above the valence band or electron acceptor sites below the conduction band will extend the absorption spectrum of the material to longer wavelength. In this way, a larger part of the solar spectrum can be utilized for photocatalytc reactions. In this study, the heterojunction structure was employed to reduce recombination and extend the light absorption range in order to enhance the overall photocatalytic activity. Doping was used to extend the light absorption range for the photocatalyst. Figure 1.10 illustrates the formation of two different heterojunction structures. In both cases, two semiconductors, one with a bigger and one with a narrower band gap, are in contact at an inter-crystalline boundary.

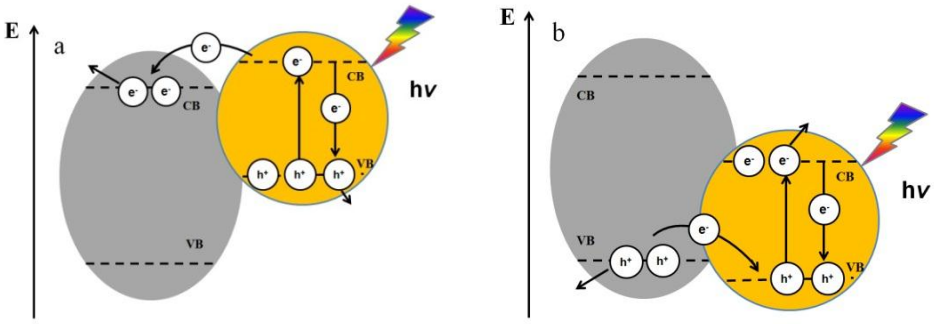

Figure 1.10 Schematic diagram of the movement of electrons and holes in (a) A-type and (b) B-type heterojunction structures during visible light irradiation.

In type A, the CB of the semiconductor with the smaller band gap is more negative than that with the bigger band gap. Electrons can be excited by photon with the energy of the smaller band gap, and are subsequently transferred to the CB of the bigger band gap semiconductor. The photo-generated holes remain confined to the material with the smaller band gap. This effectively counter-acts bulk electron-hole recombination, and increases the probability that the electrons and holes reach the surface of the particle. Therefore, this heterojunction structure reduces recombination and extends the light absorption range. A similar strategy is employed in the type B heterojunction. Electrons on the VB of bigger band gap semiconductor will be donated into the VB of smaller band gap semiconductor to recombine with the photo-generated holes, when electron excitation occurs on the smaller band gap semiconductor. In this process, the holes transfer into the second semiconductor, and the photo-generated electrons remain in the material in which they were formed.

In addition, doping with foreign elements is another method to narrow the threshold energy for photoexcitation. Various doped TiO_2 materials have been reported which display photocatalytic activity under visible light excitation, whereas pure TiO_2 requires UV excitation.

The type of doping can be classified as: metal doping and non-metal doping.

Figure 1.11 shows the configuration of the band structure for Fe doped and N doped TiO_2.

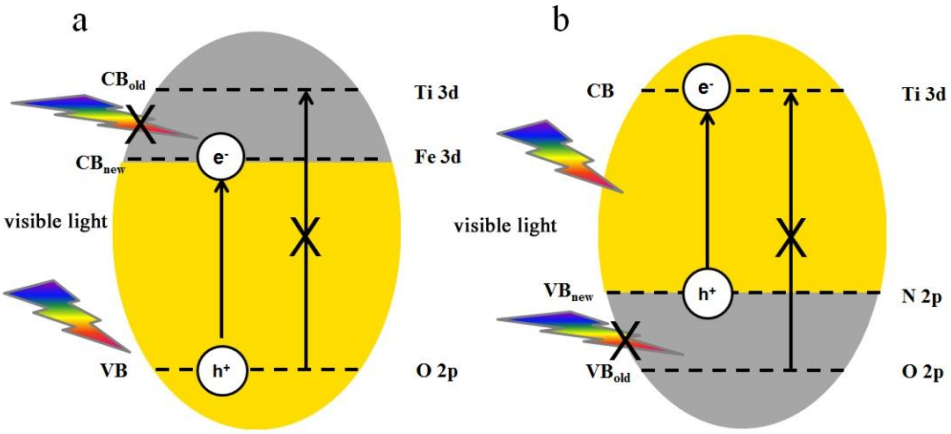

Figure 1.11 Energy band level of (a) N doped TiO_2 and (b) Fe doped TiO_2.

For metal doped TiO_2, the 3d orbitals of Fe significantly affect the d-band derived electronic configurations of the CB. The effect is to lower the CB so as to narrow the overall band gap, and the new CB originates from 3d orbitals of Fe and Ti. The CB edge depends on the dopant concentration, distribution of dopants and the energy level of dopants within the TiO_2 lattice. Certain metals doped into TiO_2 increase the life time of the photo-generated pairs [135, 136]. However, electron trapping by metal centers, high cost for metal doping and the higher conduction band position are disadvantages of metal doped TiO_2. Since Asahi et al. obtained N doped TiO_2 in 2001 [137], nonmetal doped TiO_2 has been widely studied. N, C, S, P, F, B doped TiO_2 were reported to exhibit visible light response [138-143]. The theory is similar to that used to

describe metal-doped TiO_2. In the case of N doped TiO_2, the new VB derived from 2p orbitals of N and O is much higher in energy than the originating VB derived from 2p orbitals of O. Therefore, the band gap of TiO_2 narrows significantly, and the TiO_2 is able to adsorb visible light. In summary for TiO_2, the primary reason of doped TiO_2 with enhanced photocatalytic activity under visible light irradiation could be due to modification of the electronic state of TiO_2 extended the light adsorption range.

1.4.4 The states of photocatalyst in industry

Three different modes of contacting are possible between a solid catalyst, a liquid, and a gas: are slurry state, a fixed bed, and a fluidized state. Therefore, the reactor can be classified based on the employed photocatalyst states into slurry reactors, fixed bed reactors and fluidized bed reactors (see figure 1.12) [144].

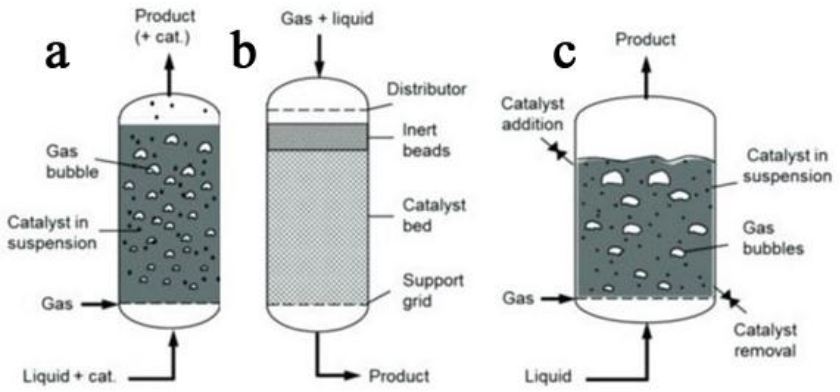

Figure 1.12 Three types of reactor: (a) slurry reactors, (b) fixed bed reactors and (c) fluidized bed reactors [145].

The suspended slurry is a powder photocatalyst directly dispersed in a solution, which provides a good contact between liquid and solid. The small particle size required is beneficial because it reduces bulk recombination. However, because of the small particle size, it is difficult to separate the photocatalyst from the treated water, leading to limited practical value. Fixed state photocatalysts include supported, film and filled photocatalysts. Their advantage is that the photocatalyst can be recovered and reused after reaction. Commonly used supports for supported photocatalyst are sand, glass, non-woven fabrics, zeolites, molecular sieves, glass fiber, hollow glass beads, activated carbon, silica, and stainless steel. There are some requirements in the selection of the support:

1. The support has to be transparent so as not to reduce the incoming light intensity;
2. The support should offer a large surface area so as to increase the reaction area;
3. The support has to present a good mechanical strength and resistance to corrosion;
4. The support cannot poison the catalyst, it is best to enhance the activity of the photocatalyst;
5. Low cost and easy preparation.

Thin film photocatalysts are prepared as a thin film on the surface of a support.

Compared to the supported photocatalyst, the thin film photocatalyst is easily retained in the reactor. However, the contact area between photocatalyst and substrate and the irradiated area are significantly reduced in this geometry, resulting in a low reaction efficiency. For the filled photocatalyst, the filled catalyst with an appropriate particle size fills in the reactor. The disadvantage is that utilization efficiency of light is low because the catalyst has a light-shielding effect on the photoreaction. Photocatalysts for use in fluidized beds and slurry reactors are similar, but the particle size of the fluidized photocatalyst is much large than the slurry-type. The catalyst is agitated and prevented from settling out by aeration during the reaction.

It is obviously that good dispersion and reaction efficiency are achieved in the slurry reactor. But the solid-liquid separation is difficult, so that the catalyst cannot be reused. Therefore, only fixed bed and fluidized bed reactors are used in the industry.

1.4.5 Photocatalysts based on Metal Organic Frameworks

Metal organic frameworks (MOFs) are highly porous structures which consist of coordinated metal ion centers and polyatomic organic bridging ligands [146, 147]. Due to their outstanding properties, such as porosity, large specific surface area, easily controllable framework and relatively good thermostability, MOFs have attracted much attention and are widely investigated for hydrogen

storage [148-152], as catalysts [153-157], chemical sensors [158, 159], for gas separation [160, 161], electrochemical applications [162] and optics [163]. In contrast, only a small number of MOFs have been reported for the application of dye degradation [164, 165], photochemical synthesis [166] and hydrogen production [167]. MOFs have a good potential in the efficient conversion of solar energy into chemical energy. Some MOF photocatalysts are to be reviewed in the following studies.

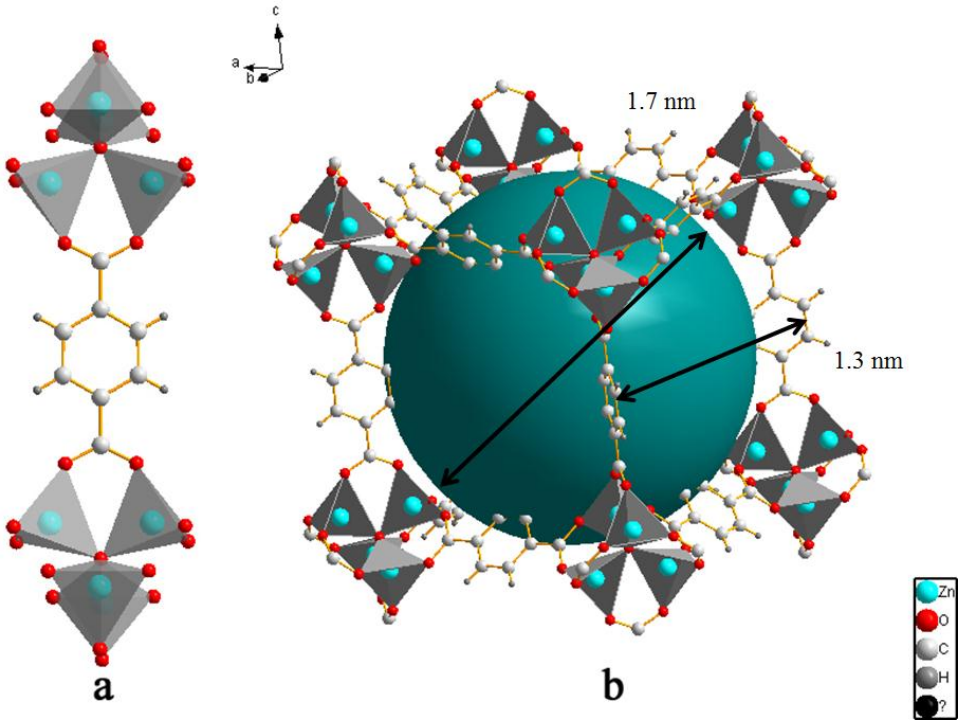

Figure 1.13 Structure of MOF-5: (a) $[Zn_4O]^{6+}$ clusters connected orthogonally by terephthalate ligands; (b) structure along [001] with the cage as turquoise sphere.

MOF-5 was the first reported structure whose photocatalytic behavior had

been reported [168]. MOF-5 has a microporous structure and is composed of Zn_4O clusters connected orthogonally by terephthalic acid ligands (see figure 1.13). The diameter of the windows and the cage size of MOF-5 are 1.3 and 1.7 nm, respectively. In this study, the conduction band edge of MOF-5 was calculated to be at 0.2 V versus NHE, and the band gap was estimated to be 3.4 eV. MOF-5 exhibited comparable activity in the degradation of phenol in aqueous solutions to P25, a commercial TiO_2 that is frequently used as benchmark for photocatalytic activity.

Fu et al. synthesized an amine-functionalized MOF (NH_2-MIL-125(Ti)) which consisted of cyclic octamers of TiO_4 octahedra connected by 2-amino terephthalic acid linkers. They reported a good visible light response of this material [169]. Figures 1.14a and b show the crystal structure of NH_2-MIL-125(Ti) with a micropore cage, which indicates that the top window of NH_2-MIL-125(Ti) is about 0.7 nm and the side window is around 0.9 nm. NH_2-MIL-125 displayed comparable activity in the reduction of CO_2 in aqueous solutions to that of the N doped TiO_2. Figure 1.14b illustrates the proposed mechanism for the CO_2 reduction with triethanolamine (TEOA) as sacrificial electron donor under visible light irradiation.

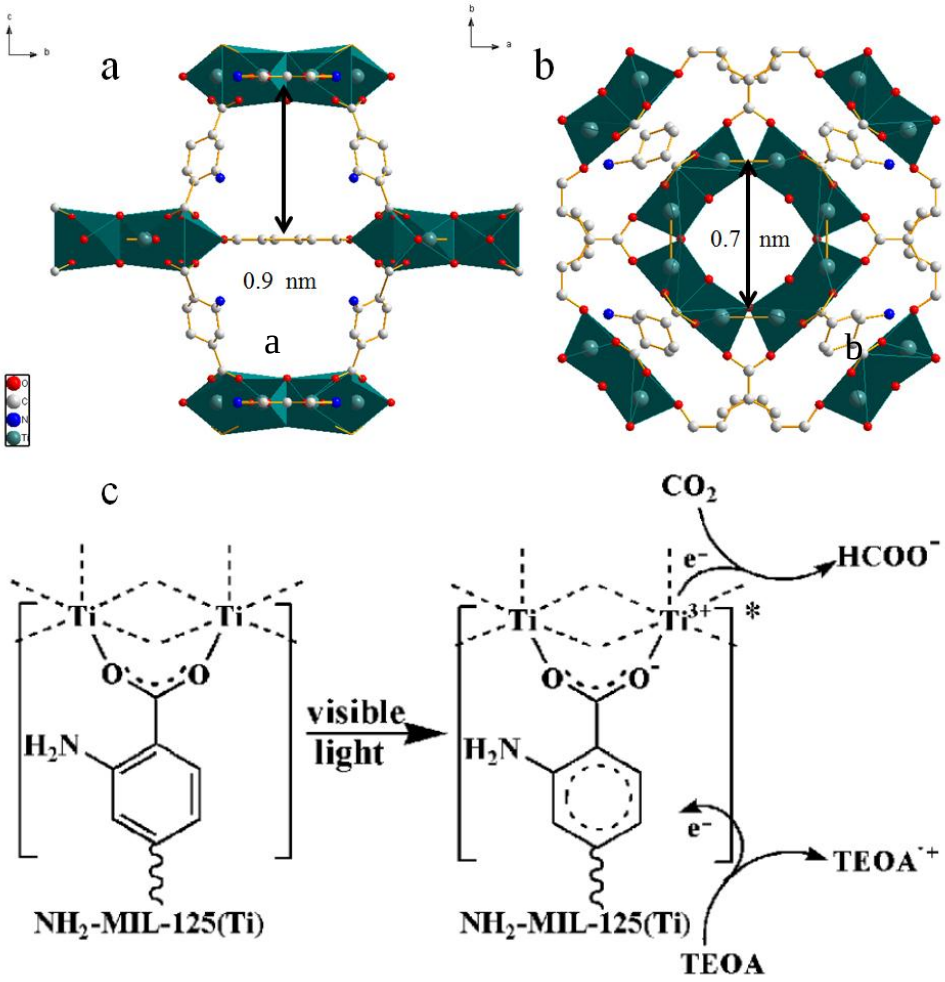

Figure 1.14 Crystal structure of NH_2-MIL-125(Ti): (a) side view and (b) top view; (c) Proposed mechanism for the CO_2 reduction under visible light irradiation.

Long et al. reported that NH_2-UIO-66 could be used for selective aerobic oxygenation [170]. NH_2-UIO-66 consists of hexametric $[Zr_6H_4O_8]^{12+}$ units and 2-amino terephthalate linkers and presents a micropore cage of 1.5 nm. In this study, various organic compounds including alcohols, olefins and cyclic alkanes were examined. Figure 1.15 illustrates the structure and photocatalytic mechanism of NH_2-UIO-66. A hole is generated on the linker and an electron

is promoted to the zirconium oxide cluster when visible light irradiate the NH_2-UIO-66.

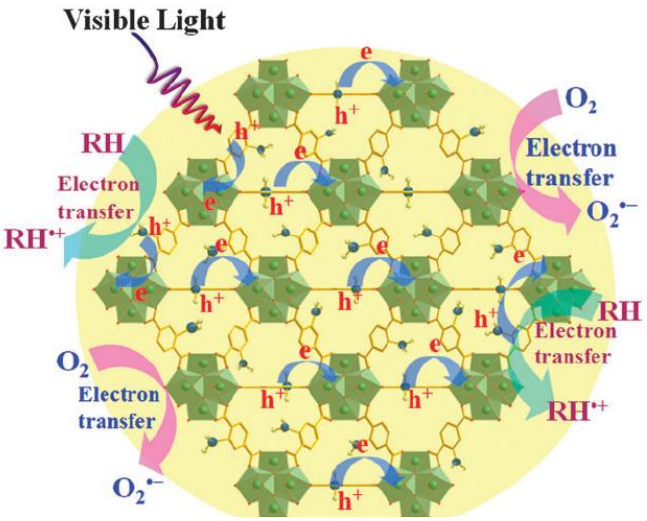

Figure 1.15 Structure and photocatalytic mechanism of NH_2-UIO-66.

1.5 Aim and outline of the thesis

As mentioned above, water pollution has become one of the most urgent problems facing the world. The discharge of untreated waste water does not only threaten human beings but also affects ecological systems causing the collapse of the aqueous ecosystem. Among the pollutants, heavy metal ions and organic pollutants are the most toxic species. Therefore, it is vital to efficiently remove heavy metal ions and organic dyes from waste water. The main aim of this study was to develop novel materials to remove Cr(VI) and dye from waste water. Metal organic frameworks were therefore evaluated as adsorbents to remove Cr(VI). Molecular doping is a new concept to control

the band gap of organic or hybrid semiconductors by employing different molecular species. The rational synthesis of heterojunction structures between metal organic frameworks and metal oxides as photocatalysts is a pioneering discovery and as such, these composites open opportunities to new area: inorganic and organic hybrid heterojunction photocatalyst.

The specific aims of this research were to:

1. To develop adsorbents for the removal of chromium (VI) from aqueous solutions based on metal organic frameworks (MOF), i.e., UIO-66, NH_2-UIO-66, NH_2-MIL-125(Ti) and NH_2 modified KIT-6 (Chapter 3 and 4).
    - Characterization of the as-synthesized materials employing various characterization techniques such as powder X-ray diffraction (XRD), transmission electron microscopy and nitrogen adsorption (BET).
    - An investigation of the adsorption process such as adsorption isotherms, thermodynamic study, and kinetic study desorption.
2. One-step solvothermal synthesis of mesoporous molecule-doped TiO_2 with high visible light response and photocatalytic activity (Chapter 5)
    - Preparation of different molecule-doped TiO_2.
    - Characterization of the as-synthesized materials employing various characterization techniques such as powder XRD, BET, scanning

electron microscopy (SEM), UV-vis diffuse reflectance spectroscopy (DRS) and flat band potential.

- Photocatalytic activity of samples over Rhodamine B.

3. NH_2-MIL125(Ti)/TiO_2 and NH_2-MIL125(Ti)/BiOBr heterojunctions with enhanced photocatalytic activity (Chapter 6 and 7)
   - Preparation of different NH_2-MIL125(Ti) based heterojunctions.
   - Characterization of the as-synthesized materials employing characterization techniques such as powder XRD, BET, SEM, transmission electron microscopy (TEM), DRS and flat band potential.
   - Photocatalytic activity of samples over Rhodamine B.
   - Study of active species during the photocatalytic reaction.
   - Mechanism study of the enhanced activity by forming heterojunctioned composites.

1.6 References

[1] S. Kulshreshtha, Water Resour. Manag., 12 (1998) 167.

[2] J. Hrubec, Quality and treatment of drinking water, Springer, Berlin Heidelberg 1998.

[3] United States Environmental Protection Agency, Environmental progress and challenges: EPA's update, Washington DC 1988.

[4] C.S.C. Wong, X. Li, I. Thornton, Environ. Pollut., 142 (2006) 1.

[5] F.E.O. Raymond, A. Wuana, ISRN Ecology, 2011 (2011) 20.

[6] Y.C. Sharma, A guide to the economic removal of metals from aqueous solutions, John Wiley & Sons, Inc., New York 2011.

[7] N.P. Cheremisinoff, Handbook of water and wastewater treatment technology, Marcel Dekker Inc., New York 2002.

[8] H. Jabeen, V. Chandra, S. Jung, J.W. Lee, K.S. Kim, S.B. Kim, Nanoscale, 3 (2011) 3583.

[9] X.S. Wang, Z.Z. Li, S.R. Tao, J. Environ. Manage., 90 (2009) 721.

[10] E.L. Hawley, R.A. Deeb. M.C. Kavanaugh, J.A. Jacobs, Treatment technologies for chromium(VI), in: chromium(VI) handbook, CRC Press, Florida 2005.

[11] M. Uysal, I. Ar, J. Hazard. Mater., 149 (2007) 482.

[12] S.T. Farrell, C.B. Breslin, Environ. Sci. Technol., 38 (2004) 4671.

[13] S. Gupta, B.V. Babu, Chem. Eng. J., 150 (2009) 352.

[14] C.W. Bishop, J.C. Knutson, C.R. Valliere, Method of treating prostatic diseases using delayed and/or sustained release vitamin D formulations, in, Google Patents, 1998. US5795882 A

[15] D. Mohan, S. Rajput, V.K. Singh, P.H. Steele, C.U. Pittman Jr, J. Hazard. Mater., 188 (2011) 319.

[16] G. Anger, J. Halstenberg, K. Hochgeschwender, C. Scherhag, U.

Korallus, H. Knopf, P. Schmidt, M. Ohlinger, Chromium compounds, in: Ullmann's encyclopedia of industrial chemistry, Wiley-VCH, , Weinheim 2000.

[17] H. Zheng, R. Li, S. Cao, Environ. Sci. Technol., 45 (2011) 9822.

[18] World Health Organization, Guidelines for drinking-water quality - 4th ed., in: Guideline values for individual chemicals, by source category, Malta 2011.

[19] U.S. Environmental Protection Agency, 2011 Edition of the drinking water standards and health advisories, in: drinking water standards and health advisories, U.S. Environmental Protection Agency 2011.

[20] EU's Drinking Water Standards, Council Directive 98/83/EC on the quality of water intented for human consumption. Adopted by the Council, in: Chemical parameters 1998.

[21] Ministry of Health of the People's Republic of China, Standard for drinking water quality, Beijing 2006.

[22] Singapore National Environment Agency, environmental public health act, in: environmental public health (quality of piped drinking water) regulations 2008.

[23] I. Ali, M. Asim, T.A. Khan, J. Environ. Manag., 113 (2012) 170.

[24] I. Ali, H.Y. Aboul-Enein, Chiral pollutants: sources and distribution, in: chiral pollutants: distribution, toxicity and analysis by chromatography

and capillary electrophoresis, John Wiley & Sons, Ltd, England 2004.

[25] B. Damià, Emerging organic pollutants in waste waters and sludge, Springer, Berlin 2005.

[26] M.A. Katzenberg, H.R. Krouse, Can. Soc. Forensic Sci. J., 22 (1989) 7.

[27] M. van der Perk, Soil and water contamination, 2nd ed., CRC Press/Balkema, Leiden, The Netherland 2012.

[28] Attorney General's Chambers, The sewerage and drainage (trade effluent) regulations: requirements for discharge of trade effluent into public sewer, Singapore, 1999. Available online: http://statutes.agc.gov.sg/aol/search/display/view.w3p;page=0;query=CompId%3Aadc249d9-fcff-4dd0-9f3b-4be8d8d22ca2%20ValidTime%3A20120524000000%20TransactionTime%3A20120524000000;rec=0 Accessed 22-10-2014

[29] T. Robinson, G. McMullan, R. Marchant, P. Nigam, Bioresour. Technol., 77 (2001) 247.

[30] E.A. Clarke, R. Anliker, Organic dyes and pigments, in: anthropogenic compounds, Springer, Berlin Heidelberg 1980.

[31] Colour Index, Colour index international, fourth edition online, in, Society of Dyers and Colourists and the American Association of Textile Chemists and Colorists, Bradford, England, 2001. http://www.colour-index.com/

[32] L. Greer, S. E. Keane, Z. Lin, NRDC's ten best practices for textile mills to save money and reduce pollution, Natural Resources Defense Council, 2010.

[33] S. Zaharia, D. Suteu, Muresan, A.; Muresan, R.; Popescu, A., Environ. Eng. Manage. J., 8 (2009) 1359.

[34] C. Zaharia, D. Suteu, Textile organic dyes – characteristics, polluting effects and separation/elimination procedures from industrial effluents – a critical overview, in: Industrial wastewater treatment, recycling and reuse, Elsevier, Oxford, UK 2014.

[35] Z. Wang, M. Xue, K. Huang, Z. Liu, Textile dyeing wastewater treatment, in: Advances in treating textile effluent, InTech, 2011.

[36] DoWater.com, DoWater.com, Guizhou, China, 2012. http://www.dowater.com/jishu/2012-04-23/81969.html.

[37] N. Kongsricharoern, C. Polprasert, Water Sci. Technol., 31 (1995) 109.

[38] A.K. Golder, A.K. Chanda, A.N. Samanta, S. Ray, Sep. Sci. Technol., 76 (2011) 345.

[39] G. Mouedhen, M. Feki, M. De Petris-Wery, H.F. Ayedi, J. Hazard. Mater., 168 (2009) 983.

[40] N. Kongsricharoern, C. Polprasert, Water Sci. Technol., 34 (1996) 109.

[41] Y. Xing, X. Chen, D. Wang, Environ. Sci. Technol., 41 (2007) 1439.

[42] F. Gode, E. Pehlivan, J. Hazard. Mater., 119 (2005) 175.

[43] B. Galán, D. Castañeda, I. Ortiz, Water Res., 39 (2005) 4317.

[44] S. Edebali, E. Pehlivan, Chem. Eng. J., 161 (2010) 161.

[45] J.C. Seaman, P.M. Bertsch, L. Schwallie, Environ. Sci. Technol., 33 (1999) 938.

[46] M.J. Alowitz, M.M. Scherer, Environ. Sci. Technol., 36 (2002) 299.

[47] P.R. Wittbrodt, C.D. Palmer, Environ. Sci. Technol., 29 (1995) 255.

[48] L.B. Khalil, W.E. Mourad, M.W. Rophael, Appl. Catal. B-Environ., 17 (1998) 267.

[49] A.I. Alonso, B. Galán, M. González, I. Ortiz, Ind. Eng. Chem. Res., 38 (1999) 1666.

[50] A.I. Alonso, C.C. Pantelides, J. Membr. Sci., 110 (1996) 151.

[51] M. Camino, M.G. Bagur, M. Sanchez-Vinas, D. Gazquez, R. Romero, J. Anal. At. Spectrom., 16 (2001) 638.

[52] A. Bhowal, S. Datta, J. Membr. Sci., 188 (2001) 1.

[53] I. Ortiz, M.F. San Román, S.M. Corvalán, Ind. Eng. Chem. Res., 42 (2003) 5891.

[54] M.A. Hasan, Y.T. Selim, K.M. Mohamed, J. Hazard. Mater., 168 (2009) 1537.

[55] C.A. Kozlowski, W. Walkowiak, Water Res., 36 (2002) 4870.

[56] K.A. Matis, P. Mavros, Sep. Purif. Rev., 20 (1991) 1.

[57] Z. Song, C.J. Williams, R.G.J. Edyvean, Water Res., 34 (2000) 2171.

[58] R. Bala, A.K. Thukral, Int. J. Phytoremediati., 13 (2011) 465.

[59] S.D. Huang, C.F. Fann, H.S. Hsieh, J. Colloid Interface Sci., 89 (1982) 504.

[60] G. Bayramoglu, M.Y. Arica, J. Hazard. Mater., 187 (2011) 213.

[61] L. Deng, Z. Shi, B. Li, L. Yang, L. Luo, X. Yang, Ind. Eng. Chem. Res., 53 (2014) 7746.

[62] W. Jiang, Q. Cai, W. Xu, M. Yang, Y. Cai, D.D. Dionysiou, K.E. O'Shea, Environ. Sci. Technol., 48 (2014) 8078.

[63] M. Bhaumik, A. Maity, V.V. Srinivasu, M.S. Onyango, J. Hazard. Mater., 190 (2011) 381.

[64] V.K. Gupta, D. Pathania, S. Agarwal, S. Sharma, Environ. Sci. Pollut.Res., 20 (2013) 2632.

[65] P. Lakshmipathiraj, S. Umamaheswari, G.B. Raju, S. Prabhakar, G. Caroling, S. Kato, T. Kojima, Environ. Prog. Sustain. Energy., 32 (2013) 35.

[66] M. Jain, V.K. Garg, K. Kadirvelu, Bioresour. Technol., 102 (2011) 600.

[67] S.R. Chowdhury, E.K. Yanful, A.R. Pratt, J. Hazard. Mater., 235–236 (2012) 246.

[68] P. Yuan, D. Liu, M. Fan, D. Yang, R. Zhu, F. Ge, J. Zhu, H. He, J. Hazard. Mater., 173 (2010) 614.

[69] K. Parida, K.G. Mishra, S.K. Dash, J. Hazard. Mater., 241–242 (2012)

395.

[70] S. Goswami, S.C. Bhat, U.C. Ghosh, Water Environ. Res. , 78 (2006) 986.

[71] S. Goswami, U.C. Ghosh, Water SA, 31 (2005) 597.

[72] U. Ghosh, M. Dasgupta, S. Debnath, S. Bhat, Water, Air, Soil Pollut., 143 (2003) 245.

[73] L.A. Rodrigues, L.J. Maschio, R.E. da Silva, M.L.C.P. da Silva, J. Hazard. Mater., 173 (2010) 630.

[74] A.A. Muxel, S.M.N. Gimenez, F.A. de Souza Almeida, R.V. da Silva Alfaya, A.A. da Silva Alfaya, CLEAN–Soil, Air, Water, 39 (2011) 289.

[75] W. Yu, L. Zhang, H. Wang, L. Chai, J. Hazard. Mater., 260 (2013) 789.

[76] X. Dong, L.Q. Ma, Y. Li, J. Hazard. Mater., 190 (2011) 909.

[77] K. Selvi, S. Pattabhi, K. Kadirvelu, Bioresour. Technol., 80 (2001) 87.

[78] M.A. Atieh, Procedia. Environ. Sci., 4 (2011) 281.

[79] N.P. Tantak, S. Chaudhari, J. Hazard. Mater., 136 (2006) 698.

[80] H. An, Y. Qian, X. Gu, W.Z. Tang, Chemosphere, 33 (1996) 2533.

[81] P. Gregory, C.V. Stead, J. Soc. Dyers Colour., 94 (1978) 402.

[82] P.K. Malik, S.K. Saha, Sep. Sci. Technol., 31 (2003) 241.

[83] K. Swaminathan, S. Sandhya, A.S. Carmalin, K. Pachhade, Y.V. Subrahmanyam, Chemosphere, 50 (2003) 619.

[84] L. Szpyrkowicz, C. Juzzolino, S.N. Kaul, Water Res., 35 (2001) 2129.

[85] S.F. Kang, C.H. Liao, H.P. Hung, J. Hazard. Mater., 65 (1999) 317.

[86] F. Harrelkas, A. Azizi, A. Yaacoubi, A. Benhammou, M.N. Pons, Desalination, 235 (2009) 330.

[87] I.K. Konstantinou, T.A. Albanis, Appl. Catal. B-Environ., 49 (2004) 1.

[88] R.J. Tayade, T.S. Natarajan, H.C. Bajaj, Ind. Eng. Chem. Res., 48 (2009) 10262.

[89] W. Kang, C.S. Spanjers, R.M. Rioux, J.D. Hoefelmeyer, J. Mater. Chem. A, 1 (2013) 7717.

[90] N. Mohan, N. Balasubramanian, J. Hazard. Mater., 136 (2006) 239.

[91] M. Panizza, G. Cerisola, Appl. Catal. B-Environ., 75 (2007) 95.

[92] S. Raghu, C. Ahmed Basha, J. Hazard. Mater., 149 (2007) 324.

[93] W.I. Jose, Typical state-of-the-art researches & applications of environmental biotechnology in the Philippines. http://nsspo.com/p1/Research_Apps_Biotech.htm.

[94] Y.C. Sharma, A guide to the economic removal of metals from aqueous solutions, Wiley, Canada 2012.

[95] J. Olivier, J. Por. Mater., 2 (1995) 9.

[96] Micromeritics Instrument Corporation, Surface Area. http://www.particletesting.com/Services-Provided/Surface-Area.aspx.

[97] S. Brunauer, P.H. Emmett, E. Teller, J. Am. Chem. Soc., 60 (1938) 309.

[98] M. Owlad, M. Aroua, W. Daud, S. Baroutian, Water, Air, Soil Pollut.,

200 (2009) 59.

[99] C. Selomulya, V. Meeyoo, R. Amal, J. Chem. Technol. Biotechnol., 74 (1999) 111.

[100] N.K. Hamadi, X.D. Chen, M.M. Farid, M.G.Q. Lu, Chem. Eng. J., 84 (2001) 95.

[101] S.-J. Park, W.-Y. Jung, J. Colloid Interface Sci., 243 (2001) 316.

[102] Kobya, M. Kobya, Adsorp. Sci. Technol., 22 (2004) 51.

[103] F. Di Natale, A. Lancia, A. Molino, D. Musmarra, J. Hazard. Mater., 145 (2007) 381.

[104] C. Xu, B. Qiu, H. Gu, X. Yang, H. Wei, X. Huang, Y. Wang, D. Rutman, D. Cao, S. Bhana, Z. Guo, S. Wei, ECS J. Solid State Sci. Tech., 3 (2014) M1.

[105] R.L. Goswamee, P. Sengupta, K.G. Bhattacharyya, D.K. Dutta, Appl. Clay Sci., 13 (1998) 21.

[106] N.K. Lazaridis, D.D. Asouhidou, Water Res., 37 (2003) 2875.

[107] N.N. Das, J. Konar, M.K. Mohanta, S.C. Srivastava, J. Colloid Interface Sci., 270 (2004) 1.

[108] U. Ghosh, M. Dasgupta, S. Debnath, S. Bhat, Water, Air, Soil Pollut., 143 (2003) 245.

[109] H. Ucun, Y.K. Bayhan, Y. Kaya, A. Cakici, O. Faruk Algur, Bioresour. Technol., 85 (2002) 155.

[110] F.N. Acar, E. Malkoc, Bioresour. Technol., 94 (2004) 13.

[111] J. Romero-González, J.R. Peralta-Videa, E. Rodríguez, S.L. Ramirez, J.L. Gardea-Torresdey, J. Chem. Thermodyn., 37 (2005) 343.

[112] J.L. Gardea-Torresdey, K.J. Tiemann, V. Armendariz, L. Bess-Oberto, R.R. Chianelli, J. Rios, J.G. Parsons, G. Gamez, J. Hazard. Mater., 80 (2000) 175.

[113] G. Rojas, J. Silva, J.A. Flores, A. Rodriguez, M. Ly, H. Maldonado, Sep. Sci. Technol., 44 (2005) 31.

[114] V.M. Boddu, K. Abburi, J.L. Talbott, E.D. Smith, Environ. Sci. Technol., 37 (2003) 4449.

[115] D.C. Sharma, C.F. Forster, Bioresour. Technol., 52 (1995) 261.

[116] D.C. Sharma, C.F. Forster, Process Biochem., 30 (1995) 293.

[117] M. Rao, A.V. Parwate, A.G. Bhole, Waste Manage., 22 (2002) 821.

[118] B. Bayat, J. Hazard. Mater., 95 (2002) 275.

[119] S.S. Banerjee, M.V. Joshi, R.V. Jayaram, Sep. Sci. Technol., 39 (2005) 1611.

[120] V. Gupta, D. Mohan, S. Sharma, K. Park, Environmentalist, 19 (1998) 129.

[121] A. Kay, M. Graetzel, J. Phys. Chem., 97 (1993) 6272.

[122] H. Alarcón, G. Boschloo, P. Mendoza, J.L. Solis, A. Hagfeldt, J. Phys. Chem. B, 109 (2005) 18483.

[123] J. Araña, J.M. Doña-Rodríguez, O. González-Díaz, E. Tello Rendón, J. Mole. Catal. A: Chem., 215 (2004) 153.

[124] A. Fujishima, K. Honda, Nature, 238 (1972) 37.

[125] A.L. Pruden, D.F. Ollis, J. Catal., 82 (1983) 404.

[126] D.F. Ollis, J. Catal., 88 (1984).

[127] N. Serpone, D. Lawless, R. Khairutdinov, J. Phys. Chem., 99 (1995) 16646.

[128] V. Augugliaro, V. Loddo, M. Pagliaro, G. Palmisano, L. Palmisano, - Clean by Light Irradiation. The Royal Society of Chemistry, Cambridge, UK 2010.

[129] D.O. Scanlon, C.W. Dunnill, J. Buckeridge, S.A. Shevlin, A.J. Logsdail, S.M. Woodley, C.R.A. Catlow, M.J. Powell, R.G. Palgrave, I.P. Parkin, G.W. Watson, T.W. Keal, P. Sherwood, A. Walsh, A.A. Sokol, Nature Mater, 12 (2013) 798.

[130] S. Shenawi-Khalil, V. Uvarov, E. Menes, I. Popov, Y. Sasson, Appl. Catal., A, 413–414 (2012) 1.

[131] S.U.M. Khan, M. Al-Shahry, W.B. Ingler, Science, 297 (2002) 2243.

[132] M.A. Fox, M.T. Dulay, Chem. Rev., 93 (1993) 341.

[133] M.R. Hoffmann, S.T. Martin, W. Choi, D.W. Bahnemann, Chem. Rev., 95 (1995) 69.

[134] I. Bedja, P.V. Kamat, J. Phys. Chem., 99 (1995) 9182.

[135] W. Choi, A. Termin, M.R. Hoffmann, J. Phys. Chem., 98 (1994) 13669.

[136] E.C. Butler, A.P. Davis, J. Photochem. Photobiol. A, 70 (1993) 273.

[137] R. Asahi, T. Morikawa, T. Ohwaki, K. Aoki, Y. Taga, Science, 293 (2001) 269.

[138] C. Di Valentin, G. Pacchioni, A. Selloni, S. Livraghi, E. Giamello, J. Phys. Chem. B, 109 (2005) 11414.

[139] H. Irie, Y. Watanabe, K. Hashimoto, Chem. Lett., 32 (2003) 772.

[140] X. Chen, C. Burda, J. Am. Chem. Soc., 130 (2008) 5018.

[141] K. Yang, Y. Dai, B. Huang, J. Phys. Chem. C, 111 (2007) 18985.

[142] J.K. Zhou, L. Lv, J. Yu, H.L. Li, P.-Z. Guo, H. Sun, X.S. Zhao, J. Phys. Chem. C, 112 (2008) 5316.

[143] S. In, A. Orlov, R. Berg, F. Garc á, S. Pedrosa-Jimenez, M.S. Tikhov, D.S. Wright, R.M. Lambert, J. Am. Chem. Soc., 129 (2007) 13790.

[144] F. Bensebaa, Nanoparticle Technologies: From Lab to Market. Elsevier, UK 2013.

[145] J. A. Moulijn，M. Makkee，A. E. V. Diepen, Chemical Process Technology. John Wiley & Sons Ltd., UK 2013.

[146] O.M. Yaghi, H. Li, J. Am. Chem. Soc., 117 (1995) 10401.

[147] O.M. Yaghi, G. Li, H. Li, Nature, 378 (1995) 703.

[148] M. Dincă, J.R. Long, Angew. Chem. Int. Ed., 47 (2008) 6766.

[149] M. Dincă, A. Dailly, Y. Liu, C.M. Brown, D.A. Neumann, J.R. Long, J.

Am. Chem. Soc., 128 (2006) 16876.

[150] M. Dincă, W.S. Han, Y. Liu, A. Dailly, C.M. Brown, J.R. Long, Angew. Chem. Int. Ed., 46 (2007) 1419.

[151] M. Latroche, S. Surblé, C. Serre, C. Mellot-Draznieks, P.L. Llewellyn, J.-H. Lee, J.-S. Chang, S.H. Jhung, G. Férey, Angew. Chem. Int. Ed., 45 (2006) 8227.

[152] G. Férey, C. Mellot-Draznieks, C. Serre, F. Millange, J. Dutour, S. Surblé, I. Margiolaki, Science, 309 (2005) 2040.

[153] N.T.S. Phan, T.T. Nguyen, P. Ho, K.D. Nguyen, ChemCatChem, 5 (2013) 1822.

[154] S.T. Meek, J.A. Greathouse, M.D. Allendorf, Adv. Mater., 23 (2011) 249.

[155] Y. Liu, W. Xuan, Y. Cui, Adv. Mater., 22 (2010) 4112.

[156] B. Yuan, Y. Pan, Y. Li, B. Yin, H. Jiang, Angew. Chem. Int. Ed., 49 (2010) 4054.

[157] D. Farrusseng, S. Aguado, C. Pinel, Angew. Chem. Int. Ed., 48 (2009) 7502.

[158] G. Lu, J.T. Hupp, J. Am. Chem. Soc., 132 (2010) 7832.

[159] B. Liu, J. Mater. Chem., 22 (2012) 10094.

[160] T.H. Bae, J.S. Lee, W. Qiu, W.J. Koros, C.W. Jones, S. Nair, Angew. Chem. Int. Ed., 49 (2010) 9863.

[161] J.R. Li, R.J. Kuppler, H.C. Zhou, Chem. Soc. Rev., 38 (2009) 1477.

[162] A. Morozan, F. Jaouen, Energy Environ. Sci., 5 (2012) 9269.

[163] C. Wang, T. Zhang, W. Lin, Chem. Rev., 112 (2011) 1084.

[164] J.R. Choi, T. Tachikawa, M. Fujitsuka, T. Majima, Langmuir, 26 (2010) 10437.

[165] C.F. Zhang, L.G. Qiu, F. Ke, Y.J. Zhu, Y.P. Yuan, G.S. Xu, X. Jiang, J. Mater. Chem. A, 1 (2013) 14329.

[166] T. Toyao, M. Saito, Y. Horiuchi, K. Mochizuki, M. Iwata, H. Higashimura, M. Matsuoka, Catal. Sci. Technol., 3 (2013) 2092.

[167] T. Toyao, M. Saito, S. Dohshi, K. Mochizuki, M. Iwata, H. Higashimura, Y. Horiuchi, M. Matsuoka, Chem. Commun., 50 (2014) 6779.

[168] M. Alvaro, E. Carbonell, B. Ferrer, F.X. Llabrés i Xamena, H. Garcia, Chem-Eur. J., 13 (2007) 5106.

[169] Y. Fu, D. Sun, Y. Chen, R. Huang, Z. Ding, X. Fu, Z. Li, Angew. Chem. Int. Ed., 51 (2012) 3364.

[170] J. Long, S. Wang, Z. Ding, S. Wang, Y. Zhou, L. Huang, X. Wang, Chem. Commun., 48 (2012) 11656.

Chapter 2 Experimental

This chapter will briefly discuss the main characterization techniques employed in this research.

2.1 X-ray Powder Diffraction

X-ray diffraction (XRD) is a major technique and it is always employed to identify the structure of crystalline materials. It has offered a qualitative method to identify the compounds present in crystalline powders as well as the crystal structure of pure single crystals. There is a specified X-ray powder diffraction pattern for one crystalline material, and the specified XRD pattern can be used to serve as a "fingerprint" to identify the crystal structure of samples. In addition, X-ray crystallography is able to provide some information, such as the interatomic distances, dimensions, angles and phases of the unit cell. Figure 2.1 shows conditions for Bragg reflection from scattering centers confined to a set of equidistant, parallel planes, when X-ray photons strike the sample. A crystal with planes oriented at an angle θ to an incident x-ray beam of wavelength λ will diffract the rays, according to the Bragg's equation can successfully calculate the distance between two planes [1].

$$n\lambda = 2d \sin\theta \qquad (2.1)$$

where n is an integer normally taken as 1, d is the interplanar spacing, θ is the angle of diffraction and called the Bragg angle, and λ is the wavelength of the monochromatic X-ray.

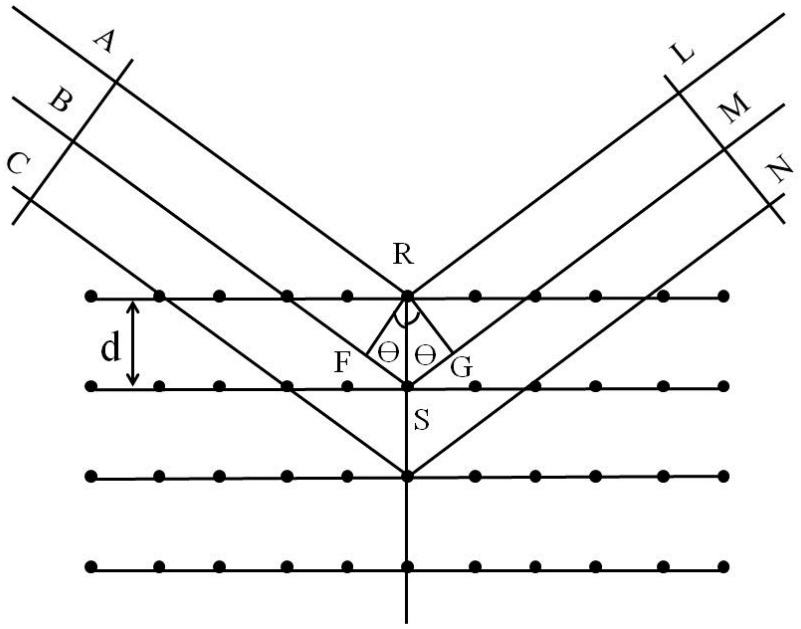

Figure 2.1 Condition for Bragg reflection from scattering centers confined to a set of equidistant parallel planes [2].

For powder diffraction, some of the crystallites will be orientated to satisfy the Bragg condition for each set of planes (*hkl*), then different planes will provide rise to intensity at the correspondingly diffraction angles.

The diffractometer used for our study operates in a θ-θ geometry where the sample is kept horizontal and both the x-ray source and the detector move. It is

equipped with a Cu anode and variable primary and secondary beam slits. The Cu anode was operated at 40 kV and 40 mA and the measured area was kept constant at 20 x 20 mm. The sample was ground into a fine powder and pressed tightly on the sample holder to obtain a smooth flat surface. The typical parameters for the XRD measurement of UIO-66 and NH_2-UIO-66 is as follows: 2θ range from 5^o-50^o with a step size of 0.02^o and a dwell time of 1s/step. For TiO_2 and NH_2-MIL-125(Ti) based samples, the diffractograms were recorded from 2θ of 5^o to 120^o, using a step size of 0.02^o and a dwell time of 1s/step.

2.2 BET surface area and porosity measurement

BET surface area measurement technique is always employed to study the surface area and porosity of the solid samples. The theory was discussed in chapter 1.

Nitrogen adsorption isotherms of the catalysts were measured with a Micromeritics TriStar 3000 instrument. The solid samples (0.03 - 0.07 g) were first degassed at 130 ^oC in a flow of nitrogen for 4 h prior to test in order to remove any adsorbed moisture and solvent. The samples in quartz tubes were then transferred to the Tri Star 3000, which can measure isotherms of three samples simultaneously. Nitrogen adsorption isotherms were recorded at the temperature of liquid nitrogen (77 K). The isotherm is measured from about 1

mbar (100 Pa) to 1 bar (101300 Pa). The resolution of the pressure sensors is 0.01 mbar (1 Pa). Gaseous nitrogen was introduced in small doses under equipment control, and about 100 points each are recorded on the adsorption and desorption branch of the isotherm. Recording of one complete isotherm takes about 10 hours and is normally done overnight. From the adsorption isotherm, the BET surface area and the pore size distribution are calculated using the theories explained in Chapter 1. The pore size distribution was determined from the desorption isotherm using the Barrett, Joyner, Halenda (BJH) theory [3]. There are 6 types of isotherms as illustrated in Figure 2.2.

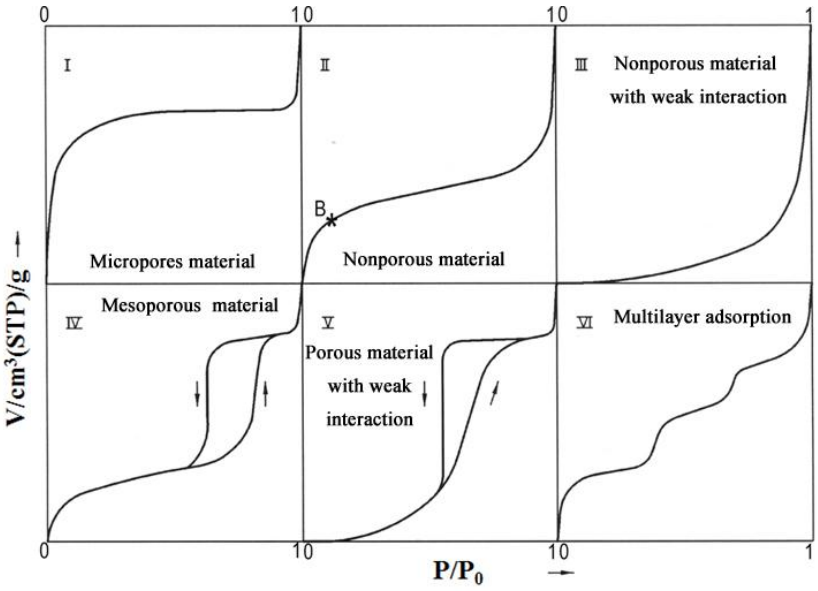

Figure 2.2 Different types of adsorption-desorption isotherms.

2.3 Scanning electron microscopy

The scanning electron microscopy (SEM) is a type of electron microscope，

which is able to generate a high resolution image of a sample surface by using electrons instead of light [4]. Due to the mechanism of image formation, the SEM image has a very large depth of focus which gives the images the characteristic three-dimensional appearance which makes it easy the evaluate the surface structure of the sample. The resolution of the SEM is determined by the size of the scanning beam and can be as good as a few nm. Figure 2.3 shows schematic drawing of a SEM. In the SEM, a beam of electrons is produced from an electron gun in a vacuum. The electron beam is then collimated by the electromagnetic first and second condenser lenses, subsequently focused by an objective lens, and then raster-scanned across the surface of the sample by electromagnetic deflection coils. There are various signals (secondary electrons, internal currents, photon emissions, etc.) generated when the beam interacts with the sample. Secondary electrons are measured by a scintillation material which produces a flash of light for each electron. The light is then detected and amplified by a photomultiplier tube. By correlating the sample scan position with the resulting signal, an image can be created. The illumination and shadowing show a fairly natural looking surface topography.

Backscattered electrons (BSE) are the high-energy electrons reflected or back-scattered originating from the elastic interaction between incident electrons and the solid sample. The backscattered electron detector is

employed to detect the backscattered electrons in order to obtain contrast between areas with different chemical compositions, because the scattering cross-section of heavy elements (high atomic number) is much higher than that of light elements.

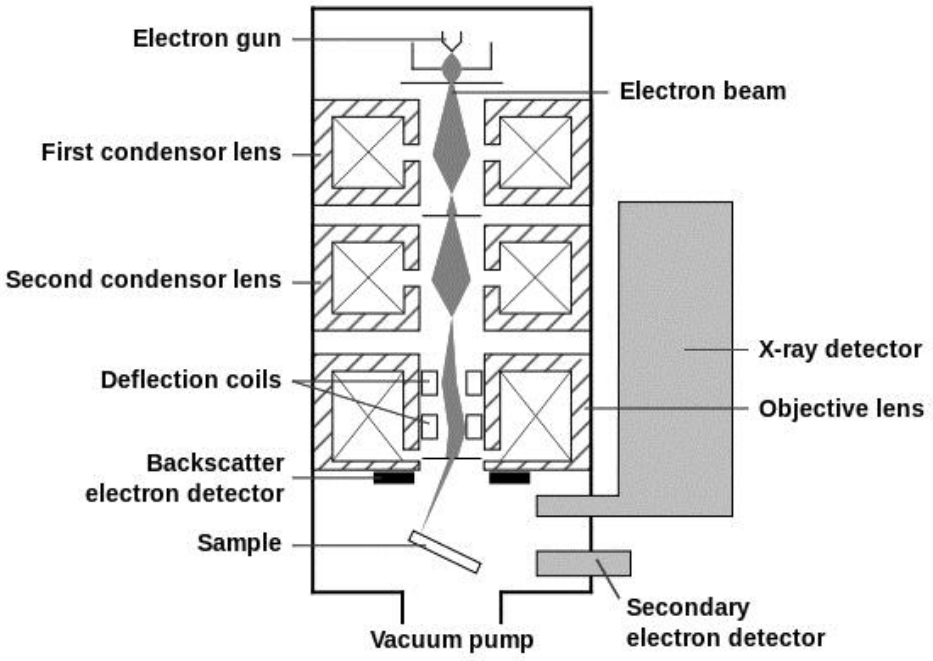

Figure 2.3 Schematic drawing of SEM [5].

In addition, the energy dispersive X-ray analysis can be done in this system, because the X-ray detector can capture the emission of an X-ray originating in the interaction of the primary beam with atoms in the sample. Therefore, the elements of sample can be characterized by the emitted X-ray energy.

In this research, the SEM was primarily employed to study the topography and morphology of the solid sample. The SEM images were obtained on a JEOL

JSM-6701F SEM (field-emission) at a voltage of 5 kV. The samples were coated with Pt with 20 mA and 30 s by JFC-1600 auto fine coater. The plot of film thickness versus sputtering time is given in Figure 2.4.

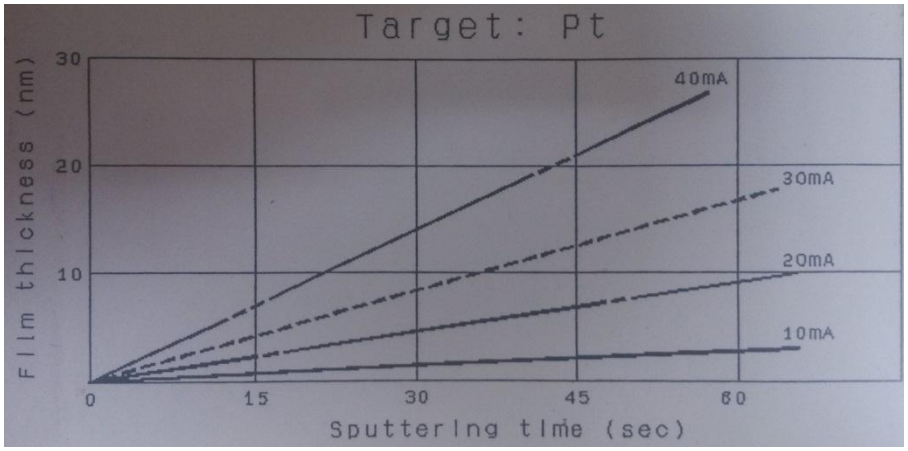

Figure 2.4 The plot of film thickness versus sputtering time from JFC-1600 auto fine coater

2.4 Transmission electron microscopy

Transmission Electron Microscopy (TEM) is a microscopy technique employed to generate high-magnification images, when a thin specimen interacts with with a high energy (typically > 100 keV) electron beam [6]. Electrons are used instead of light because they are elementary particles displaying wave-particle duality where the wavelength is much shorter than that of light. This makes it possible to get high resolution images. The wavelength of an electron accelerated through an electric field U is given by the de Broglie equation:

$$\lambda = \frac{h}{m_0 v\sqrt{1-v^2/c^2}} = \frac{h}{\sqrt{2m_0 eV - [1+\frac{eV}{2m_0 c^2}]}} \quad (2.2)$$

where h = Planck's constant (6.626×10^{-34} J s), m_0 = rest mass of the electron (9.109×10^{-31} kg), v = velocity of the electron, c = speed of light (2.998×10^{8}m/s) and V = beam acceleration voltage. Thus, the de Broglie's wavelength of 200keV electrons is 2.5 pm. The very high resolution of about 100 pm is due to the picometer range of the electron wavelength. There are principally two modes in TEM: imaging or diffracting mode, the principles of which are shown in Figure 2.5.

The imaging mode is employed in our experiment. In this mode (see Figure 2.5a), mass-thickness contrast, diffraction contrast and phase contrast are created from the interaction between incoming electrons and the material. Since the TEM operates in transmission and avoids multiple scattering of the electrons, the sample needs to be very thin (no more than a few atomic layers). Because the deflection in the TEM is produced from interactions between electrons and the atoms of the sample, a thick material with large atomic number atoms will deflect more incident electrons than a thin material with light elements.

The diffraction contrast originates from the different orientation of crystalline phases in the sample, and the phase contrast is always directly related to the

atomic structure of material. The incident electron beam will be fully scattered when the orientation of a crystallite relative to the electron gun and to the observation direction happens to agree with the Bragg condition. High resolution imaging can be achieved mainly due to the phase contrast feature. The selected area electron diffraction (SAED) aperture allows the diffraction mode (see Figure 2.5b).

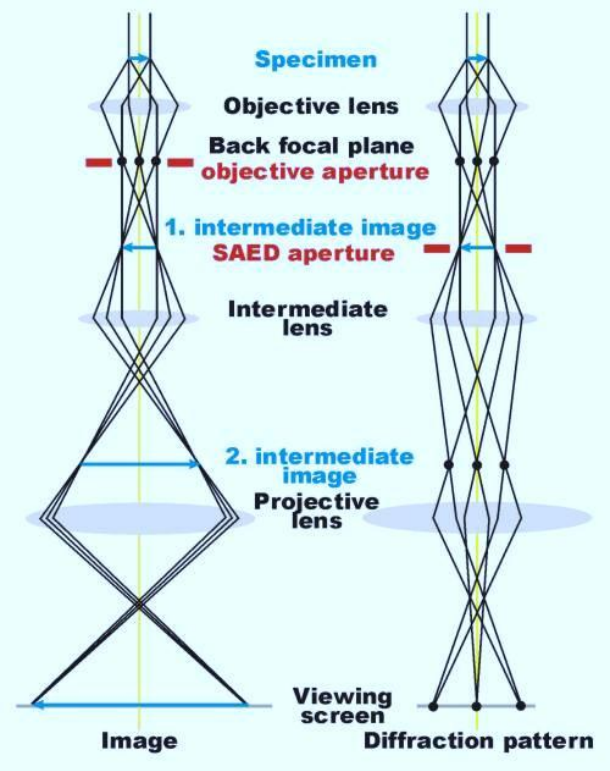

Figure 2.5 Operating modes of TEM: (a) imaging mode and (b) diffracting mode. Both modes can be interchanged by adjusting the objective and SAED aperture [7].

A JEOL 3010 transmission electron microscope operated at 200 kV is employed in this research. For sample preparation, 5 mg of finely ground samples were suspended in 5 mL of 2-propanol (IPA) and the suspensions

were sonicated for 5 min. Two drops of the suspension were placed onto a carbon-coated copper grid and dried at room temperature overnight. The copper grid was gently placed onto the sample holder and inserted into the TEM instrument for measurements.

2.5 UV-vis molecular absorption spectroscopy

UV-vis molecular absorption spectroscopy is employed for qualitative and quantitative determination of aromatic and unsaturated liquid samples of organic compounds and inorganic ions which are containing π-electrons or non-bonding electrons (n-electrons). Those aromatic and unsaturated compounds can absorb the ultraviolet or visible light energy in order to excite electrons from bonding molecular orbitals into higher anti-bonding molecular orbitals. The lower the energy gap between the HOMO and the LUMO, the longer the wavelength of light is needed to absorb. The chromophores, like C=C, C=O, C=N, are defined as the molecular groups that are able to absorb visible or UV light.

Figure 2.6 illustrates the construction principle of a double beam UV/VIS absorption spectrophotometer. The incident beam from one of two light source (D_2 lamp for UV and W lamp for visible and NIR) goes through a scanning monochromator. The monochromatized beam it split by a quartz half mirror into two beams. One beam passes through a quartz cell containing the sample,

while the other travels through a quartz cell containing the blank. Photomultipliers convert these lights signals into electric current and the electric circuity compares the two currents to calculate the absorbance I/I_o. The results are then stored on file and converted to absorption spectra displaying % absorption, % transmission or absorbance.

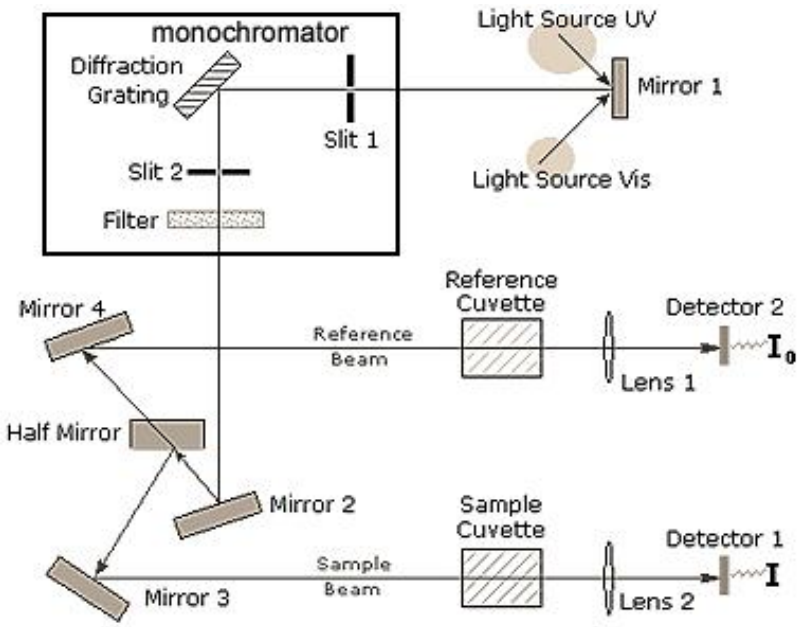

Figure 2.6 A dual-beam UV-vis spectrophotometer [8].

The Bouguer-Lambert-Beer law is used to describe the correlation between the adsorption behavior of a sample as well as the concentration and the thickness of this sample in the solution. The quantitative determination is based on the Bouguer-Lambert-Beer law:

$$A = l\,g\left[\frac{I_0}{I}\right] = -\varepsilon \cdot c \cdot d \qquad (2.3)$$

where A is the measured absorbance, in Absorbance Units (AU), I_0 is the light intensity of the incident radiation, I is light intensity of transmitted radiation, ε is molar extinction coefficient ($L \cdot mol^{-1} \cdot cm^{-1}$), c is concentration ($mol \cdot L^{-1}$) of the sample, and d is thickness of the solution (cm) (thickness of UV cell). There is a linear relationship between absorbance and the concentration of the sample due to the ε and d are constants.

In this research, a UV-vis spectrophotometer (Shimadzu, UV-1601) was employed to evaluate the concentration of the samples. Distilled water was used as a reference. The concentration of different samples was determined at different wavelength. The thickness of the solution is 1.000 cm.

2.6 UV-vis diffuse reflectance spectroscopy

UV-visible diffuse reflectance spectroscopy is employed to determine the absorption of light and band gap energy of powdered samples based on the reflection of light in the UV and visible region by the sample. The ratio of the light scattered from the sample and the scattered light from an ideal non-absorbing reference sample is evaluated as a function of the wavelength λ in a DRS spectrum. Figure 2.7 illustrates the schematic diagram of a diffuse reflectance spectrophotometer with integrating sphere. The incident beam coming from the light source (D_2 lamp and W lamp) travels through a monochromator and it split by the beam splitter into two beams. Subsequently,

one beam is directed towards the sample, and the other towards the reference. In each case, the incident beam is partially absorbed and partially scattered. The scattered radiation from the sample is collected in an integrating sphere and detected.

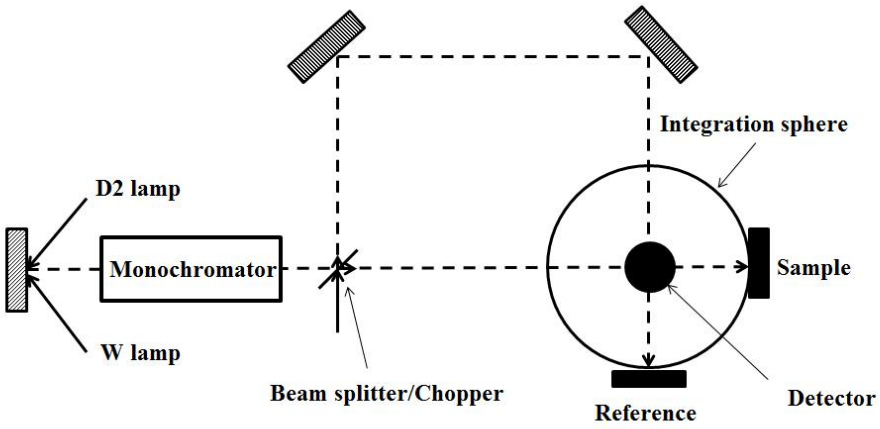

Figure 2.7 Schematic diagram of a diffuse reflectance spectrophotometer with integration sphere [9].

The Kubelka-Munk theory can be employed to describe the correlation of the diffuse reflection of the sample and absorption coefficient and scattering coefficient (S) for infinitely thick samples [10].

$$F(R_\infty) = \frac{(1-R_\infty)^2}{2R_\infty} = \frac{\alpha}{S} \qquad (2.4)$$

where R_∞ is the diffuse reflection of the sample, α is absorption coefficient and S is the scattering coefficient for powdered samples.

The band gap of a semiconductor photocatalyst is defined as the difference

between the top of the VB and the bottom of the CB. For direct band gap materials, this corresponds the minimum photon energy required to excite an electron from HOMO to LUMO. For powder samples, this can be obtained from the diffuse reflectance UV-vis absorption spectra. As mentioned in Chapter 1, there are two basic types of electron transition states: direct transitions and indirect transitions. The magnitude of the absorption depends on the joint density of states, i.e., the density of occupied states at the top of the valence band, and the density of empty states at the bottom of the conduction band. The onset of absorption is therefore not a sharp step, but rather gradual. The band gap can be extrapolated from the following equation:

$$\alpha h\nu = \mathrm{A}\left(h\nu - \mathrm{E_g}\right)^{\mathrm{n}/2} \tag{2.5}$$

where α, ν, E_g, and A are the absorption coefficient, incident light frequency, band gap, and a constant, respectively. The exponent n depends on the nature of the optical transition of the semiconductor (n = 1 for a direct transition and n = 4 for an indirect transition) [11]

For this work, the diffuse reflectance spectra were recorded with a Shimadzu UV-2450 UV-Visible spectrophotometer with diffuse reflectance accessory ISR-240A. $BaSO_4$ was employed as the reference. The band gaps were obtained from the plot of $(\alpha h\nu)^2$ versus the energy of light for indirect band gap semiconductors or the plots of $(\alpha h\nu)^{1/2}$ versus the energy of light for direct

band gap semiconductors. Figure 2.8 shows a DRS of anatase TiO_2.

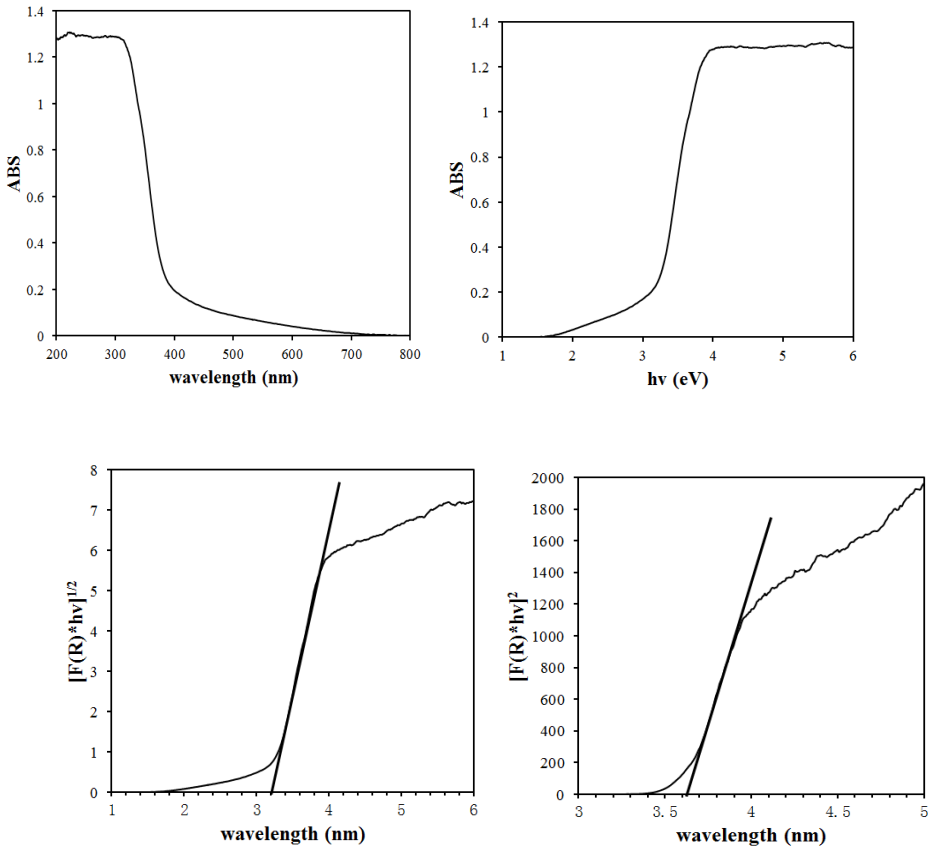

Figure 2.8 DRS of anatase TiO_2, the plot of (a) ABS versus the wavelength of light, (b) ABS versus the energy of light, (c) $(F(R)hv)^{1/2}$ versus the energy of light for direct band gap semiconductors and (d) $(F(R)hv)^2$ versus the energy of light for indirect band gap semiconductors.

2.7 References

[1] R.E. Dinnebier, S.J.L. Billinge, Powder diffraction : Theory and practice, RSC, Cambridge, UK 2008.

[2] Y. Waseda, E. Matsubara, K. Shinoda, Scattering and diffraction, in: X-ray diffraction crystallography, Springer, Berlin Heidelberg 2011.

[3] Elliott P. Barrett , Leslie G. Joyner , Paul P. Halenda, J. Am. Chem. Soc., 73 (1951) 373.

[4] J.W. Niemantsverdriet, Spectroscopy in Catalysis, VCH, New York 1993.

[5] Wikipedia, Scanning electron microscope, 2014. http://en.wikipedia.org/wiki/Scanning_electron_microscope.

[6] J.M. Thomas, C. Ducati, Transmission electron microscopy, in: Characterization of solid materials and heterogeneous catalysts, Wiley-VCH Verlag GmbH & Co. KGaA, Weinheim, Germany 2012.

[7] D. Williams, C.B. Carter, The instrument, in: Transmission electron microscopy, Springer, US 2009.

[8] E.N. Ramsden, A-level chemistry - Detection and analysis, Nelson Thornes, Lincoln, UK 1996.

[9] B.M. Weckhuysen, R.A. Schoonheydt, Catal. Today, 49 (1999) 441.

[10] P. Kubelka, F. Munk, Z. Tech. Phys. 12(1931) 593.

[11] D.G. Barton, M. Shtein, R.D. Wilson, S.L. Soled, E. Iglesia, J. Phys. Chem. B, 103 (1999) 63

Chapter 3. Removal of Chromium (VI) in Aqueous Solution by Zirconium based Metal Organic Framework UIO-66

3.1 Introduction

Removal of heavy metal ions especially in low concentrations from industrial effluents has attracted increasing attention in the past decades. Chromium (VI) is one of the most toxic heavy metal and a major pollutant among the heavy metal ions in waste, because it is highly mobile, carcinogenic and mutagenic to the living organisms [1-3]. Therefore it is extremely important to reduce or remove Cr(VI) from industrial effluents before discharging them to the environment. Among all water treatment techniques, adsorption presents low cost, large adsorption capacity and high efficacy. Metal oxides [4-6], hydrous metal oxides, hybrid materials [7], biomaterials [8], modified zeolites, polymers [9], activated carbon [10] and carbon nanotubes [11] have been widely used for Cr(VI) removal.

MOFs are a new class of highly ordered coordination polymers (CPs) [12], consisting of metal clusters and multifunctional organic ligands. The emergence of MOFs could be traced back to the early 90s of the last century, a number of research groups were working on it, especially Robson, Hoskins [13, 14] and Yaghi [15] groups. MOFs are attractive because they provide

various pore size, high surface area and easily controllable framework. Therefore, MOFs have attracted considerable attention and have been widely investigated for catalysis [16-19], chemical sensors [20, 21], gas separation [22, 23] and other areas [24-26]. Currently, the most highlighted point is that MOF are new class of adsorbent material with strong potential for gas adsorption.

Among the reported MOFs, the Zirconium based metal organic framework UIO-66 exhibits excellent thermostability and superior chemical stability and thus could offer a wide range of potential applications. In particular, UiO-66 exhibits superior structural stability in water and this stability can be retained the damage of frameworks during the adsorption. These properties make UiO-66 a particularly promising candidate for adsorption in water treatment.

In this study, Zirconium based metal organic framework UIO-66 is for the first time reported as adsorbent to remove heavy metal ions. In this study, we characterized the point of zero charge, BET surface area and XRD of UIO-66 and describe the kinetics, isotherm and thermodynamics of Cr(VI) adsorption from aqueous solution onto UIO-66.

3.2 Experimental

3.2.1 Materials

Terephthalic acid was used as organic linker and Zirconium (IV) chloride served as metal source, which were purchased from Sigma-Aldrich. Potassium dichromate ($K_2Cr_2O_7$) with purity of 99.9% from Merck was used for preparing a chromium(VI) solution in deionized water. Other chemicals such as NaOH, KOH, HCl and DMF were supplied by Merck and used without further purification.

3.2.2 Synthesis of UIO 66

The zirconium-based UIO-66 was synthesized following a previously reported method [27]. The synthesis involved the heating of a dissolving mixture of $ZrCl_4$ (0.053 g, 0.227 mmol) and 4-benzenedicarboxylic acid (H_2BDC) (0.034g, 0.227 mmol) in N,N'- dimethylformamide (DMF) (24.9 g, 340 mmol) at 120 ℃ for 24 h in a autoclave. UIO-66 was obtained as a white powder, which was filtered and washed with ethanol. The precipitate was further dried at 100 ^{o}C overnight.

3.2.3 Characterization

Powder X-ray diffraction (XRD) was carried out on a Siemens D5005 diffractometer equipped with variable slits and a copper anode (Cu Kα, λ 1.5418 Å). The diffractograms were recorded over a 2θ range from 5 °to 50 °.

The N_2 adsorption–desorption isotherms were measured at 77 K with a Micromeritics Tristar 3000. The specific surface areas were evaluated by the Brunauer–Emmett–Teller (BET) equation. .

The solid samples (0.03 - 0.07 g) were first degassed at 130 ^{o}C in a flow of nitrogen for 4 h prior to test

3.2.4 Determination of the point of zero charge

The point of zero charge of the UIO-66 was measured as described by Xiao et al. [28]. The initial pH values (pH_i) of 10 ml of a 0.1M NaCl solution were adjusted to obtain pH from 2 to 12 by addition of 0.1 mol/L HCl or NaOH. Subsequently, 20 mg of UIO-66 was added to each sample. The experiments were carried out in a thermostated shaker at 150 rpm and 25 ^{o}C for 2 h. After equilibration, the suspensions were filtered and the final pH values of the solution (pH_f) were measured. The pH_{PZC} was obtained from the plots pH_f versus pH_i. An example of such a measurement is given in Fig. 3.4 on p. 85.

3.2.5 Adsorption studies

A stock solution of Cr(VI) (20 mmol/L, 1040 mg/L) was prepared by dissolving the required amount of potassium dichromate ($K_2Cr_2O_7$) in distilled water. The desired concentrations of Cr(VI) ranging from 52 mg/L to 520 mg/L were then obtained by dilution with distilled water. Batch Cr(VI) adsorption experiments were carried out by contacting 20 mg of the adsorbent samples with 10 mL of the aqueous solution containing different initial concentrations of chromate. The experiments were performed in a thermostated shaker at 150 rpm and 25 ^{o}C for 2 h. The solid material was then removed by filtration, and an aliquot of the filtrate was added to a buffer solution and the residual Cr(VI) concentration was determined from the UV absorption at 350 nm. The Cr(VI) concentration remaining in the adsorbent phase was calculated according to

$$Q_e = \frac{(C_0 - C_e)V}{w} \tag{3.1}$$

where C_0 and C_e are the initial and equilibrium concentrations (mg/L) of Cr(VI) solution, respectively; V is the volume (L) of Cr(VI) solution; and w is the weight (g) of the adsorbent.

In order to examine the effect of pH on the adsorption of Cr(VI) on the adsorbent, before mixing with adsorbent, the initial pH of each solution was

adjusted to an appropriate value by adding 0.1 M HCl or/and NaOH solutions.

3.2.6 Effect of pH on the adsorption capacity

The experiments were carried out by contacting 20 mg of the adsorbent samples with 10 mL of the aqueous solution buffered at different pH from 2 to 11 at 298 K, and initial Cr(VI) concentrations are 208 and 416 mg/L, respectively.

3.2.7 Kinetic study

The experiments were carried out by contacting 20 mg of the adsorbent samples with 10 mL of the aqueous solution for 120 min at 298 K and pH 2, and initial Cr(VI) concentrations are 208 and 416 mg/L, respectively.

3.2.8 Adsorption isotherms

The experiments were carried out by contacting 20 mg of the adsorbent samples with 10 mL of the aqueous solution with different temperature from 298 to 328 K at pH 2, and initial Cr(VI) concentrations are 208 and 416 mg/L, respectively.

3.2.9 Effect of competing anions

The experiments were carried out by contacting 20 mg of the adsorbent samples with 10 mL of the aqueous solution containing different salts in addition to Cr(VI). The conditions were pH 2 and 298 K, and initial Cr(VI) concentrations of 208 and 416 mg/L were used. The initial Cl^-, NO_3^-, $H_2PO_4^-$ concentrations are 8 mmol/L and SO_4^{2-} concentration is 4 mmol/L.

3.2.10 Desorption

The adsorbent that had been used for the adsorption from a 208 mg/L Cr(VI) solution was separated from the solution by filtration and dried in an oven at 80 ^oC. Subsequently, the dried adsorbent was added to 10 ml of 8 mM phosphate buffer (pH=6), and agitated for 1h. The adsorbent was then filtered out, and the concentration of the desorbed Cr(VI) in the filtrate was measured by UV.

3.2.11 Reusability of UIO-66

The UIO-66 was filtered out from desorbed solution and was washed 3 times by 10 ml DI water, then dried the UIO-66 in an oven at 80 ^oC. Subsequently, the dried adsorbent was used for another batch adsorption.

3.3 Results and discussion

3.3.1 XRD and BET measurements

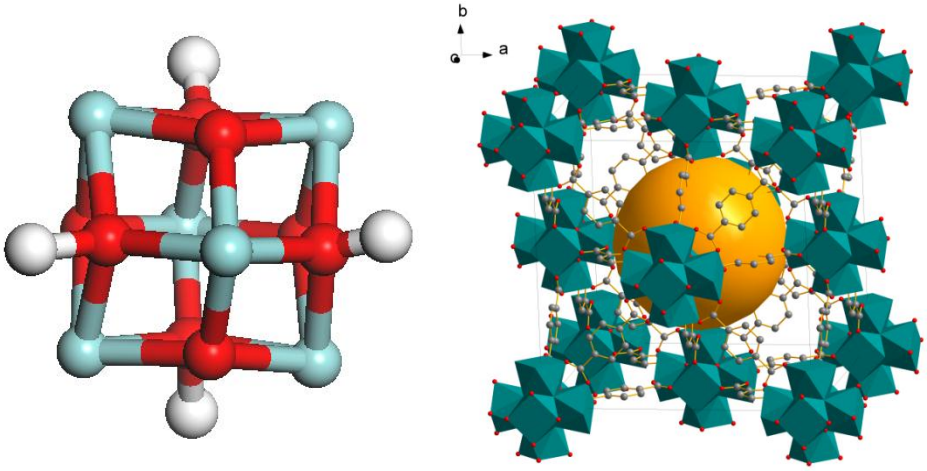

Figure 3.1 (a) $[Zr_6H_4O_8]^{12+}$ metal oxide clusters unit of UIO-66 and (b) structural scheme of UIO-66. The orange sphere in the center indicates the free pore size.

Figure 3.1 illustrates the structure of UIO-66. UIO-66 consists of hexameric $[Zr_6H_4O_8]^{12+}$ units and terephthalate linkers. The structure belongs to the Fm-3m space group. Therefore, UIO-66 possesses a highly ordered microporous structure, where the diameter of the windows and the cage size are 0.8 and 1.5 nm, respectively.

The BET isotherm of the as-synthesized UIO-66 was found in this study to be of type IV (see figure 3.2). The presence of additional mesoporosity could be due to the formation of interspace between the individual UIO-66 crystallites. As expected, UIO-66 possesses a large surface area of 869 m^2/g and large total

pore volume of 1.19 cm^3/g.

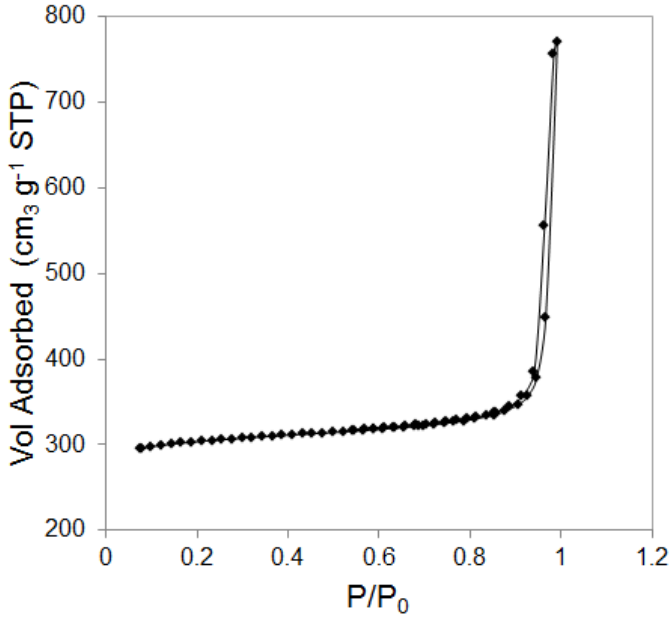

Figure 3.2 Nitrogen adsorption–desorption isotherm of the as-synthesized UIO-66.

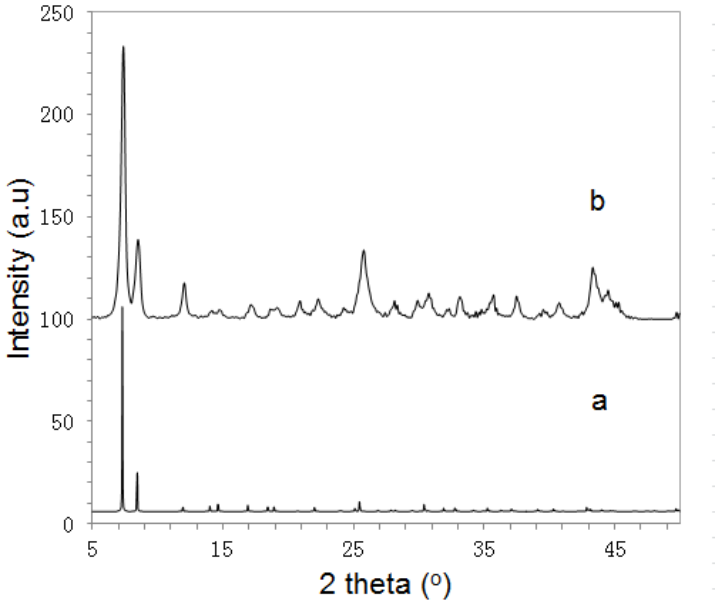

Figure 3.3 XRD patterns obtained from as-synthesized UIO-66, a) simulated UIO-66, b) experimental UIO-66.

Figure 3.3 presents the simulated and experimental XRD patterns of UIO-66. As illustrated, all the diffraction peaks of experimental UiO-66 are compatible with simulated data, confirming the successful synthesis of UiO-66.

3.3.2 The effect of pH

The pH of a solution plays an important role in the adsorption process because the charge type and ionic state of the surface and of the adsorbent will have a big effect on the interaction between adsorbent and adsorbate. The ionic state of the adsorbent surface is determined by the pH_{zpc} (zero point of charge) value.

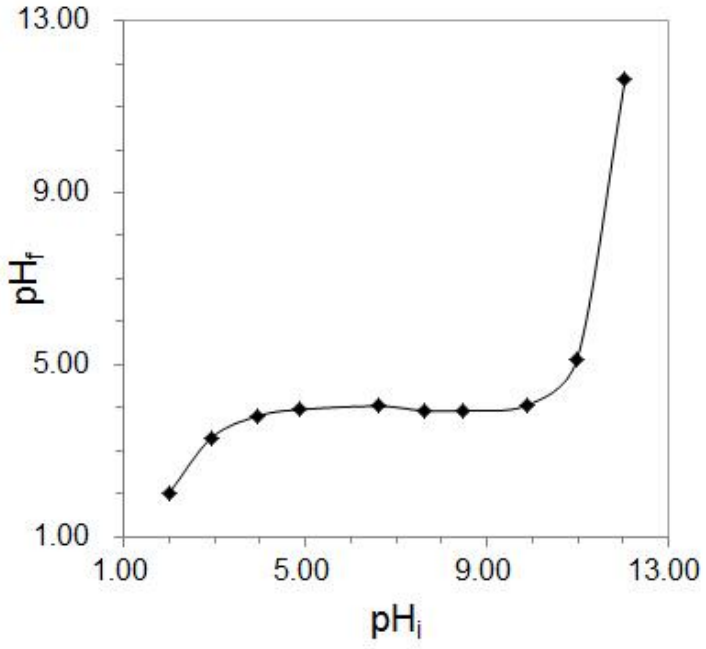

Figure 3.4 pH_f as a function of pH_i, the point of zero charge for UIO-66

Figure 3.4 indicates that obtained pH_{zpc} value of UIO-66 is 4.0, and the surface charge of the adsorbent is positive at pH lower than pH_{zpc}. It is obvious that UIO-66 is able to take more charge at low pH and theoretically absorb more Cr(VI). In order to examine the above statement, the effect of pH on the removal of Cr(VI) by UIO-66 was studied within the pH range of 2-11 at an initial Cr(VI) concentration of 208 mg/L and with adsorbent dose of 2.0 g/L UIO-66.

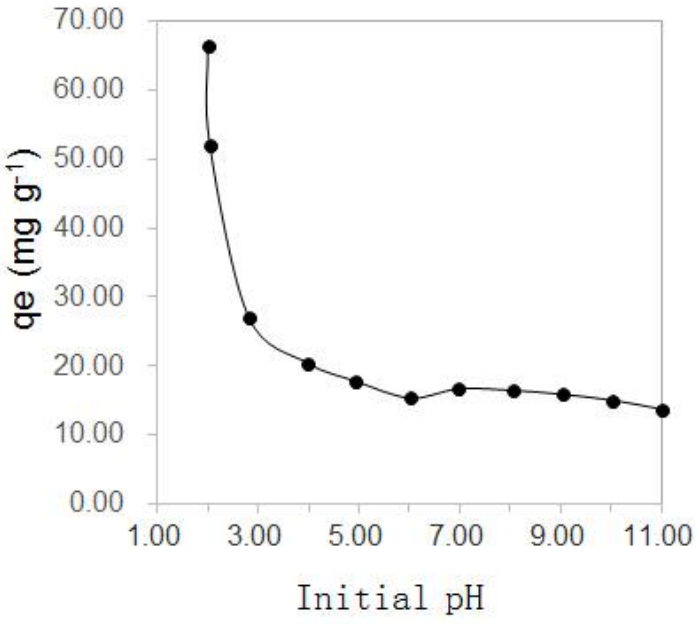

Figure 3.5 The effect of solution pH for Cr(VI) adsorption on UIO-66 (C_0=208ppm; T = 298 K; adsorbent dose=2g/L; pH 2)

The result is displayed in Figure 3.5. It reveals that the amount of removed Cr (VI) increases with decreasing pH. Obviously, the adsorption capacity of UIO-66 increases gradually from pH 11 to 4, while the adsorption capacity

increases sharply for pH values lower than 3.0.

The form in which Cr(VI) species exist in aqueous solution depend on the Cr (VI) concentration and the solution pH. The predominant species of Cr (VI) in solution include chromate (CrO_4^{2-}), dichromate ($Cr_2O_7^{2-}$) and hydrogen dichromate ($HCrO_4^-$).

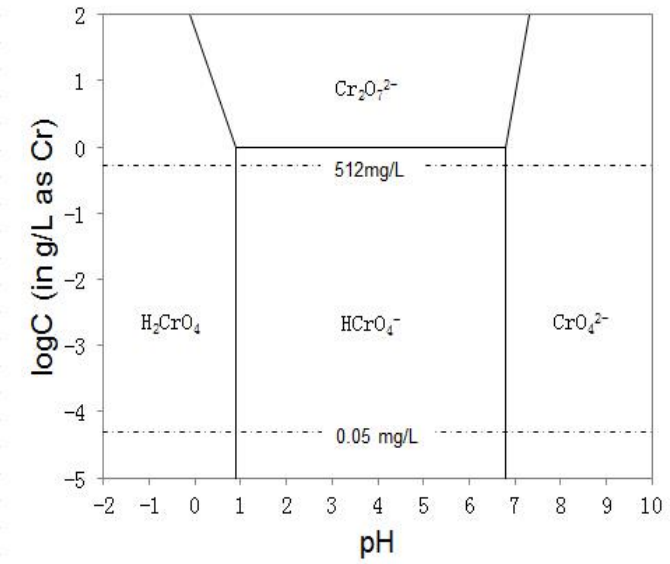

Figure 3.6 the predominance diagram showing the relative distribution of various Cr(VI) species in water as a function of pH and total Cr(VI) concentration.

Figure 3.6 (b) presents the predominance diagram showing the relative distribution of various Cr(VI) species in water as a function of pH and total Cr(VI) concentration [29, 30]. The area between two horizontal dashed lines shows the range of Cr(VI) concentration between 512mg/L and 0.05 mg/L as Cr(VI). From the above figure, indicating hydrogen dichromate ($HCrO_4^-$) is

the most predominance species for this experimental total Cr(VI) concentration.

Figure 3.7 displays a schematic diagram of the pH effect on UIO-66. The Zr_6O_{32} cluster consists of $[Zr_6H_4O_8]^{12+}$ units and the oxygens of the terephthalate linkers. If the pH of the solution is less than the value of pH_{zpc}, then more H^+ will be adsorbed on the surface of Zr_6O_{32} cluster on account of forming a positively charged double-electric layer. The density of positive charge in the Stern layer will increase with increasing H^+ concentration. Since Cr(VI) species take negative charge, there is a favorable Cr(VI) adsorption on to the UIO-66 in low pH.

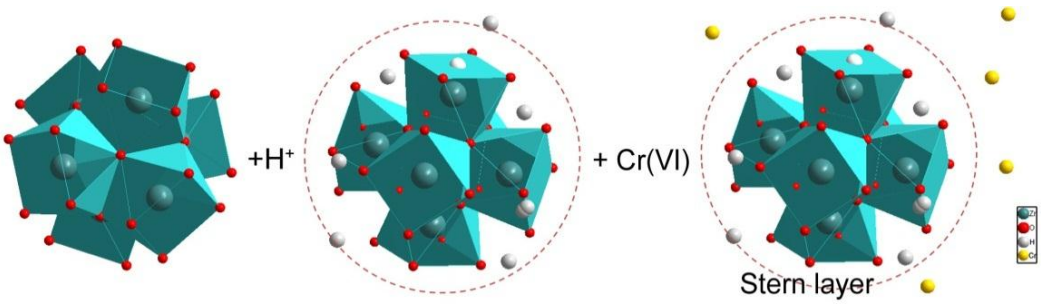

Figure 3.7 The schematic diagram of pH effect on UIO-66

3.3.3 Kinetic study

Figure 3.8 illustrates the kinetic curves for the removal of Cr(VI) from aqueous solutions. There are two concentrations curves, and the two curves indicate that the time of equilibrium depends on the initial concentration of

Cr(VI). Both curves attained values above 80% of adsorption capacity at equilibrium. The adsorption process at both concentrations was very rapid, being nearly completed within the first 10 min of interaction. The primary reason of superior removal of Cr(VI) in aqueous solution on UIO-66 could be due to UIO-66 presented a high order porous structure and big total pore volume of UIO-66 so that the Cr(VI) can penetrate into the pore easily.

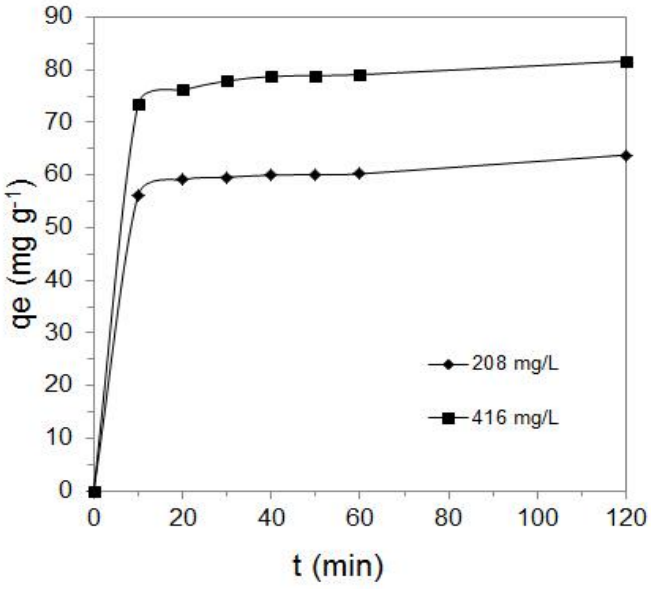

Figure 3.8 Amount adsorbed against time at two different initial Cr(VI) concentrations (T = 298 K; adsorbent amount = 2g dm^{-3}; pH 2).

Kinetic modeling is very important both in evaluation of adsorption rates and in investigation of possible reaction mechanisms. Several kinetic models including pseudo-first-order equation, pseudo-second-order equation and an

intraparticle diffusion equation are commonly used to examine which mechanism controls the adsorption process.

The linear pseudo-first-order equation, pseudo-second-order equation and intraparticle diffusion equation are given as follows:

$$log(q_e - q_t) = logq_e - \frac{k_1 t}{2303} \quad (3.2)$$

$$\frac{t}{q_t} = \frac{1}{k_2 q_e^2} + \frac{t}{q_e} \quad (3.3)$$

$$q_t = k_{dif} t^{0.5} \quad (3.4)$$

Where q_e and q_t are adsorption capacity of the adsorbent (mg/g) at equilibrium and at time t (min); k_1 and k_2 are the pseudo-first-order and pseudo-second-order rate constants, k_{dif} is the intraparticle diffusion rate constant.

The first-order constant k_1 and equilibrium adsorption density q_e were calculated by the slopes and intercepts of plots of log(q_e-q_t) versus t (see Figure 3.8). Similarly, the second-order constant k_2 and equilibrium adsorption density q_e were obtained by the plots tq_t^{-1} versus t (see Figure 3.10). And the k_{dif} can be simply got by plots q_t versus $t^{0.5}$. A comparison results with the correlation coefficients is listed in table 3.1. Among the three models, the second-order kinetic model gives the best fit; the plot exhibits extremely

straight lines with the best correlation coefficient. Therefore, the pseudo-second-order equation could be sufficient to describe the mechanism of interactions between UIO-66 and Cr(VI).

Table 3.1 comparison of the pseudo first-order, second-order and intraparticle diffusion adsorption constants at different initial concentration.

$C_{0\ (mg/L)}$	First-order model			Second-order model			Intraparticle diffusion	
	k_1 (min^{-1})	q_1 (mg g^{-1})	r^2	k_2 (min^{-1})	q_2 (mg g^{-1})	r^2	K_{dif} (mg $min^{-0.5}g^{-1}$)	r^2
208	0.037	19.56	0.582	21.96	61.03	1	4.971	0.582
416	0.047	24.75	0.693	12.31	80.49	1	6.409	0.571

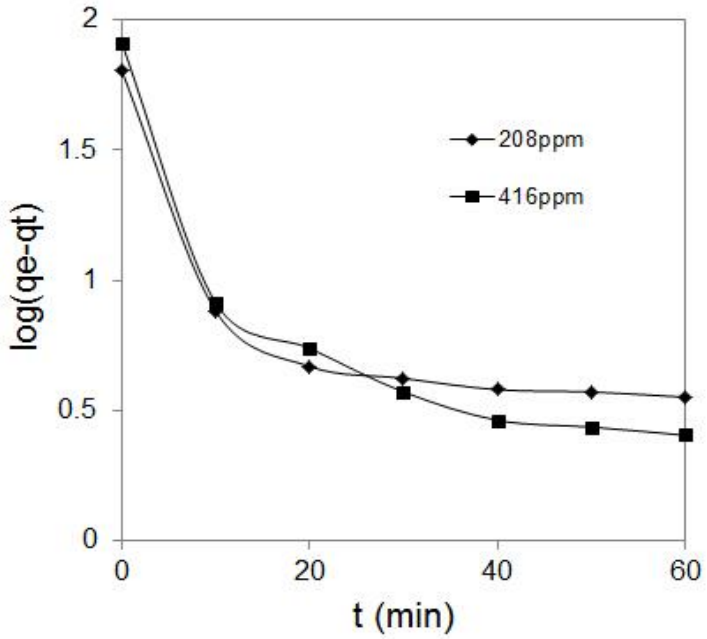

Figure 3.9 Pseudo-first-order kinetics for Cr(VI) adsorption on UIO-66.

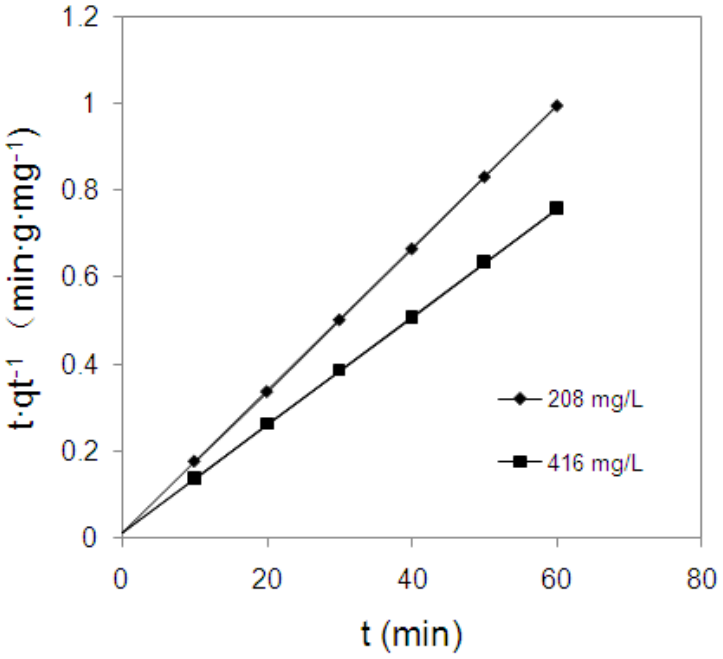

Figure 3.10 Pseudo-second-order kinetics for Cr(VI) adsorption on UIO-66.

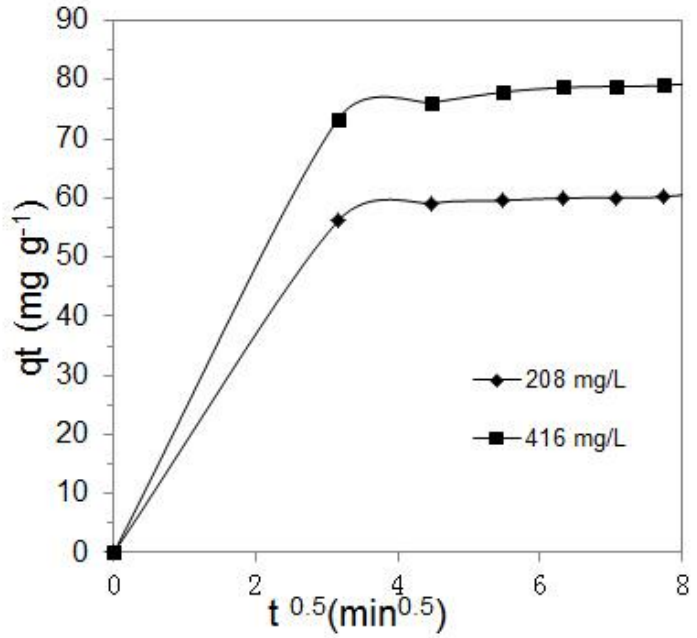

Figure 3.11 Interparticle diffusion kinetics for Cr(VI) adsorption on UIO-66.

3.3.4 Adsorption isotherms

The Langmuir and the Freundlich isotherms are the most widely used models in order to describe adsorption behavior. The Langmuir isotherm has been extensively used to describe the adsorption of heavy metals, dyes, organic pollutants, etc. It applies to monomolecular layer adsorption. This isotherm is described as a homogeneous one assuming that all the adsorption sites have equal adsorbent affinity and that the adsorption at one site does not impact on the adsorption at an adjacent site. The Langmuir isotherm is utilized to obtain a maximum adsorption capacity produced from the complete monolayer coverage of adsorbent surface. The isotherm equation is represented as follow:

$$\frac{C_e}{q_e} = \frac{1}{Q_0 b} + \frac{C_e}{Q_0} \tag{3.5}$$

where b is an adsorption equilibrium constant (L/mg) that is related to the apparent energy of adsorption and Q_0 (mg/g) is the quantity of adsorbent required to form a single monolayer on a unit mass of adsorbent and q_e (mg/g) is the amount adsorbed per unit mass of adsorbent when the equilibrium concentration is C_e (mg/L).

Figure 3.12 shows that a plot of (C_e/q_e) versus C_e yield a straight line. This indicates that the Langmuir equation describes the adsorption equilibrium reasonably well. The constants Q_0 and b were determined from the slope and

the intercept of this line.

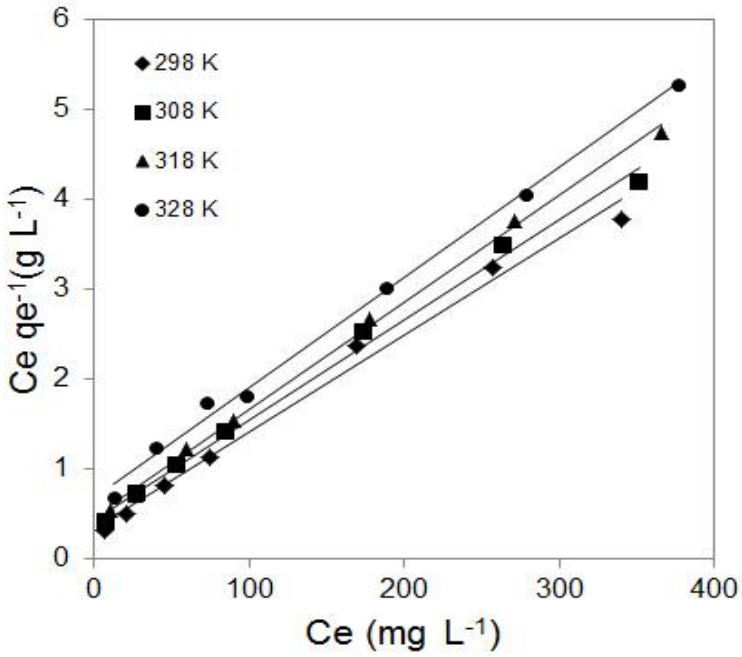

Figure 3.12 Langmuir isotherm for Cr(VI) adsorption on UIO-66(adsorbent dose = 2g dm^{-3}; pH 2; t = 60 min).

A further analysis of the Langmuir equation can be carried out according to the basis of a dimensionless equilibrium parameter, R_L (separation factor), given by [31]:

$$R_L = \frac{1}{1+bC_0} \tag{3.6}$$

The value of R_L lies between 0 and 1 for a favorable adsorption, while $R_L > 1$ for unfavorable sorption, and $R_L = 1$ for linear sorption, while the adsorption operation is irreversible if $R_L = 0$.

The Freundlich isotherm describes that the ratio of the amount of solute adsorbed on a given mass of adsorbent to the concentration of solute in the solution is not be constant at different concentrations. For many systems, the molar heat of adsorption decreases with increasing extent of adsorption. This has been well dealt with by the Freundlich isotherm, which had previously been viewed as an empirical isotherm. For adsorption from solution, the Freundlich isotherm is expressed as follow:

$$logq_e = logK_F + \frac{1}{n} logC_e \quad (3.7)$$

where K_F is the Freundlich constant, which indicates the relative adsorption capacity of the adsorbent related to the bonding energy, and n is the heterogeneity factor representing the deviation from linearity of adsorption and is also known as the Freundlich coefficient. q_e is the amount adsorbed per unit mass of the adsorbent (mg/g) at the equilibrium concentration C_e (mg/L).

Figure 3.13 shows the plot of log q_e versus log C_e which are able to be employed to obtain the Freundlich coefficients. Furthermore, a comparison result of Langmuir and Freundlich isotherm parameters is shown in table 3.2.

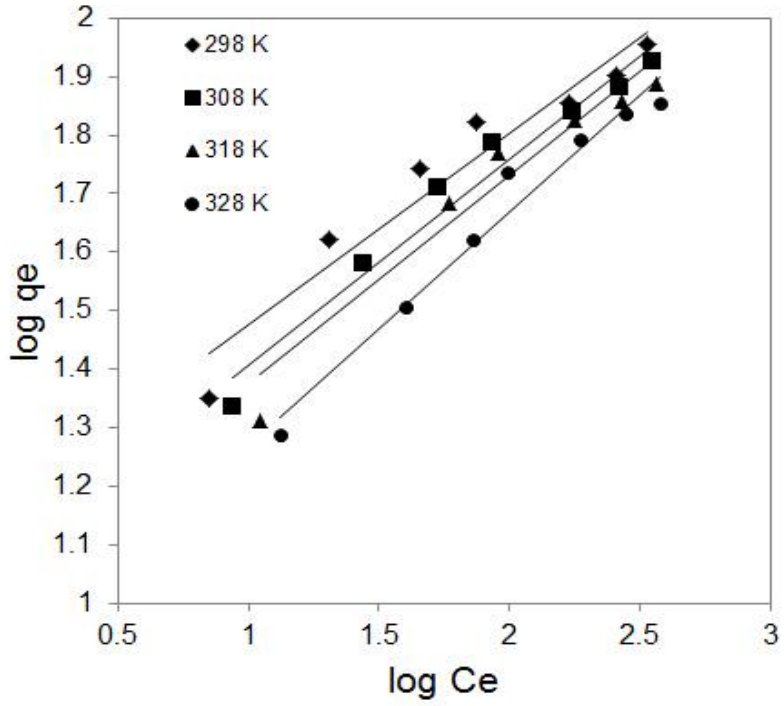

Figure 3.13 Freundlich isotherm for Cr(VI) adsorption on UIO-66(adsorbent dose = 2g dm^{-3}; pH 2; t = 60 min).

Based on the correlation coefficient, it is found that the adsorption is better described with the Langmuir model than with the Freundlich isotherm. The adsorption capacity decreased from 93 mg/g to 81.8 mg/g with an increase of temperature from 298 to 328 K. Additionally, as discussed in a previous report [32], the Langmuir constant b can indicate the adsorption ability, where a larger b value reflects a greater adsorption affinity. A steady decrease in b values with increasing temperature in Table 3.2 proves that the affinity of Cr (VI) over UIO-66 decreases with the rise in temperature from 298K to 328 K. The raw data of adsorption isotherm study is shown in Table 3.3.

Table 3.2 Langmuir and Freundlich isotherm parameters for adsorption of Cr(VI) on UIO-66.

T (K)	Langmuir constants				Freundlich constants		
	Q_0 (mg g^{-1})	B (L mg^{-1})	R_L	r^2	K_F (mg g^{-1})	1/n	r^2
298	93	0.033	0.069	0.989	2.124	1.148	0.935
308	89.8	0.026	0.085	0.994	2.253	1.055	0.964
318	83.7	0.026	0.084	0.998	2.270	1.020	0.935
328	81.8	0.018	0.119	0.996	2.509	0.871	0.967

Table 3.3 Raw data of adsorption isotherm study at different temperature.

T (K)	C_0 (ppm)	52	104	156	208	312	416	520
298	Ce (ppm)	7.13	20.50	45.35	75.26	169.22	256.88	340.07
	Qe (mg/g)	22.45	41.75	55.32	66.37	71.38	79.56	89.96
308	Ce (ppm)	8.72	27.81	53.32	85.82	173.65	264.21	351.89
	Qe (mg/g)	21.64	38.09	51.34	61.09	69.18	75.90	84.06
318	Ce (ppm)	11.01	27.31	59.18	90.12	178.02	271.45	365.61
	Qe (mg/g)	20.49	38.34	48.41	58.94	66.99	72.28	77.20
328	Ce (ppm)	13.22	39.74	72.47	98.65	187.64	278.54	377.02
	Qe (mg/g)	19.39	32.13	41.77	54.68	62.18	68.73	71.49

3.3.5 Effect of competing anionn

In most cases, industrial effluents contain several kinds of anions. Therefore, it is necessary to investigate the performance of the adsorpens in a solution that contains mixed anions. In the present study, the interference of other ions, such as Cl^-, SO_4^{2-}, NO_3^-, $H_2PO_4^-$ were examined.

Figure 3.14 shows that some ions had a significant effect on the removal of Cr(VI). Particularly $H_2PO_4^-$ and SO_4^{2-} show a pronounced negative effect for removal of Cr(VI) on UIO-66. However, the singly charged anions Cl^- and NO_3^- had almost no effect on the adsorption of Cr(VI) onto UIO-66.

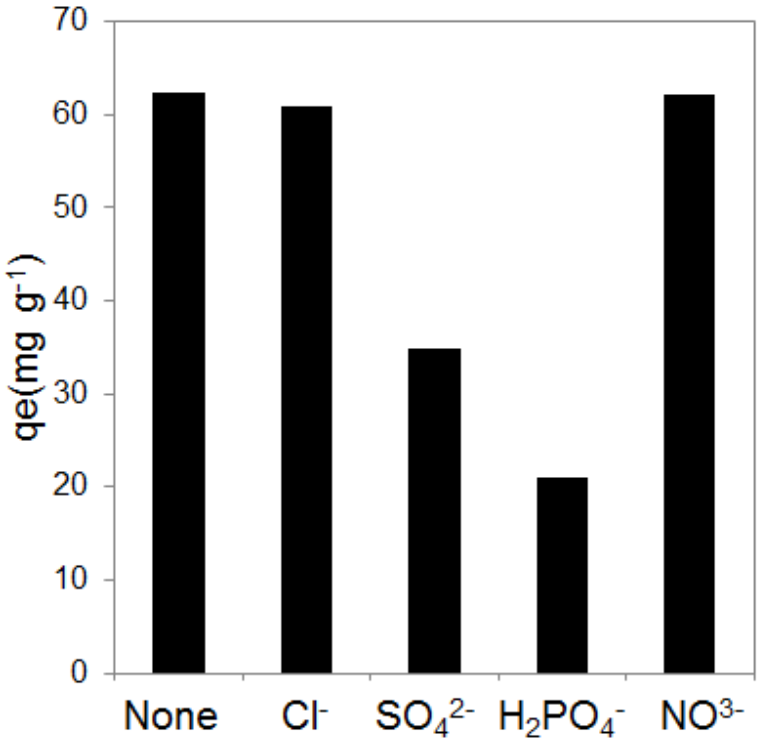

Figure 3.14 The effect of various competing anions for Cr(VI) adsorption on UIO-66.

3.3.6 Desorption

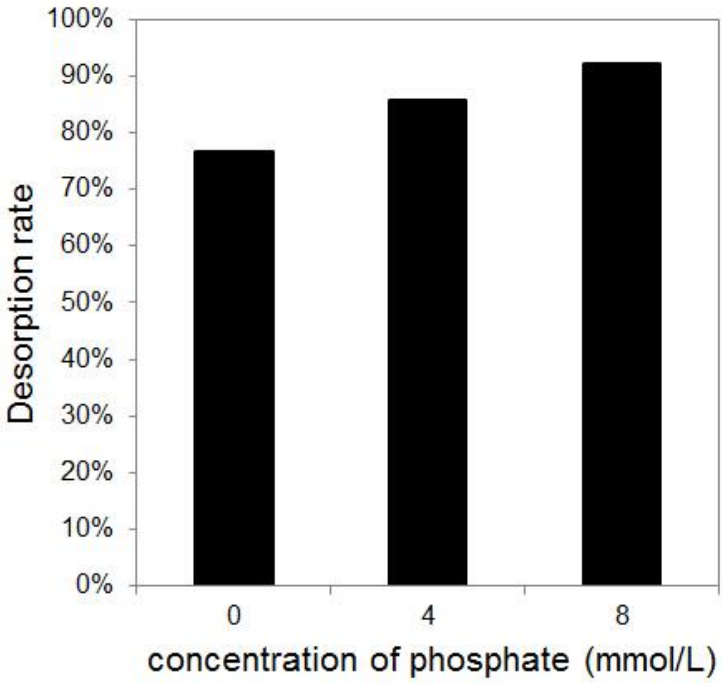

Figure 3.15 Desorption of Cr(VI) from UIO-66 with various initial $H_2PO_4^-$ concentrations. (Cr(VI) initial concentration = 208 mg/L; adsorbent dose = 2g/L; time = 60min; T = 298K; pH = 6)

Reusability is a critical factor for any adsorbent used in an industrial application. Reusable adsorbent can significantly reduce the overall cost in the whole industrial process. Desorption tests were conducted to regenerate chromium-adsorbed UIO-66 using $H_2PO_4^-$ solution for desorption of Cr(VI). Figure 3.16 shows that the amount of the desorbed Cr(VI) increased with increase of the phosphate concentration. However, about 7% of the Cr(VI) was still immobilized on the adsorbent when the $H_2PO_4^-$ and HPO_4^{2-} total

concentration was 8 mmol/L. That indicates the Cr(VI) adsorption on UIO-66 is not completely reversible, thus chemisorptions, physisorptions and ion-exchange mechanisms are operative in the adsorption process. Only the Cr(VI) ions that are adsorbed by physisorption and ion-exchange are desorbed.

3.3.7 Reusability of UIO-66

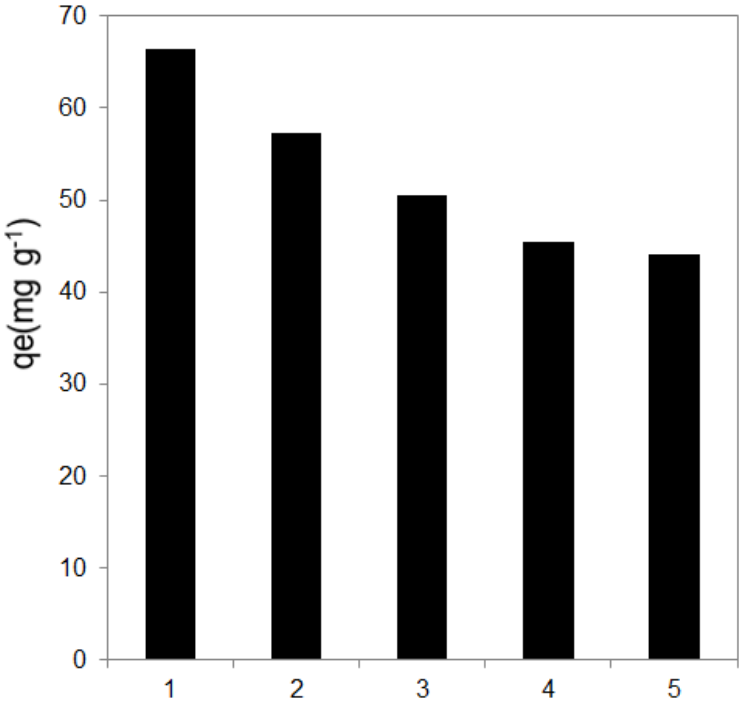

Figure 3.16 Adsorption capacity of UIO-66 in five runs adsorption study.

The reusability result of the UIO-66 is shown in Figure 3.16. After desorption of Cr(VI), the UIO-66 were filtered from the solution. The UIO-66 was used for another batch adsorption after washing by DI water. The subsequent cycles indicated a somewhat lower adsorption capacity, this could be due to the phosphate poisoned adsorption sites. Compared with first run adsorption, the

adsorption capacity of second, third, fourth and fifth runs dropped to 86%, 76%, 68% and 67% of first run adsorption capacity, respectively.

3.4 Conclusion

This is the first report of heavy metal removal from aqueous solution by MOFs. The kinetics of Cr(VI) adsorption on UIO-66 can be described by the pseudo-second order model, showing that the adsorption rate decreased with rising of Cr(VI) initial concentration. The removal of Cr(VI) tended to increase with a decrease of pH value. The Langmuir model was found to describe the adsorption equilibrium process appropriately. Using this model, the maximum adsorption capacity was 93 mg/g at 298 K. Cr(VI) adsorption was greatly reduced when SO_4^{2-} or $H_2PO_4^-$ were present in similar concentrations. A Cr(VI) desorbability of approximately 93% was obtained with water at pH 6 in the presence of phosphate. In summary, the UIO-66 exhibits the excellent potential for application to control Cr(VI) pollution because of its high adsorption capacity and satisfactory usability.

3.5 References

[1] M. Uysal, I. Ar, J. Hazard. Mater., 149 (2007) 482.

[2] S. Gupta, B.V. Babu, Chem. Eng. J., 150 (2009) 352.

[3] L.C. Hsu, S.L. Wang, Y.M. Tzou, C.F. Lin, J.H. Chen, J. Hazard. Mater.,

142 (2007) 242.

[4] P. Yuan, D. Liu, M. Fan, D. Yang, R. Zhu, F. Ge, J. Zhu, H. He, J. Hazard. Mater., 173 (2010) 614.

[5] S.R. Chowdhury, E.K. Yanful, A.R. Pratt, J. Hazard. Mater., 235–236 (2012) 246.

[6] K. Parida, K.G. Mishra, S.K. Dash, J. Hazard. Mater., 241–242 (2012) 395.

[7] S.S. Liu, Y.Z. Chen, L. De Zhang, G.M. Hua, W. Xu, N. Li, Y. Zhang, J Hazard Mater, 190 (2011) 723.

[8] X. Dong, L.Q. Ma, Y. Li, J. Hazard. Mater., 190 (2011) 909.

[9] W. Yu, L. Zhang, H. Wang, L. Chai, J. Hazard. Mater., 260 (2013) 789.

[10] N.F. Fahim, B.N. Barsoum, A.E. Eid, M.S. Khalil, J Hazard Mater, 136 (2006) 303.

[11] M.A. Atieh, Procedia. Environ. Sci., 4 (2011) 281.

[12] S.R. Batten1, N.R. Champness, X.M. Chen,J. Garcia-Martinez, S. Kitagawa, L. Öhrström,M. O'Keeffe, M.P. Suh, J. Reedijk, Pure Appl. Chem., 85 (2013) 1715.

[13] B. F. Hoskins, R. Robson, J. Am. Chem. Soc., 112 (1990) 1546.

[14] B.F. Abrahams, B.F. Hoskins, D.M. Michail, R. Robson, Nature 369 (1994) 727.

[15] O.M. Yaghi, H. Li, J. Am. Chem. Soc., 117 (1995) 10401.

[16] N.T.S. Phan, T.T. Nguyen, P. Ho, K.D. Nguyen, ChemCatChem, 5 (2013) 1822.

[17] S.T. Meek, J.A. Greathouse, M.D. Allendorf, Adv. Mater., 23 (2011) 249.

[18] B. Yuan, Y. Pan, Y. Li, B. Yin, H. Jiang, Angew. Chem. Int. Ed., 49 (2010) 4054.

[19] D. Farrusseng, S. Aguado, C. Pinel, Angew. Chem. Int. Ed., 48 (2009) 7502.

[20] G. Lu, J.T. Hupp, J. Am. Chem. Soc., 132 (2010) 7832.

[21] B. Liu, J. Mater. Chem., 22 (2012) 10094.

[22] T.H. Bae, J.S. Lee, W. Qiu, W.J. Koros, C.W. Jones, S. Nair, Angew. Chem. Int. Ed., 49 (2010) 9863.

[23] J.R. Li, R.J. Kuppler, H.C. Zhou, Chem. Soc. Rev., 38 (2009) 1477.

[24] A.C. McKinlay, R.E. Morris, P. Horcajada, G. Férey, R. Gref, P. Couvreur, C. Serre, Angew. Chem. Int. Ed., 49 (2010) 6260.

[25] A. Morozan, F. Jaouen, Energy Environ. Sci., 5 (2012) 9269.

[26] C. Wang, T. Zhang, W. Lin, Chem. Rev., 112 (2011) 1084.

[27] J.H. Cavka, S. Jakobsen, U. Olsbye, N. Guillou, C. Lamberti, S. Bordiga, K.P. Lillerud, J. Am. Chem. Soc., 130 (2008) 13850.

[28] L. Xiao, W. Ma, M. Han, Z. Cheng, J Hazard Mater, 186 (2011) 690.

[29] J.N. Butler, Ionic equilibrium, New York., 1967.

[30] J.J. Morgan, W. Stumm, Aquatic chemistry, JohnWiley and Sons, New York 1996.

[31] L. Wei, G. Yang, R. Wang, W. Ma, J Hazard Mater, 164 (2009) 1159.

[32] J. Das, B. Sairam Patra, N. Baliarsingh, K.M. Parida, J Colloid Interface Sci, 316 (2007) 216.

Chapter 4.Removal of Chromium (VI) from Aqueous Solution by Amino-Functionalized Inorganic / Organic Hybrid Materials

4.1 Introduction

The adsorption capacity for polar organic compounds or heavy metal ions of an adsorbent is usually determined by the type and density of polar functional groups on the surface of the material. Carboxyl groups, sulfonic acid groups, phosphoric acid groups, mercapto groups and nitrogen-containing groups (primary amine, secondary amine, tertiary amine, quaternary amine, amide and imidazole) are common functional groups. Complexation, electrostatic interaction, hydrophobic interaction, ion exchange, and hydrogen bonding, either individually or in combination, may occur simultaneously in adsorption process for one material. Surface modification of materials can improve the adsorption performance of an adsorbent. The adsorption capacity of an adsorbent will be raised significantly by increasing the density of functional groups on the surface of the adsorbent or by employing a porous material as adsorbent which can provide a high surface area.

Nitrogen-containing groups are promising for the selective adsorption of Cr(VI). Cr(VI) exists as $HCrO_4^-$ or other anionic species, as we discussed in Chapter 3. Which species are present depends strongly on pH and Cr(VI)

concentration. At neutral and acidic pH, an adsorbent modified with nitrogen-containing groups will be in the protonated, positively charged form, and therefore exhibits high adsorption capacity for anions. Several adsorbents modified with nitrogen-containing groups will be reviewed in the following paragraphs.

Zhao et al. prepared magnetic polymers containing various amounts of glycidylmethacrylate and ethylenediamine-functionalized Fe_3O_4 to remove Cr(VI) [1]. These ethylenediamine-functionalized Fe_3O_4 magnetic polymers exhibited adsorption capacity of 32.2 – 61.4 mg/g.

Li et al. used amino-functionalization of mesoporous silica, grafted by [1-(2-amino-ethyl)-3-aminopropyl] trimethoxysilane (AAPTS), to remove Cr(VI) from aqueous solutions [2]. They observed that the maximum Cr(VI) loadings at 25, 35 and 45 ^{o}C can reach 118.6, 148.7 and 172.6 mg/g, respectively. The binding affinity between adsorbent and Cr(VI) raised up with increasing of temperature in this study.

Bhaumik et al. prepared a polypyrrole/Fe_3O_4 magnetic nanocomposite via in situ polymerization of pyrrole monomer for the removal of Cr(VI) [3]. In this study, the Langmuir model described the adsorption very well and the adsorption kinetics could be fitted with a pseudo-second-order rate model. The monolayer adsorption capacity as calculated from the Langmuir isotherm was

169.5 mg/g.

Yoshitake et al. explored amino-functionalized MCM-41 and SBA-1 for Cr(VI) removal in the batch mode [4]. The Cr(VI) adsorption data reported in this study are listed in table 4.1

Table 4.1 Adsorption capacity of different amino-functionalized MCM-41 and SBA-1 (from reference [4])

Adsorbents	Adsorption capacity (mg/g)
N-MCM-41[a]	52.9
NN-MCM-41[b]	92.1
NNN-MCM-41[c]	115.2
N-SBA-1	94.2
NN-SBA-1	178.4
NNN-SBA-1	210.8

[a)] N means modified by 3-aminopropyltrimethoxysilane; [b)] NN modified by [1-(2-aminoethyl)-3-aminopropyl] trimethoxysilane; [c)] NNN means modified by (trimethoxysilyl) propyldiethylenetriamine.

It was found that the support with the bigger pores (SBA-1) showed almost twice the adsorption capacity. In addition, a more complexing ligand could bind much more chromate.

In the present study, several amino-functionalized metal organic frameworks were prepared and studied as adsorbents for Cr(VI) from aqueous solution. The materials investigated were modified KIT-6, NH_2-UIO-66, NH_2-MIL-125(Ti), aminopropyltrimethoxysilane modified KIT-6 and (trimethoxysilyl) propyldiethylenetriamine modified KIT-6. All those materials present a high surface area and porous properties as well as a high surface concentration of N containing functionalities.

Metal organic frameworks were introduced in Chapter 1 and 3. NH_2-UIO-66 consists of hexametric $[Zr_6H_4O_8]^{12+}$ units and 2-amino terephthalate linkers and presents a micropore cage of 1.5 nm with windows of 0.8 nm. NH_2-MIL-125(Ti) consists of cyclic octamers of TiO_4 octahedra connected by 2-amino terephthalic acid linkers, which has a micropore cage of 1.7 nm, top windows of 0.7 nm and side window of 0.9 nm. Since the diameter of $HCrO_4^-$ is only ~0.4 nm, Cr(VI) can easily penetrate the frameworks of MOFs.

KIT-6 is a cubic mesoporous silica with 3D pores larger than 5 nm, which presents *Ia3d* space group [5]. It also provides a large BET surface area of 800 m^2/g and high pore volume reaching 1.05 cm^3/g.

4.2 Experimental

4.2.1 Synthesis of the adsorbents

Synthesis of NH_2-UIO-66

The zirconium-based NH_2-UIO-66 was synthesized following a reported method [6]. The synthesis involved the heating of a dissolved mixture of $ZrCl_4$ (0.053 g, 0.227 mmol) and 2-aminoterephthalic acid (H_2ATA) (0.041g, 0.227 mmol) in N, N`- dimethylformamide (DMF) (24.9 g, 340 mmol) at 120 ℃ for 24 h in an autoclave. This led to the formation of NH_2-UIO-66 as a yellow powder, which was filtered and washed with ethanol. The precipitates were further dried at 100 ^oC overnight.

Synthesis of NH_2-MIL-125(Ti)

The NH_2-MIL-125(Ti) was synthesized following ref [7]. 2-Aminoterephthalic acid (0.5435g, 3 mmol) and tetraisopropyl titanate $Ti(OCH(CH_3)_2)_4$ (0.22ml, 0.75 mmol) were added into a solution containing dimethylformamide (9 ml) and dry methanol (1 ml). The mixture was sonicated for 5 min at room temperature, transferred to a 30 ml autoclave and heated at 150 ^oC for 3days. A yellow powder was obtained, which was filtered and washed with ethanol. The precipitates were then dried at 130 ^oC overnight.

Synthesis of KIT-6

The siliceaous mesoporous material KIT-6 was prepared by following ref. [5] using Pluronic P123 (an amphiphilic ethylene oxide-propylene oxide block copolymer $EO_{20}PO_{70}EO_{20}$, MW = 5800, Aldrich) as structure directing agent. In a typical synthesis, 6 g of P123 was dissolved in 217 g of distilled water, and 11.8 g of concentrated HCl (35%) and 6 g of 1-butanol were added subsequently under vigorous stirring at 35 ^{o}C. After 1 h stirring, 12.9 g of TEOS was added dropwise at 35 ^{o}C. The mixture was stirred for another 24 h at 35 ^{o}C. Finally, the solution was transferred to a Teflon liner and subjected to hydrothermal treatment in an autoclave at 120 ^{o}C for 24 h. The solid product obtained after hydrothermal treatment was then filtered without washing and dried at 100 ^{o}C overnight. The template was removed by extraction in an ethanol-HCl mixture, followed by calcination at 550 ^{o}C for 2 h.

Synthesis of amino-functionalized KIT-6

The KIT-6 was dried at 130 ^{o}C for 12 h in an oven in order to remove water adsorbed on the surface, and then 0.5g of KIT-6 was stirred vigorously in 10ml of toluene containing 2.0 ml of (3-aminopropyl) triethoxysilane (APTES, $H_2N(CH_2)_3Si(OC_2H_5)_3$). As reported in ref. [8], the solvent greatly influences the concentration of functional groups that can be grafted to the surface of the silica, and toluene was found to be the best solvent that resulted in the highest loading of amino groups. Therefore, toluene was employed as solvent in this

study. The modified KIT-6 was recovered by filtration as a white powder and washed with 2-propanol to remove residual APTES that remained after the reflux of reactant mixture at 110 ^{o}C for 12h. Finally, the functionalized material, denoted as N-KIT-6, was dried in an oven at 80 ◦C for 12 h. Similarly, 0.5g of KIT-6 and 2.5ml of N1-(3-trimethoxysilylpropyl) diethylenetriamine (DETA, $H_2N(CH_2)_2NH(CH_2)_2NH(CH_2)_3Si(CH_3O)_3$) were added in 10ml of toluene. The DETA modified KIT-6 was denoted as NNN-KIT-6.

4.2.2 Characterization

Powder X-ray diffraction (XRD) was carried out on a Siemens D5005 diffractometer equipped with variable slits and a copper anode (Cu Kα, λ 1.5418 Å). The diffractograms were recorded over a 2θ range of 5 ° to 50 ° for MOFs. The diffractograms of the mesoporous silica materials KIT, N-KIT-6 and NNN-KIT-6 were recorded at small angles over 2θ from 0.6 ° to 5 °.

4.2.3 Adsorption studies

A stock solution of Cr(VI) (20 mmol/L, 1040 mg/L) was prepared by dissolving the required amount of potassium dichromate ($K_2Cr_2O_7$) in distilled water. Then, the desired concentration of Cr(VI) ranging from 52 mg/L to 520 mg/L was obtained by dilution with distilled water. Batch Cr(VI) adsorption experiments were carried out by contacting 20 mg of the adsorbent samples

with 10 mL of the aqueous solution of different initial concentration. The experiments were performed in a thermostat shaker at 150 rpm and 25 ^{o}C for 2 h. The suspensions were then filtered out, and the residual Cr(VI) in the filtrate was added to a buffer solution and measured by UV at 350 nm. The Cr(VI) concentration that remained in the adsorbent phase was calculated according to

$$Q_e = \frac{(C_0 - C_e)V}{w} \quad (4.1)$$

where C_0 and C_e are the initial and equilibrium concentrations (mg/L) of Cr(VI) solution, respectively; V is the volume (L); and w is the weight (g) of the adsorbent.

In order to examine the effect of pH on the adsorption of Cr(VI) on the adsorbent, the initial pH of each solution was adjusted to the appropriate value by adding 0.1 mol/L HCl or/and NaOH solutions before mixing with the adsorbent.

4.2.4 Kinetic study

The experiments were carried out by contacting 20 mg of the adsorbent samples with 10 mL of the aqueous solution at 298 K and pH 2, and the initial Cr(VI) concentration is 416 mg/L.

4.2.5 Adsorption isotherms

The experiments were carried out by contacting 20 mg of the adsorbent samples with 10 mL of the aqueous solution at 298 K and pH 2.

4.2.6 Thermodynamic study

The experiments were carried out by contacting 20 mg of the adsorbent samples with 10 mL of the aqueous solution at different temperatures from 298 to 328 K at pH 2, and initial Cr(VI) concentration is 416 mg/L.

4.2.7 Treatment for low concentration of Cr(VI)

0.1g of adsorbent was added to a solution with pH = 2, and the final pH was adjusted to 2 by 0.1 mol/L HCl. This process converts all amino groups into ammonium salts. The adsorbent was then recovered by filtration and dried at 80 ^{o}C for overnight.

The experiments with low concentration of Cr(VI) were carried out by contacting 20 mg of the adsorbent samples with 10 mL of the aqueous solution of initial concentration of 26 and 52 ppm, respectively. The samples were thermostated in a water bath at 25 ^{o}C for overnight. The solids were then filtered out, and filtrate was again filtered through a 0.2 μm filter.

Subsequently, the residual Cr(VI) in the filtrate was determined at 540 nm using the diphenylcarbazide method [9].

4.2.8 Desorption

The adsorbent that was used for the adsorption of 416 mg/L of Cr(VI) solution was separated from the solution by filtration and dried in oven at 80 ^{o}C. The dried adsorbent was added to 10 ml of water, and the pH was subsequently adjusted to 8 by NaOH. The solution was agitated for 1h. The adsorbent was then filtered out, and the residual Cr(VI) in the filtrate was measured by UV.

4.3 Results and discussion

4.3.1 X-ray diffraction pattern

Figure 4.1 shows the X-ray diffraction patterns obtained from as-synthesized NH_2-UIO-66 and NH_2-MIL-125(Ti). All the diffraction peaks of the materials NH_2-UIO-66 and NH_2-MIL-125(Ti) are identical to their corresponding simulated data, confirming the successful synthesis of NH_2-UIO-66 and NH_2-MIL-125(Ti).

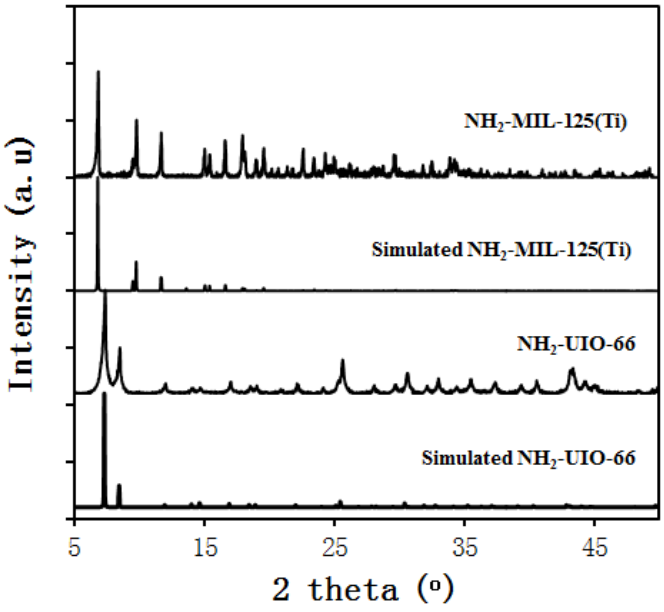

Figure 4.1 X-ray diffraction patterns obtained from as-synthesized NH_2-UIO-66, NH_2-MIL-125(Ti) and simulated NH_2-UIO-66, NH_2-MIL-125(Ti).

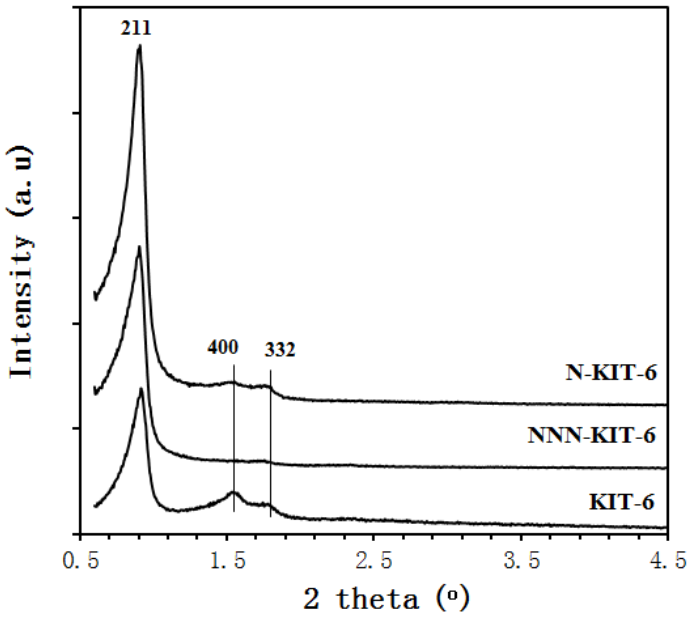

Figure 4.2 Low angle X-ray diffraction patterns obtained from KIT-6, N-KIT-6 and NNN-KIT-6.

Figure 4.2 shows the low angle X-ray diffraction patterns of the KIT-6, N-KIT-6 and NNN-KIT-6. There is a sharp intense peak at 2 theta = 0.92 corresponding to (2 1 1) and a shoulder peak for (2 2 0) plane in KIT-6, N-KIT-6 and NNN-KIT-6. Moreover, (4 0 0) and (3 3 2) peaks are also found in the low angle X-ray diffraction pattern. This indicates that the samples of KIT-6, N-KIT-6 and NNN-KIT-6 are highly ordered mesoporous with Ia3d space group and confirms the successful synthesis of KIT-6 based materials.

4.3.2 BET measurements

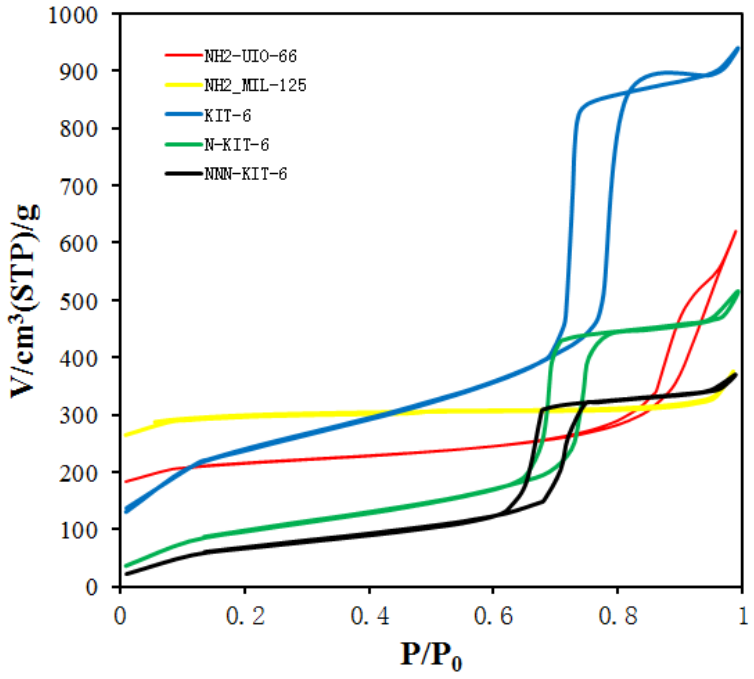

Figure 4.3 Nitrogen adsorption–desorption isotherm of the NH_2-UIO-66, NH_2-MIL-125(Ti), KIT-6, N-KIT-6 and NNN-KIT-6.

The N_2 adsorption–desorption isotherms are shown in Figure 4.3. The N_2 gas adsorption–desorption measurements of all the materials presented type IV

isotherms except NH_2-MIL-125(VI) which showed a type I isotherm typical for a microporous structure.

Figure 4.4 shows the BJH pore size distribution of the as-synthesized NH_2-UIO-66, NH_2-MIL-125(Ti), KIT-6, N-KIT-6 and NNN-KIT-6. These curves confirm the mesoporous structures of KIT-6, N-KIT-6 and NNN-KIT-6. Among them, the mesopores in NH_2-UIO-66 show a broad distribution centered at about 16.7 nm. The formation of mesopores in NH_2-UIO-66 could be due to the formation of interspace between the NH_2-UIO-66. The dominant pores of KIT-6, N-KIT-6 and NNN-KIT-6 were of 7.4, 6.3 and 5.7 nm, respectively.

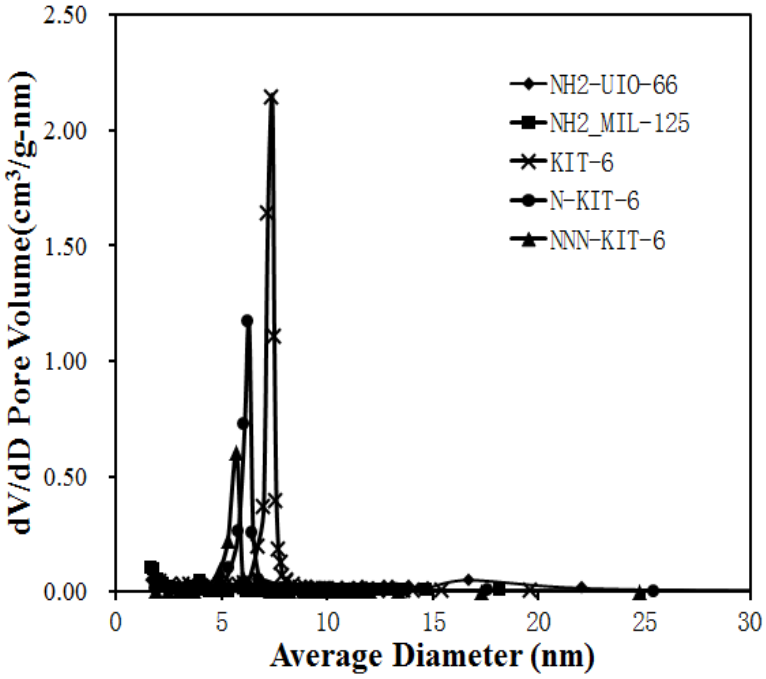

Figure 4.4 BJH pore size distribution of the NH_2-UIO-66, NH_2-MIL-125(Ti), KIT-6, N-KIT-6 and NNN-KIT-6.

The surface area, pore volume and pore diameter of the NH_2-UIO-66, NH_2-MIL-125(Ti), KIT-6, N-KIT-6 and NNN-KIT-6 are listed in Table 4.2.

All materials had high surface area and very high total pore volume. The pore diameter of KIT-6 was reduced by 1.1 and 1.7 nm after ATPES and DETA modification, respectively. Figure 4.5 shows sketches of the pores of N-KIT-6 after modification, the functional group bend down due to the hydrogen bond between amine group to hydroxyl group or amine group to amine group [10]. Therefore, the surface of KIT-6 is not densely functionalized, because the length of $H_2N(CH_2)_3Si$ and $H_2N(CH_2)_2NH(CH_2)_2NH(CH_2)_3Si$ are about 0.97 and 1.6 nm.

Table 4.2 Surface area, pore volume and pore diameter of the NH_2-UIO-66, NH_2-MIL-125(Ti), KIT-6, N-KIT-6 and NNN-KIT-6.

Samples	Surface area (m^2/g)	Pore volume (cm^3/g)	Pore size (nm)
NH_2-UIO-66	657	0.960	16.7
NH_2-MIL-125(Ti)	857	0.408	-
KIT-6	811	1.454	7.4
N-KIT-6	351	0.798	6.3
NNN-KIT-6	250	0.573	5.7

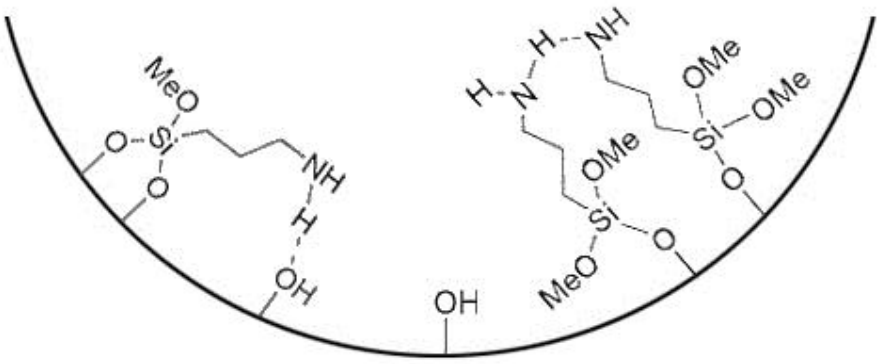

Figure 4.5 The sketches of the pores of N-KIT-6 after modification.

4.3.3 Kinetic study

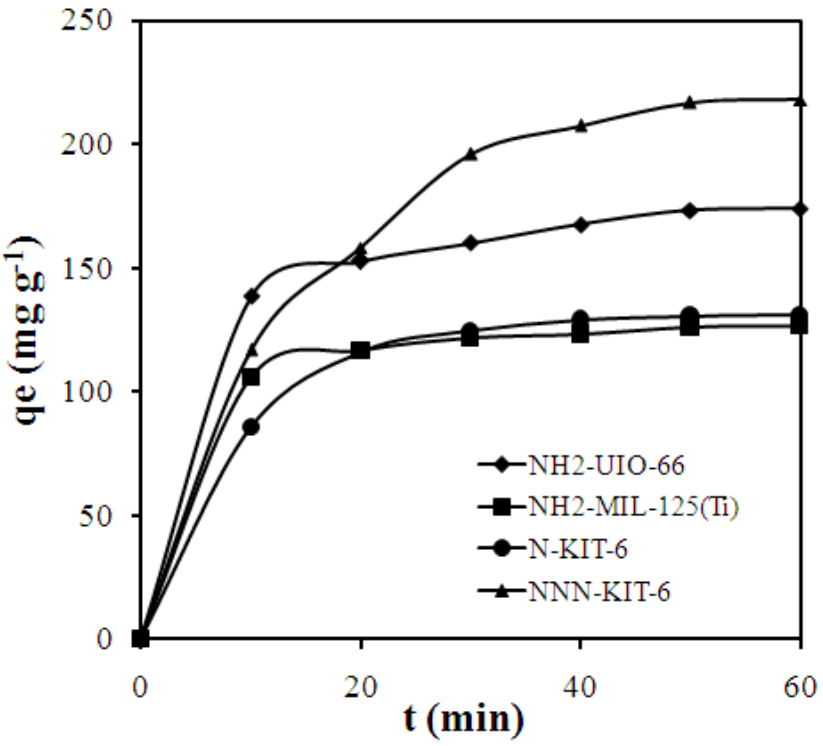

Figure 4.6 Amount of Cr(VI) adsorbed on NH_2-UIO-66, NH_2-MIL-125(Ti), N-KIT-6 and NNN-KIT-6 versus adsorption time (416 ppm initial Cr(VI) concentration; T = 298 K; adsorbent dose = 2g dm^{-3}; pH 2).

Figure 4.6 illustrates the kinetic curves for removal of Cr(VI) from aqueous solutions over NH_2-UIO-66, NH_2-MIL-125(Ti), N-KIT-6 and NNN-KIT-6, respectively. The adsorbed amount of curves of NH_2-UIO-66, NH_2-MIL-125(Ti), N-KIT-6 achieves above 80% of adsorption capacity at equilibrium in the first 20 min, indicating that those materials have high adsorption rate. Although NNN-KIT-6 presented a relative low adsorption rate, it showed an amazing adsorption capacity. The primary reason of those materials with high adsorption rate could be due to their highly ordered porous structure and big total pore volume, which enable the Cr(VI) to penetrate into the pore easily and interact with the materials.

Kinetic modeling is very important both to evaluate adsorption rates and to identify possible reaction mechanisms. Several kinetic models including pseudo-first-order, pseudo-second-order and the intraparticle diffusion model are frequently used to study the controlling mechanism of adsorption process.

The linear pseudo-first-order equation, pseudo-second-order equation and intraparticle diffusion equation are given as follows:

$$log(q_e - q_t) = log(q_e) - \frac{k_1 t}{2.303} \quad (4.2)$$

$$\frac{t}{q_t} = \frac{1}{k_2 q_e^2} + \frac{t}{q_e} \quad (4.3)$$

$$q_t = k_{dif} t^{0.5} \quad (4.4)$$

where q_e and q_t are adsorption capacity of the adsorbent (mg/g) at equilibrium and at time t (min); k_1 and k_2 are the pseudo-first-order and pseudo-second-order rate constants; k_{dif} is the intraparticle diffusion rate constant.

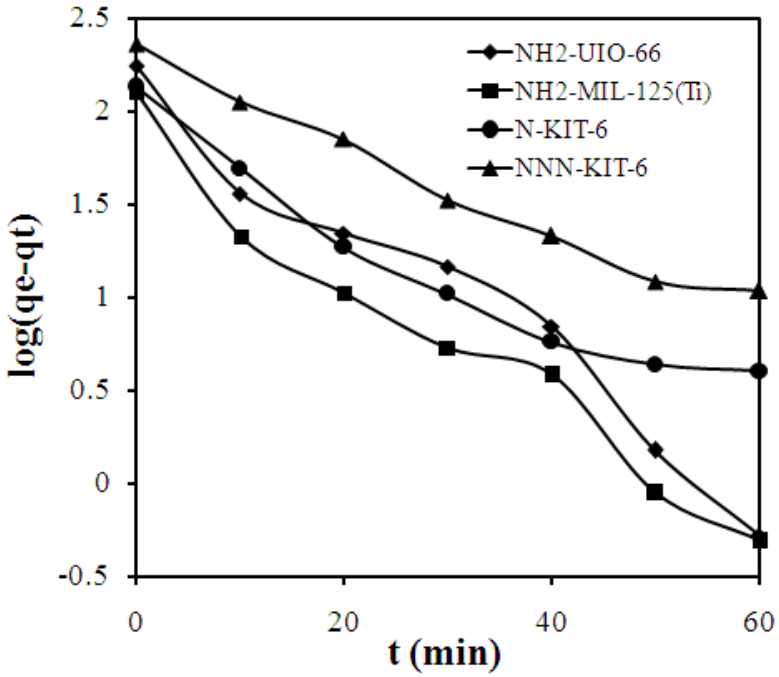

Figure 4.7 Pseudo-first-order plot for Cr(VI) adsorption onto the NH_2-UIO-66, NH_2-MIL-125(Ti), N-KIT-6 and NNN-KIT-6.

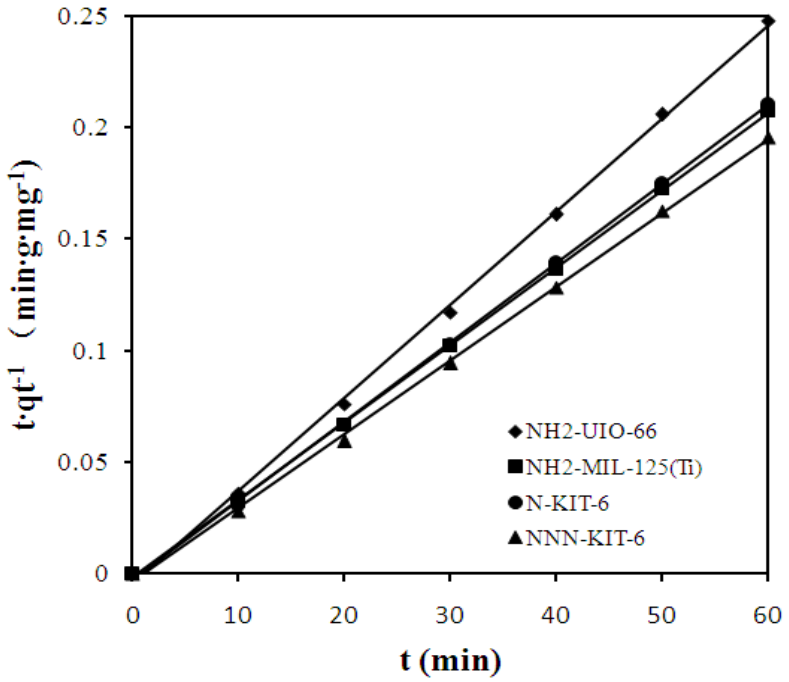

Figure 4.8 Pseudo-second-order plot for Cr(VI) adsorption on as-synthesized NH_2-UIO-66, NH_2-MIL-125(Ti), N-KIT-6 and NNN-KIT-6.

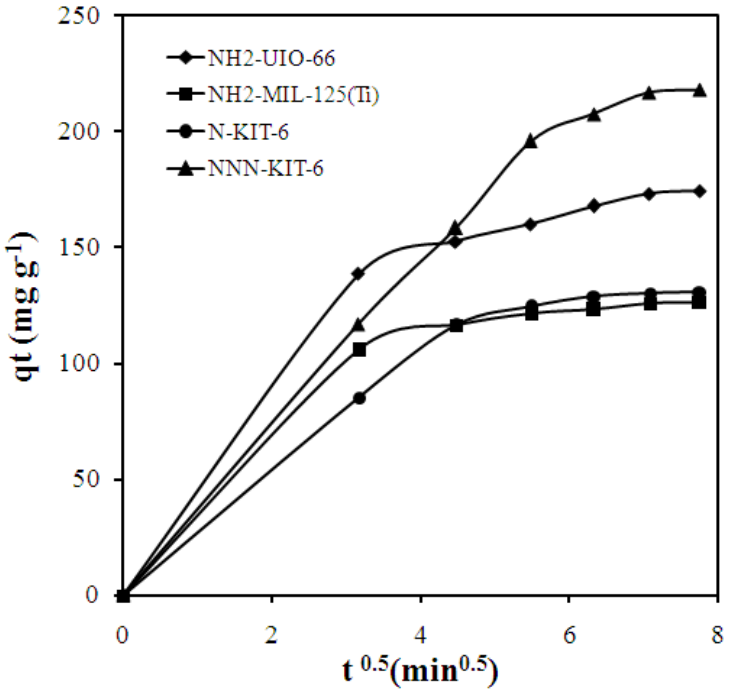

Figure 4.9 Interparticle diffusion kinetics for Cr(VI) adsorption on as-synthesized NH_2-UIO-66, NH_2-MIL-125(Ti), N-KIT-6 and NNN-KIT-6.

The first-order constant k_1 and equilibrium adsorption density q_e were calculated by the slopes and intercepts of $\log(q_e-q_t)$ versus t plots (see Figure 4.7). Similarly, the second-order constant k_2 and equilibrium adsorption density q_e were obtained by the tq_t^{-1} versus t plots (see Figure 4.8). And the k_{dif} can be simply got by q_t versus $t^{0.5}$ plots (see Figure 4.9). Comparison results with the correlation coefficients are listed in Table 4.3. Of the three models tested, the second-order kinetic model gives the best straight-line fit and the best correlation coefficient. Therefore, the pseudo-second-order equation could be sufficient to describe the mechanism of interactions between the adsorbents and Cr(VI).

Table 4.3 Comparison of the pseudo first-order, second-order and intraparticle diffusion adsorption constants by using different adsorbents.

Samples	First-order model			Second-order model			Intraparticle diffusion	
	k_1 (min^{-1})	q_1 (mg/g)	r^2	k_2 (L mg^{-1} min^{-1})	q_2 (mg/g)	r^2	K_{dif} (mg $min^{-0.5}$ g^{-1})	r^2
NH_2-UIO-66	0.088	146.9	0.964	3.65	239.2	0.998	21.31	0.830
NH_2-MIL-125(Ti)	0.085	77.8	0.965	7.04	287.9	0.999	15.36	0.790
N-KIT-6	0.0575	84.9	0.925	4.26	281.9	0.999	26.92	0.883
NNN-KIT-6	0.0530	195.4	0.978	2.94	302.7	0.999	29.15	0.959

4.3.4 Adsorption isotherms

Langmuir and Freundlich isotherms are the most widely used models to describe the adsorption behavior. The Langmuir isotherm has been extensively used to describe the adsorption of heavy metals, dyes, organic pollutants, etc. It is used for monomolecular layer adsorption. This isotherm is described as a homogeneous one assuming that all the adsorption sites have equal adsorbent affinity and that the adsorption at one site does not impact on the adsorption at an adjacent site. The Langmuir isotherm is utilized to obtain a maximum adsorption capacity produced from the complete monolayer coverage of adsorbent surface. The isotherm equation is represented as follow:

$$\frac{C_e}{q_e} = \frac{1}{Q_0 b} + \frac{C_e}{Q_0} \tag{4.5}$$

where b is an adsorption equilibrium constant (L/mg) that is related to the apparent energy of adsorption, Q_0 is the quantity of adsorbent required to form a single monolayer on a unit mass of adsorbent (mg/g), and q_e is the amount adsorbed per unit mass of adsorbent (mg/g) when the equilibrium concentration is C_e (mg/L).

Figure 4.10 shows that a plot of (C_e/q_e) versus C_e yields a straight line indicating that the Langmuir equation describes the adsorption equilibrium well. The constants Q_0 and b were determined from the slope and the intercept

of this line.

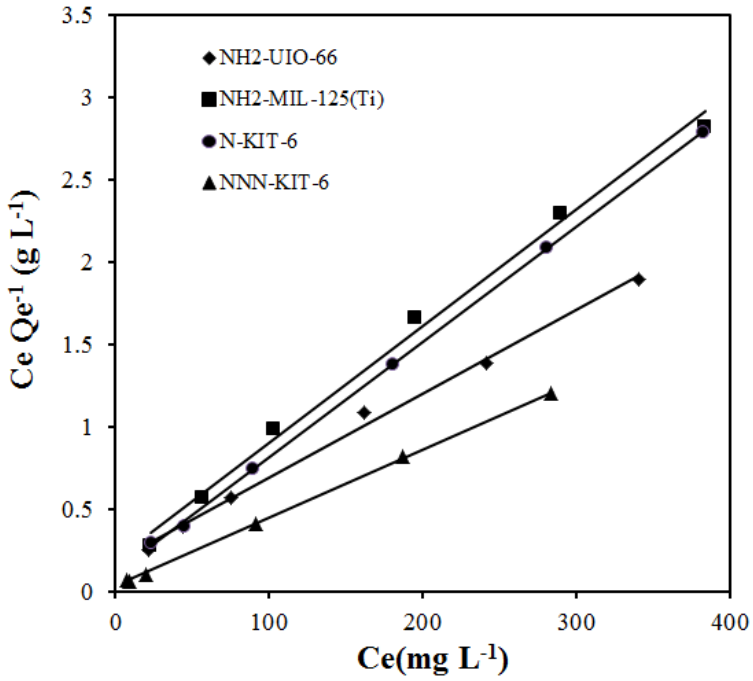

Figure 4.10 Langmuir isotherm for Cr(VI) adsorption on as-synthesized NH_2-UIO-66, NH_2-MIL-125(Ti), N-KIT-6 and NNN-KIT-6 (adsorbent dose = 2g dm^{-3}; pH 2; t = 60 min).

A further analysis of the Langmuir equation can be carried out according to the basis of a dimensionless equilibrium parameter, R_L (separation factor), given as follows [11]:

$$R_L = \frac{1}{1+bC_0} \tag{4.6}$$

The value of R_L lies between 0 and 1 for a favorable adsorption, while $R_L > 1$ for unfavorable sorption, and $R_L = 1$ for linear sorption, while the adsorption

operation is irreversible if $R_L = 0$.

The Freundlich isotherm predicts that the ratio of the amount of solute adsorbed on a given mass of adsorbent to the concentration of solute in the solution is not constant at different concentrations. For many systems, the molar heat of adsorption decreases with increasing saturation of the surface. This has been well dealt with by the Freundlich isotherm, which has previously been viewed as an empirical isotherm. For adsorption from solution, the Freundlich isotherm is expressed as follow:

$$logq_e = logK_F + \frac{1}{n} logC_e \quad (4.7)$$

where K_F is the Freundlich constant, which indicates the relative adsorption capacity of the adsorbent and is related to the bonding energy, and n is the heterogeneity factor representing the deviation from linearity of adsorption and also known as the Freundlich coefficient. q_e is the amount adsorbed per unit mass of the adsorbent (mg/g) at the equilibrium concentration C_e (mg/L).

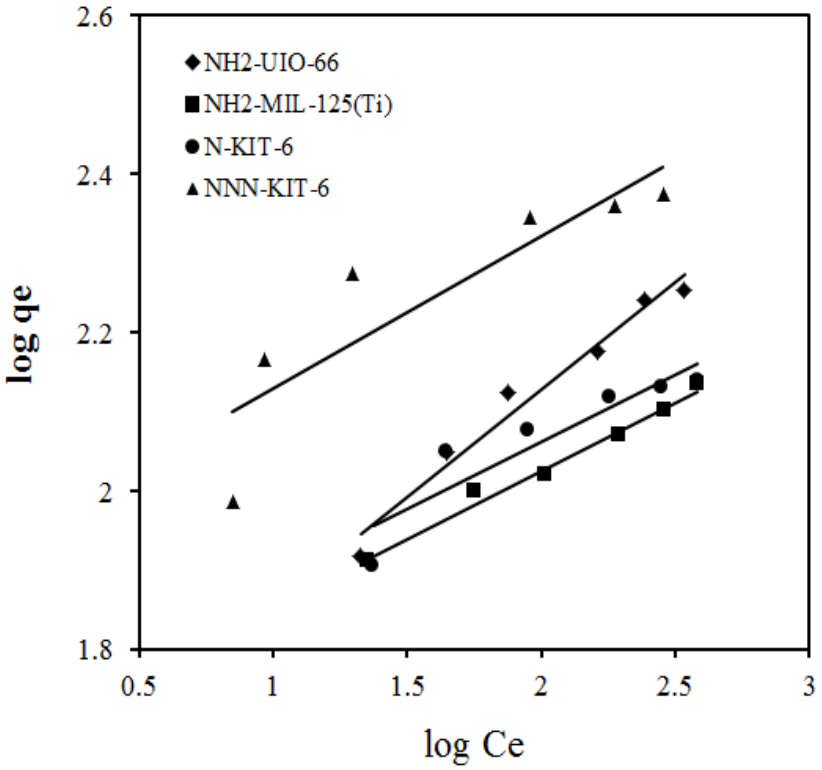

Figure 4.11 Freundlich isotherm for Cr(VI) adsorption on as-synthesized NH_2-UIO-66, NH_2-MIL-125(Ti), N-KIT-6 and NNN-KIT-6 (adsorbent dose = 2g dm^{-3}; pH 2; t = 60 min).

Figure 4.11 shows the plots of log q_e versus log C_e which are able to be employed to obtain the Freundlich coefficients. Furthermore, comparison results of Langmuir and Freundlich isotherm parameters are shown in Table 4.4.

Table 4.4 Langmuir and Freundlich isotherm parameters for adsorption of Cr(VI) onto NH_2-UIO-66, NH_2-MIL-125(Ti), N-KIT-6 and NNN-KIT-6.

Samples	Langmuir constants				Freundlich constants		
	Q_0(mg g^{-1})	b(L mg^{-1})	R_L	r^2	K_F(mg g^{-1})	1/n	r^2
NH_2-UIO-66	195.4	0.0285	0.0777	0.996	4.872	0.2721	0.972
NH_2-MIL-125(Ti)	140.5	0.0363	0.0622	0.994	5.376	0.1717	0.987
N-KIT-6	142.9	0.0615	0.0376	0.999	5.592	0.1701	0.845
NNN-KIT-6	241.3	0.1275	0.0185	0.999	6.922	0.1935	0.779

It can be found that all the adsorption of NH_2-UIO-66, NH_2-MIL-125(Ti), N-KIT-6 and NNN-KIT-6 agreed well with Langmuir model based on the correlation coefficient, and the theoretical saturated adsorption capacity are 195.4, 140.5, 142.9 and 241.3 mg/g, respectively. Additionally, based on the previous report [12] that the Langmuir constant b can indicate the adsorption ability, the larger b value reflects the greater adsorption affinity. The data in Table 4.4 prove that the affinity of Cr (VI) over amino-functionalized KIT-6 is much stronger than that over amino-functionalized MOFs. In addition, Table 4.5 lists maximum adsorption capacity values reviewed in literature for the adsorption of Cr(VI) on different materials.

Table 4.5 Summary of adsorption capacity values of Cr(VI) on different adsorbents reported in literature.

Adsorbent	Q_0 (mg/g)	Ref.
UIO-66	93.0	Chapter 3
NH_2-UIO-66	195.4	This study
NH_2-MIL-125(Ti)	140.5	This study
N-KIT-6	142.9	This study
NNN-KIT-6	241.3	This study
Activated alumina	7	[13]
Activated charcoal	13	[13]
Amorphous aluminium oxide	78	[14]
Amino-functionalization of mesoporous silica	118.6 – 172.6	[2]
Carbon nanotubes	4	[15]
Cotton Fiber/ZrO2	69	[16]
Calcined bauxite	2	[17]
Calcined Mg-Al LDH	235.45	[18]
Calcined Mg–Al–CO_3 hydrotalcite	120	[19]
Ethylenediamine-functionalized Fe_3O_4	32.2 – 61.4	[1]
Hydrous ferric oxide	36	[20]
Hydrous stannic oxide	3	[21]
Hydrous titanium oxide	30	[22]
Hydrous zirconium oxide	61-66	[23]
Iron oxide	23	[24]
Iron–nickel oxide	30	[11]
Maghemite	19	[25]
Montmorillonite-supported magnetite	15	[26]
N-MCM-41	52.9	[4]
NN-MCM-41	92.1	[4]
NNN-MCM-41	115.2	[4]
N-SBA-1	94.2	[4]
NN-SBA-1	178.4	[4]
NNN-SBA-1	210.8	[4]
Polypyrrole/Fe_3O_4	169.5	[3]
STAC-modified rectorite	21	[27]

4.3.5 Treatment for low concentration of Cr(VI)

Cr(VI) initial concentrations of 26 ppm and 52 ppm were examined in order test if chromium removal down to levels required for safe drinking water was possible. Table 4.6 shows the Cr(VI) residue concentration in water after adsorption by using different adsorbent. The N-KIT-6 and NNN-KIT-6 exhibited satisfactory removal efficiency, with a final Cr(VI) residue concentration in water is below the legal limit of 0.05 ppm after adsorption.

Table 4.6 Cr(VI) residue concentration in water after adsorption by using NH_2-UIO-66, NH_2-MIL-125(Ti), N-KIT-6 and NNN-KIT-6 at Cr(VI) initial concentration of 26 and 52 ppm, respectively.

Adsorbent	$C_{Cr(VI)}$ (ppm), ($C_{initial}$ = 26 ppm)	$C_{Cr(VI)}$ (ppm), ($C_{initial}$ = 52 ppm)
NH_2-UIO-66	0.620	0.999
NH_2-MIL-125(Ti)	5.98	14.71
N-KIT-6	0.020	0.028
NNN-KIT-6	0.028	0.048

4.3.6 Desorption

Reusability of adsorbents is quite important in industrial process, because it can significantly reduce the overall cost and also makes the process more

environmentally friendly. Desorption tests were carried out to regenerate chromium-loaded NH_2-UIO-66, NH_2-MIL-125(Ti), N-KIT-6 and NNN-KIT-6 using NaOH solution for desorption of Cr(VI).

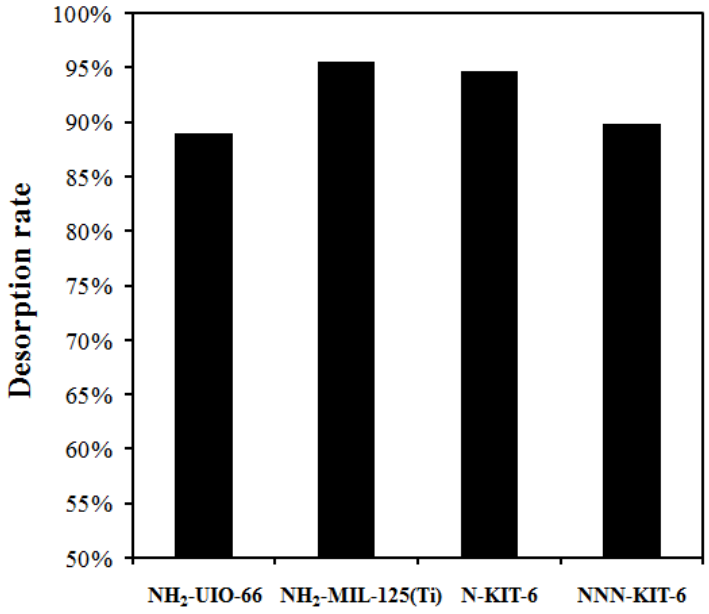

Figure 4.12 Desorption of Cr(VI) from NH_2-UIO-66, NH_2-MIL-125(Ti), N-KIT-6 and NNN-KIT-6. (Adsorbent dose = 2g/L; time = 60min; T = 298K; final pH = 8).

Figure 4.12 shows desorption of Cr(VI) from NH_2-UIO-66, NH_2-MIL-125(Ti), N-KIT-6 and NNN-KIT-6. Desorption from NH_2-MIL-125(Ti) and N-KIT-6 is much more complete than from the other two adsorbents. The results of these desorption experiments indicate that the Cr(VI) adsorption onto NH_2-UIO-66, NH_2-MIL-125(Ti), N-KIT-6 and NNN-KIT-6 are not completely reversible, and thus that chemisorption, physisorption and

ion-exchange mechanisms are operative in the adsorption process. Only the Cr(VI) ions that are adsorbed by physisorption and ion-exchange are desorbed.

4.4 Conclusion

This is the first report of heavy metal removal from aqueous solution by amino-functionalized MOFs and KIT-6. The kinetics of Cr(VI) adsorption onto NH_2-UIO-66, NH_2-MIL-125(Ti), N-KIT-6 and NNN-KIT-6 can be successfully described by the pseudo-second order model. The adsorption isotherms could be fitted very well with the Langmuir model, and the adsorption capacity of NH_2-UIO-66, NH_2-MIL-125(Ti), N-KIT-6 and NNN-KIT-6 are 195.4, 140.5, 142.9 and 241.3 mg/g, respectively. In this study, amino-functionalized KIT-6 shows relatively high adsorption capacity and satisfactory removal efficiency, but its synthesis is more complex. In contrast, the synthesis of amino-functionalized MOFs is a one-pot synthesis, and the sorbent can be recycled. Therefore amino-functionalized MOFs are suitable for pretreatment of waste water, while because of their strong affinity to Cr(VI), amino-functionalized KIT-6s are suitable for final polishing of waste water to reach drinking water standards.

In summary, amino-functionalized inorganic and organic hybrid materials show a high adsorption capacity, efficiency and reusability, and thus they exhibit an excellent potential for application to control Cr(VI) pollution.

4.5 References

[1] Y.G. Zhao, H.Y. Shen, S.D. Pan, M.Q. Hu, J. Hazard. Mater., 182 (2010) 295.

[2] J. Li, X. Miao, Y. Hao, J. Zhao, X. Sun, L. Wang, J. Colloid Interface Sci., 318 (2008) 309.

[3] M. Bhaumik, A. Maity, V.V. Srinivasu, M.S. Onyango, J. Hazard. Mater., 190 (2011) 381.

[4] H. Yoshitake, T. Yokoi, T. Tatsumi, Chem. Mater., 14 (2002) 4603.

[5] F. Kleitz, S. H. Choi, R. Ryoo, Chem. Commun., (2003) 2136.

[6] J.H. Cavka, S. Jakobsen, U. Olsbye, N. Guillou, C. Lamberti, S. Bordiga, K.P. Lillerud, J. Am. Chem. Soc., 130 (2008) 13850.

[7] Y. Fu, D. Sun, Y. Chen, R. Huang, Z. Ding, X. Fu, Z. Li, Angew. Chem. Int. Edit., 51 (2012) 3364.

[8] K.K. Sharma, T. Asefa, Angew. Chem., 119 (2007) 2937.

[9] Y.C. Zhang, J. Li, M. Zhang, D.D. Dionysiou, Environ. Sci. Technol., 45 (2011) 9324.

[10] J.C. Hicks, R. Dabestani, A. C. Buchanan III, C.W. Jones, Chem. Mater. 18 (2006) 5022

[11] L. Wei, G. Yang, R. Wang, W. Ma, J Hazard Mater., 164 (2009) 1159.

[12] J. Das, B. Sairam Patra, N. Baliarsingh, K.M. Parida, J Colloid Interface Sci, 316 (2007) 216.

[13] S. Mor, K. Ravindra, N.R. Bishnoi, Bioresource Technol., 98 (2007) 954.

[14] E. Álvarez-Ayuso, A. Garc á-S ánchez, X. Querol, J. Hazard. Mater., 142 (2007) 191.

[15] M.A. Atieh, Procedia. Environ. Sci., 4 (2011) 281.

[16] A.A. Muxel, S.M.N. Gimenez, F.A. de Souza Almeida, R.V. da Silva Alfaya, A.A. da Silva Alfaya, CLEAN – Soil, Air, Water, 39 (2011) 289.

[17] S.S. Baral, S.N. Das, P. Rath, G.R. Chaudhury, Biochem Eng J., 34 (2007) 69.

[18] R.L. Goswamee, P. Sengupta, K.G. Bhattacharyya, D.K. Dutta, Appl. Clay Sci., 13 (1998) 21.

[19] N.K. Lazaridis, D.D. Asouhidou, Water Res., 37 (2003) 2875.

[20] S. Goswami, S.C. Bhat, U.C. Ghosh, Water Environ. Res., 78 (2006) 986.

[21] S.G.a.U.C. Ghosh, Water SA, 31 (2005) 597.

[22] U. Ghosh, M. Dasgupta, S. Debnath, S. Bhat, Water, Air, Soil Pollut., 143 (2003) 245.

[23] L.A. Rodrigues, L.J. Maschio, R.E. da Silva, M.L.C.P. da Silva, J Hazard Mater., 173 (2010) 630.

[24] I.V. Goshu, Y.V. Tsarev, V.V. Kostrov, Russ. J. Appl. Chem., 82 (2009) 801.

[25] J. Hu, I.M.C. Lo, G. Chen, Sep Purif Technol., 58 (2007) 76.

[26] P. Yuan, M. Fan, D. Yang, H. He, D. Liu, A. Yuan, J. Zhu, T. Chen, J Hazard Mater., 166 (2009) 821.

[27] H. Hong, W.-T. Jiang, X. Zhang, L. Tie, Z. Li, Appl. Clay Sci., 42 (2008) 292.

4.6 Appendix

Figure 4.13 The color of NH_2-UIO-66, NH_2-MIL-125(Ti), N-KIT-6 and NNN-KIT-6.

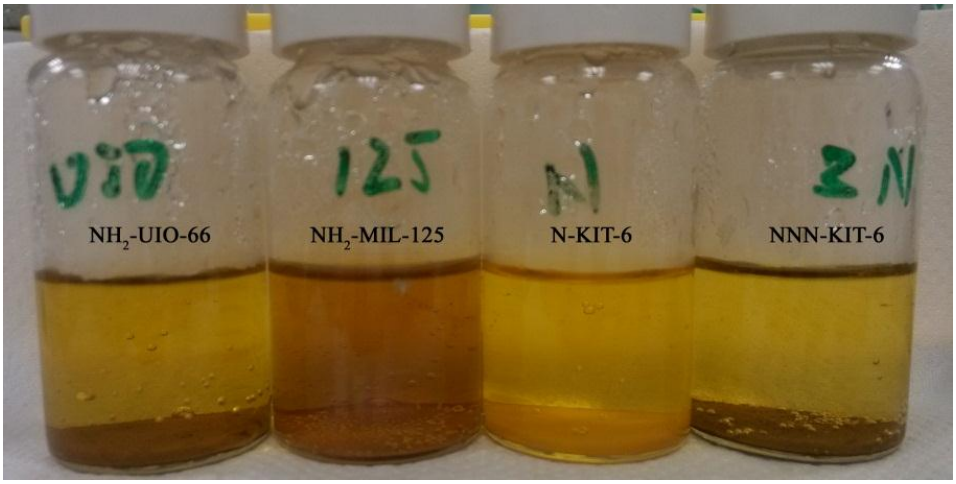

Figure 4.14 The solution and adsorbents after adsorption (initial Cr(VI) concentration = 416 ppm; adsorbent dose = 2g dm^{-3}; pH 2).

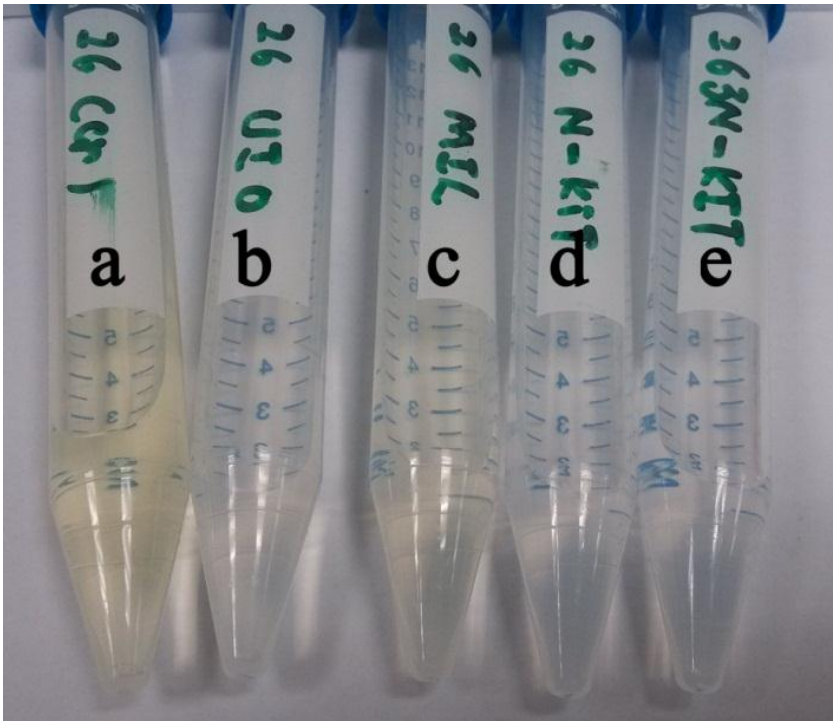

Figure 4.15 (a) 26 ppm Cr(VI) solution and the filtrate of adsorption over (b) NH_2-UIO-66 (c) NH_2-MIL-125(Ti), (d) N-KIT-6, (e) NNN-KIT-6 (initial Cr(VI) concentration = 26 ppm; adsorbent dose = 2g dm^{-3}).

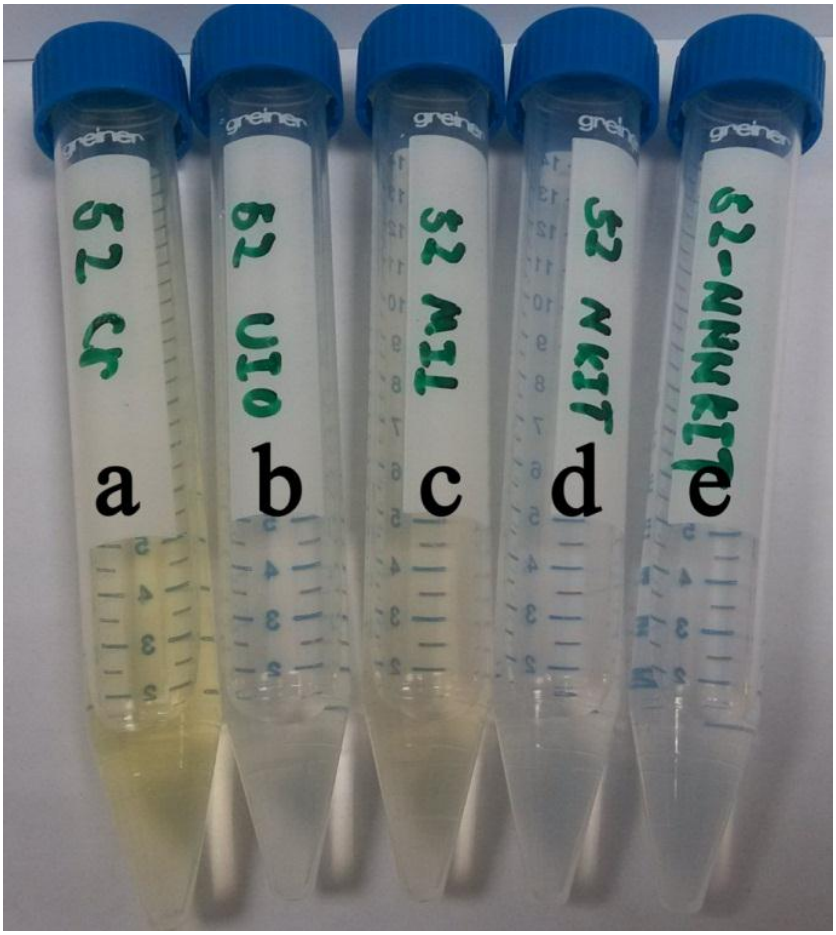

Figure 4.16 (a) 52 ppm Cr(VI) solution and the filtrate of adsorption over (b) NH_2-UIO-66 (c) NH_2-MIL-125(Ti), (d) N-KIT-6, (e) NNN-KIT-6 (initial Cr(VI) concentration = 52 ppm; adsorbent dose = 2g dm^{-3}).

Chapter 5 One-pot solvothermal synthesis of mesoporous molecules-doped TiO_2 with high visible light response, photocatalytic activity and controllable band gaps

5.1 Introduction

The efficient utilization of solar energy in water splitting and photocatalytic degradation of organic pollutants has attracted much attention over the last few decades [1]. Among various metal oxides and chalcogenides that have been investigated as photocatalysts, titanium dioxide (TiO_2) plays a special role because of its stability, availability, and low toxicity. Recent progress in the synthesis and applications of TiO_2 nanoparticles has been reviewed in a special volume of Chemical Reviews [2-4]. However, the band gap of TiO_2 is rather large, 3.0-3.2 eV. Therefore, TiO_2 can only be excited by UV-light which accounts for merely 4% of the solar energy compared to 45% for visible light.[2] Doping with foreign elements was the most successful approach to reduce the threshold energy for photoexcitation, and ions or atoms such as Fe^{3+} [5], V^{5+} [6], Cr^{3+} [7], Ru^{2+} [8], La^{3+} [9], Ce^{4+} [10], N [11], C [12], S [13], F [14], P [15] and B [16] have been introduced into the lattice of TiO_2 to modify the electronic properties.

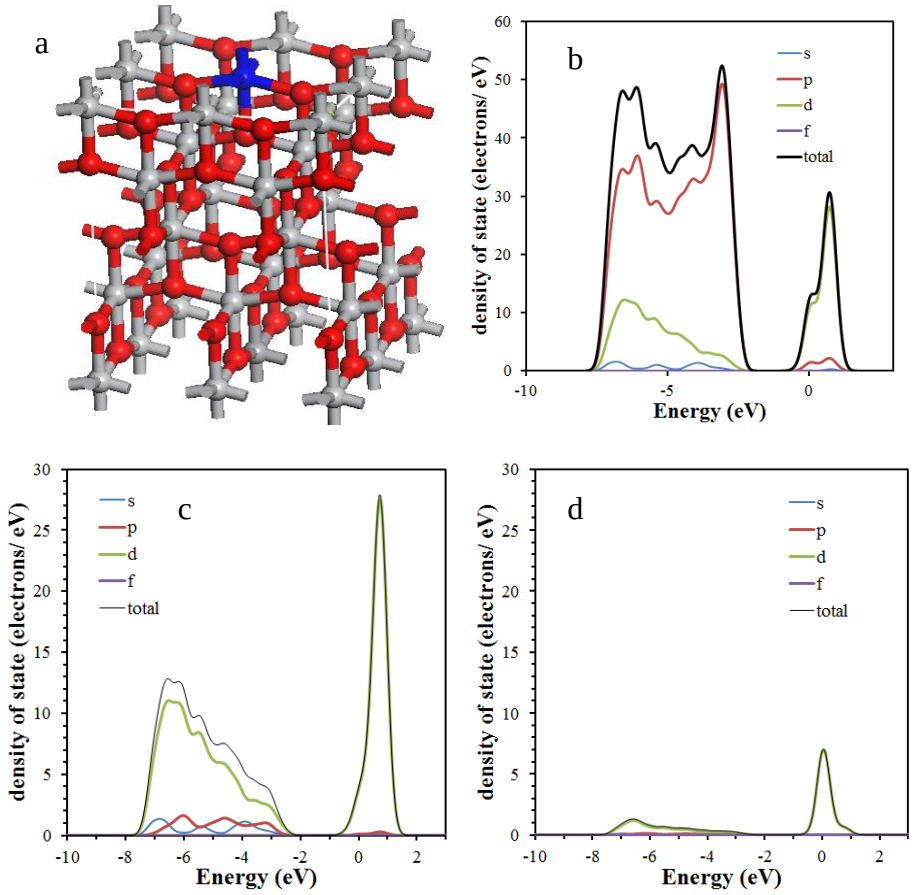

Figure 5.1 (a) Model of V-doped TiO_2 (red = oxygen, grey = titanium, blue = vanadium), (b) partial density of states (PDOS) of CB of V-doped TiO_2, (c) PDOS of Ti in CB of V-doped TiO_2 and (d) PDOS of V in CB of V-doped TiO_2.

Figure 5.1 shows a model of V-doped TiO_2 and the band structure of V-doped TiO_2. Material studio V6.1 was employed to model and calculate the V-doped TiO_2 with Density Functional Theory using the CASTEP code. An anatase V-doped TiO_2 with Ti/V ratio = 27 : 1 was created and optimized with the GGA PBE method. The CB of V-doped TiO_2 is made up of 3d orbitals of Ti and V (see Figure 5.1b, c and d). The calculations show that V contributes 20%

of the total electron density in the CB of the V-doped TiO_2 even though it amounts to only 3.6 atom% of the cationic sites in the lattice.

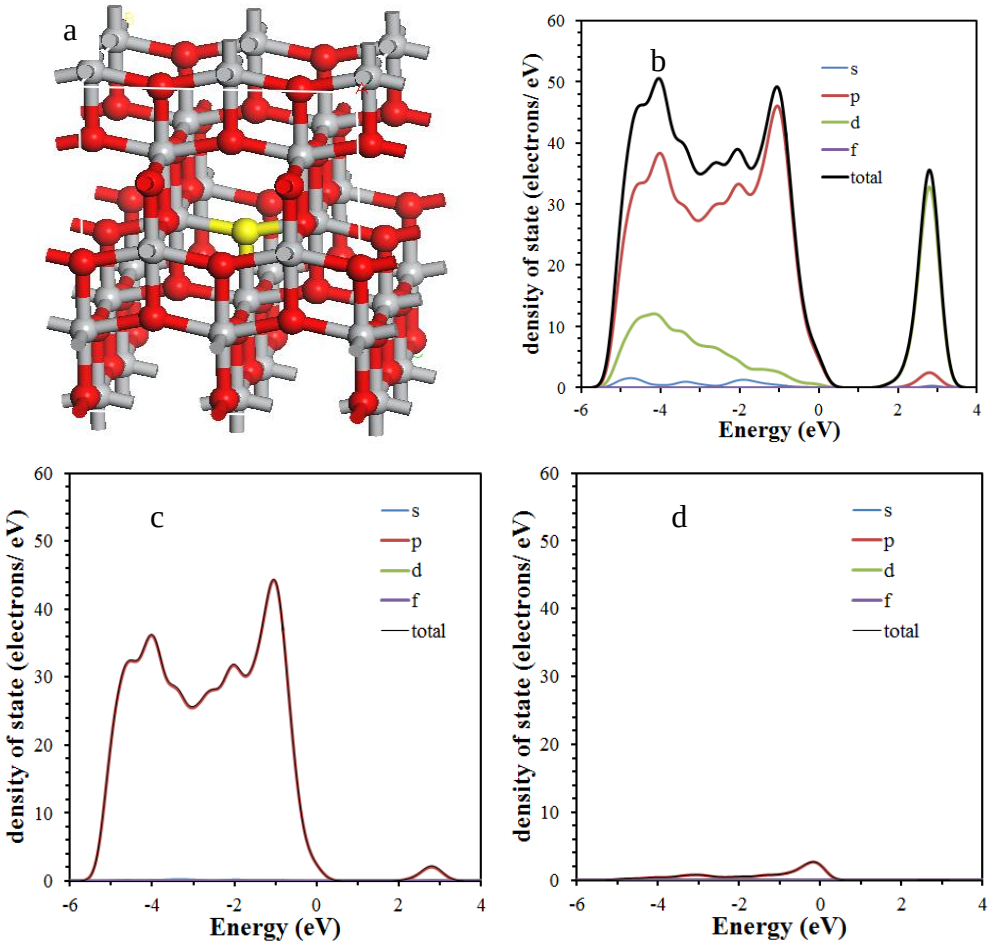

Figure 5.2 (a) Model of N-doped TiO_2 (red = oxygen, grey = titanium, yellow nitrogen), (b) PDOS of VB of states of N-doped TiO_2, (c) PDOS of O in CB of N-doped TiO_2 and (d) PDOS of N in CB of N-doped TiO_2.

Figure 5.2 shows the N-doped TiO_2 model and the composition of the VB of N-doped TiO_2. Again, Material studio V6.1 was used to model and calculate the N-doped TiO_2, with an O/N ratio = 27 : 1 in N-doped TiO_2. The VB of N-doped TiO_2 originated from 2p orbitals of O and N (see Figure 5.2b, c and

d), and N slightly influenced the VB of N-doped TiO_2.

Figure 5.3 illustrates a model of anatase TiO_2 and PDOS of anatase TiO_2, and calculated maximum adsorption between CB and VB is 4.38 eV (283 nm).

Compared with anatase TiO_2, the maximum adsorption between CB and VB of V-doped TiO_2 and N-doped TiO_2 shift to 3.79 eV (327 nm) and 3.86 eV (321 nm), respectively. Therefore the doped elements are able to affect the band structure of TiO_2 so as to influence the band gap of TiO_2.

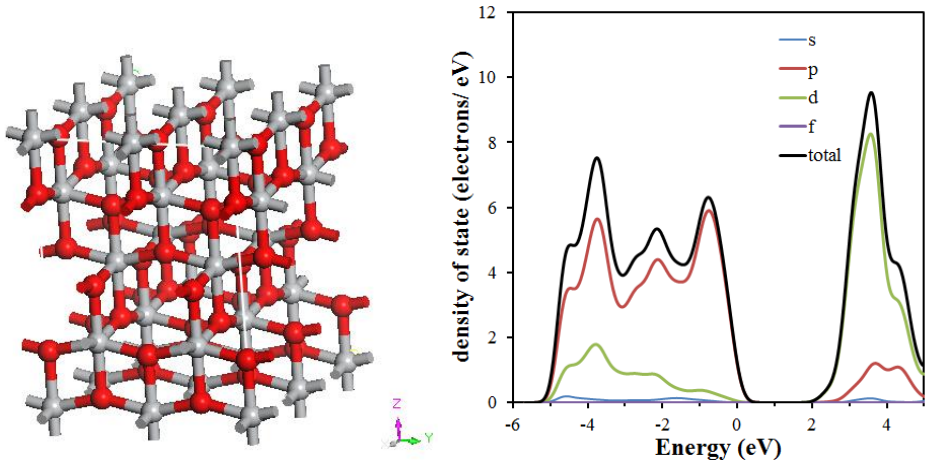

Figure 5.3 (a) Model of anatase TiO_2 (red = oxygen, grey = titanium) and (b) PDOS of anatase TiO_2.

We report here a new concept: molecules-doped TiO_2 with controllable band gap. In molecules-doped TiO_2, anchoring functional molecules are incorporated as linker into the crystal structure. Functional groups of the linker, normally carboxylate, can connect the metal centers. To prepare this material,

a one-pot solvothermal preparation was employed. The molecules-doped TiO_2 exhibited a mesoporous structure derived from the crystalline anatase phase. It is highlighted by a wide visible range response and remarkable photocatalytic activity.

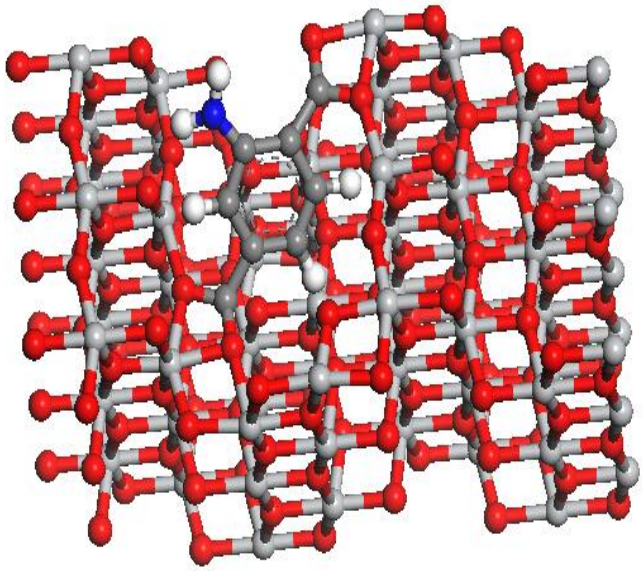

Figure 5.4 Model of molecular doped TiO_2 (red = oxygen, grey = titanium, blue nitrogen, white: hydrogen). Dopant: 2-amino-1,4-phthalic acid

Molecule-doped BiOCl was synthesized to further explore the universal principle of molecular doping. BiOCl has attracted much attention because of its ability for degradation of organic contaminants in wastewater. It is a highly efficient photocatalyst and simple to prepare [17-19]. Unfortunately, traditional preparations of BiOCl result in a non-porous material with low surface area of 1.469 m^2/g. The BiOCl only shows photocatalytic activity under irradiation with UV light [20]. But, we report a flower-like mesoporous

BiOCl with a higher surface area of 25 m^2/g. The molecule-doped BiOCl presented an impressive photocatalytic activity both in visible and in IR range.

5.2 Experimental

5.2.1 Materials

Synthesis of 2-aminoterephthalic acid doped TiO_2

Different amounts of 2-aminoterephthalic acid (H_2ATA) (0.6, 0.3, 0.15 mmol) and tetraisopropyl titanate $Ti(OCH(CH_3)_2)_4$ (1.77ml, 6 mmol) were added into a solution containing dimethylformamide (DMF) (8 ml), dry MeOH (2 ml) and water (0.1 ml, 5.55 mmol). The mixture was sonicated for 5 min at room temperature and was then transferred to a 30 ml autoclave and heated to 150 ^oC for 3 days. A yellow powder was obtained, which was filtered and washed with ethanol. The precipitate was then dried at 130 ^oC overnight. The series of 2-aminoterephthalic doped TiO_2 materials were denoted as A-TiO_2-10, A-TiO_2-20, A-TiO_2-40, respectively.

Synthesis of terephthalic acid doped TiO_2

A similar synthesis procedure was employed for the preparation of the materials of the terephthalic acid doped TiO_2 series, where 2-aminoterephthalic acid was replaced by terephthalic acid. The materials in

this series of terephthalic doped TiO_2 were denoted as B-TiO_2-10, B-TiO_2-20, and B-TiO_2-40, respectively.

Synthesis of 2-nitroterephthalic doped TiO_2

A similar synthesis procedure was also employed to prepare the 2-nitroterephthalic acid doped TiO_2 materials, but here, 2-aminoterephthalic acid was replaced by 2-nitroterephthalic acid. The samples in this series are denoted as N-TiO_2-10, N-TiO_2-20, N-TiO_2-40, respectively.

Synthesis of a mixture of terephthalic and 2-aminoterephthalic doped TiO_2

In the same way, a series of TiO_2 materials containing both terephthalic and 2-aminoterephthalic acid as dopands was prepared where the 2-aminoterephthalic acid was replaced by a mixture of terephthalic and 2-aminoterephthalic acid (mole ratio = 1:1). The materials of this series are denoted as M-TiO_2-10, M-TiO_2-20, M-TiO_2-40, respectively.

Synthesis of pure TiO_2

A similar synthesis procedure was employed in the preparation of the pure TiO_2, but without any organic molecules presented.

In the codes representing the different samples, A = 2-aminoterephthalic, B = terephthalic, N = 2-nitroterephthalic acid; the last number represents the molar

ratio of Ti/doped molecular (2-aminoterephthalic acid, terephthalic acid, 2-nitroterephthalic acid).

Synthesis of 2-nitroterephthalic acid doped BiOCl

2-Aminoterephthalic acid (0.0131 g, 0.1 mmol) and $Bi(NO_3)_3$ (0.9701g, 2.0 mmol) were added into a solution containing dimethylformamide (5 ml) and dry methanol (5 ml). NaCl (0.1169g, 2 mmol) was added into another solution containing dimethylformamide (5 ml), dry methanol (5 ml) and water (0.1 ml). The NaCl solution was added dropwise under vigorous stirring 30 min at room temperature, transferred to a 30 ml autoclave and heated at 120 ^{o}C for 16h. A yellow powder was obtained, which was filtered and washed with ethanol. The precipitate was then dried at 100 ^{o}C overnight.

5.2.2 Characterization

The diffractograms of XRD were recorded for 2θ between 5 ° to 85 °.

The sample was degassed under N_2 at 130 ^{o}C for 4 h prior to test for measurement of N_2 adsorption–desorption isotherms.

5.2.3 Simulation of A-TiO_2-X

A crystal slab of A-TiO_2-X was simulated by Material Studio. The geometry of the simulated A-TiO_2-X was optimized with the GGA PBE method of the

CASTEP package. The X-ray diffraction pattern was simulated using the Reflex module of Material Studio.

5.2.4 Evaluation of the photocatalytic activity

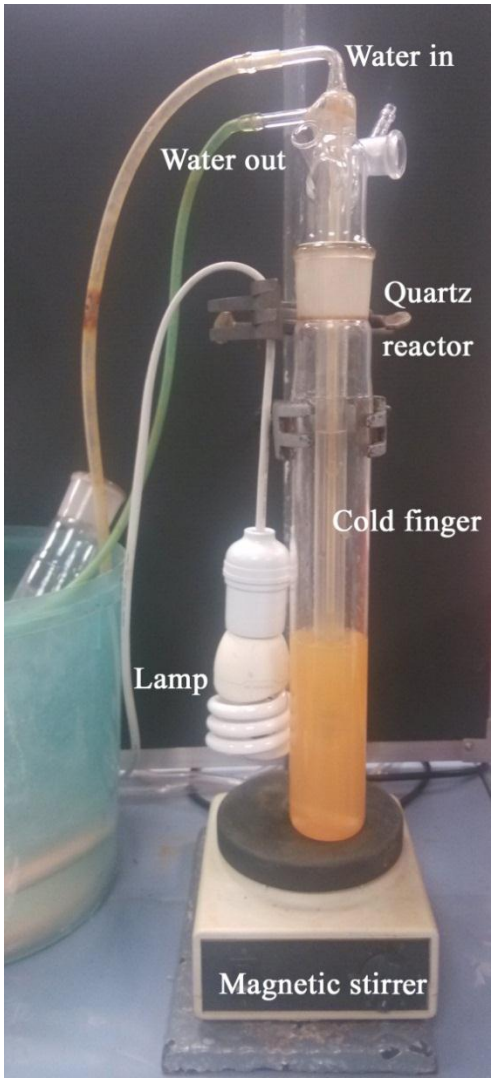

Figure 5.5 Setup of the photocatalytic reaction

The photocatalytic activities of samples were evaluated by degradation of Rhodamine B (RhB) (20 ppm) under irradiation with a 15 W Philips daylight

fluorescent lamp at room temperature in air. The setup of the reaction is given in Figure 5.5. All experiments were carried out with 25 mg of the catalyst suspended in 50 ml of the aqueous RhB solution. Prior to irradiation, the solutions were magnetically stirred for 1 hour in the dark to establish the adsorption equilibrium. Aliquots of 3 ml were removed at regular time intervals. After centrifugation to remove the catalyst, the concentration of RhB was determined from its absorption maximum at 554 nm using a UV-vis spectrophotometer (UV-1601, Shimadzu).

The used catalyst was washed with deionized water, dried overnight at 130 ^{o}C and tested in a fresh RhB solution. Three measurements were typically carried out.

5.2.5 Investigation of the photocatalytic mechanism

To gain more insight into the photocatalytic mechanism, isopropyl alcohol, $KBrO_3$, and ethylenediaminetetracetic acid (EDTA) were introduced as scavengers for hydroxyl radical ($HO^{\cdot}$), superoxide radical ($O_2^{-\cdot}$), and holes (h^+), respectively [21, 22]. The scavenger was added to the RhB solution before the addition of catalyst. The quantities used were 500 mmol/L isopropanol, 3.0 mmol/L $KBrO_3$, and 1 mmol/L EDTA. For experiments under N_2 purging, the N_2 gas was bubbled through the solution, keeping all other conditions the same.

5.2.6 Evaluation of the photocatalytic activity under irradiation of IR light over A-BiOCl-10.

The photocatalytic activities of the samples were evaluated by degradation of Rhodamine B (RhB) (20 ppm) under irradiation with a 250 W Infrared lamp (Philips BR125 IR 250W E27 230-250V Red 1CT) at room temperature in air. The remaining visible portion of the spectrum as well as longer wavelengths of IR which would contribute to heating of the sample was cut out using the NIR filter of an IRPrestige-21 IR spectrometer (Shimadzu) (band pass = 700 – 1100 nm), and the distance between the IR lamp and the reactor was 20 cm. A 100 ml beaker covered on all sides with aluminum foil was used as reactor. This beaker was put into a 250ml beaker that was also covered with aluminum foil to provide thermal insulation (see Figure 5.6).

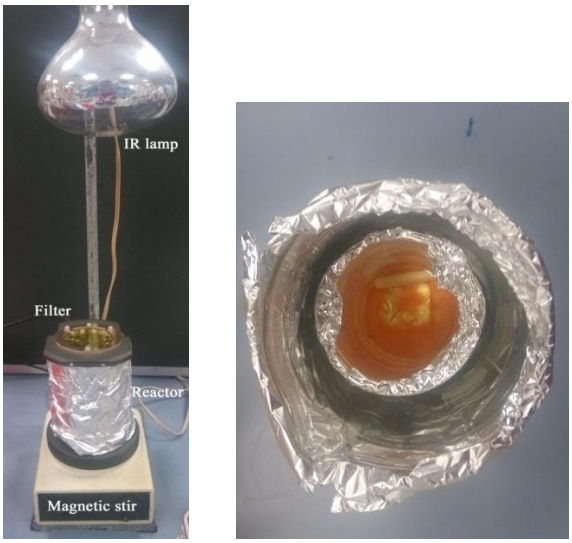

Figure 5.6 (a) Setup of the photocatalytic reaction with IR irradiation and (b) reactor covered with aluminum foil.

The experiment was carried out with 25 mg of the catalyst suspended in 50 ml of aqueous RhB solution. Prior to irradiation, the solutions were magnetically stirred for 1 hour in the dark to establish the adsorption equilibrium. Aliquots of 3 ml were removed at regular time intervals. After centrifugation to remove the catalyst, the concentration of RhB was determined photometrically.

5.2.7 Pathways and mechanism of RhB photodegradation

To research the pathways and mechanism of RhB photodegradation, the high performance liquid chromatography (HPLC) was employed to separate the N-deethylated intermediates during the process of RhB photodegradation. UV detector was used to monitor and optimize separation condition, and the molecular structure of N-deethylated intermediates can be identified by mass spectrum (MS).

The filtrate was collected and analyzed by HPLC (Shimadzu UFLC 20A) at regular time intervals. The mobile phase was methanol/4% acetate acid solution (50:50, v/v) at a flow rate of 1.0 ml/min, and the column was a Shim-pack VP-ODS C-18 reverse-phase column (150 mm * 4.6 mm i.d., 5 μm; Shimadzu). The N-deethylated intermediates were detected with the UV detector set at 518 nm and identified by HPLC-MS (ESI) (Dionex Ultimate 3000 RSLC system with Bruker amaZonX).

5.3 Results and discussion

5.3.1 X-ray diffraction pattern

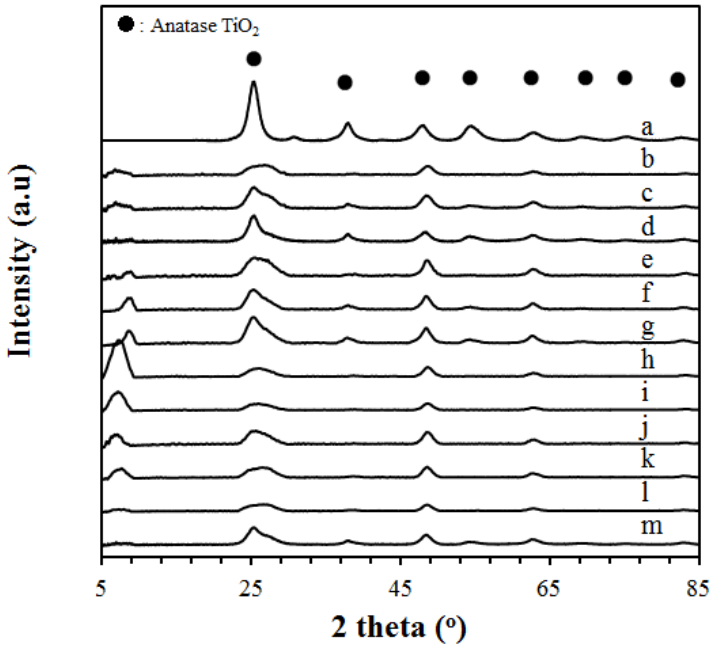

Figure 5.7 X-ray diffraction pattern obtained from as-synthesized samples (a) TiO_2, (b) B-TiO_2-10, (c) B-TiO_2-20, (d) B-TiO_2-40, (e) A-TiO_2-10, (f) A-TiO_2-20, (g) A-TiO_2-40, (h) N-TiO_2-10, (i) N-TiO_2-20, (j) N-TiO_2-40, (k) M-TiO_2-10, (l) M-TiO_2-20 and (m) M-TiO_2-40.

Figure 5.7 shows the X-ray diffraction patterns obtained from as-synthesized samples of TiO_2 and molecule-doped TiO_2. The diffraction patterns of the different molecule-doped TiO_2 samples contain all the diffraction peaks of TiO_2. All peaks were broad, indicating the relatively poor crystallinity of the material. The Bragg angles $2\theta \sim 25°$, 48°, 62° and 82° indicate that TiO_2 is in the anatase phase (ICSD No. 9852). An additional diffraction peak appears at

$2\theta \sim 7°$ for the molecule-doped TiO_2. To examine the extra peak, the model of A-TiO_2-x (Ti : dopant molecule ≈ 40:1) shown in Figure 5.3 was constructed. It can be seen that the oxygens of the carboxylic acid groups bind directly to titanium ions.

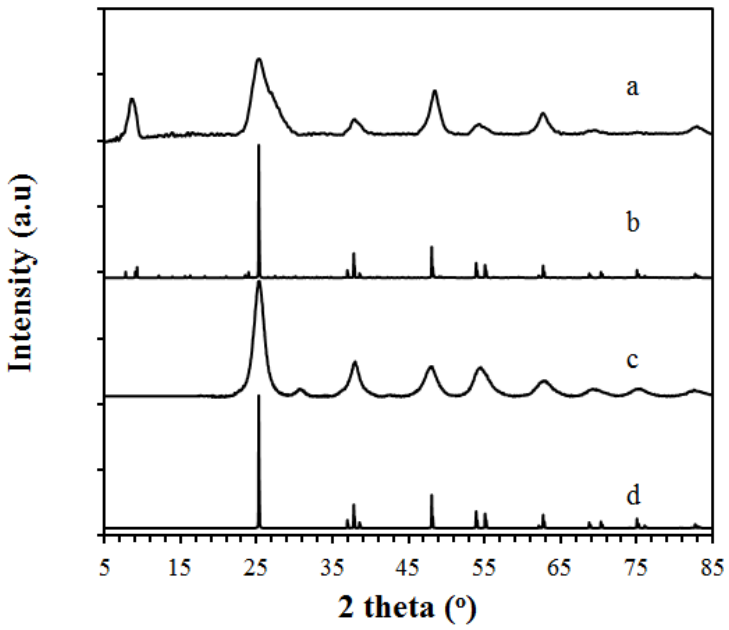

Figure 5.8 (a) Experimental and (b) simulated X-ray diffraction patterns of A-TiO-40, (c) Experimental and (d) simulated X-ray diffraction patterns of anatase TiO_2

The X-ray diffraction pattern for this model A-TiO_2-40 was simulated with material studio (V 6.1). Two extra peaks appear at $2\theta \sim 6^o$ and 8^o in the simulated X-ray diffraction pattern of A-TiO_2-40 (Figure 5.8). The observed broad peak of A-TiO_2-40 at $2\theta \sim 7°$ could be a combination of these two peaks. The agreement between the simulated and the observed diffractogram

indicates that the model describes the structure of molecular doped TiO_2 very well, and the result indicates indirectly that the Ti and the phthalate molecule were linked by chemical bonding instead of physically mixing together. Therefore, the materials exhibit a new type of doping by chemically associated molecules, and we refer to the material as a "molecule-doped" TiO_2.

5.3.2 BET measurements

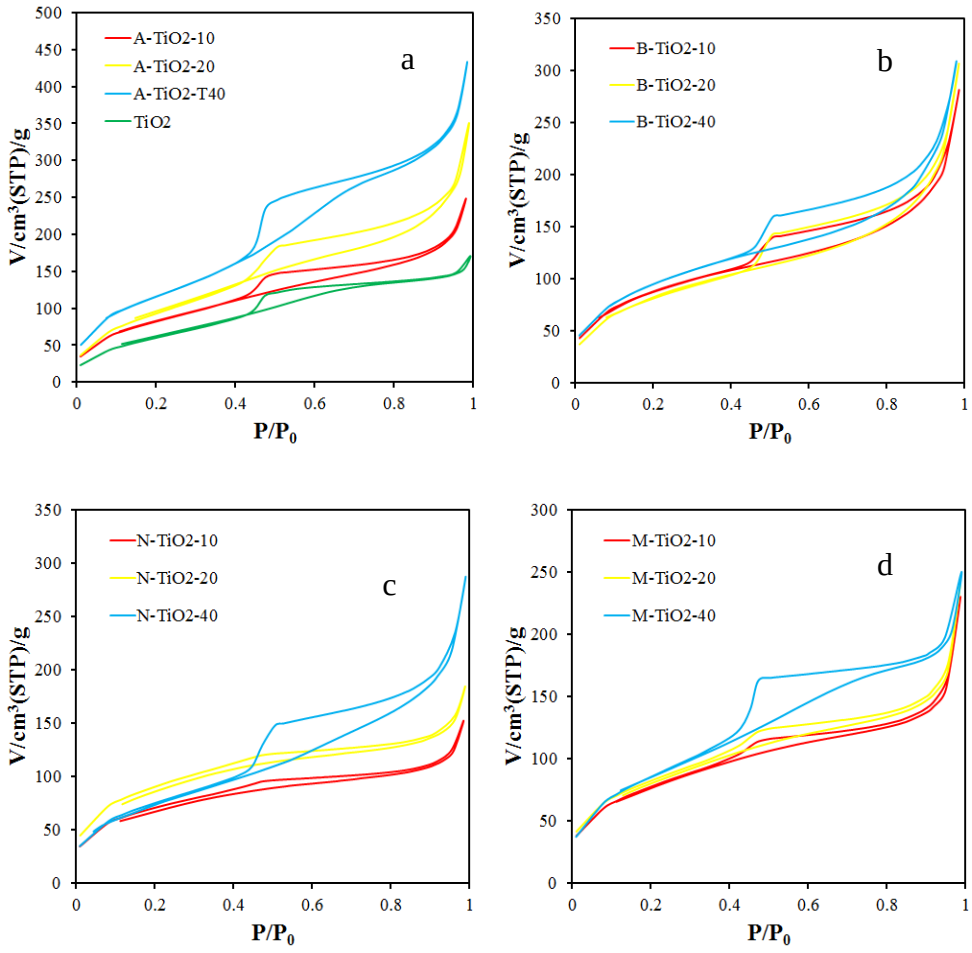

Figure 5.9 N_2 Adsorption/desorption isotherms of (a) A-TiO_2-x, (b) B-TiO_2-x, (c) N-TiO_2-x and (d) M-TiO_2-x.

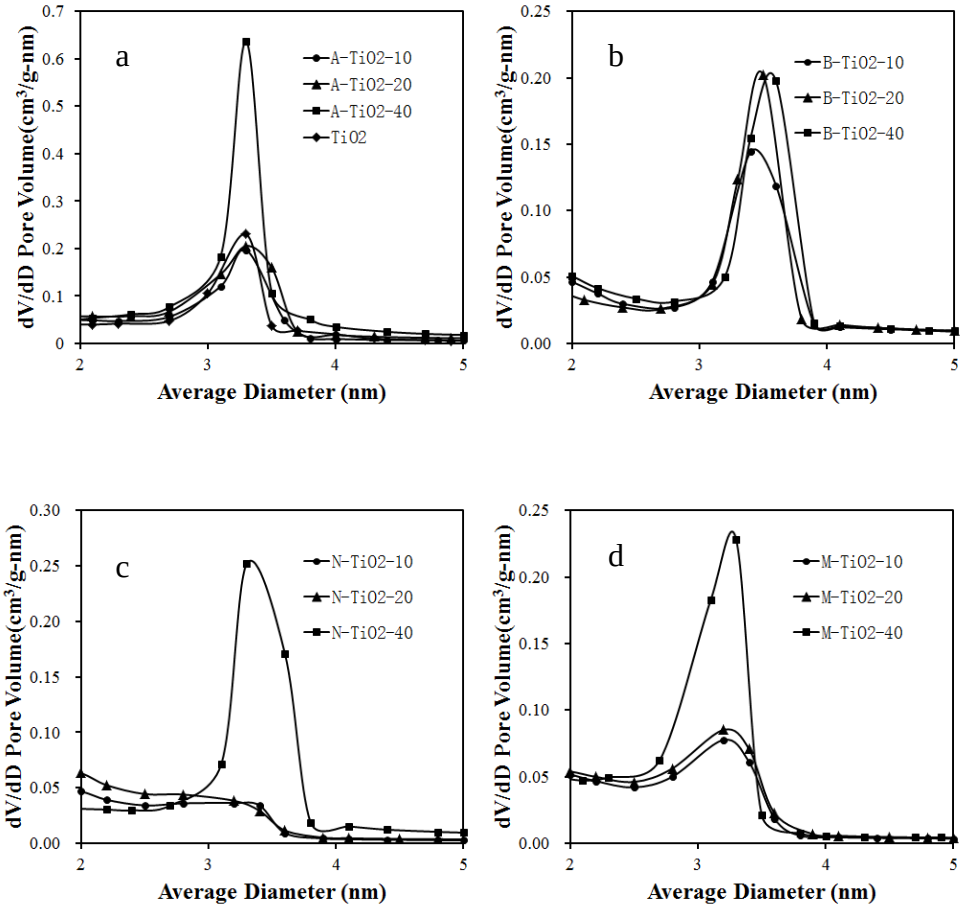

Figure 5.10 Pore size distributions of (a) A-TiO_2-x, (b) B-TiO_2-x, (c) N-TiO_2-x and (d) M-TiO_2-x.

The nitrogen adsorption-desorption isotherms and pore size distribution of the TiO_2 and different molecule-doped TiO_2 samples are given in Figure 5.9 and Figure 5.10, respectively. In addition, the values of surface area, pore volume, micropore volume and pore size distribution of TiO_2, A-TiO_2-x, B-TiO_2-x, N-TiO_2-x and M-TiO_2-x are listed in Table 5.1.

Table 5.1 Surface area, pore volume, micropore volume and pore size distribution of TiO_2, A-TiO_2-x, B-TiO_2-x, N-TiO_2-x and M-TiO_2-x.

Samples	surface area (m^2/g)	Total pore volume (cm^3/g)	Micropore volume (cm^3/g)	Pore size distribution (nm)
TiO_2	289	0.264	0	3.3
A- TiO_2-10	305	0.385	0.001	3.3
A- TiO_2-20	347	0.543	0	3.3
A- TiO_2-40	485	0.670	0	3.3
B- TiO_2-10	298	0.435	0.005	3.2
B- TiO_2-20	349	0.475	0	3.5
B- TiO_2-40	383	0.477	0	3.6
N- TiO_2-10	228	0.236	0.005	-
N- TiO_2-20	307	0.286	0	-
N- TiO_2-40	280	0.446	0	3.3
M- TiO_2-10	284	0.356	0	3.2
M- TiO_2-20	294	0.371	0	3.2
M- TiO_2-40	321	0.446	0	3.3

All materials exhibit type IV isotherms, and a hysteresis loop from P/P_o of 0.5 to ~ 0.9 indicates the presence of mesopores between 2.0 to 6.0 nm. The

isotherms of the pure TiO_2 sample show relatively low nitrogen adsorption or desorption compared to doped A-TiO_2-x and B-TiO_2-x (Figure 5.1a). It has a total pore volume of 0.269 cm^3/g with a surface area of 289 m^2/g, but its total pore volume and surface area are still much higher than P25 (a commercial TiO_2). Generally, with increase of Ti/doped molecule ratio (i.e., with decreasing amount of linker in the composite), the molecule-doped TiO_2 shows a strong trend towards higher total pore volume and surface area. Among these materials, the total pore volume and surface area of A-TiO_2-x increased significantly from 0.385 to 0.670 cm^3/g and from 305 to 485 m^2/g, respectively.

5.3.3 SEM images

Figure 5.11 shows SEM images of TiO_2 and molecule-doped TiO_2. Pure TiO_2 was composed of granular particles with various sizes up to 6 μm, while the SEM images of molecule-doped TiO_2 suggested an interesting structure that the most molecular doped TiO_2 particles were formed from an aggregation of bun-like small particles with sizes around 200 - 800 nm. A-TiO_2-10, A-TiO_2-40 and N-TiO-10 displayed a poorly defined “bun-like” structure. B-TiO_2-20, B-TiO_2-40, N-TiO_2-10 and N-TiO_2-20 showed nano-ribbons that decorated the surface.

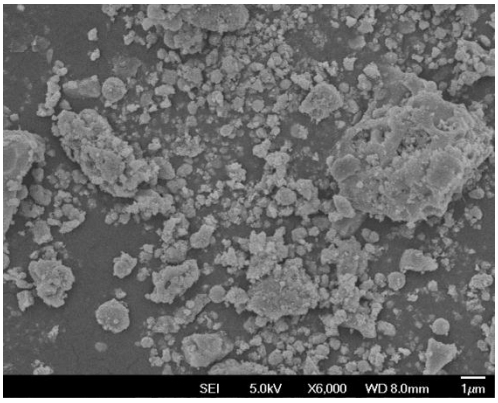
SEI 5.0kV X6,000 WD 8.0mm 1μm

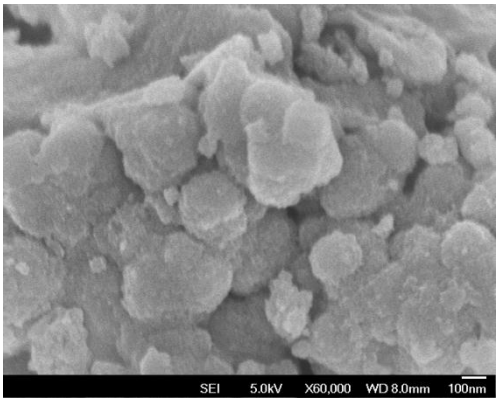
SEI 5.0kV X60,000 WD 8.0mm 100nm

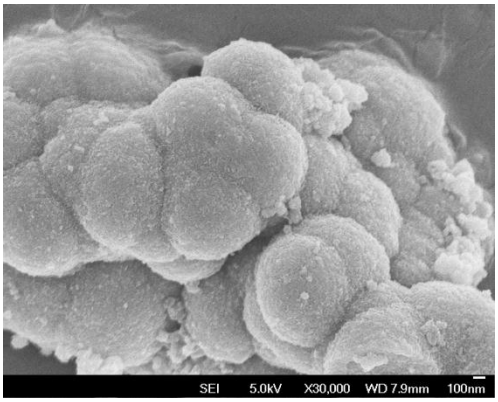
SEI 5.0kV X30,000 WD 7.9mm 100nm

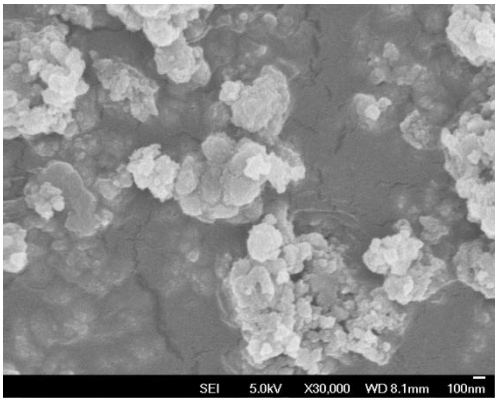
SEI 5.0kV X30,000 WD 8.1mm 100nm

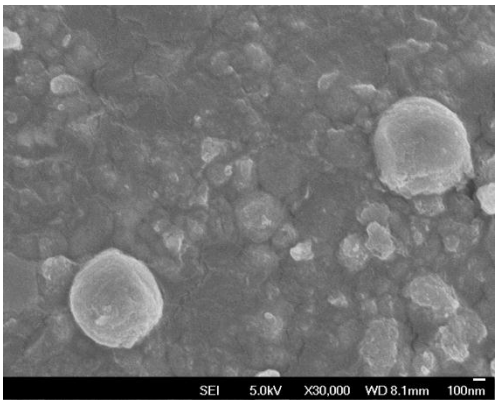
SEI 5.0kV X30,000 WD 8.1mm 100nm

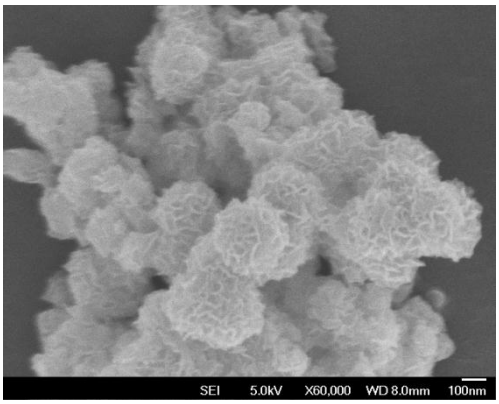
SEI 5.0kV X60,000 WD 8.0mm 100nm

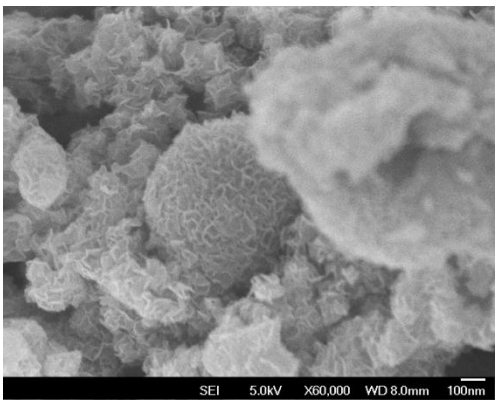
SEI 5.0kV X60,000 WD 8.0mm 100nm

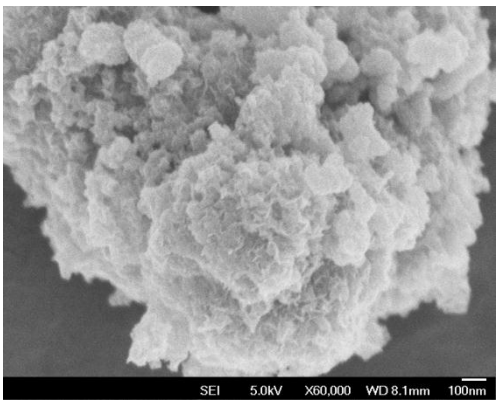
SEI 5.0kV X60,000 WD 8.1mm 100nm

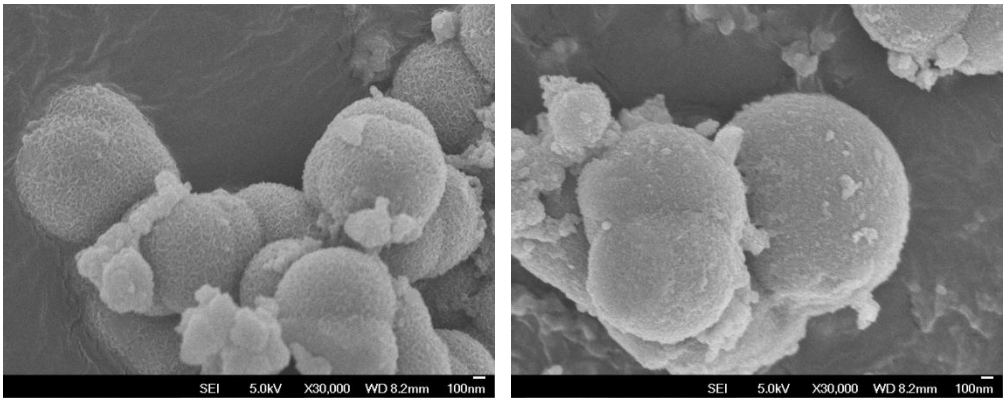

Figure 5.11 SEM images of (a) TiO_2, (b) A-TiO_2-10, (c) A-TiO_2-20, (d) A-TiO_2-40, (e) B-TiO_2-10, (f) B-TiO_2-20, (g) B-TiO_2-40, (h) N-TiO_2-10, (i) N-TiO_2-20 and (j) N-TiO_2-40.

5.3.4 UV-vis diffuse reflectance spectra

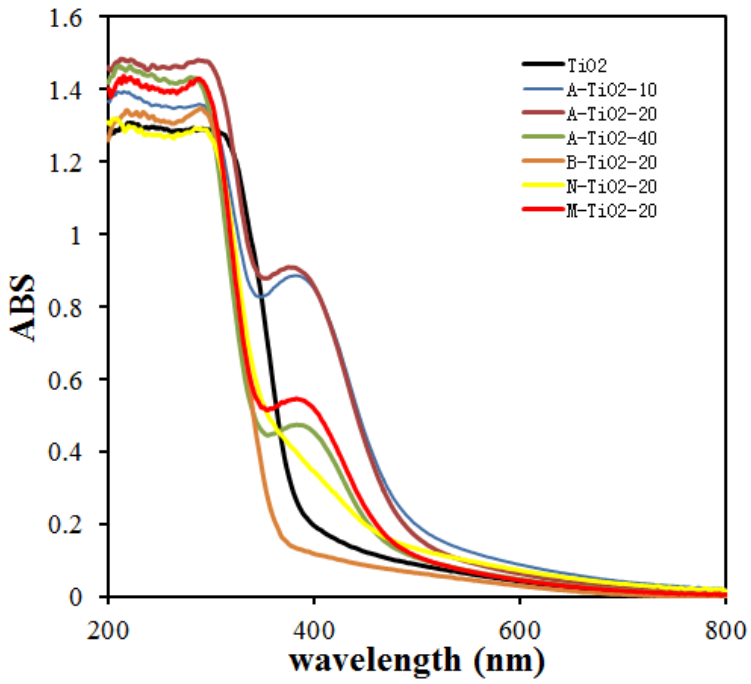

Figure 5.12 DRS of TiO_2, A-TiO_2-10, A-TiO_2-20, A-TiO_2-40, B-TiO_2-20, N-TiO_2-20 and M-TiO_2-20.

The UV-vis diffuse reflectance spectra were measured to study the optical properties of TiO_2 and molecule-doped TiO_2, and some of the results are plotted in Figure 5.12. Compared with other molecule-doped TiO_2, A-TiO_2-x shows a strong adsorption in the visible range with an edge at 550 nm and a long tail extending to 700 nm. This absorption is attributed to the amino group, an electron donating group, which can activate linker to get an easy access of electron excitation.

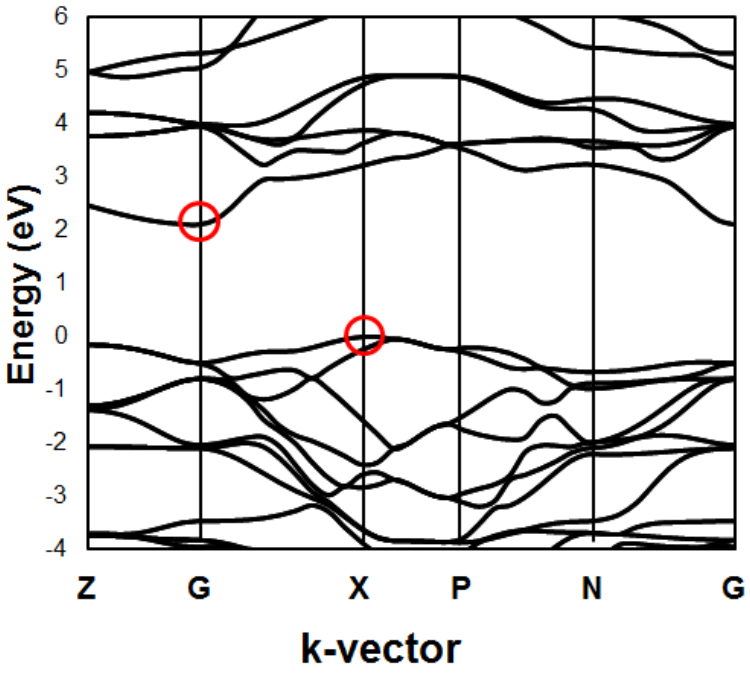

Figure 5.13 Calculated band structure for anatase TiO_2 using Density Functional Theory (CASTEP code).

The electronic band structure was calculated with Density Functional Theory using the CASTEP code (see Figure 5.13). The lowest unoccupied states are

found near the G point, but the highest occupied state is at the X direction. The calculation confirms that the band structure of TiO_2 has an indirect band gap, as reported in previous studies [23, 24].

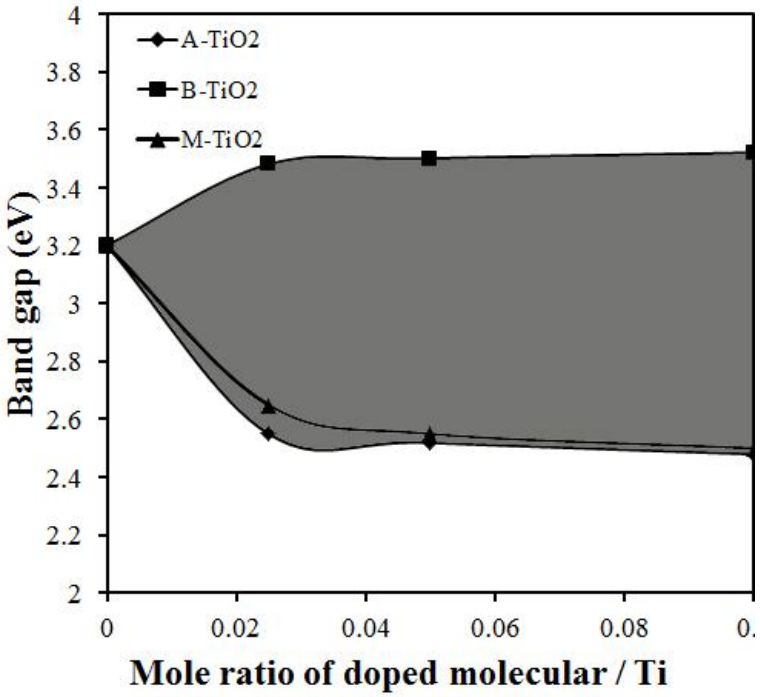

Figure 5.14 Band gap values with different mole ratio of doped molecular to Ti.

Figure 5.14 illustrates the plot of band gap values with different mole ratio of doped molecular to Ti. Any point in the gray area of Figure 5.14 can be obtained by using different ratio of 2-aminoterephthalic acid and terephthalic acid as doped molecular. M-TiO_2-x was synthesized to examine the above prediction, and the band gap of M-TiO_2-x was indeed located in between that of A-TiO_2-x and B-TiO_2-x. Therefore, any band gap from 2.48 to 3.52 eV can

be obtained by adjusting the ratio of 2-nitroterephthalic acid to terephthalic acid. The band gaps determined from the onset of the optical absorption for TiO_2, A-TiO_2-x, B-TiO_2-x, N-TiO_2-x and M-TiO_2-x were listed in Table 5.2.

Table 5.2 Band gap values of TiO_2, A-TiO_2-x, B-TiO_2-x, N-TiO_2-x and M-TiO_2-x.

Samples	Band gap (eV)	Samples	Band gap (eV)
TiO_2	3.2		
A-TiO_2-10	2.48	B-TiO_2-10	3.52
A-TiO_2-20	2.52	B-TiO_2-20	3.50
A-TiO_2-40	2.55	B-TiO_2-40	3.48
N-TiO_2-10	3.42	M-TiO_2-10	2.50
N-TiO_2-20	3.45	M-TiO_2-20	2.55
N-TiO_2-40	3.48	M-TiO_2-40	2.65

5.3.5 Photocatalytic activity

RhB was employed to examine the photocatalytic activity of molecule-doped TiO_2 under irradiation with visible light ($\lambda \geq 400$ nm). Figure 5.15 shows the photocatalytic degradation of RhB in the presence of different catalysts. There is almost no photodegradation in the absence of photocatalyst after 120 min visible light irradiation, indicating that by itself, RhB is stable enough.

Compared with Degussa's P25 (a commercial TiO_2), the molecule-doped TiO_2 showed a competitive photocatalytic activity. Among them, A-TiO_2-20 displayed the best performance, due to the fact that the amino group in A-TiO_2-20 lowers its band gap with raising the utilization of photon.

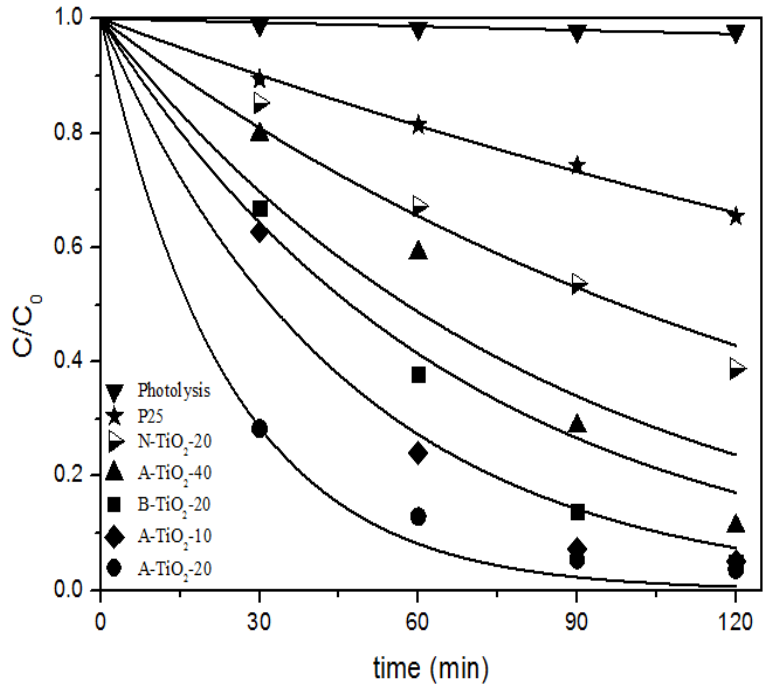

Figure 5.15 Photocatalytic degradation of RhB in the presence of different catalysts.

The kinetics of RhB degradation can be quantitatively fitted by a pseudo-first-order model as expressed by the following equation:

$$\ln\left(\frac{c_0}{c}\right) = kt \qquad (5.1)$$

where k is the pseudo-first-order rate constant.

The pseudo-first-order rate constants of P25, A-TiO_2-x, B-TiO_2-x, N-TiO_2-x and M-TiO_2-x are listed in Table 5.3. The reaction rate of A-TiO_2-20 is about 10 times faster than Degussa's P25 under identical illumination conditions.

Table 5.3 Pseudo-first-order rate constants of P25, A-TiO_2-x, B-TiO_2-x, N-TiO_2-x and M-TiO_2-x.

Samples	k (min^{-1})
P25	0.0015
A-TiO_2-10	0.0116
A-TiO_2-20	0.0146
A-TiO_2-40	0.0052
B-TiO_2-10	0.0136
B-TiO_2-20	0.0098
B-TiO_2-40	0.0056
N-TiO_2-10	0.003
N-TiO_2-20	0.0032
N-TiO_2-40	0.0036

5.3.6 The effect of some radical scavengers and N_2 purging

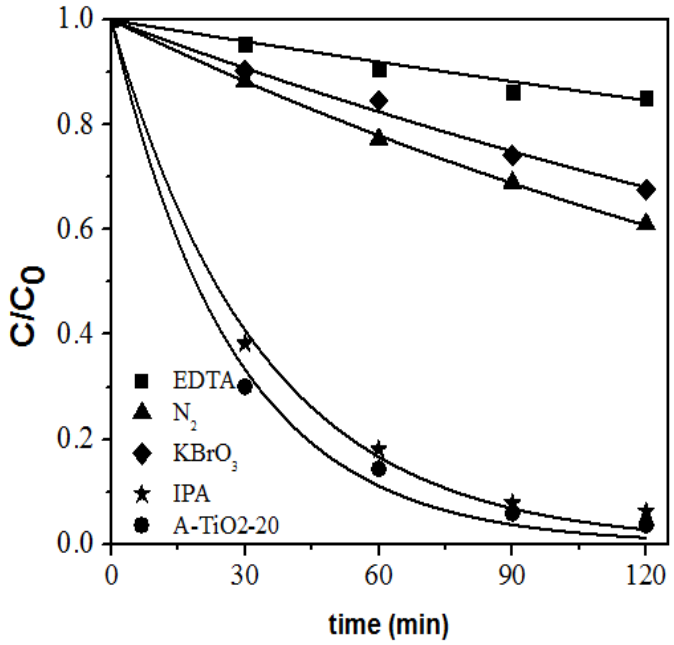

Figure 5.16 Effect of various scavengers and N_2 purging on the degradation of RhB using A-TiO_2-20 as catalyst.

In order to better understand the reaction mechanism, the effect of various scavengers and N_2 purging on the degradation of RhB using A-TiO_2-20 as catalyst are studied and shown in Figure 5.16. 2-Propanol (IPA) is a well-known scavenger of HO• radicals [25], but no significant change of the photoactivity was observed after adding IPA in this study. Therefore, A-TiO_2-20 cannot generate HO• radical in photodegradation. EDTA is always employed to block holes. There is almost no reaction after adding EDTA [26], indicating that the photo-generated hole is the most active species. In addition, the O_2^-• radical could be another active species. O_2^-• radical capture

experiment was carried out by adding $KBrO_3$ to detect the existing of O_2^{-}• radical. Being a strong oxidant, $KBrO_3$ is an effective electron acceptor which competes with oxygen [27, 28]. The result suggests that the addition of $KBrO_3$ greatly affected the photodegradation efficiency of RhB. To further prove the role of O_2^{-}• radical, a N_2 purging experiment was conducted. A similar result was obtained, the degradation efficiency decreased to 40% after 2 h due to the O_2^{-}• radical cannot be formed in the absence of O_2. Therefore, the O_2^{-}• radical was proved as one of the active species.

5.3.7 The test of reusability

The stability of A-TiO_2-20 was investigated by studying XRD pattern of the fresh and used A-TiO_2-20, as shown in Figure 5.17. There is no apparent variation in XRD pattern of A-TiO_2-20 before and after the RhB photodegradation.

The reusability experiment was carried out by collecting the A-TiO_2-20 after each cycle and then adding it for the next cycle. Furthermore, three cycles had been studied, Figure 5.18 shows that there is no significant loss in the photocatalytic activity for each cycle. A-TiO_2-20 showed high stability and reusability according to above results.

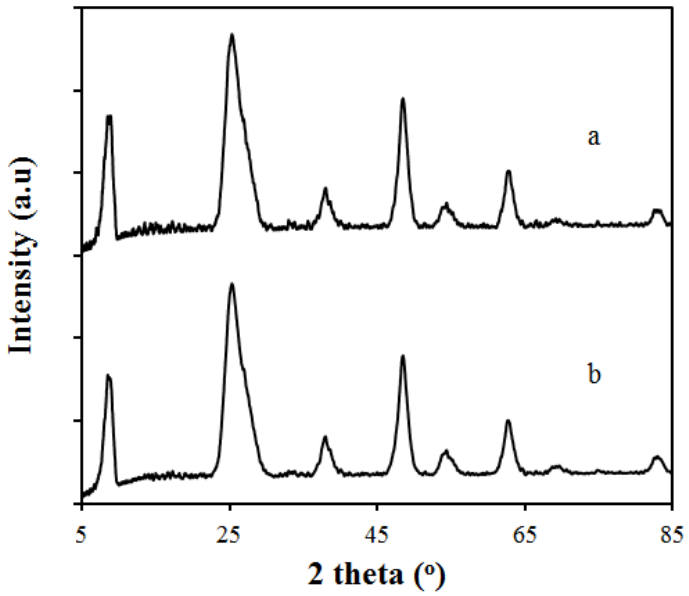

Figure 5.17 XRD patterns of the fresh A-TiO_2-20 and used A-TiO_2-20.

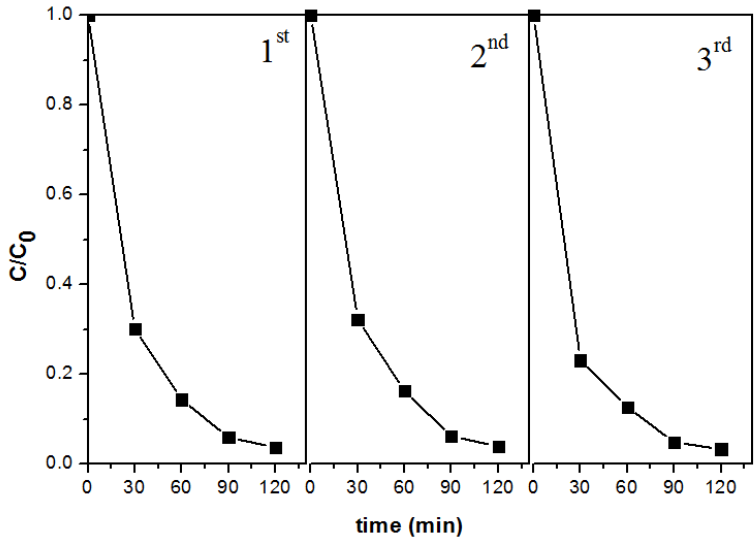

Figure 5.18 Three cycles of the RhB degradation in the presence of A-TiO_2-20 under visible light irradiation.

5.3.8 Visible light-driven 2-aminoterephthalic doped BiOCl

From the above discussion, the molecular doping leads to a controllable band gap and high surface area. To examine the universal principle of molecular doping, 2-aminoterephthalic doped BiOCl was synthesized by a similar preparation method. The X-ray diffraction patterns (Figure 5.19) obtained from A-BiOCl-10 agreed well with the patterns of BiOCl (JPCDS No.06-0249). Therefore, the preparation method of molecular doping can be employed to synthesize other materials.

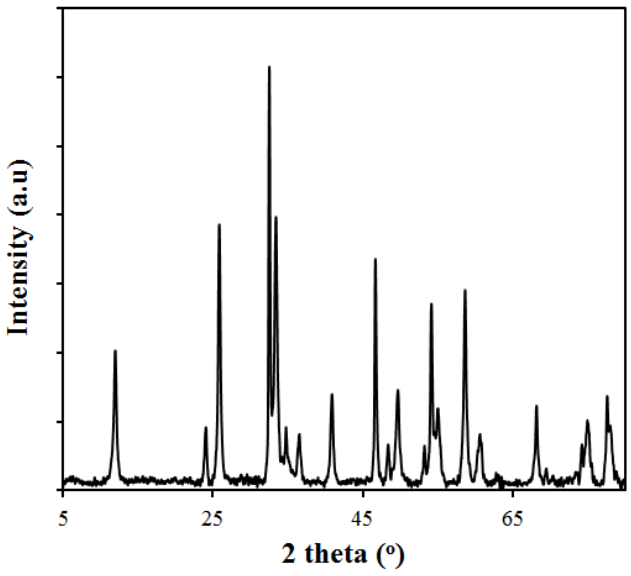

Figure 5.19 X-ray diffraction patterns obtained from A-BiOCl-10.

The N_2 adsorption–desorption isotherms of the A-BiOCl-10 and pore size distribution are shown in Figure 5.20. A-BiOCl-10 exhibits a type VI isotherm

with the presence of mesopores. The surface area and total pore volume of A-BiOCl-10 are 25 m^2/g and 0.13 cm^3/g, respectively.

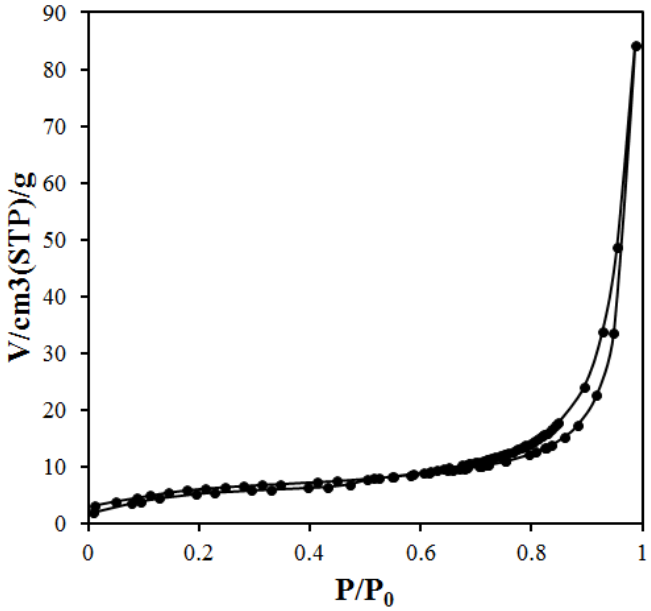

Figure 5.20 Nitrogen adsorption–desorption isotherms of A-BiOCl-10.

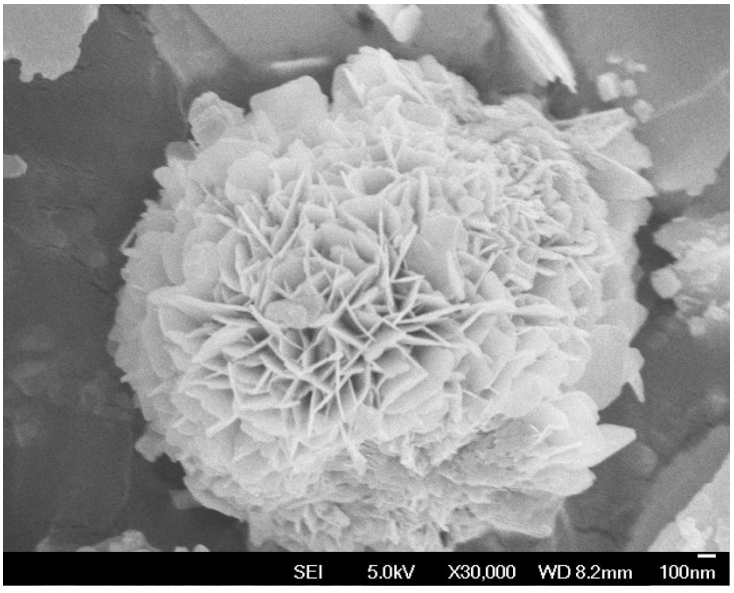

Figure 5.21 FESEM images of the as-synthesized A-BiOCl-10.

The morphology of A-BiOCl-10 was investigated in a scanning electron microscope, and a typical image is given in Figure 5.21. A flower-like particle with a diameter of ~1 μm was obtained, and the particle is formed due to the fact of aggregation of BiOCl nano plates.

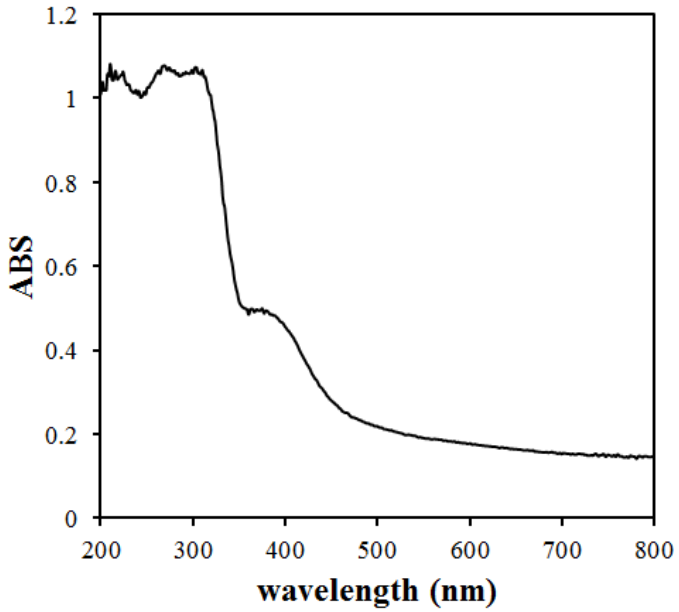

Figure 5.22 DRS of the as-synthesized A-BiOCl-10.

The result of UV-vis diffuse reflectance spectra is given in Figure 5.22. A-BiOCl-10 showed a strong adsorption in the range of visible light with the edge at ~ 550 nm and a long tail extending to IR range, and this tail could be attributed to oxygen vacancies in the crystal structure of A-BiOCl-10. The result of UV-vis diffuse reflectance spectra suggests that there is a competitive adsorption in IR range for A-BiOCl-10. The result of RhB photodegradation under irradiation of IR with IR filter is shown in Figure 5.24 (5.6 Appendix).

The pathways and mechanism of RhB photodegradation were investigated, the results are given in Figure 5.25 – 5.27 (5.6 Appendix).

5.4 Conclusion

In summary, the molecular doping as a novel concept has been demonstrated for the first time. This method opens an opportunity to purposefully design photocatalyst with desired band gap. In addition, the molecular doping improved the porosity of the material and greatly increased the surface area. The molecule-doped TiO_2 showed a controllable band gap, mesoporous structure with a high surface area up to ~ 500 m^2/g. The photocatalytic activity of TiO_2 was intensively enhanced. The versatility of this method was confirmed by preparing molecule-doped BiOCl by a similar strategy. The properties of the obtained material agree well with the expectation. Therefore, molecular doping provides valuable insight in designing novel photocatalyst.

5.5 References

[1] X. Chen, S. Shen, L. Guo, S.S. Mao, Chem. Rev., 110 (2010) 6503.

[2] X. Chen, A. Selloni, Chem. Rev., 114 (2014) 9281.

[3] L. Sang, Y. Zhao, C. Burda, Chem. Rev., 114 (2014) 9283.

[4] J. Schneider, M. Matsuoka, M. Takeuchi, J. Zhang, Y. Horiuchi, M. Anpo, D.W. Bahnemann, Chem. Rev., 114 (2014) 9919.

[5] J. Zhu, F. Chen, J. Zhang, H. Chen, M. Anpo, J. Photoch. Photobio. A, 180 (2006) 196.

[6] H. Liu, Y. Wu, J. Zhang, ACS Appl. Mater. Inter., 3 (2011) 1757.

[7] J. Zhu, Z. Deng, F. Chen, J. Zhang, H. Chen, M. Anpo, J. Huang, L. Zhang, Appl. Catal. B-Environ., 62 (2006) 329.

[8] N. Hamzah, N.M. Nordin, A.H.A. Nadzri, Y.A. Nik, M.B. Kassim, M.A. Yarmo, Appl. Catal. A, 419-420 (2012) 133.

[9] H. Gao, W. Liu, B. Lu, F. Liu, J. Nanosci. Nanotechnol., 12 (2012) 3959.

[10] S. Yuan, Y. Chen, L. Shi, J. Fang, J. Zhang, J. Zhang, H. Yamashita, Mater. Lett., 61 (2007) 4283.

[11] R. Asahi, T. Morikawa, T. Ohwaki, K. Aoki, Y. Taga, Science, 293 (2001) 269.

[12] M.Y. Xing, D.Y. Qi, J.L. Zhang, F. Chen, Chem-Eur. J., 17 (2011) 11432.

[13] M.V. Dozzi, S. Livraghi, E. Giamello, E. Selli, Photoch. Photobio. Sci., 10 (2011) 343.

[14] Y. Kuwahara, K. Maki, Y. Matsumura, T. Kamegawa, K. Mori, H. Yamashita, J. Phys. Chem. C, 113 (2009) 1552.

[15] K. Yang, Y. Dai, B. Huang, J. Phys. Chem. C, 111 (2007) 18985.

[16] X. Wang, M. Blackford, K. Prince, R.A. Caruso, ACS Appl. Mater. Inter., 4 (2012) 476.

[17] K.-L. Zhang, C.-M. Liu, F.-Q. Huang, C. Zheng, W.-D. Wang, Appl. Catal. B-Environ., 68 (2006) 125.

[18] Q. Wang, J. Hui, Y. Huang, Y. Ding, Y. Cai, S. Yin, Z. Li, B. Su, Mater. Sci. Semicond. Process., 17 (2014) 87.

[19] Y. Wang, Z.-q. Shi, C.-m. Fan, X.-g. Hao, G.-y. Ding, Y.-f. Wang, Int. J. Miner. Metall. Mater., 19 (2012) 467.

[20] S. Shenawi-Khalil, V. Uvarov b, E. Menes, I. Popov, Y. Sassona, Appl. Catal. A, 413-414 (2012) 1.

[21] H. Zhang, R. Zong, J. Zhao, Y. Zhu, Environ. Sci. Technol., 42 (2008) 3803.

[22] T.B. Li, G. Chen, C. Zhou, Z.Y. Shen, R.C. Jin, J.X. Sun, Dalton Trans., 40 (2011) 6751.

[23] R. Asahi, Y. Taga, W. Mannstadt, A.J. Freeman, Phys. Rev. B, 61 (2000) 7459.

[24] C. Qiang, C. Hong-Hong, Chin. Phys., 13 (2004) 2121.

[25] C. Shifu, J. Lei, T. Wenming and F. Xianliang, Dalton Trans., 42 (2013) 10759.

[26] S. Shenawi-Khalil, V. Uvarov, S. Fronton, I. Popov and Y. Sasson, Appl. Catal. B: Environ., 117-118 (2012) 148.

[27] Y. Oosawa, M. Gratzel, J. Chem. Soc., Perkin Trans. 1, 84 (1988) 197.

[28] S. Song, L. Xu, Z. He, J. Chen, X. Xiao, B. Yan, Environ. Sci. Technol.,

41 (2007) 5846.

5.6 Appendix

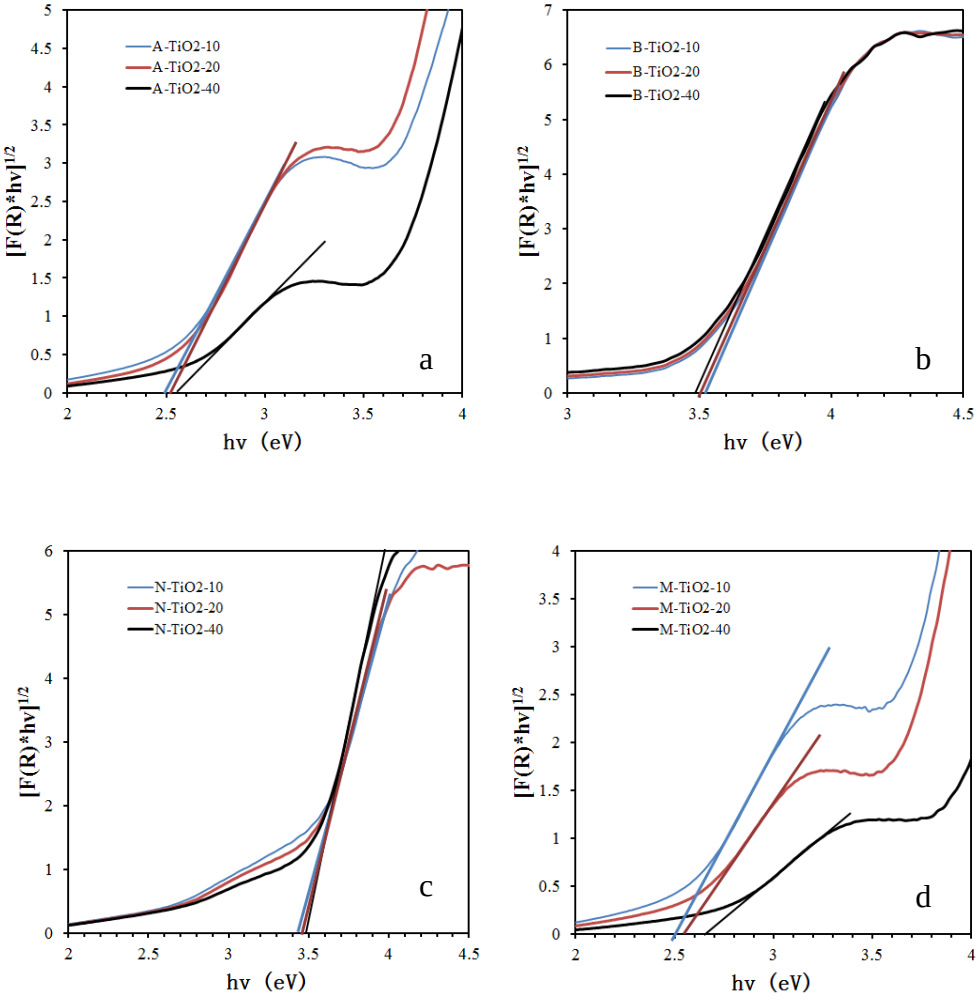

Figure 5.23 Diffuse reflectance spectra of (a) A-TiO2-x, (b) B-TiO2-x, (c) N-TiO2-x and (d) M-TiO2-x and deduction of their band gap.

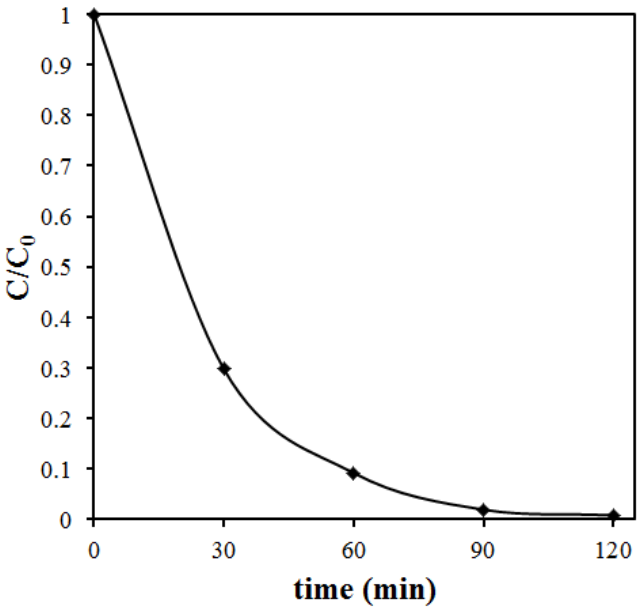

Figure 5.24 Photocatalytic degradation of RhB under irradiation of IR light over A-BiOCl-10.

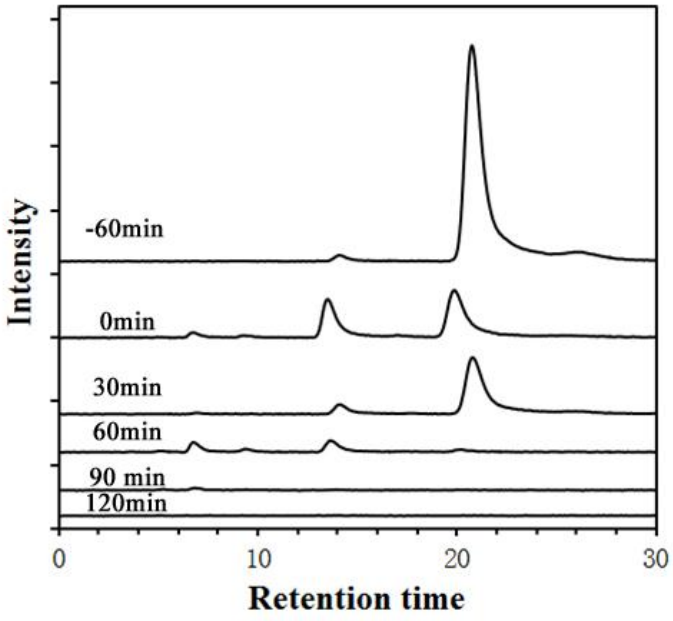

Figure 5.25 HPLC chromatograms of the N-deethylated intermediates monitored at 520 nm at -60, 0, 30, 60, 90, and 120 min.

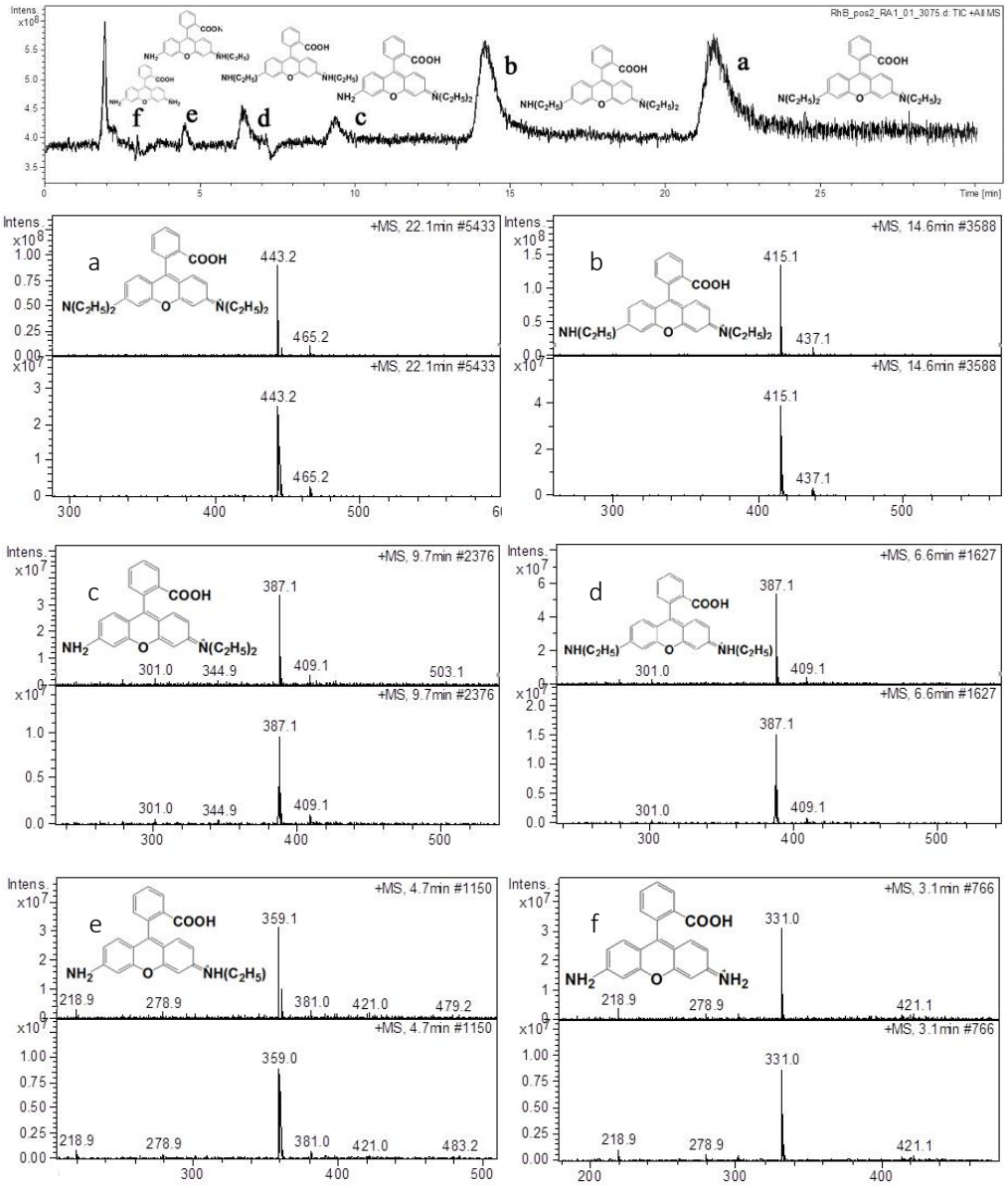

Figure 5.26 MS spectra of N-deethylated intermediates that generated in the photodegradation process. (a) RhB, (b) DER, (c) DR, (d) EER, (e) ER, (f) R.

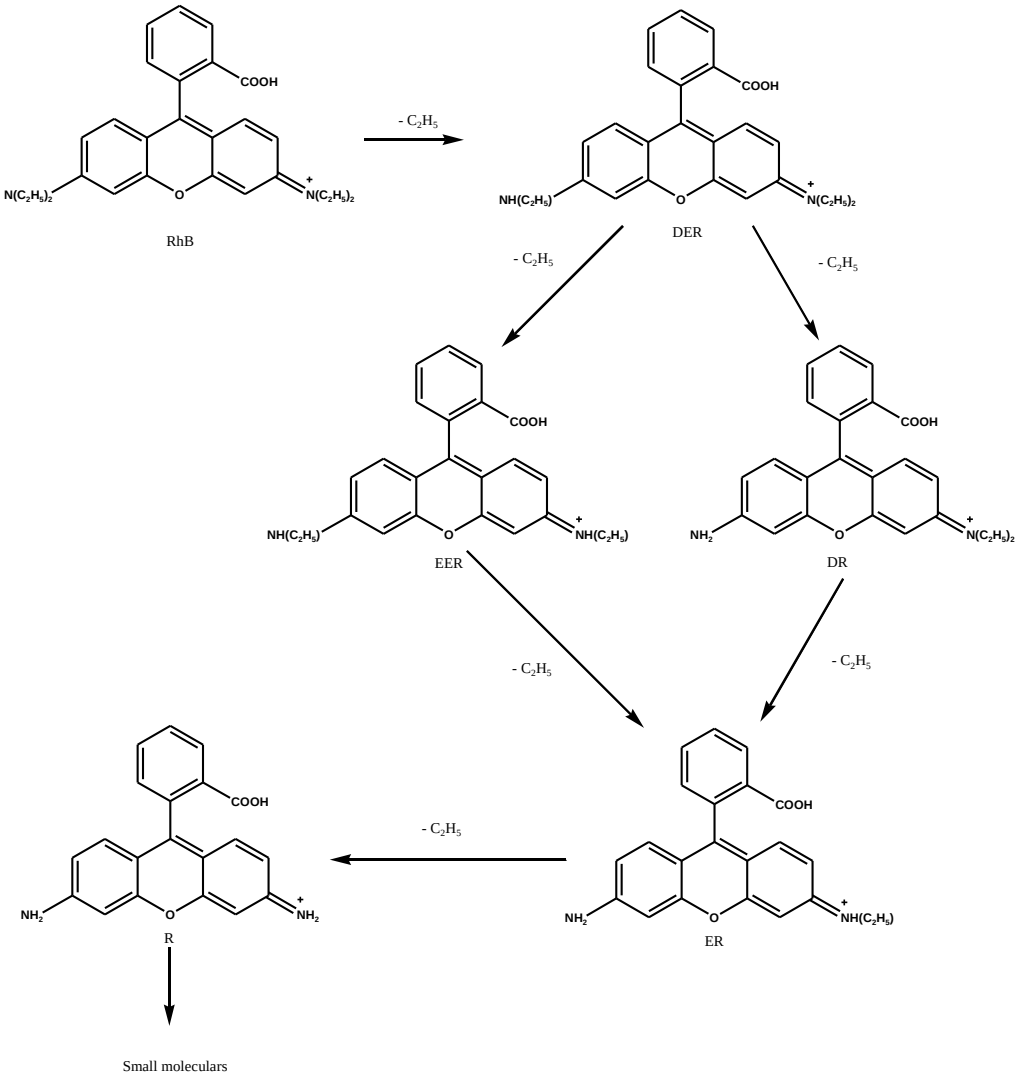

Figure 5.27 Proposed photodegradation pathway of RhB under irradiation of visible light

Chapter 6. Heterojunctions Between a Ti-containing Metal Organic Framework Material and TiO_2 Nanosheets with Unprecedented Photocatalytic Activity

6.1 Introduction

As catalysts, MOFs are limited in high temperature applications due to the organic component. On the other hand, the organic moiety can be used advantageously as light harvesters with excellent optical tunability [1]. The optical transition is due to electron transfer from the photoexcited ligand to the metal oxo cluster (LMCT) [2, 3]. In particular, the titanium-based MOF, MIL-125, is of interest due to the combination of both photocatalytically active terephthalic acid and titanium oxo clusters [4]. However, both the terephthalic linkers and titanium oxo cluster only absorb light in the uv region. Since visible light constitutes ~ 50 % of the solar energy, it is important that photocatalysts can utilize radiation in this region as compared to the 3 - 5 % that fall in the uv region. The functionalization of terephthalic acid with an amine group extends the light absorption into the visible region [5]. Introduction of amine to the ligand decreases the band gap of the MOF due to the interaction of the lone pair of electrons on nitrogen with the π^* orbitals of benzene ring. Further modification of NH_2-MIL-125(Ti) by diazotization

followed by reaction with diethylaniline yielded methyl red-MIL-125(Ti) which absorbs light over a wide range of the visible spectrum [6]. In above study, Nasalevich et al. stated that the MIL-125(Ti) series should be seen as a HOMO-LUMO formalism, because the distance between linkers of MIL-125(Ti) is around 7 Å and no efficient p–p stacking in order to keeping the electrons preferentially in a localized state. The photoactivities of visible-light driven MOFs in hydrogen production, carbon dioxide reduction, photochemical synthesis, and dye degradation have been reported [2, 7-11]. Theoretical calculations suggest that MOFs are semiconductors or insulators with band gaps that are mainly determined by the highest occupied molecular orbital (HOMO)-lowest unoccupied molecular orbital (LUMO) gaps of the linker molecules [9, 12]. The highest occupied valence bands (VB) are dominated by the contribution of the *p* atomic orbitals of carbon atoms of the aromatic rings with a small contribution of the carboxylate atoms [13]. To improve the electron-hole separation, we envisage building a composite with a tight heterojunction between the light harvesting organic linker and TiO_2. This can be carried out by extending the titanium oxo clusters to nanoplatelets. The electron can be rapidly transported away in the TiO_2 if the site of the charge photogeneration is at the junction of the linker and TiO_2.

Herein, we report a facile route for the preparation of a Ti MOF/TiO_2 heterojunctioned composite via a one-pot solvothermal treatment. From field

emission scanning electron micrographs (FESEM), it can be seen that NH_2-MIL 125(Ti) forms crystallites of ~ 200 – 350 nm with smooth surfaces. In contrast, the surfaces of the heterojunction samples are decorated with nanoribbons which are ~ 8.2 nm thick. TEM measurements show that the lattice fringes are due to (1 0 1), (1 0 3), (1 1 2) and (2 0 0) facets of anatase phase TiO_2. The structure of NH_2-MIL-125 consists of cyclic octamers of corner- and edge-sharing $TiO_5(OH)$ octahedra (Figure 6.1). The octamers are arranged in a face centered cubic packing and linked by 2-aminoterephthalic acid (bdc-NH_2) linkers. With higher amounts of tetraisopropyl titanate, TiO_6 octahedra can grow on the cyclic octamers to form the 2-dimensional TiO_2 nanoribbons.

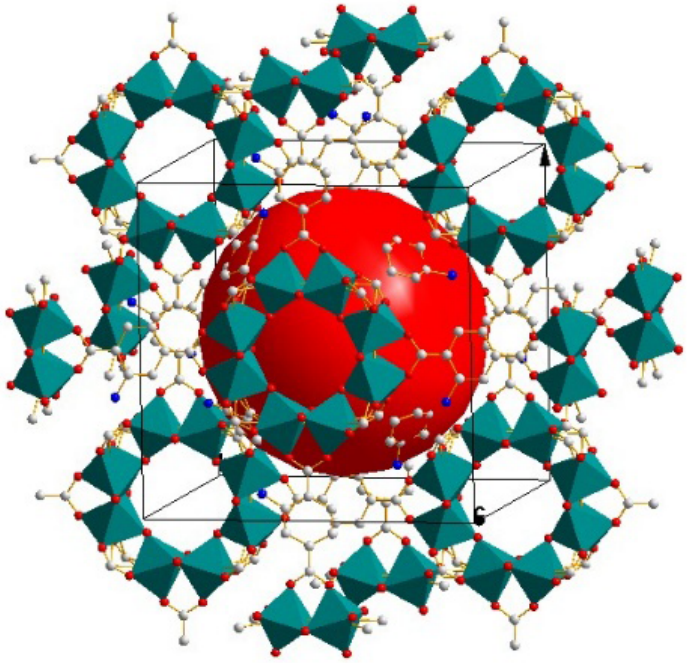

Figure 6.1 A schematic polyhedra drawing of NH_2-MIL-125 (Ti)

6.2 Experimental

6.2.1 Materials

The NH_2-MIL-125(Ti) was synthesized following Chapter 4.

To prepare NH_2-MIL-125 (Ti)/TiO_2 materials, the amount of $Ti(OCH(CH_3)_2)_4$ were increased to 1.5, 3 and 6 mmol, respectively. The samples are denoted as T-M-0.5, T-M-1, T-M-2 where T = titania, M = MIL-125 and the last number represents the molar ratio of Ti/2-aminoterepthalic acid.

6.2.2 Characterization

The diffractograms of XRD were recorded for 2θ between 5 ° to 85 °.

Prior to the measurements, the sample was degassed under N_2 at 130 ^oC for 4 h in N_2 adsorption–desorption test. The carbon, nitrogen and hydrogen content of the samples was determined by automated elemental analysis (Vario Micro Cube, Elementar Analysensysteme GmbH, Hanau, Germany).

The photoelectrical properties were determined with an IviumStat.XR potentiostat (Ivium Technologies). The working electrode was prepared on ITO glass (purchase from Singapore optics shop, 25.0 x 25.0 x 1.1mm, 8.0 - 10.0 Ohm/sq). The ITO glass was first cleaned by sonication in acetone, isopropanol and deionized water for 5 min each before drying at 80^oC. A slurry of 5 mg sample in 0.5 mL water was sonicated for 30 min. The ITO

glass was protected on one side with insulating tape while the other side was coated with 40 μL of the slurry, carefully placed on about 0.25 cm^2. A three electrode system was employed for the electrochemical measurements, using Pt and 1 M Ag/AgCl electrode as counter electrode and reference electrode, respectively. The setup of electrochemical measurements in the dark is illustrated in Figure 6.2.

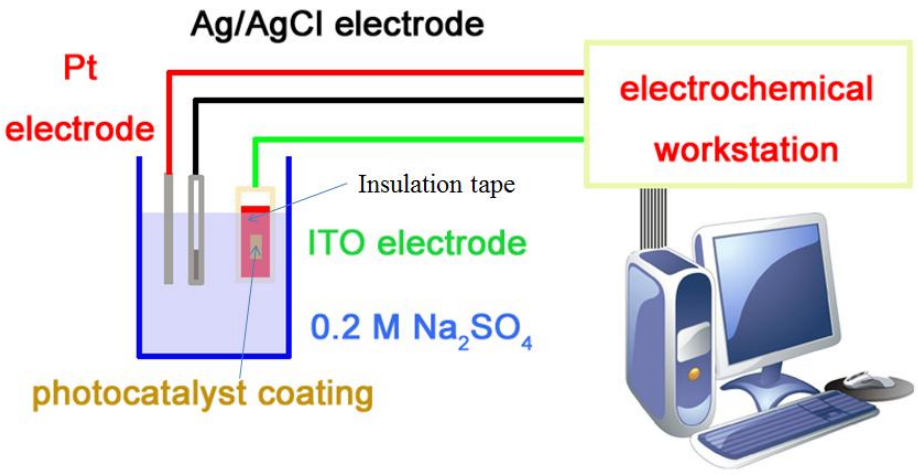

Figure 6.2 Setup of electrochemical measurements in the dark.

6.2.3 Evaluation of the photocatalytic activity

The photocatalytic activities of the pure NH_2-MIL-125 (Ti) and the heterojunctioned NH_2-MIL-125 (Ti)/TiO_2 materials were evaluated following Chapter 5. All experiments were carried out with 25 mg of the catalyst suspended in 100 ml of the aqueous RhB solution.

The used catalyst was washed with deionized water, dried overnight at 130 ^oC and tested in a fresh RhB solution. Three recycles were typically carried out.

6.2.4 Investigation of the photocatalytic mechanism

The investigation of the photocatalytic mechanism was carried out following Chapter 5.

6.3 Results and discussion

6.3.1 X-ray diffraction pattern

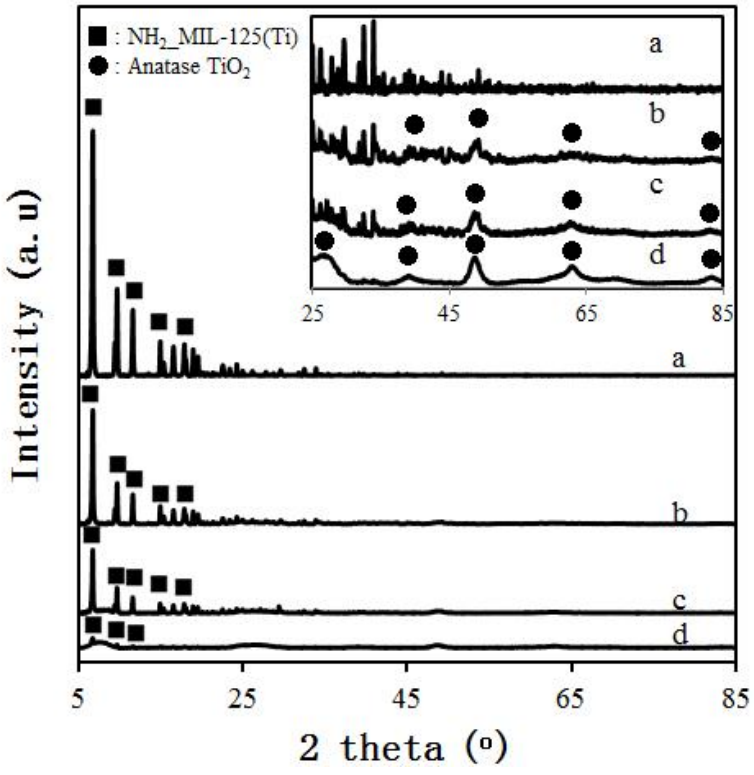

Figure 6.3 X-ray diffraction patterns obtained from as-synthesized samples, (a) NH_2-MIL-125(Ti), (b) T-M-0.5, (c) T-M-1 and (d) T-M-2.

Figure 6.3 shows the XRD patterns acquired from as-synthesized samples. Among them, T-M-0.5 shows peaks from both the MOF and TiO_2 phase. The

XRD pattern of the photocatalyst was analyzed and revealed that the sample is a mixture of two crystalline phases. One of these phases was identified as the known NH_2-MIL-125(Ti), and the other phase was identified as the anatase phase of TiO_2 (ICSD No. 9852) from the peaks at $2\theta \sim 25^o$, 48^o and 62^o. Therefore the samples were considered as heterojunctions between NH_2-MIL-125(Ti) and TiO_2

6.3.2 FESEM and TEM

In Figure 6.4, the inserts show the appearance and color of the samples with a trend of increasingly darker color. Superimposed on the micrographs are the UV-vis spectra, which show a tail into the visible range. NH_2-MIL-125(Ti) has an absorption edge at around 470 nm, while T-M-0.5, T-M-1 and T-M-2 have a relatively diffuse absorption edge at about 500, 530 and 540 nm, respectively. The FESEM micrographs show a smooth surface for pure NH_2-MIL 125(Ti), but the structure of T-M-0.5 shows nano-ribbons decorating the surface. The formation of TiO_2 nanosheets based on the MOF structure originates from the tendency of the TiO_4 octahedra to aggregate and to grow along the preferred cyclic octamer with edge and corner-sharing $TiO_5(OH)$ octahedral (green part in Figure 6.1). The thickness of the nanosheets is around 8.2 nm, which includes the Pt coating (Figure 6.4, b). Because the Ti proportion of T-M-1 and T-M-2 is much higher than that of T-M-0.5, it leads to nanosheets that are thicker and the nanosheet structure of T-M-1 and T-M-2 is not as pronounced

as in T-M-0.5.

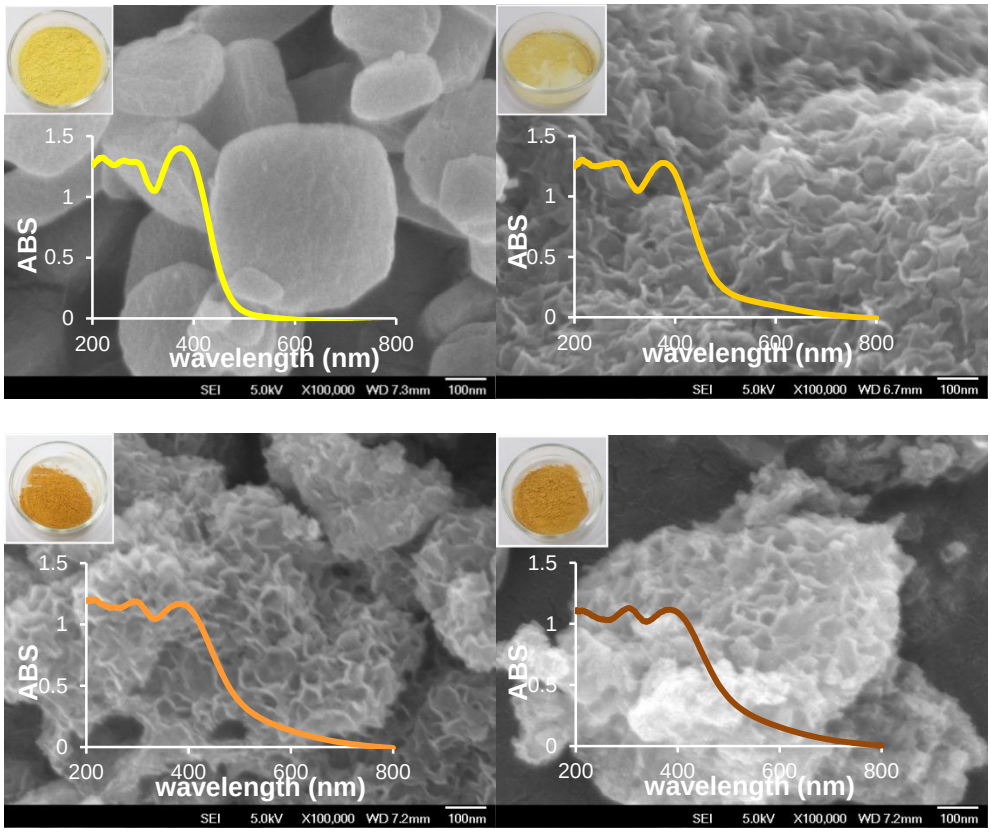

Figure 6.4 FESEM images of the as-synthesized powders (a) NH_2-MIL-125(Ti), (b) T-M-0.5, (c) T-M-1 and (d) T-M-2 with their respective UV spectra and powder colors.

High resolution TEM was carried out to further explore the structure of the heterojunction between NH_2-MIL-125(Ti) and TiO_2. Two typical TEM images are shown in Figure 6.5. Figure 6.5 (a) is a high resolution picture. The lattice fringes observed on the micrograph provides strong evidence for the formation of anatase TiO_2.

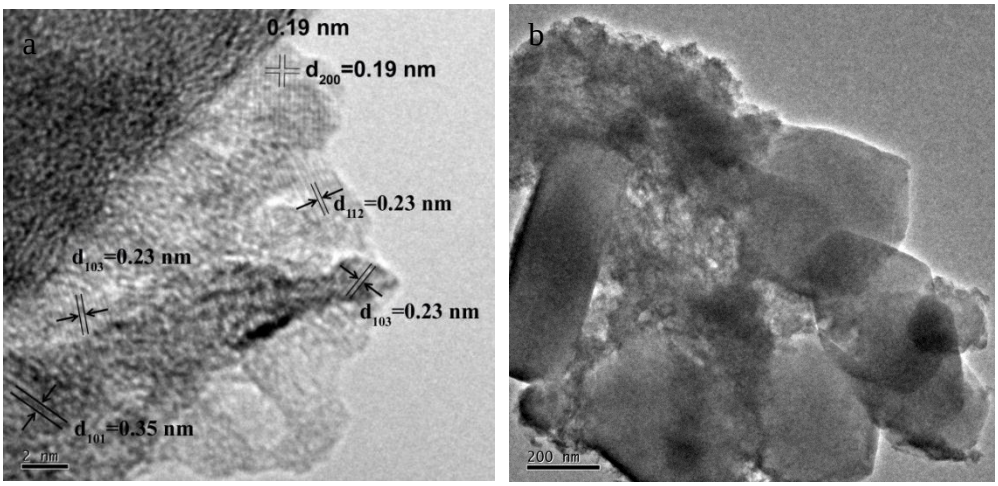

Figure 6.5 (a) high-magnification TEM image of T-M-0.5, and (b) TEM image of T-M-0.5.

Distances corresponding to the (1 0 1), (1 0 3), (1 1 2) and (2 0 0) facets of anatase phase TiO_2 were found in this TEM image. This is in full agreement with the results obtained from the powder XRD pattern discussed in 6.3.1.

The TEM image in Figure 6.5 (b) indicates that the formation rate of NH_2-MIL-125(Ti) is much faster than that of TiO_2. After the formation of NH_2-MIL-125(Ti), the growth of TiO_2 on the surface of NH_2-MIL-125(Ti) leads to aggregation of NH_2-MIL-125(Ti) and formation of a heterojunction structure.

6.3.3 BET measurements and elemental analysis

The BET surface area and pore structure of the samples were investigated based on N_2 adsorption-desorption, and the isotherms are shown in Figure 6.6. The type VI isotherms found in T-M-0.5, T-M-1, T-M-2 correspond to

mesoporous structures.

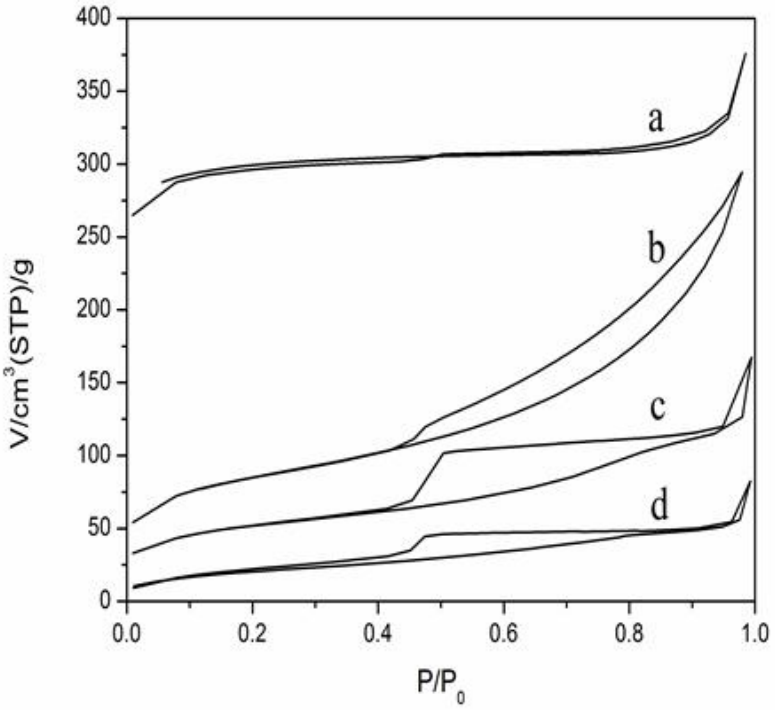

Figure 6.6 Nitrogen adsorption–desorption isotherms: (a) NH_2-MIL-125(Ti), (b) T-M-0.5, (c) T-M-1, (d) T-M-2.

Table 6.1 shows elemental analysis, the surface areas and pore size distribution values. With increase of the Ti proportion in the preparation process, the surface area decreases significantly from 857 to 72.6 m^2/g and total pore volume drops gradually from 0.58 to 0.13 cm^3/g. The drop in the total pore volume could be due to the titanium oxide growing on the MOFs surface to partially cover the pore channel.

Table 6.1 Elemental analysis, BET surface area and total pore volume of the as-synthesized samples.

Sample	$Ti(TiO_2)$: Ti(MOF)[a]	Surface Area (m^2/g)	Pore Volume (cm^3/g)
NH_2-MIL-125 (Ti)	-	857	0.58
T-M-0.5	6	272	0.46
T-M-1	19.36	147	0.26
T-M-2	50.08	72.6	0.13

a. The results were obtained from calculation of elemental analysis.

6.3.4 UV-vis diffuse reflectance spectra

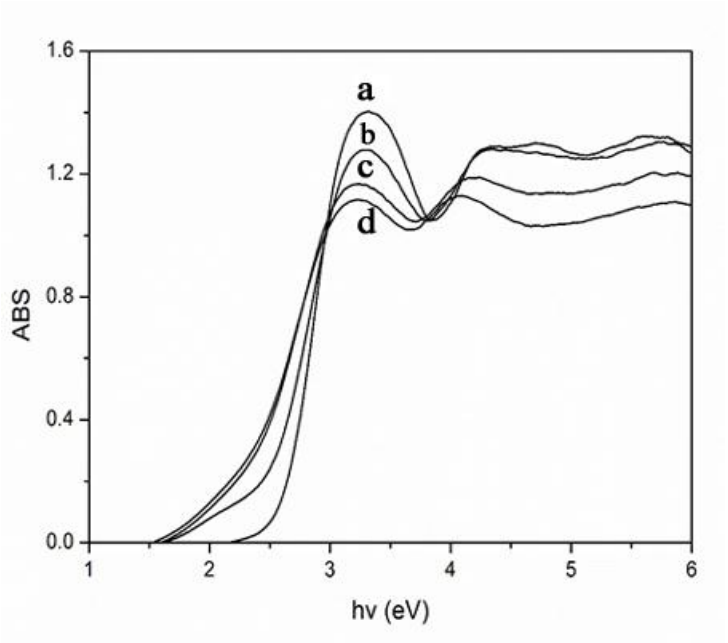

Figure 6.7 UV-Vis DRS spectrum: (a) NH_2-MIL-125(Ti), (b) T-M0.5, (c) T-M1 and (d) T-M2.

Figure 6.7 shows the UV-vis diffuse reflectance spectra of the as-synthesized samples. As can been seen above, two main band areas in those materials were displayed, the long wavelength adsorption area is LMCT band and the short wavelength adsorption area is O-Ti band.

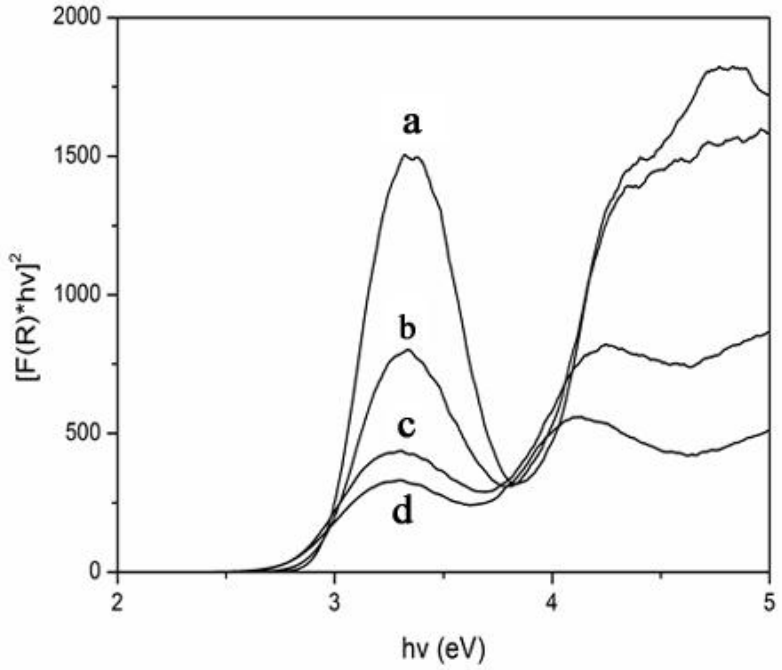

Figure 6.8 Band gap energy of LMCT band: (a) NH_2-MIL-125(Ti), (b) T-M0.5, (c) T-M1 and (d) T-M2.

The band gap energy of the samples was calculated by the following equation: [14]

$$\alpha h\nu = \mathrm{A}\left(h\nu - \mathrm{E_g}\right)^{\mathrm{n}/2} \qquad (6.2)$$

where α, ν, E_g, and A are the absorption coefficient, light frequency, band gap,

and a constant, respectively. The exponent n is determined by the type of the optical transition in the semiconductor (n = 1 for direct transition and n = 4 for indirect transition). According to previous studies, NH_2-MIL-125(Ti) exhibits the character of direct band transition [15] whereas anatase TiO_2 shows the characteristics of an indirect band transition [16]. Therefore the LMCT band was determined from plots of $(\alpha h\nu)^2$ versus energy ($h\nu$) (Figure 6.8) and the O-Ti band was determined from plots of $(\alpha h\nu)^{1/2}$ versus energy ($h\nu$) (Figure 6.9).

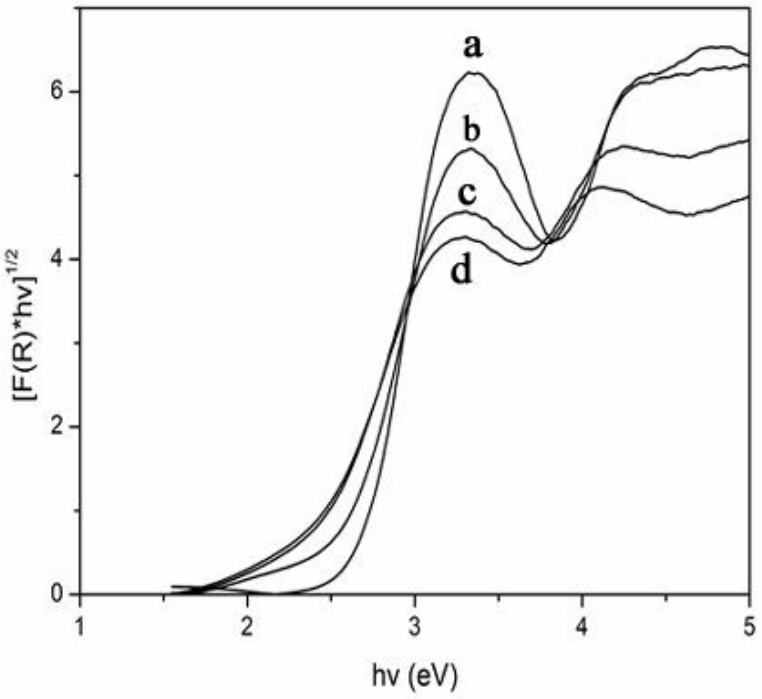

Figure 6.9 Band gap energy of O-Ti band: (a) NH_2-MIL-125(Ti), (b) T-M0.5, (c) T-M1 and (d) T-M2.

6.3.5 Photocatalytic activity

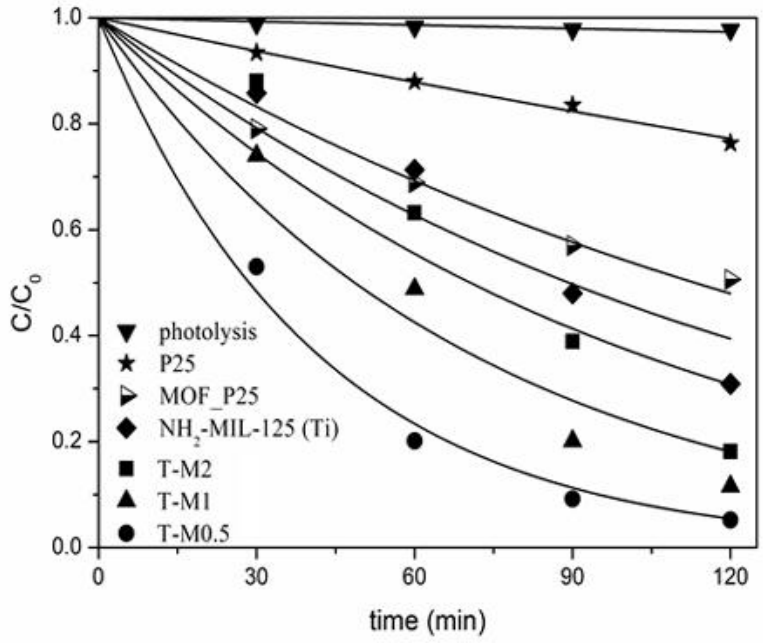

Figure 6.10 Photocatalytic degradation of RhB in the presence of different catalysts (P25, NH_2-MIL-125(Ti), T-M-0.5, T-M-1, T-M-2, mixture of MOF and P25) under visible light irradiation.

Photocatalytic activity of the samples in decomposing the organic azo-dye Rhodamine B was evaluated under irradiation with visible light ($\lambda \geq$ 420 nm)[17]. RhB is a typical pollutant in the textile industry. The variation of RhB concentration (C/C_0) as the function of visible-irradiation time is presented in Figure 6.10. For comparison, the photocatalytic activities of Degussa's P25, and a mixture of Degussa's P25 and MOF (Ti: Ti ratio is 0.75: 1), as well as the direct photolysis of RhB without any catalyst were

investigated under the same conditions.

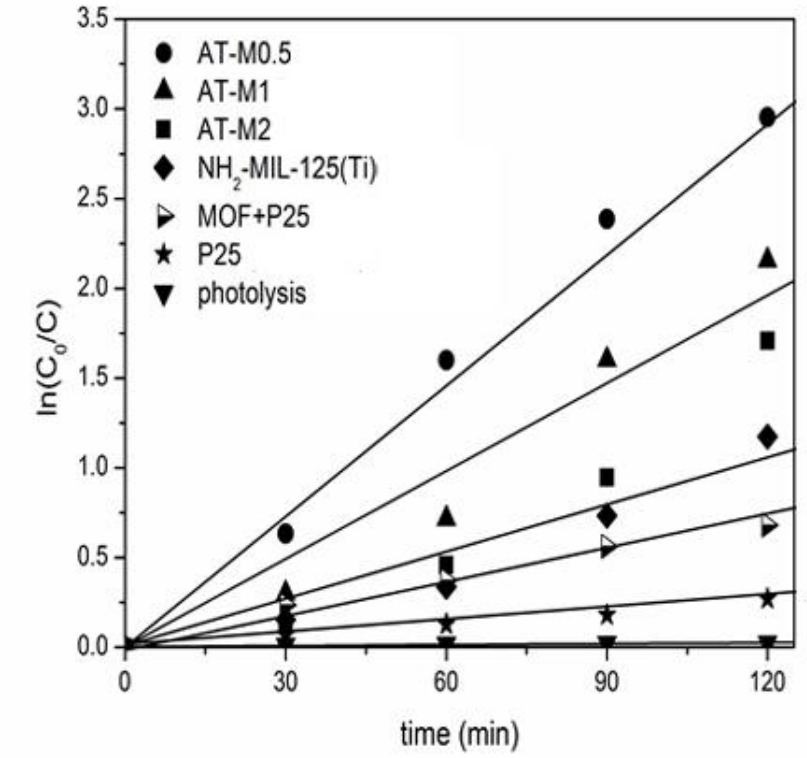

Figure 6.11 Comparison of the reaction rate constant (k) in the presence of different catalysts.

The results show that RhB is quite stable under visible light irradiation, so that the RhB degradation by photolysis alone is less than 2 % over 2 hours. The activity of P25 is moderate with about 20% decomposition after 2 h. All composites show increased activity, but T-M-0.5 is far superior. Furthermore, the kinetics of RhB degradation were studied quantitatively by applying the pseudo-first-order model as expressed by following equation:

$$\ln\left(\frac{c_0}{c}\right) = kt \quad (6.3)$$

where k is the pseudo-first-order rate constant. As seen from Figure 6.11 and Table 6.2, the reaction rate of T-M-0.5 is about 3 and 12 times as fast as that over NH_2-MIL-125(Ti) and Degussa's P25, respectively.

Table 6.2 Reaction constants of different photocatalysts in the photocatalytic degradation of RhB.

sample	k (min^{-1})
Photolysis	0.0002
P25	0.0022
NH_2-MIL-125 (Ti)	0.0086
T-M-0.5	0.0253
T-M-1	0.0169
T-M-2	0.0119
MOF+P25	0.0060

6.3.6 The effect of radical scavengers and N_2 purging

The effect of some radical scavengers and N_2 purging on the photodegradation of RhB under irradiation at visible light over T-M-0.5 was evaluated in an attempt to better understand the reaction mechanism. The 2-propanol (IPA) is a well-known scavenger of HO• [18]. In this study, the IPA did not cause any

obvious change in the photodegradation rate for RhB as shown in Figure 6.12. In order to study the role of the O_2^{-}• radical, an N_2 purging experiment was carried out to compare the results with those obtained under air–equilibrated conditions. There was a considerable drop in the decomposition efficiency with N_2 purging. Since dissolved O_2 is one of the critical reagents for the generation of O_2^{-}•, this result indicates that O_2^{-}• is another important species for the RhB degradation. Moreover, an additional experiment was tested to further explore the role of O_2^{-}• radical. Excess of $KBrO_3$ was add to the system, as the $KBrO_3$ is a strong oxidant which proved to be an effective electron acceptor replacing oxygen and can accelerate the separation of e_{CB}^{-} and h_{VB}^{+} in the photocatalyst [19, 20]. The additional $KBrO_3$ shows an inhibiting effect on the photodegradation efficiency of RhB (see Figure 6.12), but it cannot terminate the photodegradation of RhB. Therefore, it is confirmed that the O_2^{-}• radical is indeed an active species in the RhB photodegradation process over T-M-0.5. But other active species are involved in the photodegradation and those are most likely the holes in the valance band. As illustrated, the addition of EDTA much decreases the photodegradation rate, suggesting that photo-generated holes are the most active species in the degradation process.

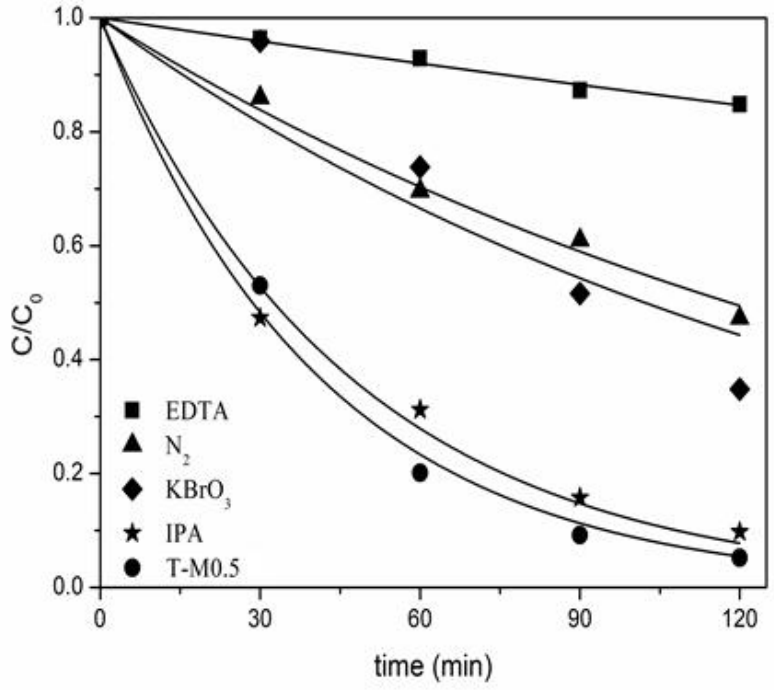

Figure 6.12 Effect of various scavengers and N_2 purging on the degradation of RhB using T-M-0.5 as catalyst.

6.3.7 The test of reusability

The stability and reusability of T-M-0.5 were investigated by studying XRD pattern of the fresh and used T-M-0.5 and collecting the T-M-0.5 after each cycle and then adding it for the next cycle. There is no apparent variation in XRD pattern of T-M-0.5 before and after the RhB photodegradation (see Figure 6.13).

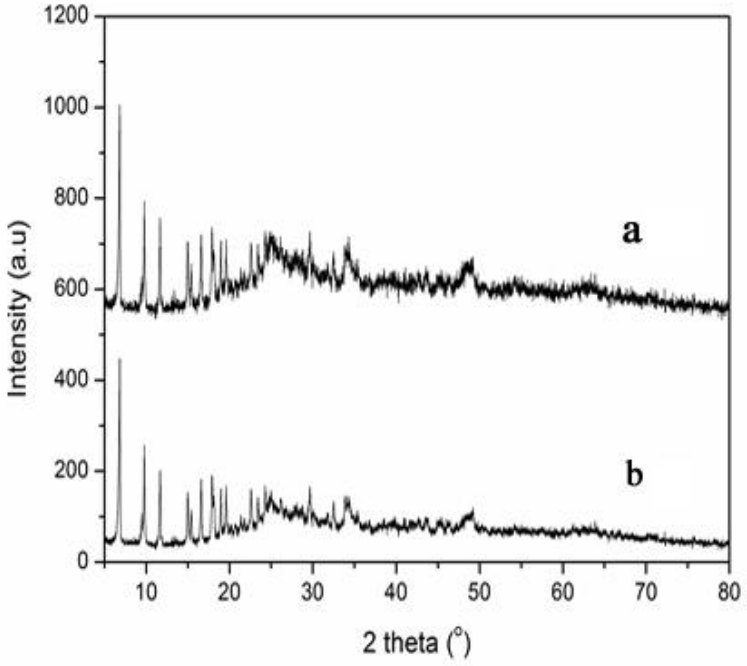

Figure 6.13 XRD patterns of the fresh T-M-0.5 and used T-M-0.5.

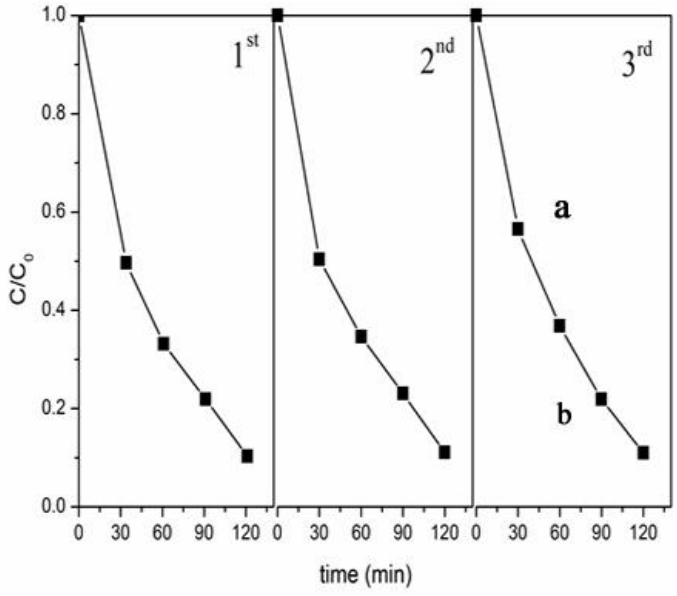

Figure 6.14 Three cycles of the RhB degradation in the presence of T-M0.5 under visible light irradiation

Furthermore, three cycles had been studied. Figure 6.14 shows that there is no significant loss in the photocatalytic activity for each cycle. T-M-0.5 showed high stability which might be due to the Ti-O cluster of MOF combined TiO_2 is fairly stable enough.

6.3.8 Photocatalytic mechanism

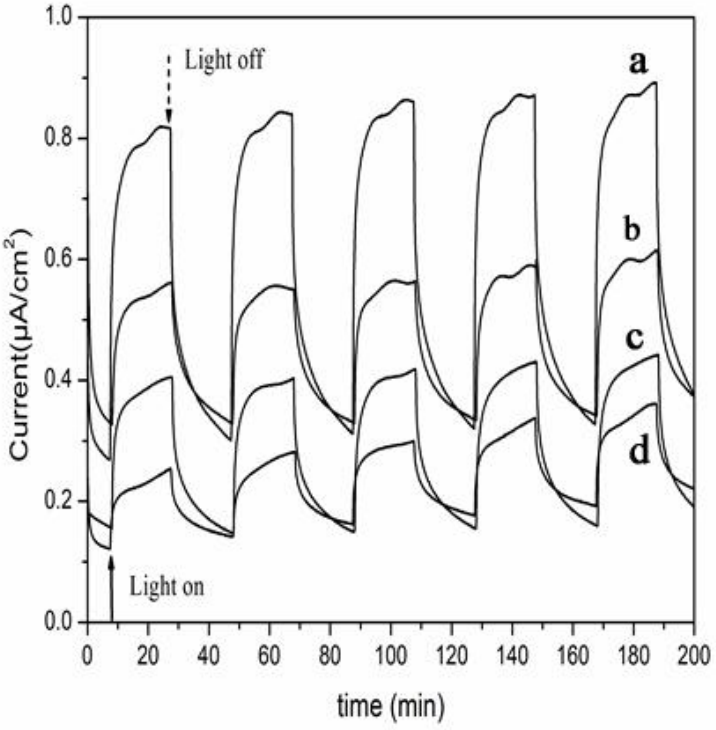

Figure 6.15 Transient photocurrent response of as-synthesized photocatalysts in 0.2 M Na_2SO_4 aqueous solution under chopped irradiation for 200 s: (a) T-M-0.5, (b) T-M-1, (c) T-M-2 and (d) NH_2-MIL-125(Ti).

In order to better understand the photocatalytic mechanism, the transient photocurrent response of as-synthesized photocatalysts was investigated under

intermittent visible light illumination. Figure 6.15 shows that the transient current generated upon photoexcitation with T-M-0.5 displayed the biggest photocurrent density which agrees with its photodegradative activity, because the amplitude of this photo-response is proportional to reaction rate.

It is known that the flat band potential of n-type semiconductors can be estimated with Mott-Schottky plot, and the CB of n-type semiconductors is quite close to the flat band potential [21, 22]. Figure 6.16 shows the Mott-Schottky plot, $1/C^2$ versus E, obtained for the NH_2-MIL-125(Ti) electrode in the dark.

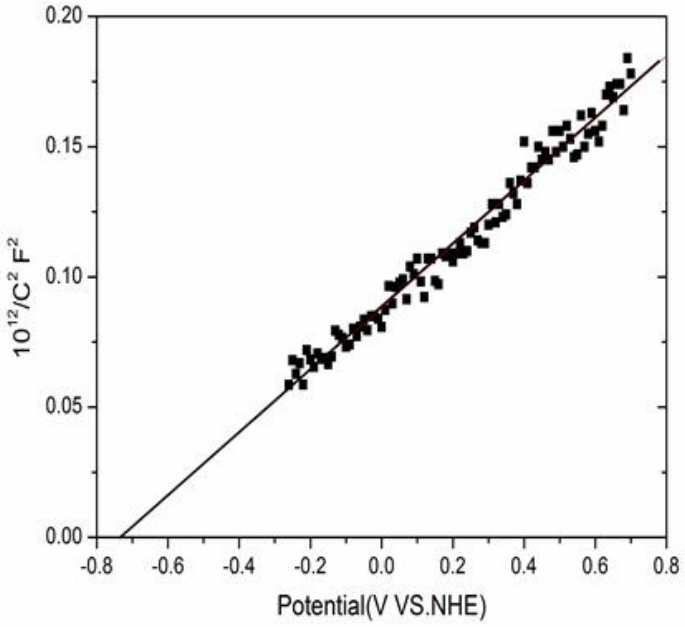

Figure 6.16 Mott-Schottky plot of T-M0.5.

The Mott-Schottky plot was obtained at a frequency of 1 kHz, and the positive slope is indicative of an n-type semiconductor. The flat-band potential is obtained as the potential for $1/C^2 = 0$ according to Mott-Schottky relationship [23, 24] (see eq 6.7).

$$\frac{1}{C_{SC}^2} = \frac{2}{e\varepsilon\varepsilon_0 N}\left(E - E_{FB} - \frac{kT}{e}\right) \tag{6.4}$$

where C_{SC} is capacitance of the space charge region, ε is dielectric constant of the semiconductor, ε_0 is permittivity of free space, N is donor density (electron donor concentration for an n-type semiconductor), E is applied potential, E_{FB} is flat-band potential.

The flat-band potential of NH_2-MIL-125(Ti) is about 0.75 V vs. NHE, which is more negative than the redox potential of H^+/H_2 (-0.41 eV), $O2^{-}\bullet/O_2$ (-0.28 eV) and CO_2/HCOOH (-0.11 eV). The electrons are theoretically able to reduce H^+, O_2 and CO_2 to H_2, $O_2^{-}\bullet$ and HCOOH, respectively. The determination of the CB and VB edges of the semiconductor by electrochemical methods is quite important for an understanding of the photodegradation mechanism. Scheme 6.1 shows the band edge positions of NH_2-MIL-125(Ti) obtained from the Mott-Schottky plot and the anatase phase of TiO_2 calculated from the atom Mullikan electronegativity according to [25, 26]

$$E_{VB} = \chi - E^e + 0.5E_g \qquad (6.5)$$

where χ is the absolute electronegativity of the semiconductor, which is defined as the geometric mean of the absolute electronegativity of the constituent atoms, E^e is the energy of free electrons on the hydrogen scale (≈4.5 eV), E_{VB} is the VB edge potential and Eg is the band gap of the semiconductor.

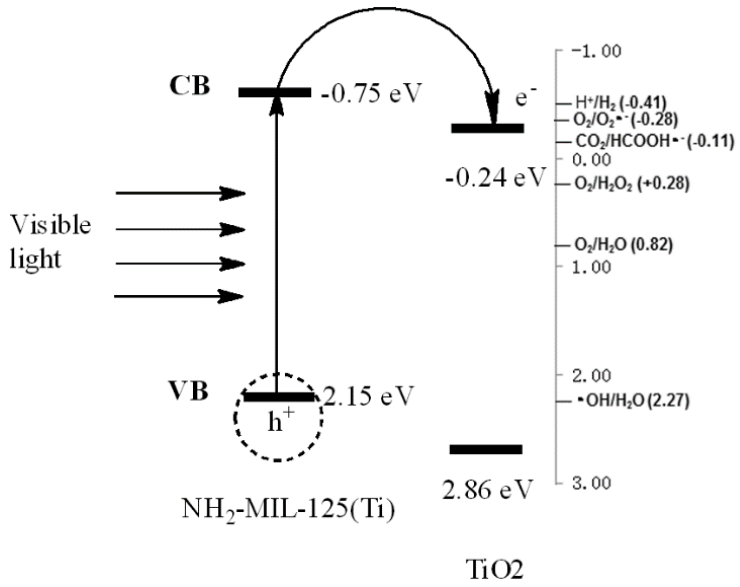

Scheme 6.1 Schematic diagram for energy band matching and flow electrons for the NH_2-MIL-125(Ti)/TiO_2 system.

The CB and VB levels of NH_2-MIL-125(Ti) are more negative than those of anatase phase TiO_2. With irradiation of visible light, an electron from the amino group of NH_2-MIL-125(Ti) can be promoted to the 3d orbital of Ti^{4+}. Thereby the nitrogen's 2p orbital of NH_2-MIL-125(Ti) becomes partially

vacant, and the electron in the 3d orbital will be donated to Ti^{4+}'s 3d orbital of anatase phase TiO_2. As a result, a hole is generated in the linker which can react with an organic pollutant. Therefore the surface area of T-M-0.5 is smaller than NH_2-MIL-125(Ti), but the heterojunction structure of T-M-0.5 is leading to a successful tuning of high photocatalytic efficiency.

6.4 Conclusion

In summary, the heterojunction between MOF and metal oxide has been reported for the first time as a high efficient visible-light photocatalyst, and this heterojunction can be easily prepared by the one-pot solvothermal treatment of tetraisopropyl titanate and 2-aminoterephthalic acid in dimethylformamide and dry methanol. It is likely that other heterojunctions between MOF and metal oxides can be obtained by this method, because many metal oxides can be synthesized from their metal alkoxide precursors. This heterojunction material demonstrates notably high photocatalytic activity in decomposing RhB in aqueous solution, whereas the individual components, NH_2-MIL-125(Ti) and TiO_2 (P25), displayed negligible efficiency. The reaction rate of T-M-0.5 is about 3 and 12 times as fast as that of NH_2-MIL-125(Ti) and of Degussa's P25, respectively. In this work, the mechanisms of heterojunction charge separation and degradation were

investigated, and the heterojunction presents a great potential in developing novel MOF-based photocatalyst.

6.5 References

[1] M.A. Nasalevich, M. van der Veen, F. Kapteijn, J. Gascon, CrystEngComm, 16 (2014) 4919.

[2] M. Alvaro, E. Carbonell, B. Ferrer, F.X. Llabrés i Xamena, H. Garcia, Chem-Eur. J., 13 (2007) 5106.

[3] T. Tachikawa, J.R. Choi, M. Fujitsuka, T. Majima, J. Phys. Chem. C, 112 (2008) 14090.

[4] M. Dan-Hardi, C. Serre, T. Frot, L. Rozes, G. Maurin, C. Sanchez, G. Férey, J. Am. Chem. Soc., 131 (2009) 10857.

[5] J. Long, S. Wang, Z. Ding, S. Wang, Y. Zhou, L. Huang, X. Wang, Chem. Commun., 48 (2012) 11656.

[6] M.A. Nasalevich, M.G. Goesten, T.J. Savenije, F. Kapteijn, J. Gascon, Chem. Commun., 49 (2013) 10575.

[7] C. Gomes Silva, I. Luz, F.X. Llabrés i Xamena, A. Corma, H. García, Chem. Eur. J., 16 (2010) 11133.

[8] F.X. Llabrés i Xamena, A. Corma, H. Garcia, J. Phys. Chem. C, 111 (2006) 80.

[9] M.C. Das, H. Xu, Z. Wang, G. Srinivas, W. Zhou, Y.F. Yue, V.N.

Nesterov, G. Qian, B. Chen, Chem. Commun., 47 (2011) 11715.

[10] C. Wang, Z. Xie, K.E. deKrafft, W. Lin, J. Am. Chem. Soc., 133 (2011) 13445.

[11] Y. Fu, D. Sun, Y. Chen, R. Huang, Z. Ding, X. Fu, Z. Li, Angew. Chem. Int. Ed., 51 (2012) 3364.

[12] B. Civalleri, F. Napoli, Y. Noel, C. Roetti, R. Dovesi, CrystEngComm, 8 (2006) 364.

[13] A. Kuc, A. Enyashin, G. Seifert, J. Phys. Chem. B, 111 (2007) 8179.

[14] M.A. Butler, J. Appl. Phys., 48 (1977) 1914.

[15] C.H. Hendon, D. Tiana, M. Fontecave, C. Sanchez, L. D'arras, C. Sassoye, L. Rozes, C. Mellot-Draznieks, A. Walsh, J. Am. Chem. Soc., 135 (2013) 10942.

[16] M. Landmann, E. Rauls, W.G. Schmidt, J. Phys.: Condens. Matter, 24 (2012) 195503.

[17] S. Shenawi-Khalil, V. Uvarov, S. Fronton, I. Popov, Y. Sasson, Appl. Catal., B, 117-118 (2012) 148.

[18] J. Li, W. Ma, Y. Huang, X. Tao, J. Zhao, Y. Xu, Appl. Catal. B-Environ., 48 (2004) 17.

[19] Y. Oosawa, M. Gratzel, J. Chem. Soc., Perkin Trans. 1, 84 (1988) 197.

[20] S. Song, L. Xu, Z. He, J. Chen, X. Xiao, B. Yan, Environ. Sci. Technol., 41 (2007) 5846.

[21] A. Ishikawa, T. Takata, J.N. Kondo, M. Kara, H. Kobayashi, K. Domen, J. Am. Chem. Soc., 124 (2002) 13547.

[22] J.S. Zhang, X.F. Chen, K. Takanabe, K. Maeda, K. Domen, J.D. Epping, X.Z. Fu, M. Antonietti, X.C. Wang, Angew. Chem. Int. Ed., 122 (2010) 451.

[23] A. J. Bard, L. R. Faulkner, Electrochemical methods, John Wiley and Sons, New York 2001.

[24] P. Schmuki, H. Böhni, J.A. Bardwell, J. Electrochem. Soc 142 (1995) 1705.

[25] A.H. Nethercot, Jr., Phys. Rev. Lett., 33 (1974) 1088.

[26] S. Shenawi-Khalil, V. Uvarov, Y. Kritsman, E. Menes, I. Popov, Y. Sasson, Catal. Commun., 12 (2011) 1136.

Chapter 7. Heterojunctions Between a Ti-containing Metal Organic Framework Material and BiOBr Nanoplates with Unprecedented Photocatalytic Activity

7.1 Introduction

A new concept of heterojunction between MOF and metal oxide was discussed in chapter 6. The MOF-based material indicates a promising path for the development of novel heterojunction photocatalysts. Although only the NH_2-MIL-125(Ti) component of NH_2-MIL-125(Ti)/TiO_2 can be excited by visible light, the heterojunction material has excellent photocatalytic activity. To improve the photocatalytic activity further, another type of heterojunction was designed, with two components that both can be excited by visible light. In this chapter, we will discuss this new type of heterojunction which is examplified by a heterojunction between MOF and metal oxyhalides. Bismuth oxyhalides (BiOXs, X = F, Cl, Br, I), a new family of promising photocatalysts with layered crystal structures [1], have attracted much attention due to their high photocatalytic activity, non-toxic property and simple preparation [2-4]. Figure 7.1 illustrates the crystal structure of BiOBr, which is made up of alternating $[Bi_2O_2]^{2+}$ and Br^- layers. The separation of photo-generated electrons and holes in bismuth oxyhalides is assisted by the internal static

electric field between the $[Bi_2O_2]^{2+}$ and the anionic halogen layers [5]. Among the various bismuth oxyhalides, BiOBr is characterized by good visible light adsorption and suitable band edges. Moreover, the bismuth oxyhalides present an indirect electron band gap, which reduces the recombination rate of photo-generated electrons and holes. The band structure of BiOBr was calculated by Density Functional Theory using CASTEP code and shown in Figure 7.2, indicating the indirect electron state of BiOBr.

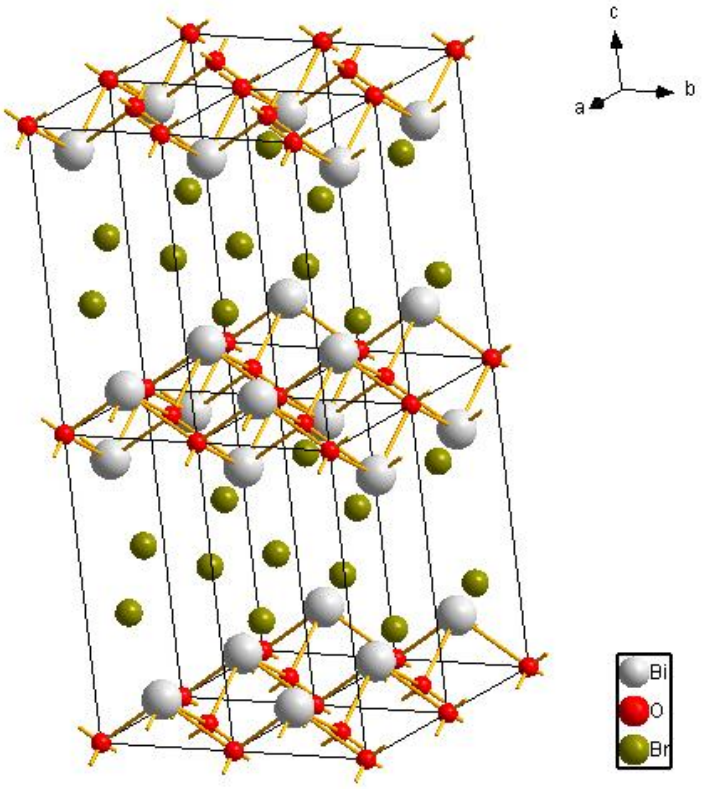

Figure 7.1 Crystal structure of BiOBr

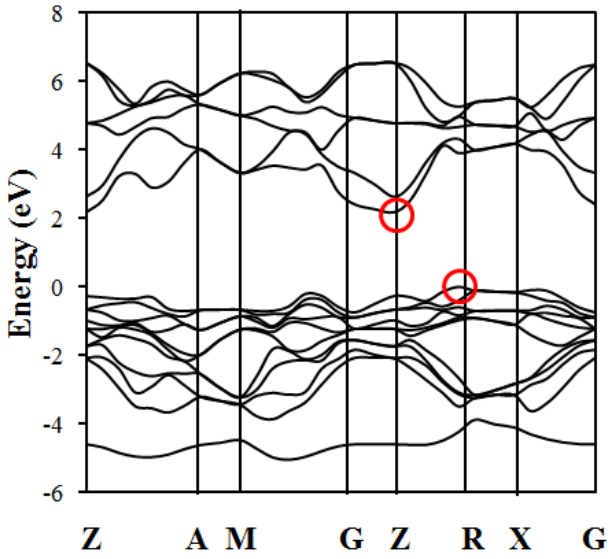

Figure 7.2 Band structure of BiOBr

Figure 7.3 shows the density of state (DOS) of Bi, O, Br in BiOBr and BiOBr. As in the previous calculations, Density Functional Theory with CASTEP code (Materials Studio V6.1) was employed to calculate the DOS of Bi, O, Br in BiOBr and BiOBr. The top of the VB of BiOBr is due to the Br 4p and O 2p orbitals as well as contributions from 6s and 6p orbitals of Bi, while the bottom of the CB consists of Bi 6p orbitals with a small contribution from Br 2p orbitals. The CB and VB can be calculated and listed in Table 7.1. Although BiOBr exhibits reasonably good photocatalytic activity, the activity can be enhanced by forming a heterojunction structure. Formation of a heterojunction with enhanced photocatalytic activity between NH_2-MIL-125(Ti) and BiOBr was predicted, because of the CB, VB edges in both materials show a good match.

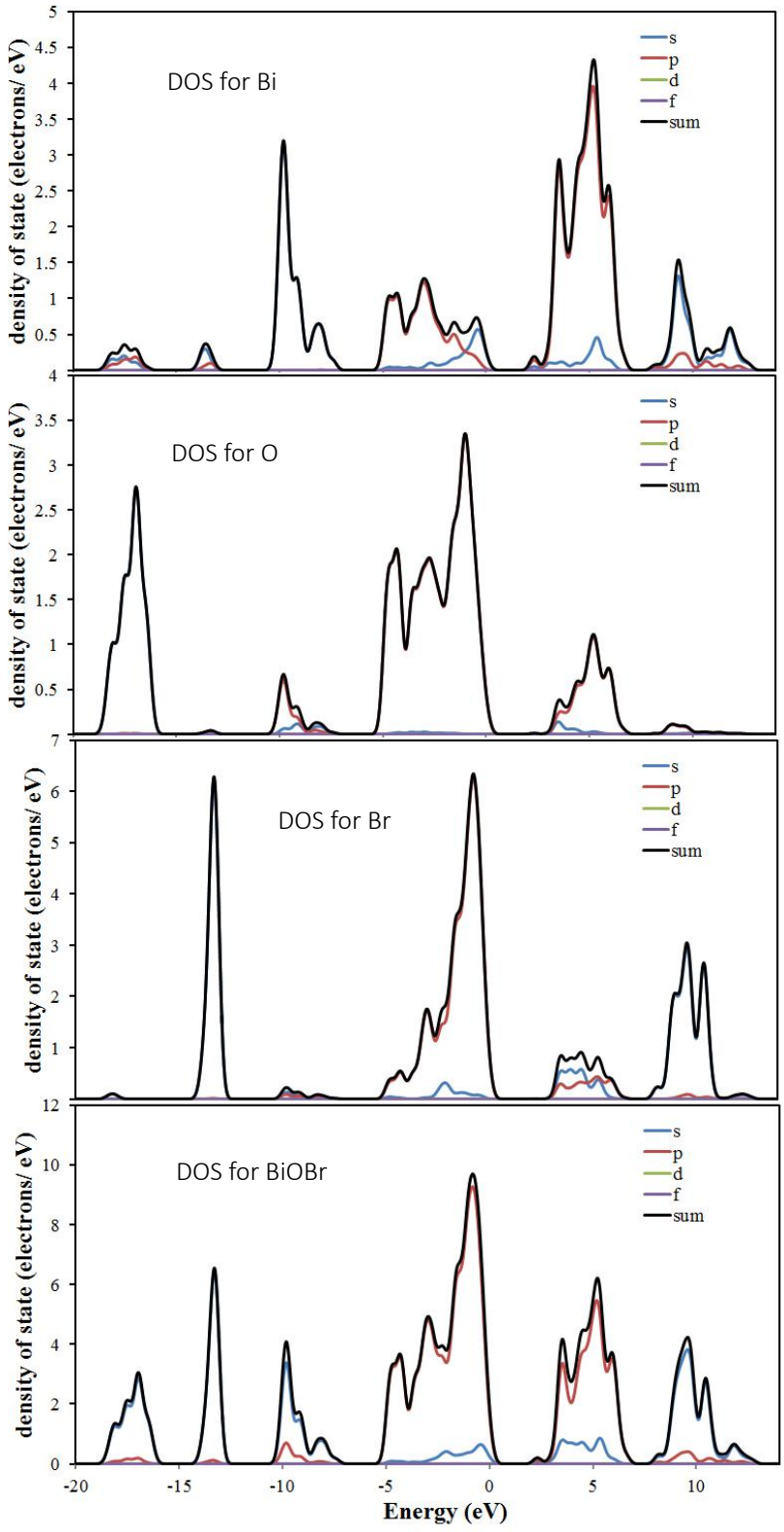

Figure 7.3 Density of state of Bi, O, Br in BiOBr and BiOBr

Table 7.1 CB and VB calculation of BiOBr

X (eV)	E_g (eV)	E_{VB} (eV)	E_{CB} (eV)
6.17	2.82	3.08	0.26

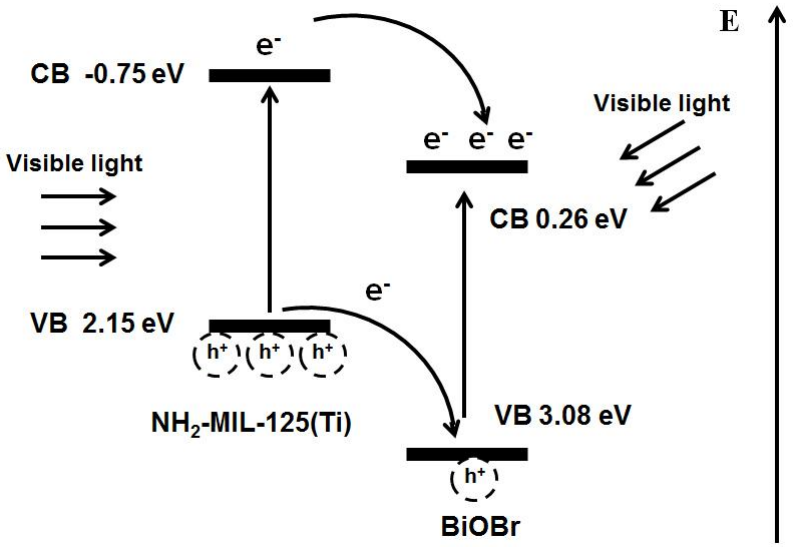

Figure 7.4 Band gap structure, edges and possible charge flow within the NH_2-MIL-125(Ti)/BiOBr heterojunction.

Figure 7.4 illustrates the band gap structure, edges and possible charge flow within the NH_2-MIL-125(Ti)/BiOBr heterojunction. The CB and VB of BiOBr are more positive than that of NH_2-MIL-125(Ti), thus the CB and VB of BiOBr are electron accepters. The photo-generated electron of NH_2-MIL-125(Ti) will be donated into the CB of BiOBr, while the electron from the VB of NH_2-MIL-125(Ti) will be donated to the VB of BiOBr. Therefore the charge flow enhances the separation of electron-hole pairs.

The properties of the heterojunctions in HN_2-MIL-125(Ti)/TiO_2 and HN_2-MIL-125(Ti)/BiOBr are compared in Table 7.2.

Table 7.2 Comparison between HN_2-MIL-125(Ti)/TiO_2 and HN_2-MIL-125(Ti)/BiOBr heterojunctions.

Materials	HN_2-MIL-125(Ti)/TiO_2	HN_2-MIL-125(Ti)/BiOBr,
Similarities	Heterojunction structure, Inorganic-organic hybrid material.	
Differences	One-pot solvothermal synthesis	Simple chemical precipitation
	One component is metal oxide (TiO_2)	One component is oxyhalide (BiOBr)
	Only one component can be excited by visible light	Both two components can be excited by visible light (Hopefully, it will be more efficient than HN_2-MIL-125(Ti)/TiO_2)

Moreover, the amino group of NH_2-MIL-125(Ti) has a lone pair electron, while Bi^{3+} can provide 6s and 6p orbitals. Because of the strong interaction between the amino group of NH_2-MIL-125(Ti) and Bi^{3+}, it is expected that plate-like BiOBr will form on the surface of NH_2-MIL-125(Ti). With this reasoning, we hoped to be able to prepare a new heterojunction, NH_2-MIL-125(Ti)/BiOBr, which should present a square NH_2-MIL-125(Ti) with plate-like BiOBr morphology. A simple chemical precipitation method was used to prepare NH_2-MIL-125(Ti)/BiOBr. XRD, SEM measurements were used to verify the predicted structure, and an investigation of

fluorescence quenching proved the interaction between amino group and Bi^{3+}. In addition, RhB decomposition was again employed to test photocatalytic activity. All results strongly agreed with our prediction. Therefore, we conclude that we succeeded to develop a simple method to synthesize heterojunctions between a MOF and a metal oxyhalide.

7.2 Experimental

7.2.1 Materials

The NH_2-MIL-125(Ti) was synthesized following the procedure outlined in Chapter 4.

Three NH_2-MIL-125(Ti)/BiOBr composites with different BiOBr contents were prepared. The BiOBr content was controlled by adjusting the precursor of BiOBr based on the molar ratio of Ti: Bi in the final composite. For the preparation of a NH_2-MIL-125(Ti)/BiOBr composite with Ti : Bi molar ratio equal to 1 : 1 (denoted as M-BiOBr-1), 0.3520 mg (0.7256 mmol) $Bi(NO_3)_3$ was dissolved in 7.5 ml MOF. Then, with vigorous stirring, 0.15 g NH_2-MIL-125(Ti) was added to the $Bi(NO_3)_3$ solution. After stirring for 30 min, 7.5 ml KBr aqueous solution (containing 0.7256 mmol KBr) was added dropwise to the suspension. Subsequently, the mixture was sonicated for 30 min at room temperature, and aged for 3 h. The product was collected by filtration, washed

thoroughly with deionized water several times, and finally dried at 120 ℃. NH_2-MIL-125(Ti)/BiOBr composites with Ti : Bi molar ratios of 2 : 1 (denoted as M-BiOBr-2) and 4 : 1 (denoted as M-BiOBr-4) were also synthesized using the same procedure except changing the amount of the precursor for BiOBr.

7.2.2 Characterization

The diffractograms of XRD were recorded for 2θ between 5 ° to 80 °.

For the N_2 adsorption–desorption isotherms measurements, the sample was degassed under N_2 at 120 ^{o}C for 6 h.

7.2.3 Examination of interaction between amino group and Bi^{3+}

The presence of an interaction between the amino group and Bi^{3+} was deduced from the quenching of the fluorescence. The 2-aminoterephthalic acid is a strong fluorophore. However, the fluorescence of 2-aminoterephthalic acid will be quenched if there is an interaction between the amino group and Bi^{3+}. MDF was employed as solvent, 9.1 mg 2-aminoterephthalic acid was dissolved in 10 DMF ($C_{2\text{-amino}}$ = 5 mmol/L). 5ml of this solution were pipetted out, and then 12.1 mg $Bi(NO_3)_3$ was added to this solution ($C_{2\text{-amino}} = C_{Bi3+}$ = 5 mmol/L). The fluorescence emission spectrum of the solution was measured using a Gilden FluoroSNS-fluorimeter. The excitation wavelength was set to 315 nm.

7.2.4 Evaluation of the photocatalytic activity

The evaluation of the photocatalytic activity was carried out as described in Chapter 6.

The used catalyst was washed with deionized water, dried overnight at 120 ^{o}C and tested in a fresh RhB solution. Three recycles were typically carried out.

7.2.5 Investigation of the photocatalytic mechanism

The investigation of the photocatalytic mechanism was conducted following the protocol given before.

7.3 Results and discussion

7.3.1 X-ray diffraction pattern

Figure 7.5 shows the X-ray diffraction patterns obtained from as-synthesized samples. These peaks of M-BiOBr-x at 2 $\theta \sim 7^{o}$, 10^{o}, 11^{o} and 14^{o} are indicative of NH_2-MIL-125(Ti), while the peaks at 2 $\theta \sim 25^{o}$, 32^{o}, 46^{o} and 57^{o} are due to BiOBr (ICSD No. 61225). The BiOBr peaks were sharp, reflective of its high crystallinity while small diffraction peaks of NH_2-MIL-125(Ti) were observed. In addition, all peaks could be assigned to either NH_2-MIL-125(Ti) or BiOBr. This confirms that in the composites, no appreciable chemical reaction occurred between NH_2-MIL-125(Ti) and BiOBr that would lead to new

compounds or phases. With increase of the amount of BiOBr precursor, the NH_2-MIL-125(Ti) XRD peak intensities decreases slightly while the BiOBr XRD peak intensities rise up gradually. Therefore the M-BiOBr-x samples were considered as heterojunctioned composites between NH_2-MIL-125(Ti) and BiOBr.

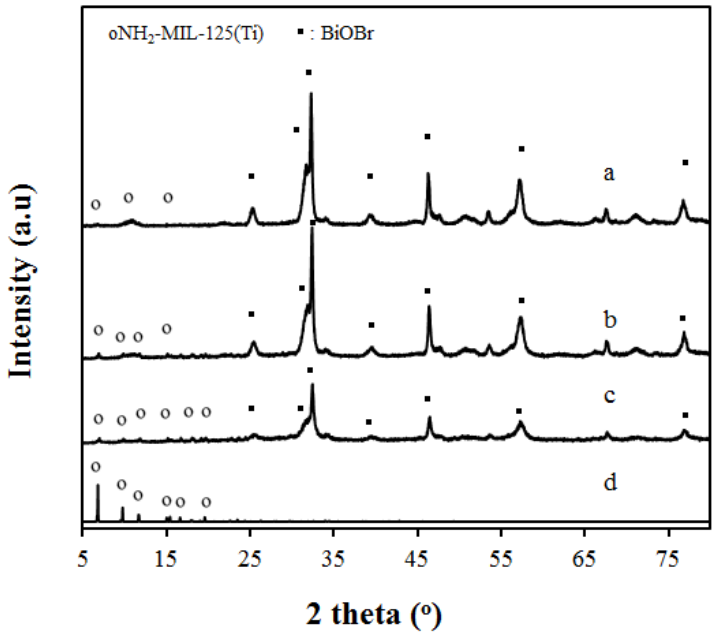

Figure 7.5 X-ray diffraction pattern obtained from as-synthesized samples (a) M-BiOBr-1, (b) M-BiOBr-2,(c) M-BiOBr-4 and (d) NH_2-MIL-125(Ti).

The peak with highest intensity at 2 θ ~ 32° corresponds to the (1 1 0) facet of BiOBr, indicating that the (1 1 0) facet is the dominant exposed facet for BiOBr. There are two possible mechanisms for the formation of a heterojunction: either the heterojunction is nucleated at the TiO_6 octahedral groups within the MOF structure, or there is the nucleation due to interaction

between Bi^{3+} and the NH_2 group at the linker. We expect that the NH_2 group of NH_2-MIL-125(Ti) will interact strongly with Bi of BiOBr. Since Bi^{3+} ion is able to provide 6s and 6p empty orbitals and the amino group of NH_2-MIL-125(Ti) has a lone electron pair, the BiOBr could grow along the surface of NH_2-MIL-125(Ti). The interaction between N and Bi was examined by examining the fluorescence. Figure 7.6 shows the fluorescence spectrum of DMF, the MDF solution containing 5 mmol/L 2-amino terephthalic acid and the MDF solution containing 5 mmol/L $Bi(NO_3)_3$ and 2-amino terephthalic acid.

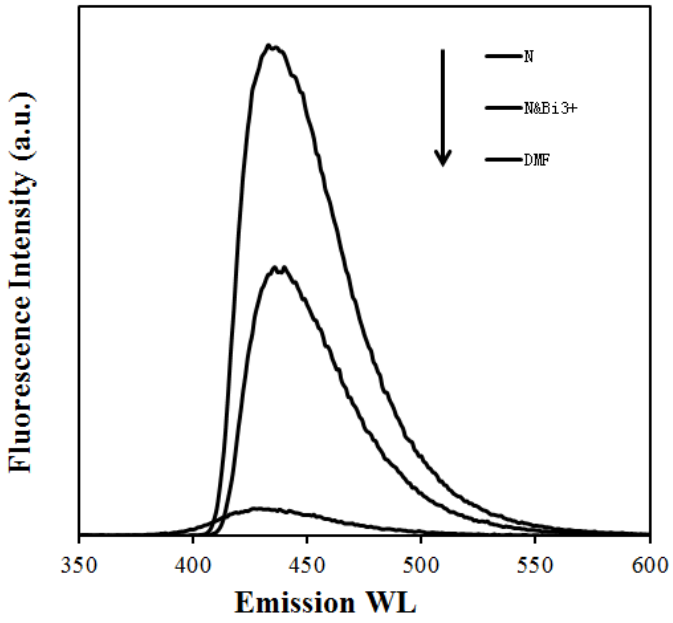

Figure 7.6 Fluorescence spectrum of DMF, the MDF solution containing 5 mmol/L 2-amino terephthalic acid and the MDF solution containing 5 mmol/L $Bi(NO_3)_3$ and 2-amino terephthalic acid.

The fluorescence of 2-amino terephthalic acid was quenched by about 50% after adding of Bi^{3+}. Therefore, there is an interaction between N and Bi. The (1 0 0), (0 0 1) and (1 1 0) facets of BiOBr are evaluated to localize the best geometry for such interation. These facets of BiOBr together with the position of the N atom are illustrated in Figure 7.7.

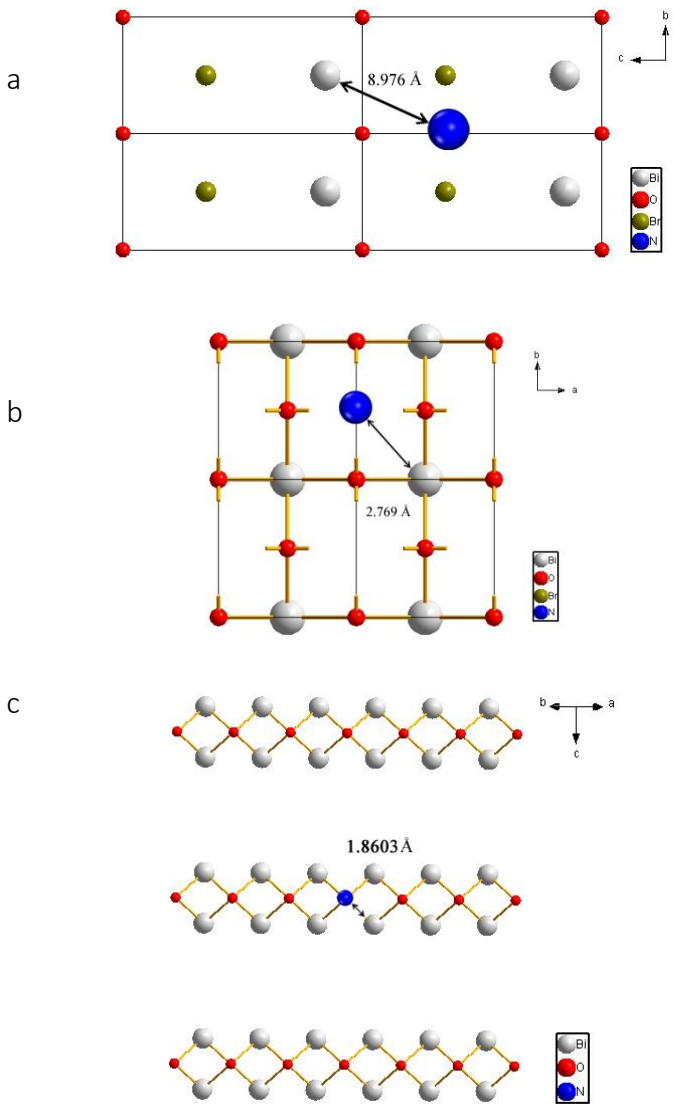

Figure 7.7 (a) (1 0 0) facet, (b) (0 0 1) facet and (c) (1 1 0) facet of BiOBr with N atom of NH_2-MIL-125(Ti).

Among those facet, the (1 1 0) allows for the strongest interaction between N and Bi because the distance between N and Bi is much shorter than for the other two facets. Therefore, growth on the (1 1 0) surface of MOF rather than other facets should be preferred. The theoretical analysis agrees well with the XRD pattern of Bi-M-x, which confirms that the interaction between the NH_2 group of the MOF and Bi^{3+} of BiOBr leads to the predicted plate-like BiOBr with dominant exposed (1 1 0) facets.

7.3.2 FESEM

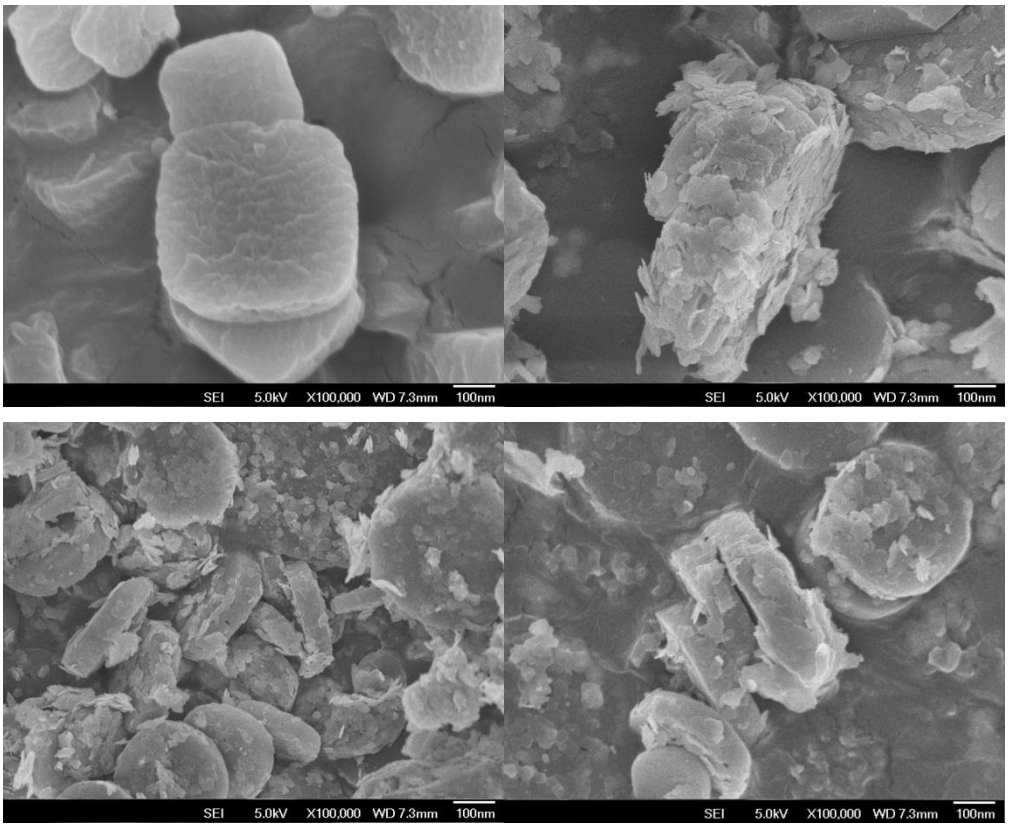

Figure 7.8 SEM images of (a) NH_2-MIL-125(Ti) (b) M-BiOBr-1, (c) M-BiOBr-2 and (d) M-BiOBr-4.

The morphology of the prepared M-BiOBr-x was examined by SEM in order to prove the prediction. Typical SEM images are shown in Figure 7.8. The NH_2-MIL-125(Ti) presented a smooth surface, but a plate-like BiOBr was grafted on the surface of NH_2-MIL-125(Ti) for M-BiOBr-x. Moreover, with increase of the amount of BiOBr precursor, the number of BiOBr plates on NH_2-MIL-125(Ti) surface increased significantly.

7.3.3 BET measurements

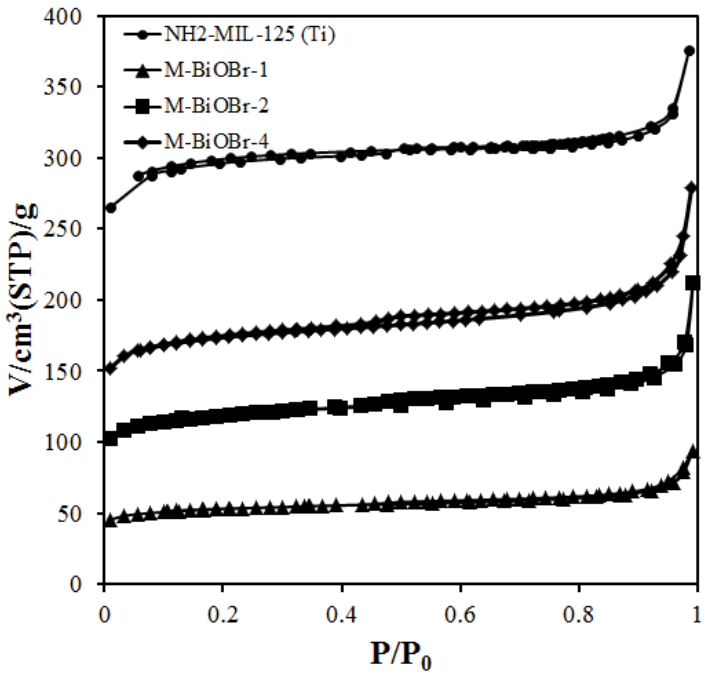

Figure 7.9 N_2 adsorption/desorption isotherms of M-BiOBr-1, M-BiOBr-2, M-BiOBr-4 and NH_2-MIL-125.

Figure 7.9 shows the N_2 adsorption/desorption isotherms of NH_2-MIL-125, M-BiOBr-1, M-BiOBr-2, M-BiOBr-4. The results indicate that NH_2-MIL-125

is a microporous material, but M-BiOBr-x have some additional mesoporosity. The wide horizontal loop (type B, characteristic for plate-like material) of the N_2 adsorption/desorption isotherms of M-BiOBr-x suggests that the mesoporosity is due to the interparticle space between the individual BiOBr crystallites.

Table 7.3 Surface area, expected surface area, pore volume, micropore volume and expected micropore volume of M-BiOBr-1, M-BiOBr-2, M-BiOBr-4 and NH_2-MIL-125.

Samples	Surface area (m^2/g)	Expected surface area (m^2/g)	Total pore volume (cm^3/g)	Micropore volume (cm^3/g)	Expected micropore volume (cm^3/g)
M-BiOBr-1	146	349	0.145	0.064	0.165
M-BiOBr-2	306	496	0.329	0.153	0.235
M-BiOBr-4	505	628	0.431	0.222	0.298
NH_2-MIL-125	857	857	0.408	0.408	0.408

The surface area, expected surface area, pore volume, micropore volume and expected micropore volume of M-BiOBr-1, M-BiOBr-2, M-BiOBr-4 and NH_2-MIL-125(Ti) are given in Table 7.3, the calculation details for the expected values are given in the Appendix. The surface areas and micropore volume of M-BiOBr-x deceased significantly after adding BiOBr. Although

there is a small difference between experimental data and expected values, the experimental data and expected values have almost the same trend. The total pore volume dropped down gradually with increase of the amount of BiOBr precursor, which could be caused by the coverage of micropores in NH_2-MIL-125(Ti) by BOBr plates.

7.3.4 UV-vis diffuse reflectance spectra

Figure 7.10 shows the UV-vis diffuse reflectance spectra of NH_2-MIL-125(Ti), M-BiOBr-1, M-BiOBr-2, M-BiOBr-4 and BiOBr. NH_2-MIL-125(Ti) and BiOBr show an adsorption just extending into the visible range with the edge at 470 and 430 nm, respectively. However, M-BiOBr-x samples adsorb strongly in the visible range with the edge at 600 nm and a long tail extending to 800 nm. Therefore, the M-BiOBr-x could enhance their photocatalytic activity. Because of the indirect electronic band gap in BiOBr, the value of the band gap energy for BiOBr is calculated to be 2.82 eV according to Figure 7.11. As mentioned in chapter 6, the band gap of NH2-MIL-125 (Ti) is 2.9 eV.

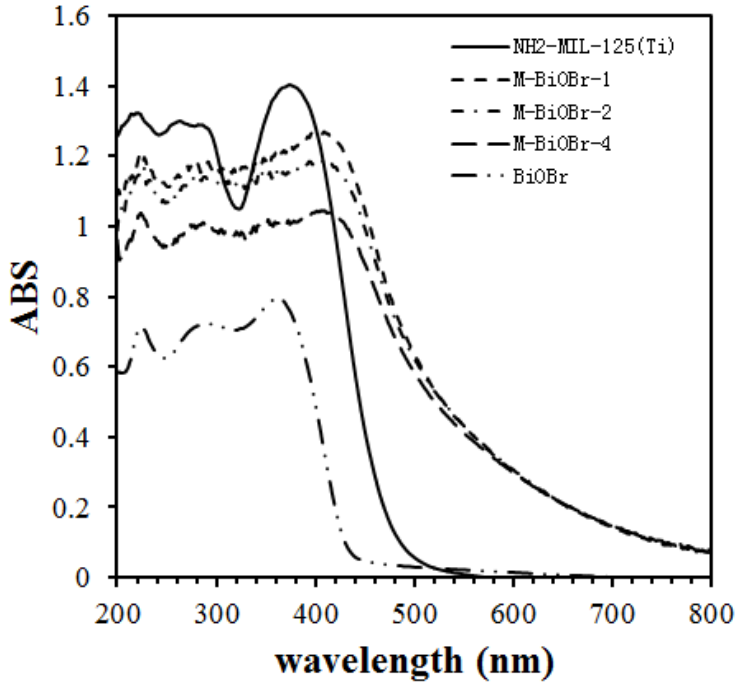

Figure 7.10 UV-vis diffuse reflectance spectra of pure NH_2-MIL-125(Ti), M-BiOBr-1, M-BiOBr-2, M-BiOBr-4 and BiOBr.

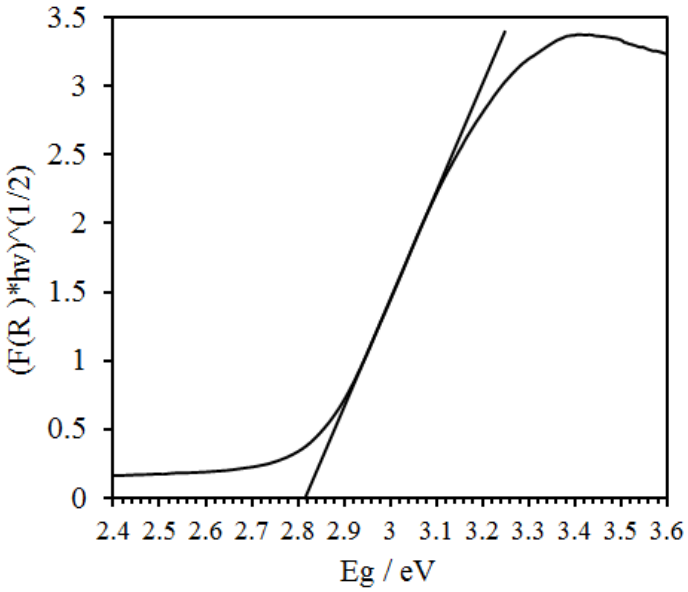

Figure 7.11 Band gap determination plots of BiOBr with indirect electron transition state.

7.3.5 Photocatalytic activity

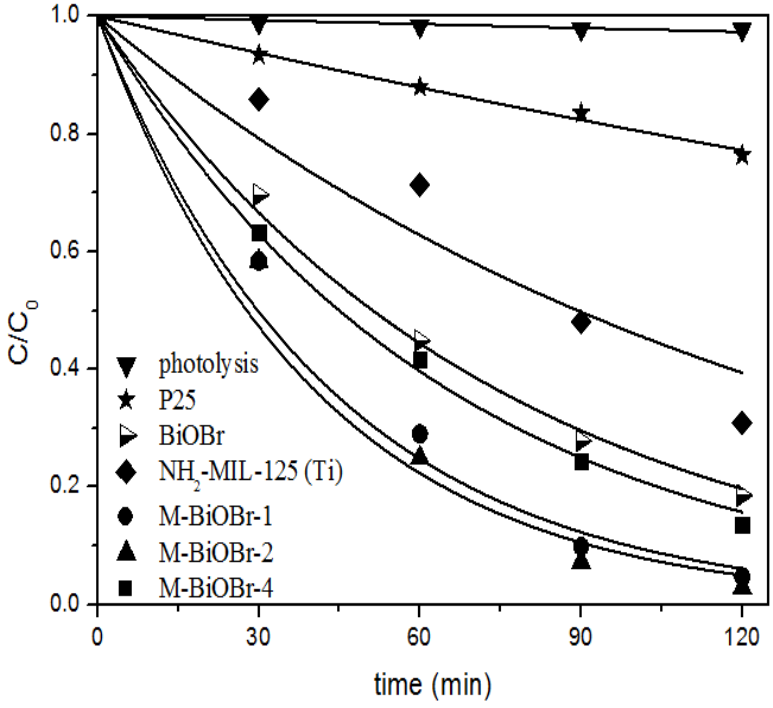

Figure 7.12 Photocatalytic degradation of RhB in the presence of different catalysts (P25, NH_2-MIL-125(Ti), Pure BiOBr, M-BiOBr-1, M-BiOBr-2 and M-BiOBr-4) under visible light irradiation.

Photocatalytic activities of the M-BiOBr-x were examined by photodegradation of the organic dye Rhodamine B under irradiation with visible light ($\lambda \geq 420$ nm). The change of RhB concentration (C/C_0) as function of irradiation time is presented in Figure 7.12. The photocatalytic activities of Degussa's P25 and direct non-catalytic photolysis of RhB were included to compare with M-BiOBr-x heterojunctions. The results suggest that compared with NH_2-MIL-125(Ti) and pure BiOBr, M-BiOBr-x heterojunctions show

good photocatalytic activities in the study of photodegradation of RhB. All composites show increased activity, while M-BiOBr-2 exhibited the best performance. The RhB was decomposed to less than 2 % during 2 hours by employing M-BiOBr-2 as photocatalyst, but P25 showed much less photocatalytic activity. In addition, the kinetics of RhB degradation were studied quantitatively by applying the pseudo-first-order model as expressed by following equation:

$$\ln\left(\frac{c_0}{c}\right) = kt \qquad (7.1)$$

where k is the pseudo-first-order rate constant.

Table 7.4 Reaction rate constant of samples in Photocatalytic degradation of RhB.

sample	k (min^{-1})
Photolysis	0.0002
P25	0.0022
NH_2-MIL-125 (Ti)	0.0086
BiOBr	0.0147
M-BiOBr-1	0.0246
M-BiOBr-2	0.0281
M-BiOBr-4	0.016

The pseudo-first-order reaction rate constants are given in Table 7.4. The reaction rate constant for M-BiOBr-2 is about 3 times bigger than that for NH_2-MIL-125(Ti), 2 times that of BiOBr, and 13 times that of Degussa's P25. This result further proves that the M-BiOBr-x are heterojunctioned structures, because of the enhanced photocatalytic activity of NH_2-MIL-125(Ti) and BiOBr.

7.3.6 The effect of some radical scavengers and N_2 purging

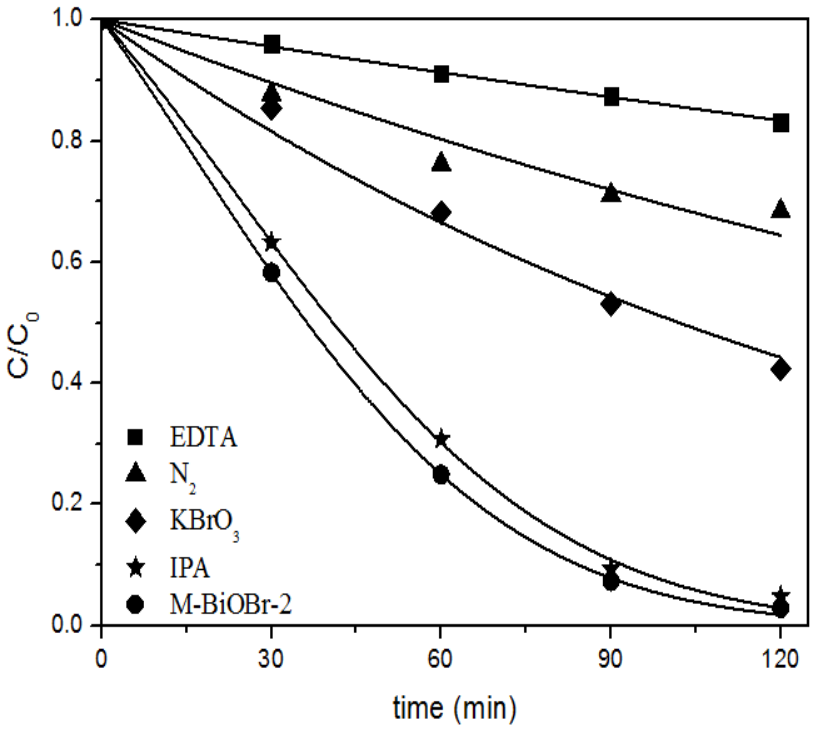

Figure 7.13 Effect of various scavengers and N_2 purging on the degradation of RhB using M-BiOBr as catalyst.

As already described in chapter 5, the photocatalytic mechanism can be unraveled by scavenging experiments with isopropyl alcohol (IPA), $KBrO_3$ and EDTA. These reagents are specific scavengers for hydroxyl radicals (HO•), superoxide radicals (O_2^-•) and holes (h^+), respectively [6-8]. IPA did not cause any obvious change in the photodegradation rate for RhB, thus HO• radicals are not produced in this photodegradation process. In order to study the role of O_2^-• radical, an N_2 purging experiment was carried out, and the results compared with air–equilibrated conditions. It can be see that there is a considerable drop in the decomposition efficiency with N_2 purging. Since dissolved O_2 is one of the critical reagents for the generation of O_2^-•, this result indicates that O_2^-• is an important species for the RhB degradation. The role of the O_2^-• radical was confirmed with an additional experiment. Excess of $KBrO_3$ was added to the system, as $KBrO_3$ is a strong oxidant which can replace oxygen as an effective electron acceptor. The reactions are described by the following equations.

$$BrO_3^- + e^- + 2H^+ \rightarrow BrO_2^{\cdot} + H_2O$$

$$BrO_3^- + 6e^- + 6H^+ \rightarrow [BrO_2^-, HOBr] \rightarrow Br^- + H_2O$$

The addition of $KBrO_3$ slows down the photodegradation of RhB (see Figure 7.13), but it cannot terminate the photodegradation of RhB. Therefore, it was confirmed that the O_2^-• radical is indeed an active species in the RhB

photodegradation process over M-BiOBr-2. However, other active species are also involved in the photodegradation and those are most likely the holes in the valance band. The addition of EDTA decreases the photodegradation rate significantly, suggesting that photo-generated holes are the most active species in the degradation process.

7.3.7 The test of reusability

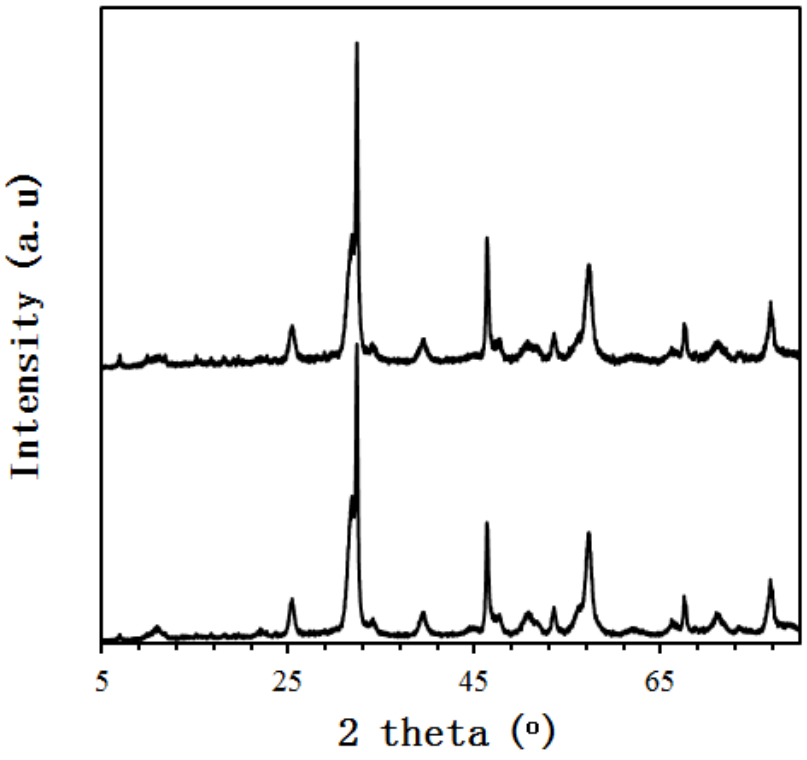

Figure 7.14 XRD patterns of the fresh M-BiOBr-2 and used M-BiOBr-2.

The reusability of catalyst is very crucial in industry, which will offer a low cost operation, and high economic value. The reusability of M-BiOBr-2 was investigated by studying XRD patterns of the fresh and used M-BiOBr-2. The used M-BiOBr-2 was collected after each cycle and then added to fresh rhodamine solution for the next cycle. Figure 7.14 indicates that there is no apparent variation in XRD pattern of M-BiOBr-2 before and after the RhB photodegradation. Figure 7.15 shows that there is no significant loss in the photocatalytic activity even after three cycles. Therefore, it can be concluded that M-BiOBr-2 shows good reusability.

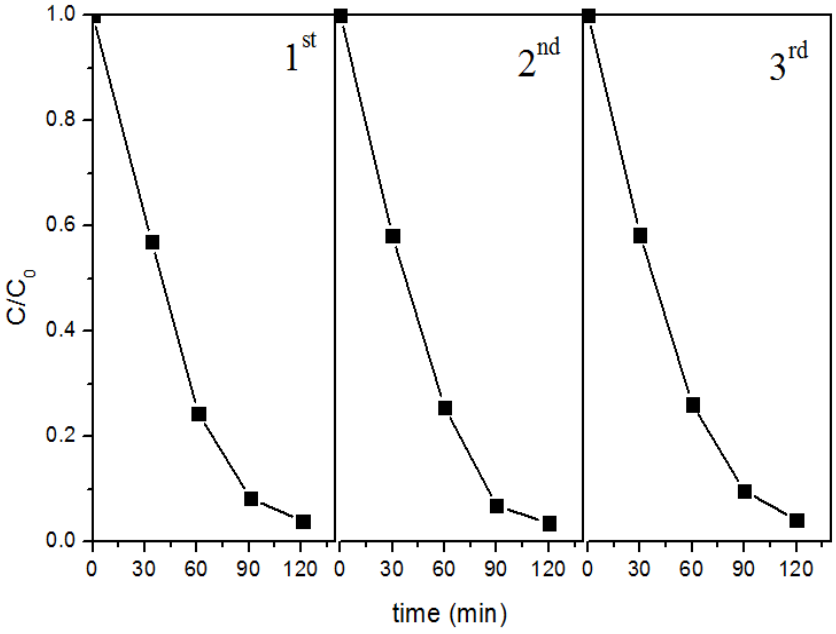

Figure 7.15 Three cycles of the RhB degradation in the presence of M-BiOBr-2 under visible light irradiation

7.4 Conclusion

The formation and morphology of a new series heterojunction between NH_2-MIL-125(Ti) and BiOBr were predicted by studying their band structure, band edges and the crystal structures of the individual compounds. The formation of heterojunctions between a MOF and a metal oxyhalide is here reported for the first time as a highly efficient visible-light photocatalyst, which was synthesized by a simple chemical precipitation reaction. Therefore, this study opens an opportunity to obtain a novel class of heterojunction between MOF and metal oxyhalide. The M-BiOBr-x showed an interesting morphology: plate-like BiOBr grafted on the surface of cubes of NH_2-MIL-125(Ti). The observed structures agreed well with the theoretical prediction. The M-BiOBr-x also presented a high surface area and a good reusability. The reaction rate under visible light irradiation is about 3 times faster over M-BiOBr-2 than over NH_2-MIL-125(Ti), and 13 times as fast as over Degussa's P25.

7.5 References

[1] K.L. Zhang, C.M. Liu, F.Q. Huang, C. Zheng, W.D. Wang, Appl. Catal. B-Environ., 68 (2006) 125.

[2] X. Lin, T. Huang, F. Huang, W. Wang, J. Shi, J. Phys. Chem. B, 110 (2006) 24629.

[3] W. Wang, F. Huang, X. Lin, J. Yang, Catal. Commun., 9 (2008) 8.

[4] S. Shenawi-Khalil, V. Uvarov, S. Fronton, I. Popov, Y. Sasson, J. Phys. Chem. C, 116 (2012) 11004.

[5] H. Zhang, L. Liu, Z. Zhou, Phys. Chem. Chem. Phys., 14 (2012) 1286.

[6] J. Li, W. Ma, Y. Huang, X. Tao, J. Zhao, Y. Xu, Appl. Catal. B-Environ., 48 (2004) 17.

[7] H. Zhang, R. Zong, J. Zhao, Y. Zhu, Environ. Sci. Technol., 42 (2008) 3803.

[8] T.B. Li, G. Chen, C. Zhou, Z.Y. Shen, R.C. Jin, J.X. Sun, Dalton Trans., 40 (2011) 6751.

7.6 Appendix

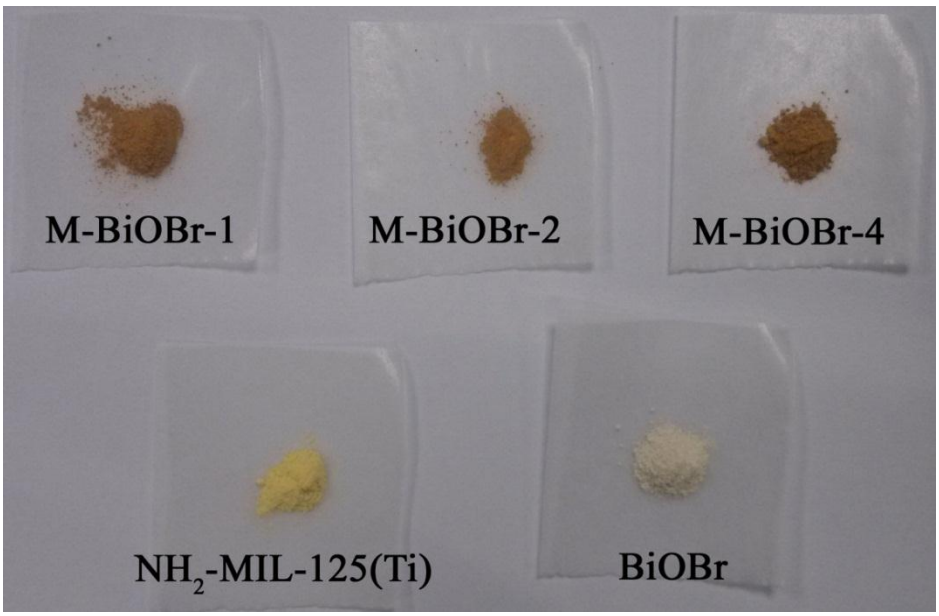

Figure 7.16 Powder samples of M-BiOBr-1, M-BiOBr-2, M-BiOBr-4 NH_2-MIL-125(Ti), and pure BiOBr.

The molecular weight of NH_2-MIL-125(Ti) $[Ti_8O_8(OH)_4(BDC\text{-}NH_2)_6]$ is 1654.02, and the molecular weight of BiOBr is 304.88. Moreover, the surface area of MOF is 857 m^2/g and BiOBr is 5.23 m^2/g [4]. Furthermore, Micropore volume of MOF is 0.408, while BiOBr is non-porous material.

Therefore:

For Bi-M-1, MOF wt (%)=1654.02/(1654.02+ 8×304.88)= 40.4%

For Bi-M-2, MOF wt (%)=1654.02/(1654.02+ 4×304.88)= 57.6%

For Bi-M-4, MOF wt (%)=1654.02/(1654.02+ 2×304.88)= 73.1%

Expected Surface area of Bi-M-1 = 857×40.4%+ 5.23×59.6% = 349.3

Expected Surface area of Bi-M-2 = 857×57.6%+ 5.23×42.4% = 495.8

Expected Surface area of Bi-M-4 = 857×73.1%+ 5.23×26.9% = 627.9

Expected Micropore volume of Bi-M-1 = 0.408×40.4% = 0.165

Expected Micropore volume of Bi-M-2 = 0.408×57.6% = 0.235

Expected Micropore volume of Bi-M-4 = 0.408×73.1% = 0.298

The NH_2-MIL-125(Ti) weight percentage, BiOBr weight percentage, expected surface area and expected Micropore volume of M-BiOBr-1, M-BiOBr-2 and

M-BiOBr-4 were given in Table 7.5

Table 7.5 NH_2-MIL-125(Ti) weight percentage, BiOBr weight percentage, expected surface area and expected Micropore volume of M-BiOBr-1, M-BiOBr-2 and M-BiOBr-4.

Samples	MOF wt (%)	BiOBr wt (%)	Expected surface area (m^2/g)	Expected Micropore volume (cm^3/g)
M-BiOBr-1	40.4	59.6	349.3	0.165
M-BiOBr-2	57.6	42.4	495.8	0.235
M-BiOBr-4	73.1	26.9	627.9	0.298

Chapter 8. Final Conclusion and future work

8.1 Final conclusion

In this thesis, we employed 5 hybrid materials as adsorbent to remove Cr(VI) from waste water (UIO-66, NH_2-UIO-66, NH_2-MIL-125(Ti), N-KIT-6 and NNN-KIT-6). These adsorbents exhibited a high adsorption capacity and good reusability. In the second part of the project, several types of hybrid visible-light-driven photocatalysts have been developed. These catalysts were evaluated for the degradation of Rhodamine B in waste water. All photocatalysts showed a strong response over the visible region and excellent photocatalytic activity. Both the adsorbents and the photocatalysts can be easily separated from the waste water and reused for the next cycle.

The studies of adsorption of Cr(VI) are the first report of a heavy metal being removed from an aqueous solution by MOFs, amino-functionalized MOFs, and amino-functionalized siliceous material KIT-6, respectively. The kinetics of Cr(VI) adsorption onto UIO-66, NH_2-UIO-66, NH_2-MIL-125(Ti), N-KIT-6 and NNN-KIT-6 can be adequately described by the pseudo-second order model. The adsorption isotherms could be fitted very well with the Langmuir model, and the adsorption capacity of UIO-66, NH_2-UIO-66, NH_2-MIL-125(Ti), N-KIT-6 and NNN-KIT-6 are 93, 195.4, 140.5, 142.9 and 241.3 mg/g, respectively. Moreover, the residual Cr(VI) concentration can be

reduced sufficiently to achieve the drinking water standards by treatment with amino-functionalized KIT-6. The UIO-66, NH_2-UIO-66, NH_2-MIL-125(Ti), N-KIT-6 and NNN-KIT-6 exhibit excellent potential for applications to control Cr(VI) pollution due to their high adsorption capacity and satisfactory reusability.

In the studies of visible-light-driven hybrid photocatalyst, the concept of "molecular doping" has been introduced for the first time. In addition, a universal scheme to construct heterojunctions between a MOF and a metal oxide or metal oxyhalide has been developed. The molecular doping opens an opportunity to purposefully design a photocatalyst with the desired band gap, and to obtain a materials with improved porosity and thereby greatly increased surface area for catalytic activity. The investigations on molecular-doped TiO_2 provide strong evidence for this theory. In addition, a molecule-doped BiOCl was synthesized to further examine the universality of the concept, and of the synthesis method. Again, the results agreed with the expectation.

The heterojunction between NH_2-MIL-125(Ti) and TiO_2 as a highly efficient visible-light photocatalyst were prepared in a one-pot solvothermal reaction. It is likely that other heterojunctions between MOF and metal oxides can be obtained by this preparation method, because many metal oxides can be synthesized from their metal alkoxide precursors. The formation and

morphology of the heterojunctions between NH_2-MIL-125(Ti) and BiOBr were predicted by studying of the band structure, band edges and crystal structure of NH_2-MIL-125(Ti) and BiOBr. The successful synthesis of the material and the results which agreed well with the prediction provides a new perspective to obtain a novel class of heterojunction between MOF and metal oxyhalides via a simple precipitation reaction. An attractive feature of these photocatalysts is that they possess competitive photocatalytic activity for the degradation of RhB under sunlight irradiation. Under these conditions, the activity is an order of magnitude better than that of P25, a benchmark commercial photocatalyst. The materials developed in the course of this thesis offer the prospect that inorganic and organic hybrid materials can find a role in water treatment in the future.

8.2 Future work

Based on the results obtained during this thesis, the following points could be addressed in future work:

1. In chapter 4, we described how amino-functionalized MOF can be used to remove Cr(VI). Although the NH_2-UIO-66 and NH_2-MIL-125(Ti) show satisfactory capability, the Zr in NH_2-UIO-66 is a relative heavy and expensive metal. NH_2-MIL-125(Ti), which contains Ti, has a lower specific weight, but is still an expensive material. Since cost will be of

primary consideration in waste water treatment, materials such as NH_2-MIL-53(Al) and NH_2-MIL-101(Al) could be promising candidates for a commercial adsorbent for removal of Cr(VI) since NH_2-MIL-53(Al) and NH_2-MIL-101(Al) will have lower material cost. These materials also have a very large surface area of 1882 m^2/g [1] and 1968 m^2/g [2], respectively.

2. The amino functionalized KIT-6 shows a good potential for water treatment, and low levels of Cr(VI) could be achieved so that the treated water conforms to the standard for drinking water. In the future, the integration of this material in a column treatment process should be investigated to establish that the material can be completely regenerated, and that the absorption level can be maintained over long periods of time.

3. The heterojunction materials containing NH_2-MIL-125(Ti)/metal oxide and NH_2-MIL-125(Ti)/metal oxyhalides that were described in chapter 6 and chapter 7 possess significantly enhanced photocatalytic activity compared with P25 for the degradation of RhB under sunlight irradiation. To further prove the universality of the concept that formation of heterojunctions between MOF and metal oxide leads to a suppression of electron-hole recombination and increased photocatalytic quantum yield, other MOF materials should be investigated. Promising candidates for

such an investigation are the systems NH_2-UIO-66, NH_2-UIO-53(Fe) and NH_2-MIL-101(Al) with various metal oxides.

8.3 References

[1] X. Cheng, A. Zhang, K. Hou, M. Liu, Y. Wang, C. Song, G. Zhang, X. Guo, Dalton Trans., 42 (2013) 13698.

[2] B. Seoane, C. T ález, J. Coronas, C. Staudt, Sep. Sci. Technol., 111 (2013) 72.